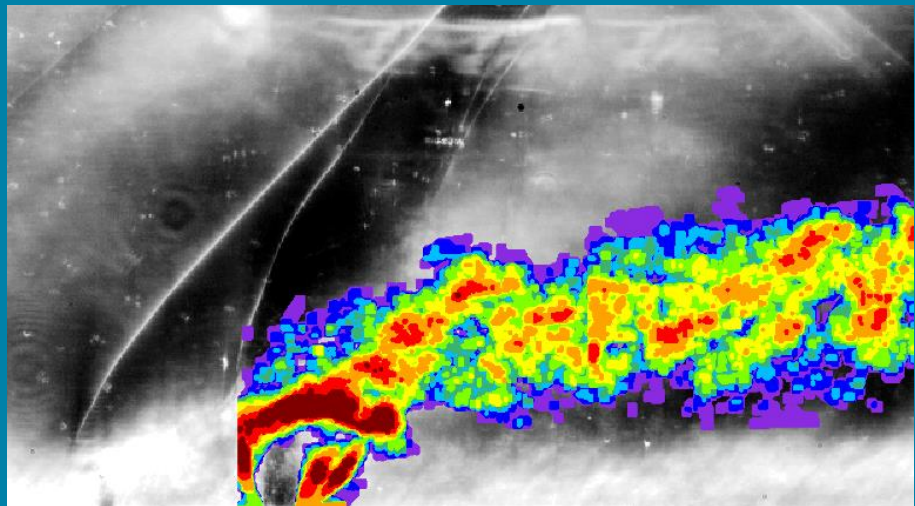# Investigation of Behaviour of Jet Shear Layer in Tandem Dual Jet Injection in Supersonic Crossflow using Schlieren Images

Jan Siemen Smink

Faculty of Engineering Technology
Program of Mechanical Engineering
Chair of Engineering Fluid Dynamics

UNIVERSITY OF TWENTE.

Preface

During my study Mechanical Engineering, I have always had a wide interest in many topics. However, over the years, it appeared that my largest interest within Mechanical Engineering was in the specialization of Fluid Dynamics and Thermal Engineering. In the run up to the Master's assignment, I had several conversations with prof. dr. ir. C.H. Venner – chairman of the Engineering Fluid Dynamics group – for finding an assignment. The moment he mentioned the possibility of doing a Master's assignment in the field of experimental supersonic flows under supervision of prof. dr. ir. H.W.M. Hoeijmakers – former chairman of the Engineering Fluid Dynamics group – , I was directly highly interested, although not having any experience with that field of study until that moment. I have not regretted choosing this assignment and it was even more interesting than could be expected beforehand. It was an assignment which combined my interests in theoretical and experimental physics, mathematics and programming.

Rapidly after the start of the Master's assignment, the Corona pandemic plagued our world and caused a change from everyday working at the university to working at home. This was an extraordinary time. As a result of the national lockdown, university facilities were not available anymore for doing experimental research, which also affected my planned research in the supersonic wind tunnel facility. However, thanks to the effort of ing. W. Lette, prof. dr. ir. H.W.M. Hoeijmakers and prof. dr. ir. C.H. Venner, the possibility was obtained to manufacture the required injection blocks and for performing the experiments during a week in July. Performing experiments within a week was challenging, but with the esteemed help of ing. W. Lette and prof. dr. ir. H.W.M. Hoeijmakers with the experiments, results could be obtained which I could analyse.

I would like to thank prof. dr. ir. H.W.M. Hoeijmakers for his supervision during my Master's assignment. I really appreciated the conversations and discussions we had during our meetings. These discussions lifted my ideas and the results to a higher level. Furthermore, I am grateful for his enthusiasm for the research, which supported me during the assignment. In addition, when there was a moment that I experienced adversity, he rapidly contacted me such that he could put this into perspective, which reassured me.

I would also like to thank ing. W. Lette – technician of the Engineering Fluid Dynamics group – for his support with respect to the experiments and their preparation. During the months of national lockdown, we had many phone calls about the possibilities for performing experiments in the supersonic wind tunnel facility and the manufacture of the injection blocks. Furthermore, he helped me during a week with performing the experiments. The collaboration and exchange of knowledge we had during these days was helpful and really pleasant.

Furthermore, I would like to thank prof. dr. ir. C.H. Venner for the many conversations we had before and during the assignment regarding the research I was doing and the prospects for doing research as a PhD student after graduation. I am grateful for his enthusiasm and inspiration for the research I was pursuing and am aiming to pursue.

Finally, I would like to thank all people standing near to me during the last year and making it a wonderful cap stone of my study Mechanical Engineering!

Enschede, November 2020

Jan Siemen Smink

Summary

In aviation, often jet engines are used for propulsion. There are several types of jet engines, each designed for a specific range of velocities of flight. For relatively low flight velocities (up to Mach 3), turbofans and turbojets are used. Ramjets are used for propulsion at flight velocities from Mach 2 to 6, while scramjets are used for flight velocities from Mach 5 and up. In scramjets, the flow is decelerated to a lower supersonic Mach number through a converging channel in which the pressure increases. In the resulting high-pressure high-temperature flow, fuel injection and combustion take place. Towards the exhaust nozzle, the flow accelerates to high supersonic speed. As a result, the aircraft experiences forward thrust.

For the efficiency of the combustion process and minimisation of the length of the scramjet engine, it is important that fuel is mixed rapidly with the air flow. For the mixing, fuel is transversely injected in the supersonic crossflow. Tandem dual jet injection has been proven to be more efficient in mixing than single jet injection. This is the motivation behind the present investigation of tandem dual jet injection in supersonic crossflow. The research question is:

What is the behaviour of the jet shear layer in tandem dual jet injection?

In analysing transverse jet injection, a number of phenomena become apparent. In front of each injection point, a bow shock forms. Downstream of the bow shock, the jet penetrates the supersonic crossflow and mixes with the flow passing through the bow shock. The upper boundary of the mixing area is determined by the (time-dependent) position of the jet upper shear layer at the upper side of the jet plume. These phenomena are observed in several studies on injection in supersonic flow but, have not been fully characterized yet for tandem dual jet injection. Therefore, for answering the research question, the behaviour of the bow shocks, the behaviour of the jet upper shear layer and the behaviour of the jet plume are investigated for different values of two parameters: the jet-to-crossflow momentum flux ratio J and the dimensionless distance between the jet orifices S. The Mach number of the crossflow is fixed at $M_c = 1.55$.

For investigation of tandem dual jet injection, experiments have been performed in the supersonic wind tunnel facility at the University of Twente. The air is injected at sonic speed into the supersonic crossflow ($M_c = 1.55$) of air. This has been performed for several combinations of J and S. The jet orifices have a diameter of $D_1 = 1$ mm and $D_2 = 2$ mm for the upstream and downstream jet, respectively, resulting in an equivalent diameter of $D_t = 2.23$ mm. In the experiments, the flow was visualized by the Schlieren technique. Using a semi-automatic algorithm, quantitative analyses have been achieved of the obtained images.

The experiments for dual jet injection showed that the bow shocks that appear in front of the two jets have an oscillatory behaviour, induced by large-scale structures. At $M_c = 1.55$, the two bow shocks merge at a certain time-averaged position ($\xi = x/D_t$, $\eta = y/D_t$), described by:

$$\xi(J, S) = 0.114 J^{-1.864} S^{4.229} \tag{1}$$

$$\eta(J, S) = 1.924 J^{-0.572} S^{1.827} \tag{2}$$

These relations are valid for at least $2.8 \leq J \leq 4.8$, $3.59 \leq S \leq 5.38$ and $M_c = 1.55$, with an upper limit of $\eta = 19.3$, due to the height of the wind tunnel in which the experiments were carried out. The position of the merger point did not appear to have an effect on the penetration of the jet shear layer

The behaviour of the jet upper shear layer as observed in the experiments endorses results in literature at comparable conditions. The time-dependent location of the jet upper shear layer that appears to be periodic is observed, which indicates the possibility of the presence of a Kelvin-Helmholtz type of instability in the shear layer. The penetration of the jet upper shear layer into the supersonic crossflow depends on J and S. At constant S, penetration increases with increasing J. Furthermore, at constant J, penetration shows to have a maximum for a certain value of S: $S_{optimal} = 4.732 J^{0.288}$. The location of the jet upper shear layer can be described by a fit without shift ($y/D_t = c_1 (x/D_t - c_3)^{c_2}$) and a fit with shift ($y/D_t = c_1 ((x/D_t - c_3)^{c_2} + c_4)$). Because of better performance, the fit with shift is recommended. Similarity analysis shows that the location of the jet upper shear layer y/D_t can be described by the following function of x/D_t, J and S:

$$\frac{y}{D_t}\left(\frac{x}{D_t}; J, S\right) = 0.432 J^{0.461} \left(2 + \exp\left(-\frac{1}{2}\left(\frac{S - 4.732 J^{0.288}}{6.103 J^{-0.521}}\right)^2\right)\right) \left(\left(\frac{x}{D_t} + 0.68\right)^{0.333} + 0.80\right) \quad (3)$$

This function is based on results for $J \in [2.8, 3.8]$, $S \in [0 : 9.87]$, $M_c = 1.55$ and validated for $J = 4.8$ with $S = [0, 5.38]$ and $M_c = 1.55$. The coefficient of determination $R^2 = 0.739$ is thought to be acceptable.

The mixing of the jet with the supersonic crossflow is dominated by the penetration of the jet upper shear layer, specifically a measure of the mixing is the bandwidth of the jet upper shear layer. Tandem dual jet injection achieves an enhanced mixing compared to single jet injection. This is also clear from an enlargement of the jet plume for tandem dual jet injection compared to single jet injection.

In conclusion, the jet shear layer in tandem dual jet injection has an oscillatory, supposedly periodic behaviour with a certain bandwidth. Its penetration into the supersonic crossflow and mixing with that crossflow is enhanced for tandem dual jet injection compared to single jet injection. At constant J, the penetration depth has an optimum for a specific value of S, while at constant S, penetration increases with increasing J.

Nomenclature

Symbol	Unit	Description
A	[m^2]	Cross-sectional area of a flow
a	[m/s]	Speed of sound
a	[m]	Horizontal dimension of an eddy
a	[m]	Part of the light source slit that is not blocked by a knife
b	[m]	Vertical dimension of an eddy
b	[m]	Width of a light source slit
$b_1, b_2, ...$	[-]	Constant
C	[-]	Contrast of a Schlieren image
C_p	[-]	Pressure coefficient
C_{ps}	[-]	Pressure coefficient at the sonic point
C_D	[-]	Drag coefficient
c	[m/s]	Local light speed
c_0	[m/s]	Light speed in a vacuum
$c_1, c_2, ...$	[-]	Constant
c_p	[J/kgK]	Specific heat at constant pressure
c_v	[J/kgK]	Specific heat at constant volume
D	[m]	Diameter of a circular shape
D_1, D_2	[m]	Diameter of the upstream and downstream jet orifices, respectively
D_t	[m]	Total or equivalent diameter
$d_1, d_2, ...$	[-]	Constant
$\vec{e}_x, \vec{e}_y, \vec{e}_z$	[-]	Unit vector
$e_1, e_2, ...$	[-]	Constant
f	[N/m^3]	Volume forces on a fluid
f	[m]	Focal point of a lens
f_j	[Hz]	Preferred mode frequency
g	[m/s^2]	Gravity constant
H	[J/kg]	Enthalpy, $H = E + \frac{p}{\rho}$
h	[J/kg]	Specific enthalpy
h	[m]	Height of a light source slit
J	[-]	Jet-to-crossflow momentum flux ratio
k	[W/mK]	Conductivity of a fluid
k	[1/m]	Wave number
$k_1, k_2, ...$	[-]	Constant
L	[m]	Characteristic length scale
M	[-]	Mach number, $\frac{u}{a}$
$\mathcal{M}$	[g/mol]	Molecular mass
$\dot{m}$	[kg/s]	Mass flow
n	[-]	Refraction index
$\vec{n}$	[-]	Normal vector
p	[N/m^2]	Pressure

Table 1: Nomenclature of parameters

p_{eb}	[N/m^2]	Effective back pressure
$\dot{Q}$	[W/m^3]	Heat source
q	[W/m^2]	Heat conduction
R	[J/kgK]	Specific gas constant
R	[m]	Radius
R^2	[-]	Coefficient of determination
Re	[-]	Reynolds number, $\frac{\rho U L}{\mu}$
$r_{j,c}$	[-]	Velocity ratio of velocity j over velocity c
S	[-]	Dimensionless dual distance between two jet orifices
S_{pivot}	[-]	Pivoting value of S whether the bow shocks merge or remain spatially separated
St	[-]	Strouhal number
s	[J/kgK]	Specific entropy
s	[m]	Distance along the jet axis
$\bar{s}$	[-]	Scaled distance along the jet axis
$s_{j,c}$	[-]	Density ratio of density j over density c
T	[K]	Temperature
T	[s]	Period of time
T_e	[s]	Exposure time of a photosensitive sensor
T_p	[s]	Pulse width or pulse time of a pulsed light source
t	[s]	Time
$\vec{t}$	[-]	Tangent vector
U	[m/s]	Velocity of a flow
u	[m/s]	(Local) velocity of a flow
x	[m]	Spatial coordinate
y	[m]	Spatial coordinate
y	[m]	Penetration depth
Y	[-]	Mass fraction
z	[m]	Spatial coordinate
α	[°]	Angle of jet incidence
β	[°]	Angle of the shock inclination w.r.t. the solid surface
β	[-]	$1 - \mathrm{M}^2$
γ	[-]	Ratio of specific heats, c_p/c_v
δ	[m]	Thickness of a shock wave
δ	[m]	Boundary layer thickness
δ	[m]	Jet shear layer thickness
δ_{BW}	[m]	Bandwidth of the jet upper shear layer
δ_{MD}	[°]	Mach disk rotation
δ_{plume}	[m]	Jet plume height
δ_s	[-]	Shock detachment distance or stand-off distance
ε	[-]	Schlieren refraction angle
ζ	[m]	Vertical displacement of a disturbance
η	[-]	Pressure ratio
η	[-]	Coordinate y/D_t of the merger point of the bow shocks
η_m	[-]	Mixing efficiency
θ	[°]	Angle of the flow inclination downstream of the shock w.r.t. the solid surface
θ_s	[°]	Inclination angle of the surface sonic point
κ	[m^3/kg]	Gladstone-Dale coefficient
λ	[m]	Wavelength
λ	[-]	Eigenvalue of a partial differential equation
μ	[Pa s]	Dynamic viscosity
μ	[°]	Mach-angle
ν	[rad]	Prandtl-Meyer function

Table 1: Nomenclature of parameters

ξ	[1/m]	$\sqrt{k^2\beta^2 + \left(\frac{2M^2}{U}\right)k\omega - \frac{\omega^2 M^2}{U^2}}$
ξ	[-]	Coordinate x/D_t of the merger point of the bow shocks
ρ	[kg/m^3]	Density of a fluid
ρ_{pix}	[pixels/m]	Pixel density of an image
τ	[N/m^2]	Shear stress within a fluid
Φ	[m^2/s]	Velocity potential
ϕ	[m^2/s]	Infinitesimal velocity potential
ω	[rad/s]	Frequency

Table 1: Nomenclature of parameters

Subscript	Description
avg	Average value
conv	Concerning a convective flow
d	In a discontinuity (of a shock)
e	Concerning passage exit conditions
i	Imaginary part of a parameter
i	Index
j	Concerning a jet flow
j	Index
MD	Concerning the Mach disk
n	Normal component of a vector
r	Real part of a parameter
t	Tangential component of a vector
0	Concerning a total physical quantity
0	Initial value
1	Upstream of a shock wave
1	The first of two parallel flows
2	Downstream of a shock wave
2	The second of two parallel flows
3	Downstream of a reflected shock
∞	Ambient region conditions

Table 2: Nomenclature of subscripts

Superscript	Description
$*$	At a throat

Table 3: Nomenclature of superscripts

x

Contents

Chapter 1

Introduction

Flying has always been the fascination of mankind. The first aircraft did not fly at high speed, but as a result of increased power of propulsion systems, the flight speed increased accordingly. The flight speed was at the start of the aviation era subsonic (from the Latin *sub* (under) and *sonus* (sound): slower than sound). However, interest in high-speed flight was rapidly growing. Flight speed increased over the years from high subsonic towards supersonic speeds (from the Latin *super* (above) and *sonus* (sound): faster than sound). The threshold of the era of supersonic aviation was the fifth Volta Conference in Rome, in 1935, titled "High Velocities in Aviation". In this by-invention-only conference, prominent fluid dynamicists such as Ludwig Prandtl, Albert Betz, Theodor von Kármán, Geoffrey Ingram Taylor and Jakob Ackeret were present [1]. Also present was Adolf Busemann, who had developed the first practical supersonic windtunnel for aerodynamic testing [2]. During the conference, he presented his advanced and in hindsight high-impact paper, called *"Aerodynamischer Auftrieb bei Überschallgeschwindigkeit"* (English: Aerodynamic Forces at Supersonic Speeds), in which he introduced the concept of the swept wing that offers potency to reduce the large drag which is experienced when flying supersonic. Therefore, it was possible to fly at larger speed before a large drag increase would be encountered [1]. From this moment on, the era of supersonic aviation has commenced.

By the end of World War II, supersonic flight became more a more dominant study of aerodynamics. The development continued with supersonic aircrafts such as the airliner Concorde and the reconnaissance aircraft Lockheed SR-71 (Blackbird) [2]. Although nowadays civil aviation concerns subsonic flight due to the large fuel consumption and sonic-boom nuisance of supersonic aviation [3], military aircrafts are capable of flying at supersonic speeds. An example is the Joint Strike Fighter (JSF) program that resulted in the F-35 Lightning II [4]. Therefore, supersonic flight is certainly a focus of aeronautical studies.

The terms subsonic and supersonic are both related to the speed of sound a. Sound propagates at a certain speed dependent on the medium in which it propagates, as well as on the temperature. For example, the speed of sound in air, at a temperature of 288 K, is 340 m/s. The velocity of an aircraft or a flow u relative to the speed of sound is expressed in terms of a dimensionless number, which is the Mach number M [5]:

$$\text{M} \equiv \frac{u}{a} \tag{1.1}$$

Therefore, aircrafts that fly slower than the speed of sound fly subsonic (M < 1) and those that fly faster than the speed of sound fly supersonic (M > 1). A regime in which both subsonic and supersonic speed is involved, is called transonic (0.8 < M < 1.2). In addition, a velocity equal to the speed of sound is called sonic speed (M = 1). Furthermore, really high velocities, M > 5, are called hypersonic [6].

When operating at speeds above the speed of sound, pressure disturbances cannot propagate in upstream direction through the flow field, because pressure disturbances move at the speed of sound. As a result, flow features such as shock waves and the so-called sonic-boom appear when increasing at the flight speed from subsonic to supersonic. Therefore, analysis of the flows at supersonic and transonic speeds involves more flow features than flows at subsonic speeds [5].

To achieve sustained supersonic flight velocities, propulsion systems are needed, appropriate for high speed. These systems produce thrust by expelling a jet of high speed flow, so that by Newton's third law

a force results in the direction of flight. Propulsion at high flight speeds can be achieved by jet engines, or rocket engines. In aviation, jet engines are mostly used. Jet engines need oxygen for combustion of fuel. That is why these air-breathing engines are limited to certain altitudes, because at too high altitude, the oxygen content of air is too low for efficient combustion [3].

Jet engines for supersonic propulsion have an approximately universal lay-out: Supersonic flow is decelerated to a lower Mach number through a converging channel in which the pressure and temperature increase. In the resulting high-pressure, high-temperature flow, (gaseous) fuel injection and combustion take place. The resulting high-pressure high-temperature flow moves through the exhaust nozzle in which the flow accelerates to high supersonic speed and is ejected in downstream direction. As a result, the aircraft experiences forward thrust.

There are a number of types of jet engines, each having their own advantages and disadvantages related to the flight speed. Figure 1.1 shows three types of jet engines: the turbojet, the ramjet and the scramjet.
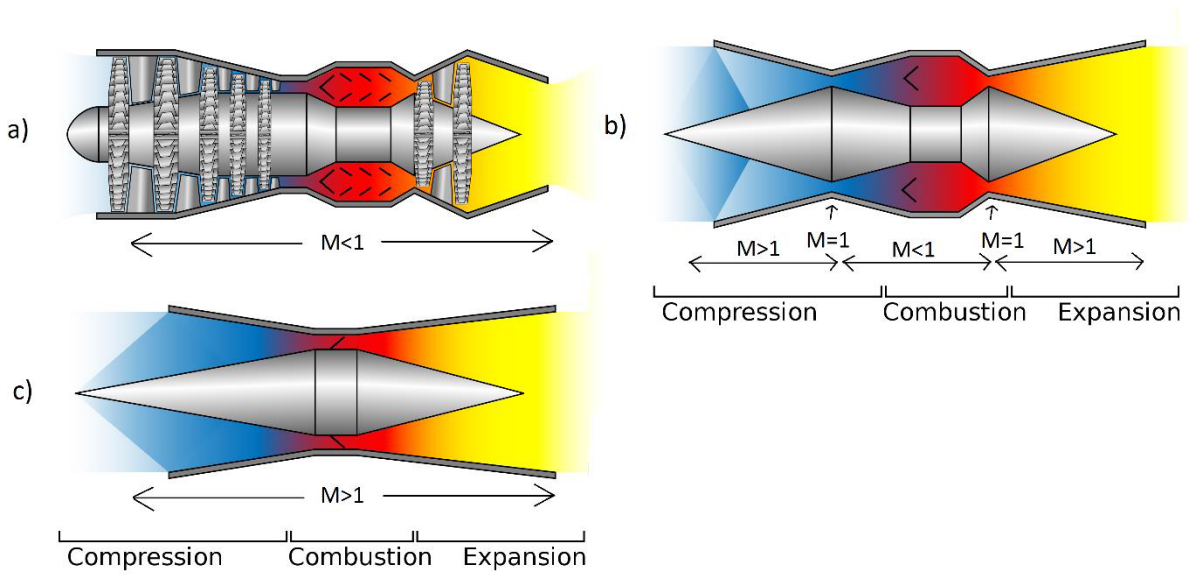

Figure 1.1: Schematic of types of jet engines for supersonic flight. a) Turbojet with subsonic internal flow. b) Ramjet with supersonic flow at inlet and outlet, but subsonic flow in the combustor. c) Scramjet in which the flow is supersonic throughout the whole engine [7].

Turbojets can be employed at relatively low supersonic speeds (M < 3), but are the most efficient at subsonic speeds. Turbojets use a compressor for compression of the incoming air. Supersonic flow input would damage the turbomachinery blades. Therefore, the compressor inlet is limited to a relatively low subsonic flow (around M = 0.3). However, due to the rotation of the blades, at the tip of the largest blades, flow velocities close to supersonic speed are obtained, despite the incoming flow of M = 0.3. That is why supersonic freestream flow is firstly slowed down to low subsonic speeds before entering the compressor [7]. The compressor is driven by a turbine downstream of the combustor. If the incoming supersonic flow has a too high velocity, then the increase of temperature and pressure may be too large for an efficient combustion process. In that case, a ramjet is a better option for propulsion.

Ramjets are employed in the range 2 < M < 6. These engines do not use a compressor with rotating parts such as a turbojet, but compress the incoming air by the so-called ram effect. That is why higher supersonic speeds are needed for operation. In the inlet, air is decelerated in the converging channel to sonic speed M = 1 at the throat, i.e. the narrowest cross-section. Subsequently, the channel expands. As a result, the flow speed within the engine is decreased to subsonic speed in the combustor. After ignition of the fuel-air mixture, the air speed increases again to supersonic speed in the diverging exhaust channel. For flight speeds towards M = 5, it is discouraged to use ramjets, because the deceleration of the flow to subsonic speed would result in a too large temperature rise and low efficiency of combustion. Therefore, at hypersonic flight speeds, scramjets are employed [8].

Scramjets (supersonic combustion ramjet) are employed at hypersonic flight speeds (M > 5), up to

about M = 12. Similar to the ramjet, flow is decelerated in the converging inlet, but now not to sonic speed but to a low supersonic Mach number by the ram effect. In contrast to the ramjet, the flow is not decelerated to subsonic speed, but remains supersonic. Otherwise, the pressure and temperature rise would possibly be too high for stable and efficient combustion. After combustion, the flow accelerates in a diverging channel to higher supersonic Mach numbers. In the combustor, fuel is injected into a supersonic crossflow. However, compared to fuel injection into a subsonic crossflow – as is the case for turbojets and ramjets – when injecting gaseous fuel into a supersonic crossflow, more complex flow features occur [8].

The focus of the present study is on the flow features that have an effect on the efficiency of combustion in a scramjet engine. For the efficiency of the combustion and minimisation of the length of the scramjet, it is important that fuel is mixed rapidly with the air flow, while maintaining the momentum of the air flow as much as possible. For the mixing, fuel is transversely injected into the supersonic crossflow. For gaseous fuel injection, the configuration of the jet is important for the mixing process. Many studies have been carried out into single jet injection into a supersonic crossflow. However, it appears that tandem dual jet injection is more efficient in mixing than single jet injection [3]. That is the motivation behind the present investigation of tandem dual jet injection in a supersonic crossflow.
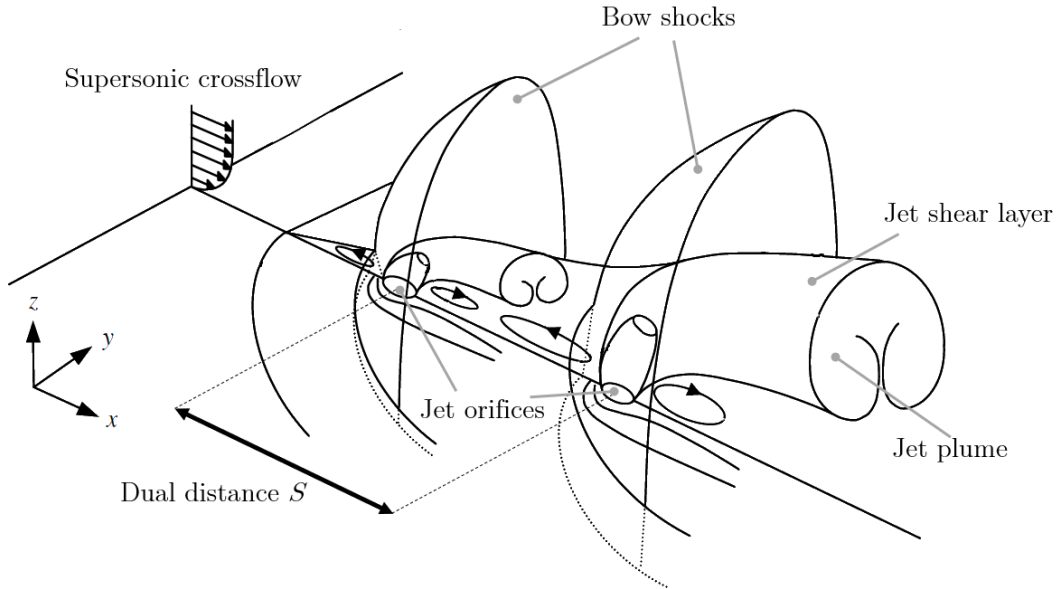
Figure 1.2: Schematic of tandem dual jet injection into a supersonic crossflow, based on [9].

In analysing transverse injection of a sonic jet, a number of phenomena become apparent, see figure 1.2. In front of each injection point, a bow shock forms. Downstream of the bow shock, the jet penetrates the crossflow and mixes with the predominantly supersonic flow that has passed through the bow shock. The upper boundary of the mixing area is determined by the (time-dependent) position of the jet shear layer that constitutes the upper side of the jet plume. These phenomena are observed in several studies of injection in supersonic flow, but have not been fully characterized yet for tandem dual jet injection.

Therefore, in this research, the behaviour of the jet shear layer in tandem dual jet injection in a supersonic crossflow will be investigated in detail. Two governing parameters, the jet-to-crossflow momentum flux ratio J (the proportion of the momentum of the jet as fraction of the momentum of the crossflow) and the dual distance S (the dimensionless distance between the two jet orifices), are leading in this investigation.

1.1 Research Goals

The research question for the present study is stated as follows:

What is the behaviour of the jet shear layer in tandem dual jet injection?

This research question is addressed through the following sub-questions:

1. What is the behaviour of the bow shocks that appear in front of each of the two jets? For which conditions do the two bow shocks merge rather than remain spatially separated? In addition, if the bow shocks merge, how is the position of the merger point of the bow shocks characterized? Does the position of this merger point have an effect on the penetration of the jet shear layer?

2. What is the behaviour of the jet upper shear layer as a function of the jet-to-crossflow momentum flux ratio J and the dimensionless dual distance S? What is an appropriate fit for describing the time-averaged location of the jet shear layer? Is there an appropriate similarity type of scaling in terms of S and J? What is the behaviour of the bandwidth in the location of the jet upper shear layer?

3. How could the jet plume be characterized from quantifications for the location of the time-averaged jet upper shear layer, the jet center line and the jet lower shear layer?

These research questions are considered, based on experimental research in the supersonic wind tunnel facility at the University of Twente, in which the flow is visualized by Schlieren techniques. Before addressing the research questions, a literature research has been performed.

Chapter 2 discourses the fundamentals of supersonic flow phenomena, with a focus on shock behaviour. Chapter 3 elaborates on jet injection in still air and gives insight in the behaviour of the jet for the case a crossflow is absent. The knowledge of chapter 2 and chapter 3 is combined in chapter 4. In this chapter, an extensive description of various phenomena occurring in single jet injection into a supersonic crossflow is presented. Focus is on the bow shock in front of the jet, the penetration of the jet into the crossflow and the behaviour of the jet shear layer. The knowledge in chapter 4 of single jet injection is extended to tandem dual jet injection in chapter 5. This chapter focuses on the behaviour of the bow shocks and the behaviour of the penetration of the two jet into the crossflow. Subsequently, chapter 6 provides a description of the Schlieren and imaging techniques as used in the experiments.

In chapter 7, the methodology of the study is detailed with respect to the wind tunnel, injection and Schlieren set-up. Also, there is another focus on the analysis methodology as applied to the results of the Schlieren images. Chapter 8 describes and analyses the results on the behaviour of the bow shocks and the behaviour of the jet. Finally, conclusions are presented in chapter 9 and recommendations for future research are provided in chapter 10.

Chapter 2

Supersonic Flow Phenomena

Supersonic flows have velocities above the speed of sound (M > 1) at every point in the flow. That is why the speed of sound a is a key parameter in supersonic flows. The definition of the speed of sound is:

$$a^2 = \left(\frac{\partial p}{\partial \rho}\right)_S \tag{2.1}$$

In this expression, p is the pressure, ρ the density and S the entropy. For a calorically perfect gas, the speed of sound can be expressed as:

$$a = \sqrt{\gamma R T} \tag{2.2}$$

In this expression, γ is the ratio of the specific heats, R is the specific gas constant and T is the absolute temperature. As a result, the Mach number (equation 1.1) for a calorically perfect gas depends on the gas composition, the temperature and the velocity.

The theory of isentropic flow is detailed in section 2.1. The flow phenomena that are seen in supersonic flows are significantly different from those in subsonic flows, despite both are fully described by the same system of equations, i.e. the Navier-Stokes equations, supplemented by thermodynamic relations. Especially characteristic for a supersonic flow is the formation of shock waves, which are fronts at which fluid is compressed. The different types of shock waves are detailed in section 2.2. Section 2.3 elaborates on the flow through nozzles and diffusers. The theory of this chapter is applied to the flow through supersonic wind tunnels in section 2.4.

2.1 Isentropic flows

The governing equations used in supersonic flows are the Navier-Stokes equations for compressible flow. These consist of mass conservation, momentum conservation (Newton's second law) and energy conservation (first law of thermodynamics). These are given in the following non-conservation form [5]:

$$
\begin{aligned}
\frac{\mathrm{D}\rho}{\mathrm{D}t} + \rho \vec{\nabla} \cdot \vec{u} &= 0 \\
\rho \frac{\mathrm{D}\vec{u}}{\mathrm{D}t} &= \rho \vec{f} - \vec{\nabla} p + \vec{\nabla} \cdot \bar{\bar{\tau}} \\
\rho \frac{\mathrm{D}E}{\mathrm{D}t} &= \rho \vec{f} \cdot \vec{u} - \vec{\nabla} \cdot (p\vec{u}) + \vec{\nabla} \cdot (\bar{\tau} \cdot \vec{u}) + \dot{Q} - \vec{\nabla} \cdot \vec{q}
\end{aligned}
\tag{2.3}
$$

in which $\vec{u}$ is the velocity vector, p is the pressure, ρ is the density and E is the total energy $E = e + \frac{1}{2}|\vec{u}|^2$, with e the internal energy. For the viscous stress tensor $\bar{\bar{\tau}}$ and the heat flux vector $\vec{q}$, additional constitutive relations are required.

In supersonic flows, the velocities are very high and therefore, the Reynolds numbers are very high too. This makes that the viscous effects are mostly confined to thin regions, which effects can often be neglected. Together with this assumption, heat conduction is neglected as well. The underlying assumption is that flow separation does not occur. Applying these simplifications to the Navier-Stokes

equations, results in the Euler equations for inviscid, non-heat-conducting flow. These are in conservation form [5]:

$$\frac{\partial U}{\partial t} + \vec{\nabla} \cdot \vec{F}^{inv} = J \tag{2.4}$$

with

$$U = \begin{pmatrix} \rho \\ \rho\vec{u} \\ \rho E \end{pmatrix}; \quad \vec{F}^{inv} = \begin{pmatrix} \rho\vec{u} \\ \rho\vec{u}\vec{u} + p\bar{I} \\ \rho\vec{u}H \end{pmatrix}; \quad J = \begin{pmatrix} 0 \\ \rho\vec{f} \\ \rho\vec{f}\cdot\vec{u} + \dot{Q} \end{pmatrix} \tag{2.5}$$

where the total enthalpy $H = E + \frac{p}{\rho}$. When not dealing with shock waves, a common assumption for a supersonic flow is isentropicity. This means that the entropy is assumed to be constant ($ds = 0$) and implies an adiabatic ($\dot{q} = 0$) and reversible process [6]. Furthermore, external forces are omitted and a calorically perfect gas is assumed. The governing equations in such processes are stated by (in 1D time-dependent cases) [5]:

$$\frac{\partial \rho}{\partial t} + \frac{\partial}{\partial x}(\rho u) = 0$$
$$\frac{\partial}{\partial t}(\rho u) + \frac{\partial}{\partial x}\left(\rho u^2 + p\right) = 0 \tag{2.6}$$
$$p = p(\rho)$$

Using these equations, the so-called the **isentropic-flow relations** are obtained [5]:

$$\frac{a^2}{a_\infty^2} = \left[1 + \frac{\gamma - 1}{2}\mathrm{M}_\infty^2\left(1 - \frac{u^2}{U_\infty^2}\right)\right]$$
$$\frac{p}{p_\infty} = \left[1 + \frac{\gamma - 1}{2}\mathrm{M}_\infty^2\left(1 - \frac{u^2}{U_\infty^2}\right)\right]^{\frac{\tau}{\gamma-1}}$$
$$\frac{\rho}{\rho_\infty} = \left[1 + \frac{\gamma - 1}{2}\mathrm{M}_\infty^2\left(1 - \frac{u^2}{U_\infty^2}\right)\right]^{\frac{1}{\gamma-1}} \tag{2.7}$$
$$\frac{T}{T_\infty} = \left[1 + \frac{\gamma - 1}{2}\mathrm{M}_\infty^2\left(1 - \frac{u^2}{U_\infty^2}\right)\right]$$

In these relations, the reference (subscript ∞) and local (no subscript) values are used and related to each other. In another form and making use of the stagnation condition ($u = 0$, $p = p_0$, $\rho = \rho_0$, $T = T_0$ and $a = a_0$), the following relations are derived from equation 2.6 [5]:

$$\frac{a_0^2}{a^2} = \left[1 + \frac{\gamma - 1}{2}\mathrm{M}^2\right]$$
$$\frac{p_0}{p} = \left[1 + \frac{\gamma - 1}{2}\mathrm{M}^2\right]^{\frac{\gamma}{\gamma-1}}$$
$$\frac{\rho_0}{\rho} = \left[1 + \frac{\gamma - 1}{2}\mathrm{M}^2\right]^{\frac{1}{\gamma-1}} \tag{2.8}$$
$$\frac{T_0}{T} = \left[1 + \frac{\gamma - 1}{2}\mathrm{M}^2\right]$$

Now, it is important to state some properties of the isentropic flow. In isentropic flow, the stagnation quantities p_0, ρ_0, T_0 and H_0 are constant [5]. This does not hold for shock waves, which result in an increase in entropy. On a streamline through a shock wave, upstream and downstream of a shock wave, isentropicity of a flow is a valid assumption as long as a streamline does not pass through a boundary layer. In the next section, shock waves are analysed and generation of entropy in a shock wave will become clear.

2.2 Shock waves

Shock waves are extremely thin regions within supersonic flows, across which flow properties change strongly. Disturbances created at a certain point in the supersonic flow cannot move upstream. That is an important reason for the presence of shock waves in supersonic flow and their absence in subsonic flow. In a subsonic flow, disturbances created at some point can travel with the flow as well as against the direction of the flow.

The transition of the flow properties across a shock wave can be approximated as being a discontinuous change, i.e. a jump. Assume region 1 as the flow upstream of a stationary shock wave and region 2 as the flow downstream of a shock wave. For these supersonic flows, it is characteristic that the Mach number of the flow in region 1 (M_1) is above 1 and that the Mach number of the flow in region 2 (M_2) is lower than M_1 (in the case of compression). Consequently, the pressure, density, temperature and entropy will increase across the shock wave, but the velocity component normal to the shock and total pressure will decrease, so there is a total pressure loss. Furthermore, a shock wave is adiabatic, so the total enthalpy will remain the same across the shock wave [6]. These observations can be derived from the **Rankine-Hugoniot relations** [5].

The Rankine-Hugoniot relations are derived from the Euler equations, as given in equations 2.4 and 2.5. In the Euler equations, discontinuous or weak solutions are allowed. The Rankine-Hugoniot relations are discontinuous solutions of these equations. There are a few assumptions for the flow through this shock wave [6]:

- The flow is inviscid $\rightarrow \bar{\bar{\tau}} = 0$

- The flow is non-heat conducting $\rightarrow \vec{q} = \vec{0}$

Furthermore, it is important to realize that the flow cannot be assumed to be insentropic within a shock wave, because within a shock wave, the entropy increases. The flow upstream and downstream of the shock wave can be assumed to be isentropic separately along streamlines. After implementing the assumptions and the jump in the Euler equations ($\left[\vec{F}^{inv} \cdot \vec{n}_d \right] = 0$), the following jump relations are obtained as Rankine-Hugoniot relations [5]:

$$[\rho \left(\vec{u} - \vec{u}_d \right) \cdot \vec{n}_d] = 0$$
$$\left[\rho[(\vec{u} - \vec{u}_d) \cdot \vec{n}_d]^2 + p\right] = 0$$
$$[\rho[(\vec{u} - \vec{u}_d) \cdot \vec{n}_d]\vec{u}_t] = \vec{0} \tag{2.9}$$
$$\left[\rho \left(h + \frac{1}{2} |\vec{u} - \vec{u}_d|^2 \right) [(\vec{u} - \vec{u}_d) \cdot \vec{n}_d] \right] = 0$$

In which $\vec{u}$ is the velocity of the flow and $\vec{u}_d$ is the velocity of the discontinuity, i.e. shock wave. Furthermore, it holds that the relative velocity $\vec{u} - \vec{u}_d = u_n \vec{n}_d + \vec{u}_t$, in which u_n is the normal component of the relative velocity and $\vec{u}_t$ is the component of the relative velocity in the tangential direction with respect to the shock wave. When rewriting equation 2.9 in terms of quantities in region 1 and region 2, the Rankine-Hugoniot relations for a shock discontinuity become [5]:

$$\rho_1 u_{n_1} = \rho_2 u_{n_2} \qquad \text{with} \quad u_n \equiv (\vec{u} - \vec{u}_d) \cdot \vec{n}_d$$
$$p_1 + \rho_1 u_{n_1}^2 = p_2 + \rho_2 u_{n_2}^2$$
$$\rho_1 u_{n_1} \vec{u}_{t_1} = \rho_2 u_{n_2} \vec{u}_{t_2} \quad \rightarrow \quad \vec{u}_{t_1} = \vec{u}_{t_2} \tag{2.10}$$
$$\rho_1 u_{n_1} H_{0,1} = \rho_2 u_{n_2} H_{0,2} \quad \text{with} \quad H_0 = h + \frac{1}{2} \left(u_n^2 + |\vec{u}_t|^2 \right)$$

Now assume a compression shock wave, in which the relative velocity decreases in terms of a decrease of the normal relative velocity u_n. This means that $u_{n1} > u_{n2}$. As a result of that, the density will be discontinuous too and will increase: $\rho_1 < \rho_2$.

When investigating these relations, it becomes clear that when the relative velocity changes (as is the case for a compression shock wave), that then the velocity component tangential to the shock wave has to remain the same. The same holds for the total enthalpy, which is defined as $H_0 \equiv h + \frac{1}{2}(u_n^2 + |\vec{u}_t|^2)$. For compression ($u_{n1} > u_{n2}$), specific enthalpy will increase ($h_1 < h_2$). Furthermore, $p_1 < p_2$ because of

the second relation in equation 2.10. Finally, the total pressure decreases as the flow passes through the shock wave, which can be derived from the decrease of the Mach number.

The Rankine-Hugoniot relations also allow a solution for an expansion shock wave, such that the Mach number increases as the flow passes through the shock wave. Consequently, the entropy will decrease, while the total pressure will increase. However, due to violation of the second law of thermodynamics, this is not a realistic physical case [5].

In the above approach, a discontinuous flow solution is taken for the shock wave. However, in reality, the discontinuity is a really thin region with high gradients in the flow variables. The inviscid flow solution steepening mechanism and the diffusive heat-conduction and viscous mechanisms will balance. The thickness of the shock wave can be estimated from a dimension analysis of the Navier-Stokes equations. In the Navier-Stokes equations, the term $\rho u^2 + p$ and $\mu \frac{\mathrm{d}u}{\mathrm{d}x}$ should be of the same order of magnitude. From derivation, it appears that the thickness of the shock wave δ can be expressed as being of the following order of magnitude [5]:

$$\frac{\delta}{L} = \frac{\mu}{\rho U L} = \frac{1}{Re} \tag{2.11}$$

with L being a reference length. Knowing that most supersonic applications will involve Reynolds numbers of order 10^6, then the thickness of the shock wave is rather small and the above approximation of a discontinuous solution of the inviscid-flow equations for the shock wave is valid [5].

Three types of shock waves will be addressed in the following section: the normal shock, the oblique shock and the bow shock.

2.2.1 Normal shock

Normal shocks often occur in nature. There are several cases in which normal shocks appear, such as part of a bow shock wave in front of a body and within an overexpanded flow through a nozzle [6]. The jumps in the physical quantities are described by the Rankine-Hugoniot relations as given in equation 2.10, but with the condition that $\vec{u}_t = \vec{0}$. This makes the third relation of equation 2.10 trivial. A schematic is shown in figure 2.1.

$$\rho_1 \qquad\qquad \rho_2$$
$$p_1 \qquad\qquad p_2$$
$$T_1 \quad \vec{u}_1 \longrightarrow \quad \vec{u}_2 \longrightarrow \quad T_2$$
$$H_{0,1} \qquad\qquad H_{0,2}$$
$$M_1 \qquad\qquad M_2$$
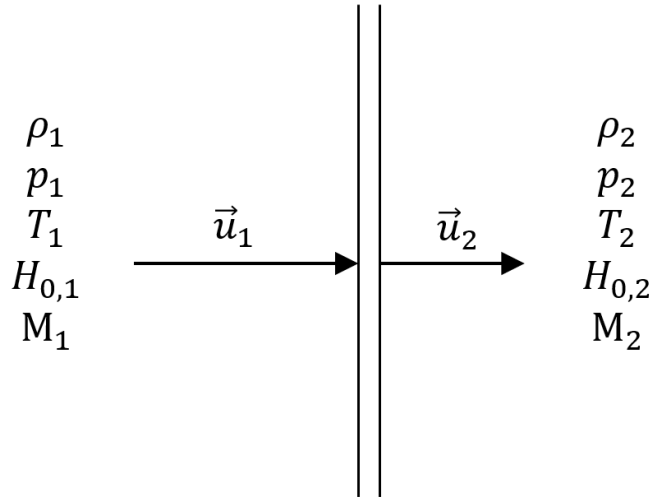
Figure 2.1: Schematic of a normal shock wave.

Using the Rankine-Hugoniot relations, the following expressions for the relation between physical quantities on the downstream side in terms of physical quantities on the upstream side of a shock wave are determined, with $M_1 > 1$. The ratios p_2/p_1 and ρ_2/ρ_1 can be determined directly from the Rankine-Hugoniot relations. Other important ratios depend on these as follows [5]:

$$\frac{\mathrm{M}_2^2}{\mathrm{M}_1^2} = \left(\frac{p_2}{p_1}\right)^{-1} \left(\frac{\rho_2}{\rho_1}\right)^{-1}$$

$$\frac{u_2}{u_1} = \left(\frac{\rho_2}{\rho_1}\right)^{-1}$$

$$\frac{T_2}{T_1} = \left(\frac{p_2}{p_1}\right) \left(\frac{\rho_2}{\rho_1}\right)^{-1} \tag{2.12}$$

$$\frac{h_2}{h_1} = \frac{e_2}{e_1} = \frac{T_2}{T_1}$$

$$\frac{p_{02}}{p_{01}} = \left(\frac{p_2}{p_1}\right)^{-\frac{1}{\gamma-1}} \left(\frac{\rho_2}{\rho_1}\right)^{\frac{\gamma}{\gamma-1}}$$

These relations above can be substituted by p_2/p_1 and ρ_2/ρ_1, resulting in the following ratios of physical variables over a normal shock wave as a function of M_1 and γ [5][6]:

$$\mathrm{M}_2 = \sqrt{\frac{1 + \frac{\gamma-1}{2}\mathrm{M}_1^2}{\gamma\mathrm{M}_1^2 - \frac{\gamma-1}{2}}}$$

$$\frac{u_2}{u_1} = \frac{1 + \frac{\gamma-1}{2}\mathrm{M}_1^2}{\frac{\gamma+1}{2}\mathrm{M}_1^2}$$

$$\frac{p_2}{p_1} = 1 + \frac{2\gamma}{\gamma+1}\left(\mathrm{M}_1^2 - 1\right)$$

$$\frac{\rho_2}{\rho_1} = \frac{\frac{\gamma+1}{2}\mathrm{M}_1^2}{1 + \frac{\gamma-1}{2}\mathrm{M}_1^2} \tag{2.13}$$

$$\frac{T_2}{T_1} = \left(1 + \frac{2\gamma}{\gamma+1}\left(\mathrm{M}_1^2 - 1\right)\right)\frac{1 + \frac{\gamma-1}{2}\mathrm{M}_1^2}{\frac{\gamma+1}{2}\mathrm{M}_1^2}$$

$$\frac{p_{02}}{p_{01}} = \left(\frac{1}{1 + \frac{2\gamma}{\gamma+1}\left(\mathrm{M}_1^2 - 1\right)}\right)^{\frac{1}{\gamma-1}} \left(\frac{\frac{\gamma+1}{2}\mathrm{M}_1^2}{1 + \frac{\gamma-1}{2}\mathrm{M}_1^2}\right)^{\frac{\gamma}{\gamma-1}}$$

$$\frac{T_{0,2}}{T_{0,1}} = 1 \quad (\text{Adiabatic})$$

The relations above show that for a normal shock wave, the flow decelerates from supersonic to subsonic flow and the higher M_1, the higher the ratio $\mathrm{M}_1/\mathrm{M}_2$ will be, thus the lower M_2 will become. For the other ratios, the same holds: the higher M_1, the larger p_2/p_1, T_2/T_1 and ρ_2/ρ_1 and the smaller p_{02}/p_{01} will become. The latter implies that the stronger the shock wave, the higher the loss in total pressure and the increase in entropy.

In the limit case of $\mathrm{M}_1 \to \infty$, some ratios have finite values:

$$\mathrm{M}_2 \to \sqrt{\frac{\gamma-1}{2\gamma}}$$

$$\frac{u_2}{u_1} \to \frac{\gamma-1}{\gamma+1}$$

$$\frac{p_2}{p_1} \to \infty$$

$$\frac{\rho_2}{\rho_1} \to \frac{\gamma+1}{\gamma-1} \tag{2.14}$$

$$\frac{T_2}{T_1} \to \infty$$

$$\frac{p_{02}}{p_{01}} \to 0$$

2.2.2   Oblique shock

Normal shock waves have stronger compressibility effects than oblique shock waves [5]. With respect to the Rankine-Hugoniot relations, the difference between normal shocks and oblique shocks is that for oblique shocks, $\vec{u}_t \neq \vec{0}$. In figure 2.2, a schematic of the flow field with an oblique shock is shown. A property of an oblique shock is that like every pressure wave, an oblique shock can be reflected within a channel with a supersonic flow [10]. More about this phenomenon is described in section 4.3.2.
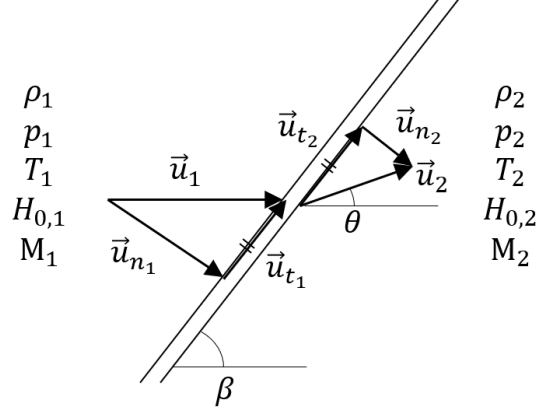

Figure 2.2: Schematic of a stationary oblique shock wave with the velocity components.

From the first and third relation of equation 2.10, it can be derived that $\vec{u}_{t_1} = \vec{u}_{t_2}$. Furthermore, two angles are introduced: β is the angle of the shock inclination with respect to the free stream and θ is the angle of the flow inclination with respect to the free stream. Note that now different components of the Mach number will be used: $\mathrm{M}_n = \frac{u_n}{a}$ for the normal velocity and $\mathrm{M} = \frac{u}{a}$ for the total velocity. Using geometrical relations, the following expressions for the Mach numbers are obtained:

$$
\begin{aligned}
\mathrm{M}_1 &= \frac{u_1}{a_1} \\
\mathrm{M}_{n_1} &= \mathrm{M}_1 \sin\beta \\
\mathrm{M}_2 &= \frac{u_2}{a_2} \\
\mathrm{M}_{n_2} &= \mathrm{M}_2 \sin(\beta - \theta)
\end{aligned}
\tag{2.15}
$$

Using the expressions above, the ratios for physical quantities over an oblique shock wave are:

$$
\begin{aligned}
\mathrm{M}_2 &= \frac{1}{\sin(\beta - \theta)} \sqrt{\frac{1 + \frac{\gamma-1}{2}\mathrm{M}_{n_1}^2}{\gamma \mathrm{M}_{n_1}^2 - \frac{\gamma-1}{2}}} \\
\frac{u_2}{u_1} &= \frac{1 + \frac{\gamma-1}{2}\mathrm{M}_{n_1}^2}{\frac{\gamma+1}{2}\mathrm{M}_{n_1}^2} \\
\frac{p_2}{p_1} &= 1 + \frac{2\gamma}{\gamma+1}\left(\mathrm{M}_{n_1}^2 - 1\right) \\
\frac{\rho_2}{\rho_1} &= \frac{\frac{\gamma+1}{2}\mathrm{M}_{n_1}^2}{1 + \frac{\gamma-1}{2}\mathrm{M}_{n_1}^2} \\
\frac{T_2}{T_1} &= \left(1 + \frac{2\gamma}{\gamma+1}\left(\mathrm{M}_{n_1}^2 - 1\right)\right)\frac{1 + \frac{\gamma-1}{2}\mathrm{M}_{n_1}^2}{\frac{\gamma+1}{2}\mathrm{M}_{n_1}^2} \\
\frac{p_{02}}{p_{01}} &= \left(\frac{1}{1 + \frac{2\gamma}{\gamma+1}\left(\mathrm{M}_{n_1}^2 - 1\right)}\right)^{\frac{1}{\gamma-1}}\left(\frac{\frac{\gamma+1}{2}\mathrm{M}_{n_1}^2}{1 + \frac{\gamma-1}{2}\mathrm{M}_{n_1}^2}\right)^{\frac{\gamma}{\gamma-1}} \\
\frac{T_{0,2}}{T_{0,1}} &= 1 \quad \text{(Adiabatic)}
\end{aligned}
\tag{2.16}
$$

The relations above are similar to the relations for the normal shock, with the difference that now explicitly the normal component of the Mach number M_{n_1} is used instead of the Mach number M_1 of the flow. When using the condition of continuity of the flow, a relation between the angles β and θ and the Mach number is obtained [5]:

$$\tan\theta = \frac{M_1^2 \sin^2\beta - 1}{\tan\beta \left[1 + \frac{1}{2}(\gamma + \cos 2\beta)M_1^2\right]} \tag{2.17}$$

Equation 2.17 is the so-called $\beta - \theta - M$-relation which gives a relation between the upstream Mach number M_1, the flow inclination θ and the shock inclination β. In figure 2.3, a plot of $\boldsymbol{\beta - \theta - M}$-**relations** for different Mach numbers is shown. In the plot, curves are present that show that β is a multivalued function of θ. So for a given θ and given M_1, there are two possibilities for β using equation 2.17. The difference of the two values of β is situated in being on the one or the other side of the maximum $\frac{\partial\theta}{\partial\beta} = 0$, i.e. when the slope of the iso-Mach line is vertical.
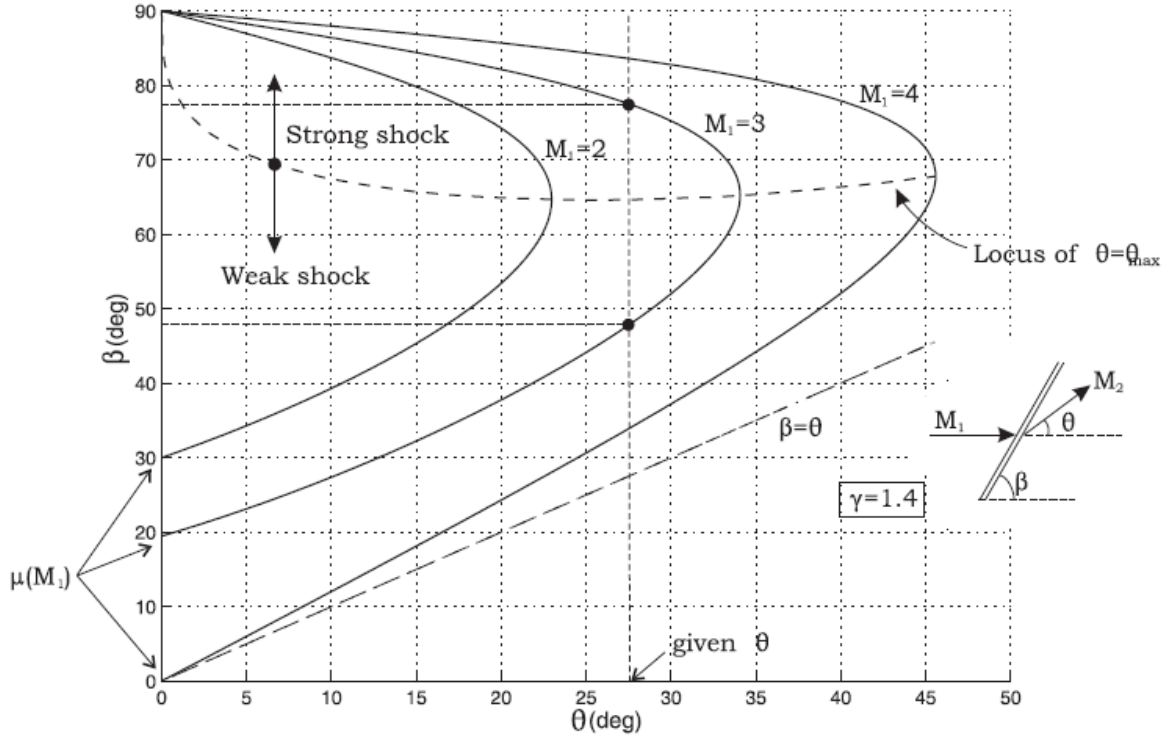

Figure 2.3: $\beta - \theta - M$-relation for several Mach numbers [5].

This maximum gives a value for the maximum permissible angle θ, which is always smaller than 45.58° for air. For $\theta > \theta_{max}$, the solution is more complex, because a straight oblique shock does not exist. Instead of a straight oblique shock, the shock will be curved, with a normal part near the wall (strong shock) and from there on a curve towards an oblique part (weak shock) of the shock with a certain β [5].

Following a curve of constant M in figure 2.3, there are two solutions for β with respect to θ. The higher value of β is the so-called strong-shock solution for which β is closest to $\pi/2$, i.e. the normal shock. The lower value of β is the so-called weak-shock solution. It appears that nature in general prefers the weak-shock solution for which θ is closest to the Mach angle μ. In the strong-shock solution, the flow becomes subsonic downstream of the shock wave and in the weak-shock solution, the flow remains supersonic [5].

If there is a small flow inclination angle, $\theta \approx 0$, then either a strong-shock solution with $\beta = 90°$ or weak-shock solution with $\beta = \mu$ is possible. Here μ is the Mach-angle, which is defined as [5]:

$$\mu = \arctan\left(\frac{1}{\sqrt{M_1^2 - 1}}\right) \qquad \text{for } M_1 > 1 \tag{2.18}$$

This equation is obtained from the analysis of characteristics for the nonlinear isentropic flow model of the Euler equations, for which the flow is assumed to be inviscid, non-heat-conducting and is not subjected to external forces or external heat sources [5]. The same expression for μ can be derived from equation 2.17, when applying $\theta = 0°$, which makes β equal to μ.

$$\mu = \arcsin\left(\frac{1}{M_1}\right) \qquad \text{for } M_1 > 1 \tag{2.19}$$

Finally, the limit for $M_1 \to \infty$ is taken in equation 2.17, which results in, using l'Hôpital's rule:

$$\tan\theta = \frac{\sin 2\beta}{\gamma + \cos 2\beta} \tag{2.20}$$

Equating the derivative equal to 0 results in the relation $\cos 2\beta = -\frac{1}{\gamma}$ for the maximum flow inclination. Using that $\gamma = 1.4$ for air, it will result in $\beta_{\theta_{max}} = 67.79°$ for $\theta_{max} = 45.58°$.

2.2.3 Bow shock

A bow shock is a wave that forms in front of a blunt body placed within a supersonic flow. This wave is detached from the body, curved and has a portion normal to the flow. Therefore, the bow shock is a combination of a normal shock and an oblique shock. If the body would be shaped such that the flow inclination angle is less than θ_{max}, then it is possible to have an oblique shock attached to the leading edge of the body. This is for example the case for wedges and sharp cones. However, bodies are often blunt, which means that the flow inclination angle is larger than 45.58°. An example of the bow shock and the flow behaviour is given in figure 2.4 [6].
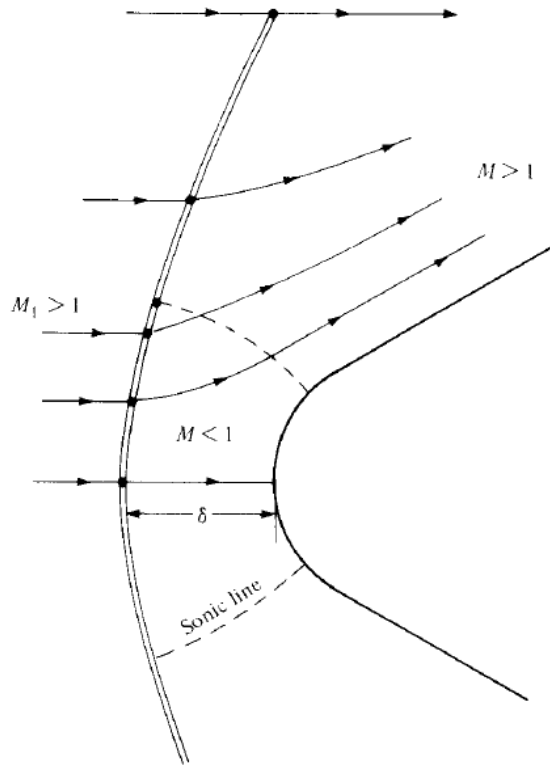

Figure 2.4: Schematic of the flow crossing a bow shock formed in front of a 2D blunt body [6].

In the case of for example a cylinder normal to the flow, a bow shock forms upstream of the cylinder, i.e. in front of the cylinder, which causes the flow to become partly subsonic. However, due to the shape of the object, the flow will accelerate to supersonic again. The interface between supersonic flow upstream and subsonic flow downstream of the bow shock is sketched by a dashed line, which is the sonic line [6].

The bow shock will be at a certain distance upstream from the body, which is called the **shock detachment distance** or **stand-off distance** δ_s. δ_s is a dimensionless number, scaled to a characteristic length. In the 1950s and 1960s, the problem of predicting this distance was a major focus of supersonic aerodynamicists [6]. A theoretical approximation of the shock detachment distance has been developed by Sinclair et al. [11]. Sinclair derived the following expression:

$$\delta_s = \frac{\beta_s^2}{\theta_s^2 \cos\beta_s} \cdot \sqrt{\frac{2 + (\gamma - 1)M_\infty^2}{2\gamma M_\infty^2 - \gamma + 1}} \tag{2.21}$$
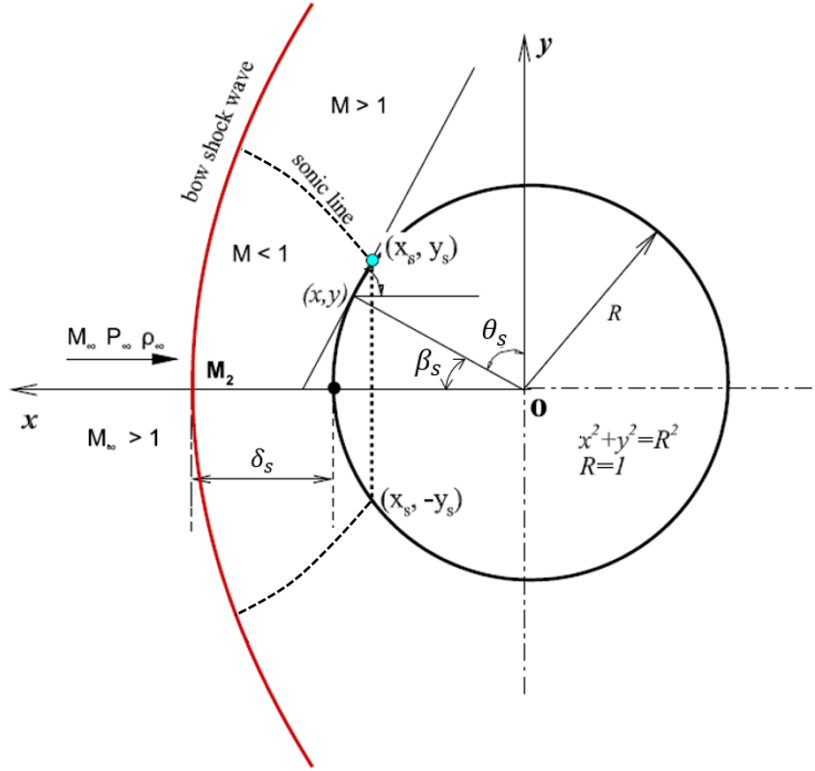

Figure 2.5: Schematic a bow shock formed in front of a cylinder [11].

In equation 2.21, the right term of the right-hand side is the Mach number downstream of the shock wave, i.e. the first expression from equation 2.16. β_s is the surface sonic angle, which is the angle between the horizontal and the position on the cylinder where at the surface the flow is sonic (the dashed line). θ_s is the inclination angle of the surface sonic point, which is about the same point as for β_s, but now with respect to the vertical. See figure 2.5. Both angles are in radians, thus: $\theta_s + \beta_s = \frac{\pi}{2}$. Using the Newtonian impact theory in the form of

$$\frac{C_{ps}}{C_{p,max}} = \sin^2\theta_s \tag{2.22}$$

and the definition of the pressure coefficient

$$C_p = \frac{2}{\gamma M_\infty^2}\left(\frac{p}{p_\infty} - 1\right) \tag{2.23}$$

it is possible to construct a relation for the angles β_s and θ_s. In this specific case of a cylinder, the following expressions for $C_{p,max}$ and C_{ps} are applied, resulting in expressions for the angles [11].

$$C_{ps} = \frac{2}{\gamma M_\infty^2} \left\{ \left(\frac{\gamma+1}{2}\right)^{-\frac{\gamma}{\gamma-1}} \left[\frac{(\gamma+1)^2 M_\infty^2}{4\gamma M_\infty^2 - 2(\gamma-1)}\right]^{\frac{\gamma}{\gamma-1}} \left[\frac{1-\gamma+2\gamma M_\infty^2}{\gamma+1}\right] - 1 \right\}$$

$$C_{p,max} = \frac{2}{\gamma M_\infty^2} \left\{ \left[\frac{(\gamma+1)^2 M_\infty^2}{4\gamma M_\infty^2 - 2(\gamma-1)}\right]^{\frac{\gamma}{\gamma-1}} \left[\frac{1-\gamma+2\gamma M_\infty^2}{\gamma+1}\right] - 1 \right\}$$

$$\theta_s = \arcsin\sqrt{\frac{C_{ps}}{C_{p,max}}}$$

$$\beta_s = \frac{\pi}{2} - \arcsin\sqrt{\frac{C_{ps}}{C_{p,max}}}$$

(2.24)

The method described above shows that the shock detachment distance depends on the location where the subsonic flow downstream of the bow shock becomes a supersonic flow. The location of this sonic line depends on the upstream Mach number M_∞ and the type of fluid (γ). The results of this method are in agreement with several experimental results, see [11].

When choosing $\gamma = 1.4$ and $M_\infty = 1.7$, the angles and shock detachment distance become: $\beta_s = 0.905$, $\theta_s = 0.666$ and $\delta_s = 1.91$, respectively. Note that δ_s is a dimensionless distance, non-dimensionalized by the radius of the cylinder. Thus in this case, the bow shock is at a distance of $1.91R$ from the cylinder.

2.2.4   Prandtl-Meyer Expansion Fan

Another type of wave, for the case of expanding flow, is the **Prandtl-Meyer Expansion Fan**. This is a two-dimensional wave that consists of an infinite number of Mach waves (calculated by equation 2.19). These waves are diverging from a sharp edge at a corner, see figure 2.6. It can be seen that the slope of the waves in the expansion fan changes with small steps.
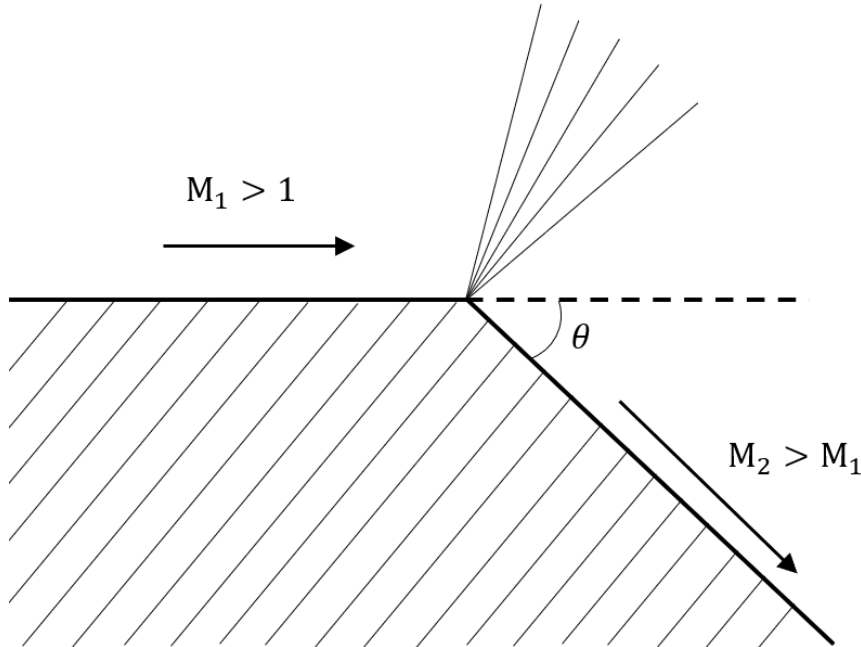

Figure 2.6: Schematic of the Prandtl-Meyer expansion fan.

In expansion of supersonic flows, the flow accelerates. Therefore, downstream of the expansion fan, the Mach number (M_2) is increased compared to the Mach number upstream (M_1). The reason that this flow solution contains an infinite number of Mach waves, is that expansion through a single shock

wave would violate the second law of thermodynamics. Therefore, the flow through every Mach wave is isentropic and so the whole expansion fan is an isentropic flow feature. As the expansion is isentropic, the total temperature T_0 and total pressure p_0 are conserved and the isentropic-flow relations can be applied [6].

In order to determine the Mach number of the flow downstream of the expansion, the Prandtl-Meyer function is used [5]:

$$\nu(\mathrm{M}) = \int \frac{\sqrt{\mathrm{M}^2 - 1}}{1 + \frac{\gamma-1}{2}\mathrm{M}^2} \frac{d\mathrm{M}}{\mathrm{M}} = \sqrt{\frac{\gamma+1}{\gamma-1}} \arctan \sqrt{\frac{\gamma-1}{\gamma+1}\left(\mathrm{M}^2 - 1\right)} - \arctan \sqrt{\mathrm{M}^2 - 1} \qquad (2.25)$$

ν is in radians and is related to the turn angle θ [6]:

$$\theta = \nu(\mathrm{M}_2) - \nu(\mathrm{M}_1) \qquad (2.26)$$

With this knowledge, it is clear that the Mach number downstream of the turn is determined by only the ratio of the specific heats γ, the turn angle θ and the upstream Mach number M_1.

There are some limiting cases. By convention, $\nu(\mathrm{M} = 1) = 0$, because this is the lower limit of supersonic flow. The upper limit of the Prandtl-Meyer function is given by:

$$\nu_{\mathrm{max}} = \frac{\pi}{2}\left(\sqrt{\frac{\gamma+1}{\gamma-1}} - 1\right) \qquad (2.27)$$

The maximum turn angle is therefore determined by the ratio of the specific heats γ. For air ($\gamma = 1.4$), this is $\nu_{\mathrm{max}} = 2.27$ rad $= 130.45°$.

The turn angle is not the only limit for increase of speed in isentropic flows. Another limit for the speed of the gas is given by energy conservation [5]:

$$\frac{1}{2}u^2 + c_p T = c_p T_0 = \text{constant} \qquad (2.28)$$

The kinetic energy for the gas is bounded by the total temperature. Therefore, the maximum speed to be obtained during expansion, which is for the case for the static temperature approaching the absolute minimum $T = 0$ K, is:

$$u_{\mathrm{max}} = \sqrt{2c_p T_0} \qquad (2.29)$$

For this maximum speed, the Mach number approaches infinity, because the speed of sound approaches zero. Note that this limiting case will never be achieved, as the gas at $T = 0$ K will be solidified. This case is not realistic and the static temperature should stag above a certain limit. Therefore, when keeping T variable, during expansion the maximum local Mach number for isentropic flows can be expressed as:

$$\mathrm{M} = \sqrt{\frac{2c_p(T_0 - T)}{\gamma R T}} = \sqrt{\frac{2}{\gamma - 1}\left(\frac{T_0}{T} - 1\right)} \qquad (2.30)$$

Figure 2.7 shows equation 2.30 as a function of the ratio of the temperature and the total temperature T/T_0. With no expansion from still air ($T/T_0 = 1$), the Mach number is of course 0. With expansion from still air, the Mach number increases and the static temperature decreases.

2.3 Nozzles and Diffusers

In supersonic flows, convergence and divergence of the flow play an important role in the control of the flow. These are applied in the design of nozzles and diffusers. In nozzles, the flow is accelerated and in diffusers, the flow is decelerated. For the analysis of these flows, quasi-one-dimensional steady flow is assumed [6]. Quasi-one-dimensional flow means that the flow is assumed uniform over the cross-section in a channel. Furthermore, it should be noted that $|\frac{\mathrm{d}A}{\mathrm{d}x}| << 1$ holds for the quasi-one-dimensional flow assumption [5].

For implementation, the steady adiabatic 1D version of the Euler equations (equation 2.4) omitting external forces is used. The flow is isentropic and hence barotropic (density is only a function of pressure).
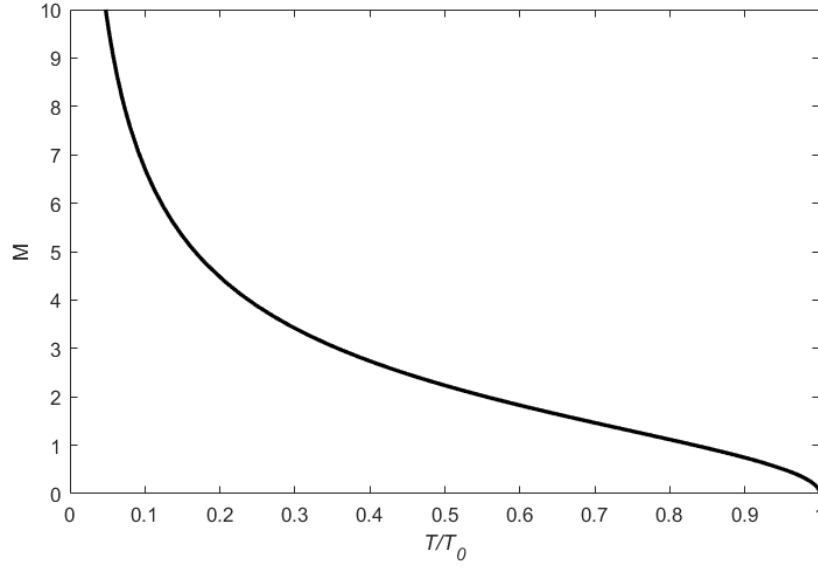
Figure 2.7: Maximum Mach number as a function of the temperature ratio T/T_0 for $\gamma = 1.4$.

When using a control volume of a stream tube, relations derived from the continuity, momentum and energy equation are obtained [5]:

$$
\begin{aligned}
\frac{1}{A}\frac{\mathrm{d}A}{\mathrm{d}x} + \frac{1}{u}\frac{\mathrm{d}u}{\mathrm{d}x} + \frac{1}{\rho}\frac{\mathrm{d}\rho}{\mathrm{d}x} &= 0 \quad \text{continuity} \\
\frac{\mathrm{d}p}{\mathrm{d}x} + \rho u\frac{\mathrm{d}u}{\mathrm{d}x} &= 0 \quad \text{momentum conservation} \\
\frac{\mathrm{d}h}{\mathrm{d}x} + u\frac{\mathrm{d}u}{\mathrm{d}x} &= 0 \quad \text{energy conservation} \\
\frac{\mathrm{d}p}{\mathrm{d}x} = \frac{\mathrm{d}p}{\mathrm{d}\rho}\frac{\mathrm{d}\rho}{\mathrm{d}x} = a^2\frac{\mathrm{d}\rho}{\mathrm{d}x} &\quad \text{isentropicity} \\
\Rightarrow \quad \frac{1}{\rho}\frac{\mathrm{d}\rho}{\mathrm{d}x} + \frac{\mathrm{M}^2}{u}\frac{\mathrm{d}u}{\mathrm{d}x} &= 0
\end{aligned}
\tag{2.31}
$$

in which M is the local Mach number. Combining the first and last equation of equation 2.31, the **area-velocity relation** is obtained:

$$
\frac{1}{A}\frac{\mathrm{d}A}{\mathrm{d}x} = (\mathrm{M}^2 - 1)\frac{1}{u}\frac{\mathrm{d}u}{\mathrm{d}x}
\tag{2.32}
$$

The area-velocity relation can be visualized the best using converging and diverging ducts, see figure 2.8. The behaviour of the flow depends on the Mach number. If the flow is subsonic (M < 1), then $\frac{1}{A}\frac{\mathrm{d}A}{\mathrm{d}x} \propto -\frac{1}{u}\frac{\mathrm{d}u}{\mathrm{d}x}$, which means that when A increases, u decreases and the other way around. This is according to intuition and the same for liquids [12]. However, for gases, a difference appears when the flow is supersonic (M > 1). The dependence then becomes $\frac{1}{A}\frac{\mathrm{d}A}{\mathrm{d}x} \propto \frac{1}{u}\frac{\mathrm{d}u}{\mathrm{d}x}$, i.e. when A increases, u increases too and the other way around. As a result, other physical quantities will increase or decrease depending on the case of a converging or diverging duct and the Mach number at inlet being subsonic or supersonic [5][6].

There are some phenomena to note. First of all, take M = 0. In that case, algebra shows that $A(x)u(x) = $ constant, which is the implication of an incompressible flow (ρ is constant). Secondly, when M = 1, it follows that $\frac{\mathrm{d}A}{\mathrm{d}x} = 0$, which means that A has an extremum. A minimum in $A(x)$ is called a throat and is required for the sonic condition M = 1. A throat does not always imply sonic flow [5]. If the flow with $\frac{\mathrm{d}A}{\mathrm{d}x} = 0$ is not sonic (M $\neq$ 1), equation 2.32 tells that $du = 0$, so the velocity has an extremum.

For the practical application of supersonic flows, a convergent-divergent channel is used, as visualized in figure 2.9 for the De Laval nozzle. These channels are often used in wind tunnels (see section 2.4). The
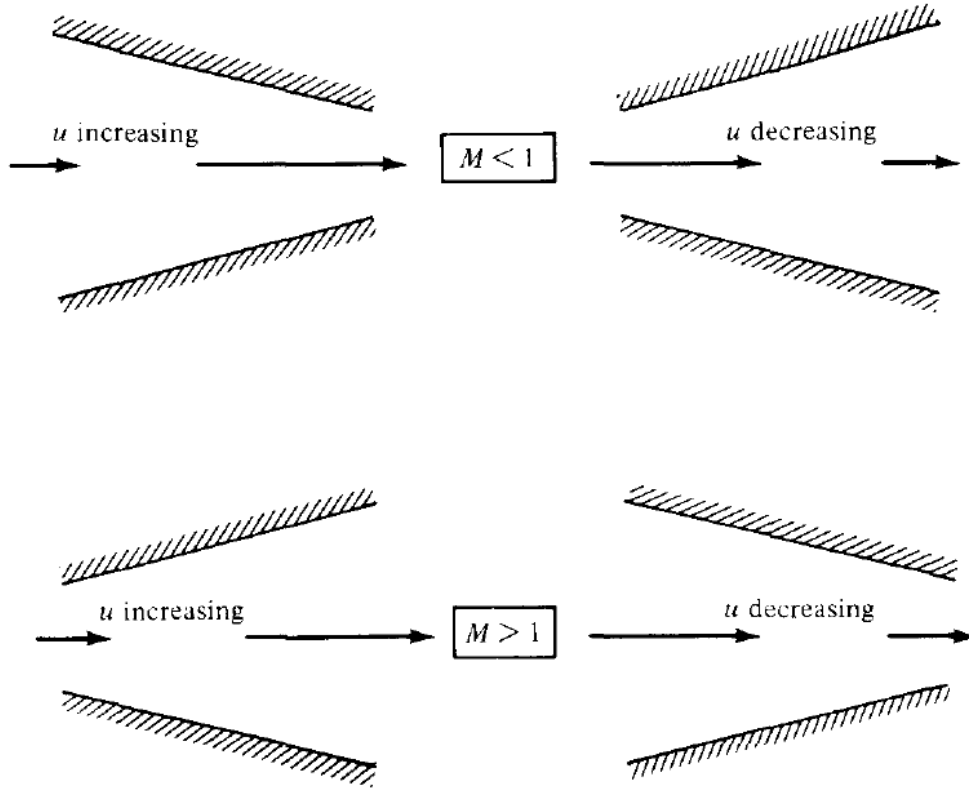
Figure 2.8: Converging and diverging ducts for subsonic and supersonic flows [6].

cross-sectional area of the throat determines the maximum mass flow, as for $M = 1$, the cross-sectional area is minimal. The mass flow is expressed as the following using mass conservation for isentropic flows [13]:
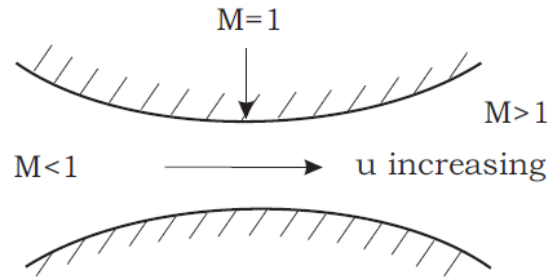

Figure 2.9: Schematic of isentropic expansion in a De Laval nozzle [5].

$$\dot{m} = \frac{A(x)p_0}{\sqrt{T_0}} \sqrt{\frac{\gamma}{R}} M(x) \left(1 + \frac{\gamma - 1}{2} M(x)^2\right)^{-\frac{\gamma+1}{2(\gamma-1)}} \tag{2.33}$$

For M $= 1$, equation 2.33 reduces to equation 2.34, denoting A^* as the cross-sectional area of the throat.

$$\dot{m} = \frac{A^* p_0}{\sqrt{T_0}} \sqrt{\frac{\gamma}{R}} \left(\frac{\gamma + 1}{2}\right)^{-\frac{\gamma+1}{2(\gamma-1)}} \tag{2.34}$$

It follows that the mass flow through a convergent-divergent channel is determined by the total pressure p_0, total temperature T_0, the type of gas (R and γ) and the cross-sectional area A^* of the throat.

Combining equation 2.33 and 2.34, the **Mach-number-area relation** is derived:

$$\frac{A(x)}{A^*} = \frac{1}{M(x)} \left[\left(\frac{2}{\gamma + 1} \right) \left(1 + \frac{\gamma - 1}{2} M(x)^2 \right) \right]^{\frac{\gamma+1}{2(\gamma-1)}} \tag{2.35}$$

Figure 2.10 shows a plot of equation 2.35. from which the principle of the choked flow is clearly shown.
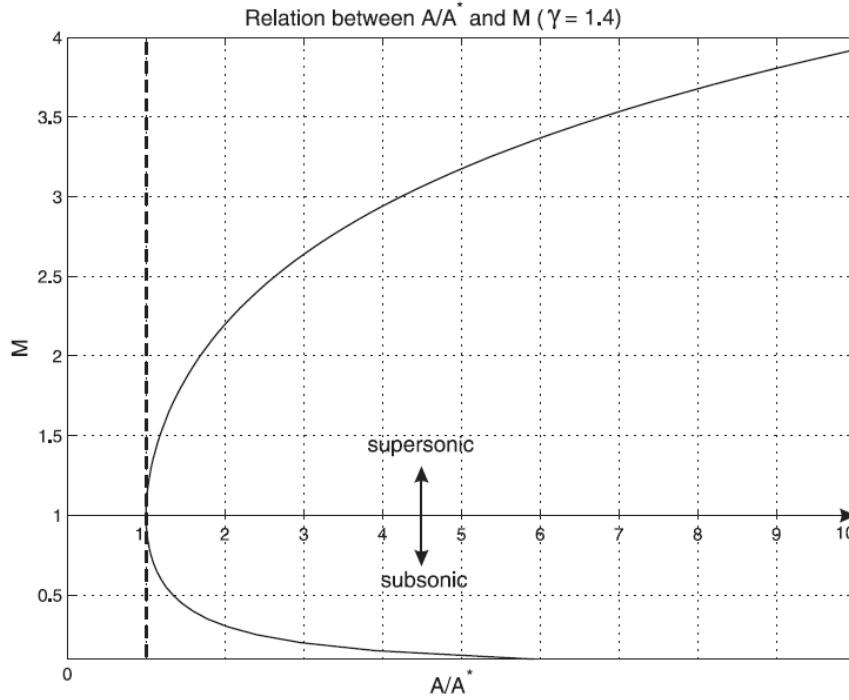

Figure 2.10: Mach-number-area relation from equation 2.35 plotted for the Mach number versus the area ratio A/A^* with A^* the area of the narrowest cross-section (throat) [5].

Convergent-divergent channels are used both for expansion and compression. In the first case, a subsonic flow is accelerated to $M = 1$ in the throat and thereafter accelerates further supersonically. In the second case, a supersonic flow is decelerated in the convergent part of the channel to $M = 1$ and thereafter decelerates further subsonically. In conclusion, a convergent-divergent channel is an appropriate configuration for converging a flow from subsonic to supersonic and the other way around [6].

2.4   Supersonic Wind Tunnels

For experimental investigation of supersonic flow, wind tunnels are used. A number of types that are used, amongst others the closed circuit return wind tunnel, the air indraft wind tunnel and the blow-down wind tunnel. The difference between these types is that the closed return wind tunnel and the air indraft wind tunnel can be in operation continuously, whereas the blow-down wind tunnel needs a refill of the upstream reservoir from time to time. Furthermore, in the closed return wind tunnel, the flow is circulated, while in the other types, air flows through the wind tunnel once.

The configuration of the test section is the same for all types of wind tunnels. As an example, see figure 2.11. It works according to the principle of a De Laval nozzle. The approaching air is initially subsonic. Then, the flow is contracted in the nozzle throat, such that the flow is accelerated to sonic speed. Downstream of the throat, the cross-section of the wind tunnel expands again, accelerating the sonic flow to supersonic speeds. After expansion, the cross-sectional area remains constant for a certain
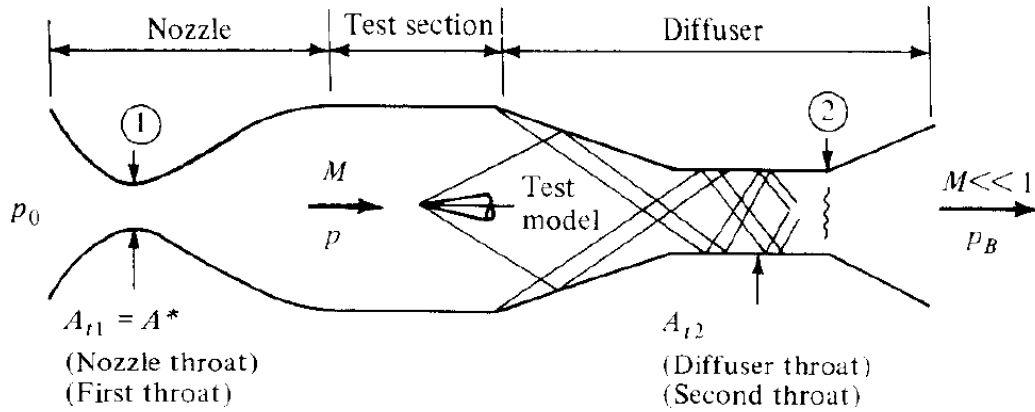
Figure 2.11: Configuration of the test section of a supersonic wind tunnel [6].

distance. This part is the test section, in which objects can be put or fluids can be injected. The flow can be investigated by many techniques, such as Schlieren (see chapter 6). Downstream of the test section, the flow is choked again in the diffuser throat to sonic speed and thereafter decelerated further to subsonic speed [6][14].

Using the isenstropic-flow relations from section 2.1, the velocity can be determined. However, another possibility is the calculation of the Mach number using the so-called Mach lines. This is a line, visible in a Schlieren image, which inclination corresponds to the Mach angle of equation 2.19. These Mach lines are caused by disturbances such as small discontinuities at the wall of the wind tunnel. In figure 2.12, a Mach line in a wind tunnel test section is made visible as a white line.
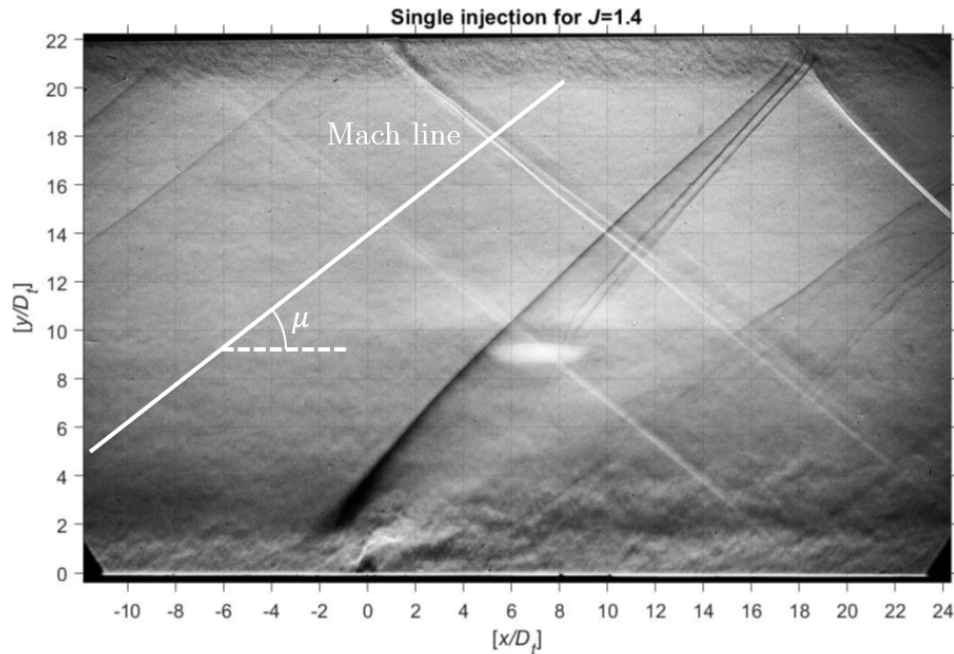
Figure 2.12: Mach line visualization in a Schlieren image from an experiment of De Maag [3] of single jet injection into a supersonic crossflow of air. Conditions: $J = 1.4$ and $M_c = 1.6$.

Chapter 3

Jet Injection in Still Air

Jet injection is the injection of a certain matter, often liquid or gas, in the form of a squirt. They are applied in several practical applications, such as injection of fuel for combustion in scramjet engines, oil-well blowouts, breaks in high-pressure systems, et cetera [15]. When considering jet injection, there are several possibilities with respect to the geometrical and physical parameters. The injection can be done for example using slots or circular orifices. Before elaborating more, the research is restricted to the injection of gas with circular injection orifices.

Jets are injected from a certain reservoir, which is also called the plenum. An example is shown in figure 3.1, where it is denoted as upstream reservoir. The parameters with subscript $_{0,j}$ are for the reservoir total quantities, the parameters with subscript $_e$ and an asterisk * are for the conditions at the orifice of the jet and the parameters for the space in which the jet is injected (ambient region) $_\infty$. On one side of the reservoir, gas is supplied and on the other side of the reservoir, the gas is ejected. Inside the reservoir, the gas is almost quiescent and therefore, the total pressure can be measured [15].

The pressure is a rather important parameter for jet injection. It is especially important to know the pressure of the reservoir of the jet with respect to the pressure in the space in which the jet is injected (ambient pressure).

The parameters that characterize the jet are the Mach number of the jet at exit M_e^*, the pressure at exit p_e^*, the orifice diameter D_e^* and the jet exit pressure ratio p_e^*/p_∞ [16].

When using compressible gases, there are three fundamental steady-flow regimes to be distinguished [15]:

1. adapted jets ($p_e^* = p_\infty$)

2. nonadapted underexpanded jets ($p_e^* > p_\infty$)

3. nonadapted overexpanded jets ($p_e^* < p_\infty$)

The nonadapted flows only occur with M_e^* at sonic or supersonic conditions, because then pressure disturbances from the ambient region are not able to propagate into the channel in order to equalize p_∞ and p_e^*. Figure 3.1 shows a sketch of the pressure distribution for adapted as well as for underexpanded flows. In this visualization, a converging nozzle is used, which accelerates the flow towards the ambient region (see section 2.3 for details about the principles). While the flow accelerates in the nozzle, the static pressure drops from $p_{0,j}$ to p_e^*, before entering the ambient region [15].

The total pressure $p_{0,j}$ determines at which velocity the flow passes through the nozzle. By calculating equation 2.8, it appear that $p_e^*/p_{0,j} = \left(\frac{\gamma+1}{2}\right)^{\frac{1}{\gamma-1}} = 0.528$ is required for having a sonic jet at the outlet of the nozzle. p_e^* should then be larger or equal to p_∞. If $p_{0,j}$ is lower than required, then the jet from the nozzle will be subsonic exit-adapted and if $p_e^*/p_{0,j} = 0.528$ and $p_e^* = p_\infty$, the jet is sonic exit-adapted (see figure 3.1). When the total pressure $p_{0,j}$ is higher than for the case of sonic exit-adapted jet, the jet will still be sonic at the orifice, but having a higher pressure than p_∞ (sonic exit-underexpanded, see figure 3.1). For the further discussion, only underexpanded sonic jets are taken into account.

Considering an underexpanded sonic jet, the pressure at the outlet p_e^* is higher than the ambient region pressure p_∞. The ambient pressure is to be achieved by the jet by an external expansion process. Due to this process, pressure fluctuations along the center line of the jet will occur (see also figure 3.1).
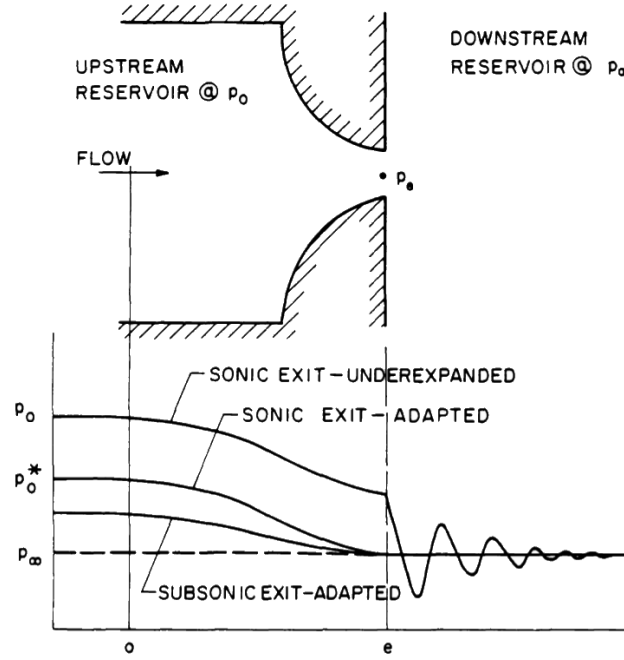
Figure 3.1: Pressure distribution inside a jet along the centerline from the reservoir to the ambient region. The upstream reservoir is the jet plenum and the downstream reservoir is the ambient region [15].

In literature, there are mainly two types of underexpanded sonic jets with the pressure ratio p_e^*/p_∞ as determining factor. For the further use, this will be called the **jet exit pressure ratio** $\eta_{e,j}$:

$$\eta_{e,j} = \frac{p_e^*}{p_\infty} \tag{3.1}$$

If $\eta_{e,j}$ is small, the jet is a **slightly underexpanded sonic jet** and if $\eta_{e,j}$ is larger, the jet is a **highly underexpanded sonic jet**. These two types of jets have their own characteristics, but the point of transition between the two regimes is not clearly defined. Giskes [7] proposed to use the term "highly" for jets featuring a so-called Mach disk – which is a normal shock – inside the jet and "slightly" for jets that do not feature a Mach disk, but only have an oblique shock structure. Ewan [16] approximates this transition as $\eta_{e,j} \leq 2$ for "slightly" and $\eta_{e,j} > 2$ for "highly".

As there are many shock structures and large differences in physical quantities within the jet flow, the density gradients are large too. This is beneficial for visualization of the jet flow by Schlieren techniques, as these techniques visualize density gradients. For more about Schlieren techniques, see chapter 6.

In the following subsections, the two types of underexpanded jets are characterized. In both cases, a uniform flow at the orifice is assumed [15].

3.1   Slightly underexpanded sonic jet

In the slightly underexpanded sonic jet, a number of phenomena are visible. Figure 3.2 shows that at the orifice of the jet, a Prandtl-Meyer expansion fan occurs around the periphery of the orifice. Because of this expansion, the flow accelerates and becomes supersonic. As a result, the pressure within the jet drops. The expansion waves reflect from the boundary with constant pressure and will intersect, which forms an intercepting shock. In the center of the jet, this intercepting shock is reflected (because of axisymmetry) as an oblique shock. Downstream of the oblique shock, the pressure is higher than upstream of the shock, which makes the jet flow to expand again at the point where the reflected oblique shock reaches the edge to the jet flow. This process then repeats, such that a set of shock structures is visible [15].

At the edge of the jet flow, a jet mixing layer is visible (figure 3.2 and 3.3). This mixing layer develops,
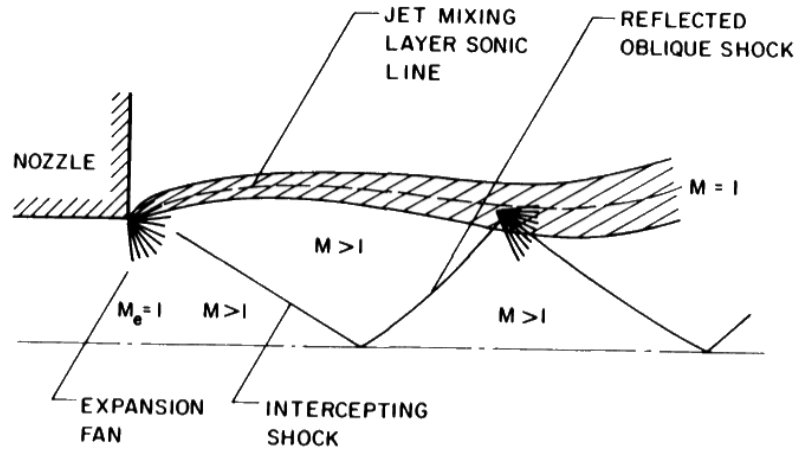
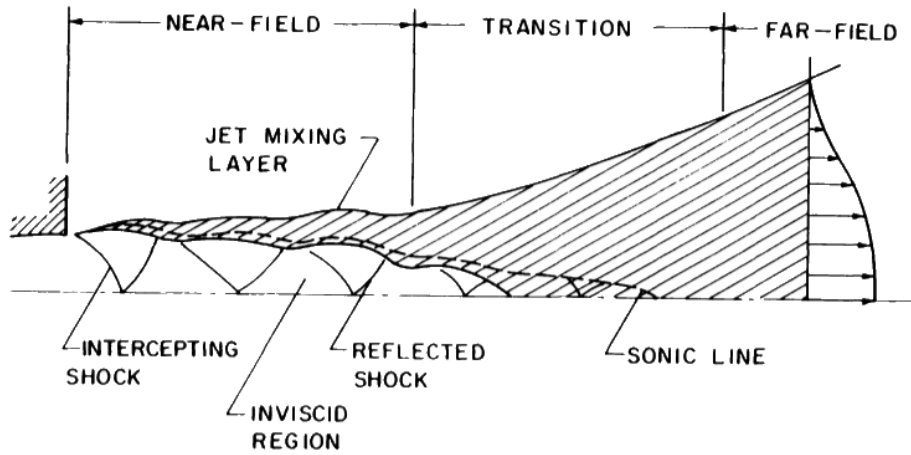Figure 3.2: Near-field region of a slightly underexpanded sonic jet [15].

Figure 3.3: Near-field, transition and far-field regions of a slightly underexpanded sonic jet [15].

such that in the end the flow adjusts to the ambient conditions. The thickness of the jet mixing layer grows with the distance from the passage exit and this viscous mixing layer contracts and weakens the shock-cell pattern, as discussed above. Within the jet mixing layer, the velocity decreases from the inner to the outer of the jet flow from supersonic to subsonic flow. Somewhere within the jet mixing layer in the near-field of the jet flow, a sonic line is present. This sonic line will move toward the center of the jet as the shock-cell pattern weakens. This is visible in the transition region (figure 3.3). When the jet mixing layer sonic line reaches the center of the jet, the full jet has become subsonic and the jet mixing layer spreads out. Then the shock structures also disappear. This subsonic jet flow region is the far-field region. In the far-field region, the subsonic jet flow has a nearly constant static pressure, in contrast to the near-field jet flow [15].

In summary, in the slightly underexpanded sonic jet, processes are present that can be divided in three regions [15][17]:

- near-field: inviscid shock-cells dominate

- transition: viscous processes become more important and the supersonic part of the jet flow decreases until the sonic line passes the jet center line

- far-field: the jet flow is fully subsonic and is a mixing process at constant pressure

3.2   Highly underexpanded sonic jet

As a result of a high pressure ratio $\eta_{e,j}$, the expansion of the jet will be stronger than for slightly underexpanded sonic jets and so will the shocks within the jet flow. Figure 3.4 shows some characteristics of the highly underexpanded jet. Expansion waves originate at the brim, which is the sharp edge of the orifice (see also section 2.2.4). These expansion waves reflect at the flow boundary (or intercepting shock) as compression waves. Coalescence of these compression waves results in the so-called **barrel shock**, which surrounds the largest supersonic flow region. If $\eta_{e,j} > 2$, the barrel shock cumulates in a normal shock and a reflected shock (figure 3.5), which results in a triple point. The normal shock is the so-called **Mach disk**. Downstream of the Mach disk, the jet flow becomes subsonic. Provided $\eta_{e,j}$ is sufficiently large, there can be a succession of barrel and normal shocks [15][16]. An example Schlieren image is shown in figure 3.6.
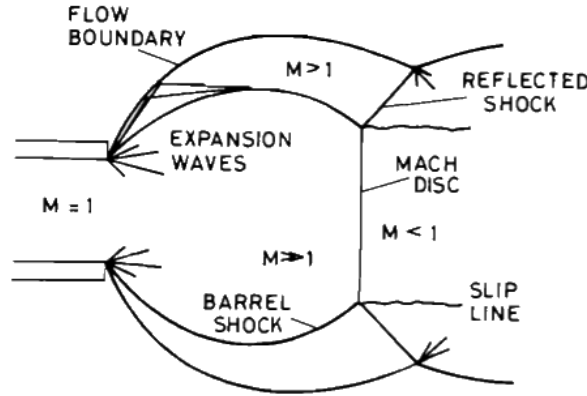
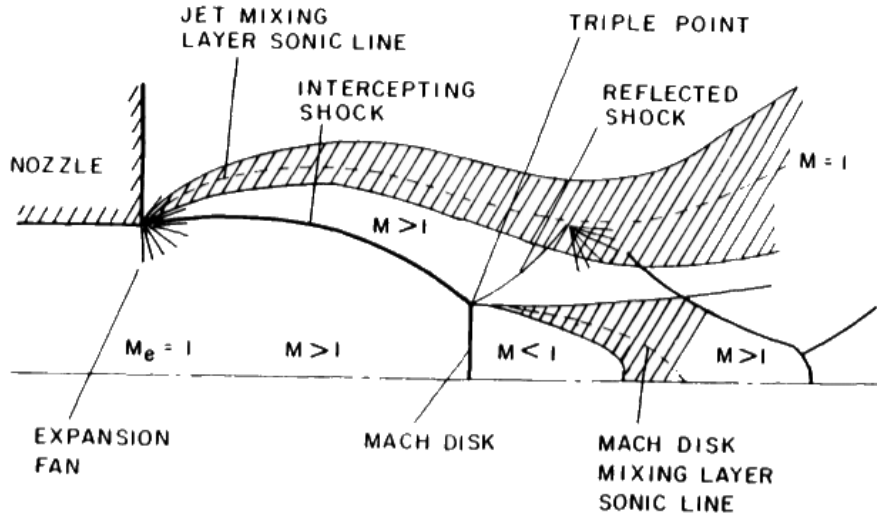Figure 3.4: Characteristics and regions around the jet exit for a highly underexpanded jet [16].

Figure 3.5: Near-field region of a highly underexpanded sonic jet [15].

At the boundary of the jet flow, a jet mixing layer forms, which increases in thickness with distance. Within this jet mixing layer, the sonic line is present. Furthermore, it appears that the flow behind the Mach disk is subsonic, but the parallel flow behind the oblique reflected shock is still supersonic (see
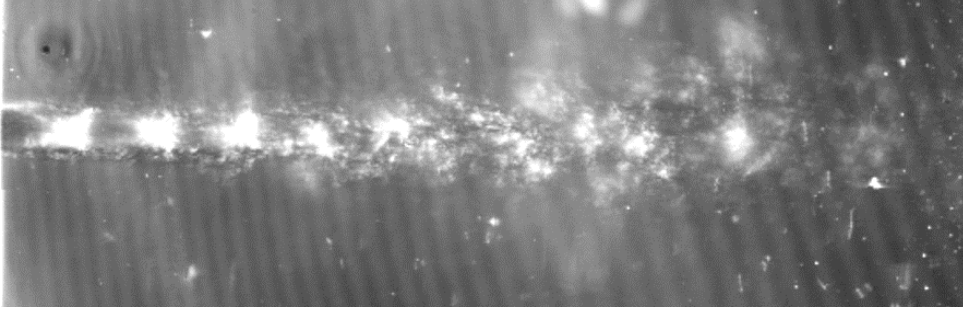
Figure 3.6: Schlieren image of a highly underexpanded jet with an underexpansion ratio $\eta_{0,j} = 5.47$.

figure 3.5). Between these two regions, another mixing layer is formed, the so-called Mach disk mixing layer. Due to the reflection of the reflected shock at the edge of the jet flow, an expansion fan is formed, which causes the subsonic flow after the Mach disk to become supersonic again, through the Mach disk mixing layer. Once the flow is supersonic, the processes as described before is repeated. Every step in this repetition, the viscous effects in the jet mixing layer and the Mach disk mixing layer make the waves weaker. In the end, a pattern as described for a slightly underexpanded sonic jet will be visible (see figure 3.3), until the full jet flow is subsonic and at constant pressure [15].

The location of the Mach disk scaled by the diameter of the jet is found to be insensitive to the nozzle lip geometry, the absolute pressure level and the specific heats (γ) [16][18]. From experiments by amongst others Crist et al. [18], it appears that the location of the Mach disk especially depends on the **underexpansion ratio**, which is defined as:

$$\eta_{0,j} = \frac{p_{0,j}}{p_{\infty}} \tag{3.2}$$

in which the ratio of the total pressure in the jet plenum and the static ambient pressure is used. The relation for the location of the Mach disk is generally characterized by a power law relation in the form of:

$$\frac{L_{MD}}{D_j} = c_1 \eta_{0,j}^{c_2} \tag{3.3}$$

Ashkenas and Sherman [19] proposed a relation for the location of the Mach disk for axisymmetric continuous jets, based on several experimental results for the range $15 \leq \eta_{0,j} \leq 17000$:

$$\frac{L_{MD}}{D_j} = 0.67 \eta_{0,j}^{\frac{1}{2}} \tag{3.4}$$

Crist et al. [18] performed experiments of jet injection with the gases nitrogen, argon, helium, helium-argon mixtures, carbondioxide, and Freon 22. They found out that the location of the Mach disk is independent of γ and that is why the results of the different gases coincide. From these experiments, they proposed a relation for the location of the Mach disk for $10 \leq \eta_{0,j} \leq 300,000$:

$$\frac{L_{MD}}{D_j} = 0.645 \eta_{0,j}^{\frac{1}{2}} \tag{3.5}$$

In addition, Orescanin and Austin [20] did measurements for the location of the Mach disk in jet injection of nitrogen and helium. They found an empirical relation for an infinite-reservoir jet for an underexpansion ratio range of $\eta_{0,j} \leq 15$:

$$\frac{L_{MD}}{D_j} = 0.53 \eta_{0,j}^{0.6} \tag{3.6}$$

In figure 3.7, equations 3.4 to 3.6 are plotted. Especially in the range $8 \leq \eta_{0,j} \leq 12$, the results of the three correlations almost coincide.
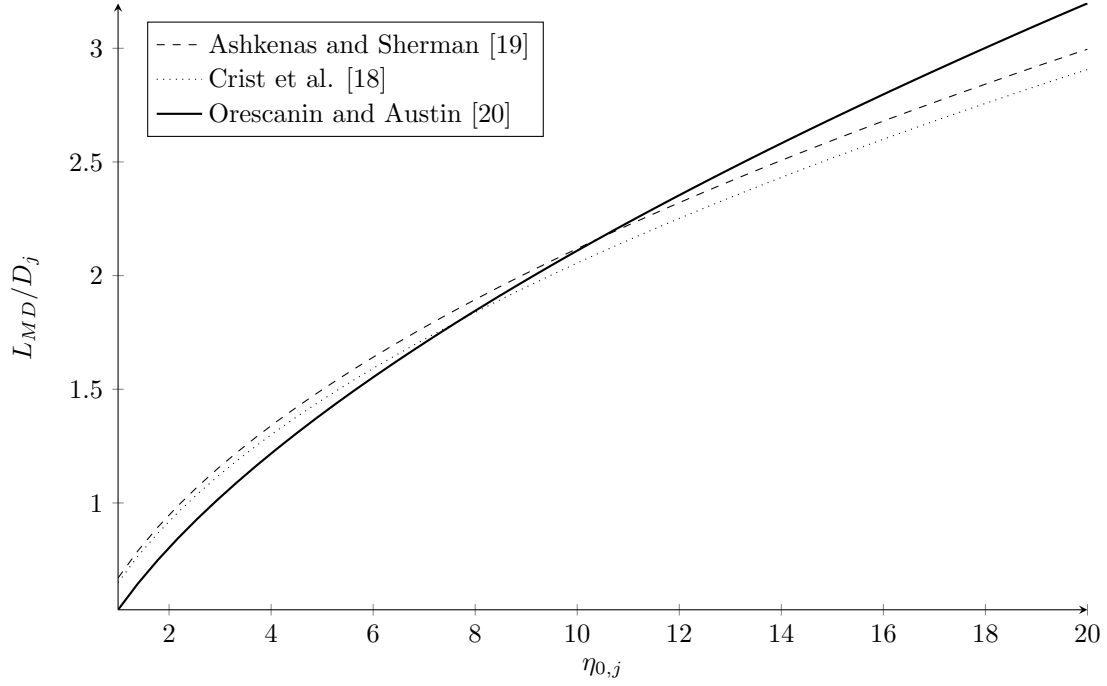
Figure 3.7: Location of the Mach disk L_{MD}/D_j versus the underexpansion pressure ratio $\eta_{0,j}$ for three relations from literature.

Comparison of several relations for the position of the Mach disk by Franquet et al. [21] results in the general recommendation for the use of equation 3.5 from Crist et al. [18] for the location of the Mach disk, as this equation is validated for a large range of $\eta_{0,j}$. However, as the range of the application is rather wide ($10 \leq \eta_{0,j} \leq 300,000$), one can propose to use equation 3.6 for lower underexpansion ratios ($\eta_{0,j} < 10$), as this equation is specifically developed to lower $\eta_{0,j}$.

Chapter 4

Single Jet Injection into Supersonic Crossflow

In chapter 1, it was described why jet injection into supersonic crossflow is important. Efficient mixing of the jet with the crossflow is desired. In order to be able to analyze and then improve this, an understanding is needed of jet injection into supersonic crossflow.

In chapter 2, the general physics of supersonic flows has been discussed and some important features in these flows have been described. Thereafter, in chapter 3, jet injection in still air is considered. The knowledge of these two chapters is combined in the present chapter. It is possible to have multiple jets, which will be discussed in chapter 5, but for the sake of clarity and simplicity, only a single jet is considered here.

First, a description of the flow structures of a jet in a supersonic crossflow is given. Some of these structures are further explained in the subsequent sections, such as the penetration depth of the jet into the supersonic crossflow and the behaviour of the jet shear layer.

4.1 Flow Structures in Single Jet Injection into Supersonic Crossflow

When considering an underexpanded sonic jet which injects transversely into a supersonic crossflow, several structures are observed. These are shown in figure 4.1 and figure 4.2.
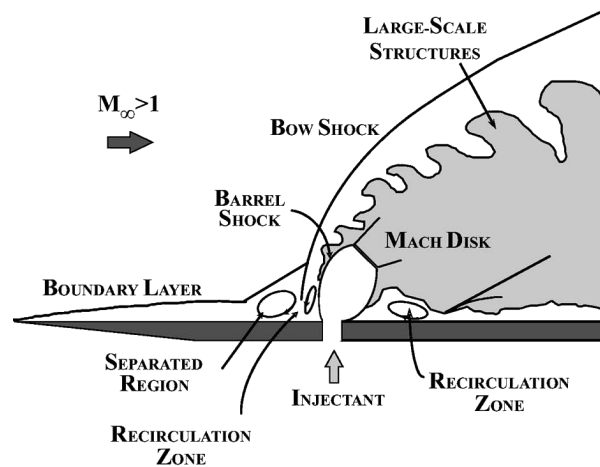

Figure 4.1: 2D schematic of flow features of underexpanded jet injection into a supersonic crossflow: near-field in a vertical plane through the centerline axis of the jet [22].
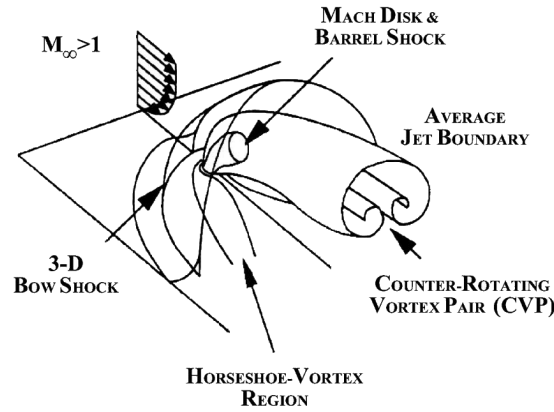
Figure 4.2: 3D schematic of time-averaged features of underexpanded jet injection into a supersonic crossflow: near-field and far-field [22].

Below, flow structures are listed and described concisely. Some specific characteristics are discussed in more detail in subsequent sections.

- Boundary layer and the flow separation zone

- Recirculation zones upstream and downstream of the jet orifice

- Horseshoe-vortex region starting in front of the jet

- Bow shock in front of the jet

- Barrel shock and Mach disk in the jet

- Jet boundary layer or jet shear layer at the upper side of the jet

- Large-scale structures in the jet shear layer

- Counter-rotating vortex pair in the far field region of the jet

The boundary layer near the wall of the supersonic crossflow is interrupted by the bow shock, created because the jet flow is an obstacle to the crossflow. In front of the bow shock, the boundary layer separates from the wall. This creates a flow separation region [22] and a separation shock above that region, which is a lambda shock (named after the shape of the shock). A lambda shock is a small weak shock that interacts with the stronger bow shock further downstream. The size of the separation zone and the size of the lambda shock mainly depend on the conditions and momentum of the supersonic crossflow [23]. As a result of this shock-boundary-layer interaction, the pressure field is rather complex [24].

Upstream and downstream of the jet orifice, recirculation zones are created. Between the bow shock and the jet, a small recirculation zone is present and downstream of the jet, a recirculation zone near the wall is featured [25]. In the boundary layer, an adverse pressure gradient is present, which drives the recirculation zone to be the start of the horseshoe-vortex region around the jet [7].

Within the structure of the underexpanded jet, a barrel shock is present, together with a Mach disk. These phenomena are described in section 4.2. The jet generates a bow shock in the supersonic crossflow [25]. Characteristics are discussed in section 4.3.

The transverse jet penetrates into the supersonic crossflow and the jet is increasingly inclined in freestream direction. This penetration is characterized by the properties of the jet flow and the supersonic crossflow, see section 4.4. Large-scale structures appear in the jet shear layer, at the interface of the jet and the flow that has passed through the bow shock. These structures make the jet to mix with the freestream that passed through the bow shock. The behaviour of the jet shear layer is discussed in section 4.5. Furthermore, the jet plume and mixing and bandwidth of the jet upper shear layer is discussed in section 4.6. Further downstream, counter-rotating vortices are present in the jet flow, which in the plane perpendicular to the freestream form a mushroom-shaped structure [26]. The jet and crossflow interaction is explained in more detail in the following sections.

4.2 Mach Disk and Barrel Shock in the Jet

In chapter 3, the phenomena of the barrel shock and Mach disk were investigated for a sonic jet in quiescent air. For the current section, this knowledge is used and applied to the interaction of a jet with a supersonic crossflow. In the following, the jet will behave as a highly underexpanded sonic jet.

Compared to the jet in quiescent air, the Mach disk is not parallel to the jet orifice. The jet is deflected in to the direction of the crossflow. For that reason, the barrel shock is deflected and the Mach disk has a rotation angle $\delta_{MD} < 90°$. Figure 4.3 shows a schematic with the involved parameters. In addition, in figure 4.4, the barrel shock and Mach disk are shown in Schlieren images. These phenomena are not everywhere equally clear, because of the interaction phenomena of the jet with the crossflow. Figure 4.4 shows that the size of the barrel shock increases with the jet-to-crossflow momentum flux ratio J. This jet-to-crossflow momentum flux ratio is the ratio of the momentum of the jet and the momentum of the crossflow and is the relative strength of the jet compared to the crossflow. This is further explained in section 4.4.
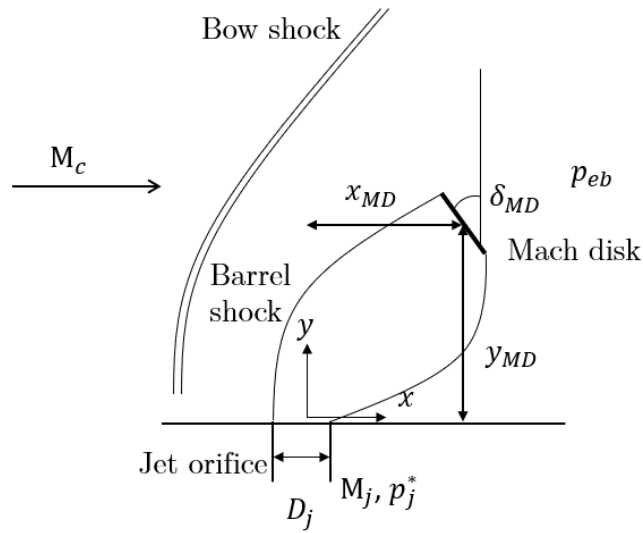

Figure 4.3: Schematic of the Mach disk and the barrel shock within the jet emanating in supersonic crossflow.
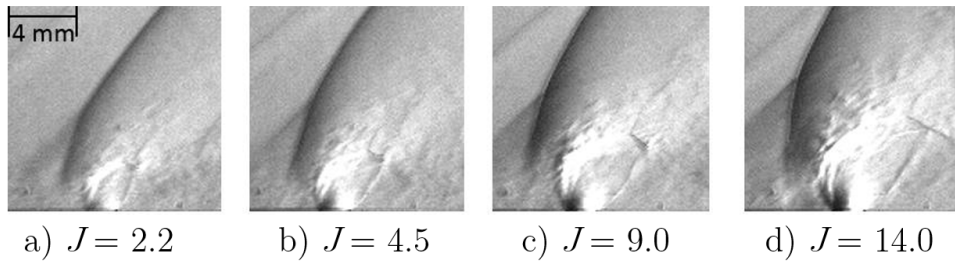

Figure 4.4: Schlieren images of jet injection into supersonic crossflow for different values of J. a) $J = 2.2$, b) $J = 4.5$, c) $J = 9.0$ and d) $J = 14.0$. The images reveal the barrel shock, Mach disk, lambda-shock and the upper side jet shear layer [7].

The jet loses a substantial part of its momentum when passing through the Mach disk, which is a normal shock. For that reason, the jet is quickly deflected into the direction of the crossflow downstream of the Mach disk [27]. The internal structure of the jet is similar to that described in section 3.2 for jet injection in still air, but then deflected [25].

Not the full flow of the jet passes through the Mach disk, a part of the gas from the orifice moves through oblique shocks in the mixing layer (as described in section 3.2). Furthermore, the barrel shock and the Mach disk may not be as clear as for a jet in quiescent air, because of the interaction of the jet with the crossflow [26]. More about the interaction with the bow shock is described in section 4.3 and more about the interaction of the jet with the crossflow is described in sections 4.5 and 4.6.

The position of the Mach disk and its orientation can be described by empirical relations, such as derived by Billig et al. [28] which they used for the verification of their model. The position of the center of the Mach disk (x_{MD}, y_{MD}) and its orientation with respect to the vertical axis δ_{MD} are expressed as [28]:

$$\frac{y_{MD}}{D_j} = M_j^{\frac{1}{4}} \left(\frac{p_j^*}{p_{eb}} \right)^{\frac{1}{2}} \tag{4.1}$$

$$\frac{x_{MD}}{y_{MD}} = 1.25 \left(1 - e^{-M_c/M_j} \right) \tag{4.2}$$

$$\delta_{MD} = \arctan \left(0.5 \frac{y_{MD}}{x_{MD}} \right) \tag{4.3}$$

These relations are valid for $1.0 \leq M_j \leq 2.2$ and $1.9 \leq M_c \leq 4.5$. In these equations, D_j is the diameter of the jet orifice, p_j^* is the static pressure at the jet orifice and p_{eb} is the **effective back pressure**. In [28], the effective back pressure is equal to $p_{eb} = \frac{2}{3} p_{t,c}$, in which $p_{t,c}$ is the Pitot pressure of the crossflow. In general, the effective back pressure is suggested to be in the form:

$$p_{eb} = c_1 p_2 \tag{4.4}$$

p_2 is the static pressure behind a normal shock in a freestream [24] and c_1 is a constant. Different authors found different values for c_1 [24][28][29]. Everett et al. [24] showed that the effective back pressure is dependent on J, see figure 4.5. This conclusion was confirmed by experiments of Gruber and Goss [29].
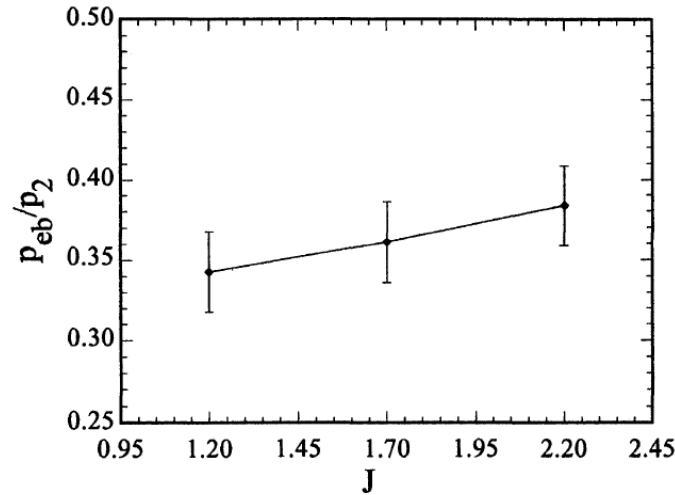
Figure 4.5: Variation effective back pressure with J [24].

In conclusion, the barrel shock and Mach disk are phenomena that are visible in jet injection in both quiescent air and supersonic crossflow, but the empirical relations for the location of the barrel shock and Mach disk are different. In addition, the appearance of the Mach disk and barrel shock in supersonic crossflow is less clear, because of the interaction phenomena of the jet with the crossflow.

4.3 Bow Shock in Front of the Jet

The bow shock in front of the jet is generated by the obstruction of the freestream flow by the jet [25]. Near the jet orifice, the shock is almost normal to the freestream. Further from the wall, the shock turns in streamwise direction, i.e. the shock becomes an oblique shock. Therefore, upon passing through the shock, close to the wall, the supersonic freestream flow is decelerated to subsonic speed [22]. Further away from the wall, where the shock is an oblique shock, the flow decelerates but stays supersonic.

4.3.1 Analysis of the Behaviour of a Flow through a Bow Shock

As an example of the effect of the bow shock, the following analysis of the bow shock in one of the experiments of Giskes [7] for sonic single jet injection in a supersonic crossflow is considered. In this experiment, air was used for both the crossflow and the jet, so $\gamma = 1.4$. The supersonic crossflow had a velocity of $M_1 = 1.6$.
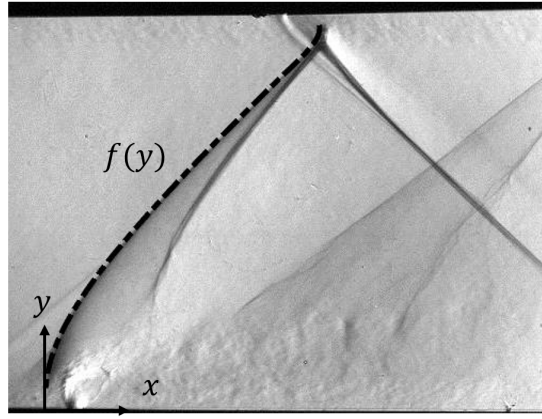

Figure 4.6: Sonic jet injection into supersonic crossflow (M = 1.6) by Giskes [7]. The bow shock is indicated as the superposed dashdotted curve.

In figure 4.6, the injection is shown at the left bottom of the image and the bow shock is shown as the superposed dashdotted curve. Figure 4.7 shows an analysis of the streamlines passing through the bow shock, when assuming no further disturbances (jet injection, reflection shocks) are present. This figure is based on the calculations as described in the following.

The bow shock is geometrically analysed with respect to the shock inclination β, which corresponds to the slope of the bow shock. If the bow shock is described as function $x = f(y)$, then the shock inclination is calculated by:

$$\beta(y) = \arctan\left(\left(\frac{\mathrm{d}f(y)}{\mathrm{d}y}\right)^{-1}\right) \tag{4.5}$$

It is clear that the inclination angle β is a function of y. Therefore, the other parameters, which are all indirectly dependent on β, are a function of y. The flow inclination angle $\theta(y)$ is calculated by equation 2.17. The results of the angles are shown in figure 4.8.

Upstream of the bow shock, the flow is assumed to be uniform at $M_1 = 1.6$ and horizontally directed, i.e. $\theta = 0$, shown in figure 4.9. For the calculations of the oblique part of the shock, the Mach number normal to the bow shock is needed. The normal component of the upstream flow field is calculated by equation 2.15. With the oblique shock relations (equation 2.16), the Mach number and normal Mach number downstream of the bow shock are calculated. The results for the Mach number and the normal Mach numbers upstream and downstream of the bow shock are shown in figure 4.9 and figure 4.10, respectively.

In figure 4.8 and figure 4.9, it can be seen that the bow shock is a partially strong ($M_2 < 1$) and a partially weaker shock ($M_2 > 1$). The local maximum for $\theta(z)$ forms the division point between the stronger and weaker part of the bow shock. This means that near the wall, the bow shock is strong and at some distance away from the wall, the bow shock is weaker. This is as expected from figure 4.6,
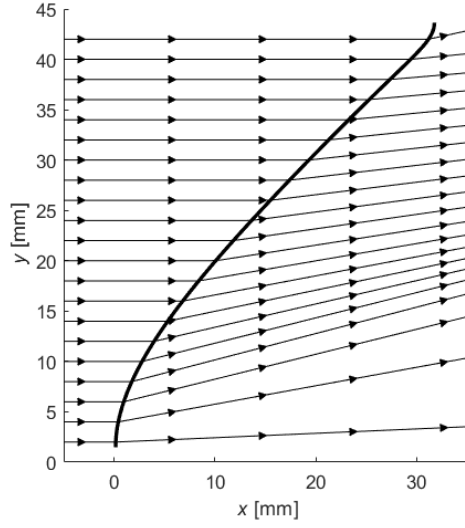
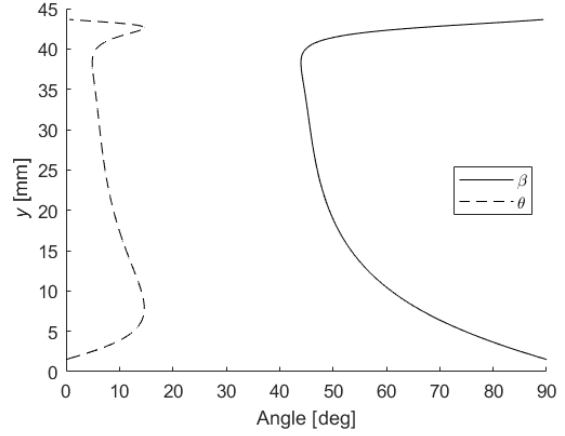Figure 4.7: Change in direction of streamlines at the bow shock.

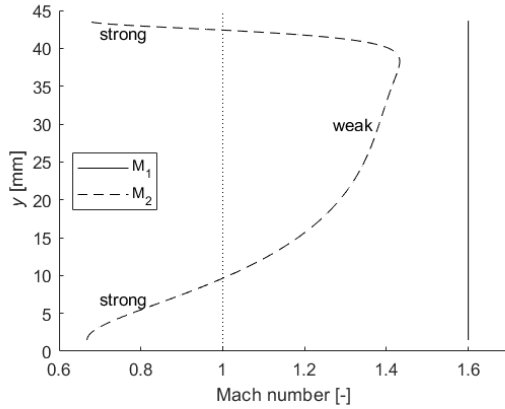Figure 4.8: Angles β and θ along the bow shock as a function of y.

Figure 4.9: Mach number upstream and downstream of the bow shock along the bow shock as a function of y.

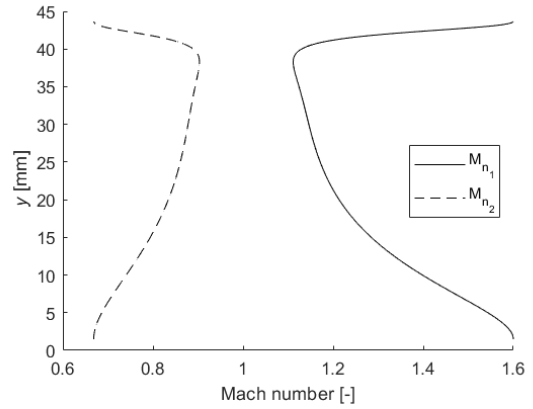

Figure 4.10: Mach number normal to the bow shock upstream and downstream of the bow shock along the bow shock as a function of y.

because near the lower wall, the bow shock is nearly vertical, which means that this part behaves as a normal shock. Near the upper wall, the bow shock reflects, which for the present conditions requires a combination of the oblique shock and a short normal shock. More details about reflections are provided in section 4.3.2. For this analysis, the reflection is not taken into consideration. The implication of the stronger part of the bow shock, which is a higher decrease in velocity, can be seen in figure 4.9.

The jump in other physical properties over the bow shock are shown in figure 4.11 and figure 4.12. The ratios of the temperature, density and pressure downstream and upstream of the bow shock are shown in figure 4.11. All these parameters increase when passing the bow shock. As expected from the relations for oblique and normal shocks, the normal part of the bow shock gives a larger increase of the static pressure, static temperature and density over the bow shock than the oblique part of the bow shock.

Figure 4.12 shows the variation of the ratio of the total pressure and its freestream value along the bow shock. The decrease in total pressure is a measure for the loss due to the shock wave. Again, it is clear that the total pressure loss is more severe for the normal shock part than for the oblique part of the bow shock.

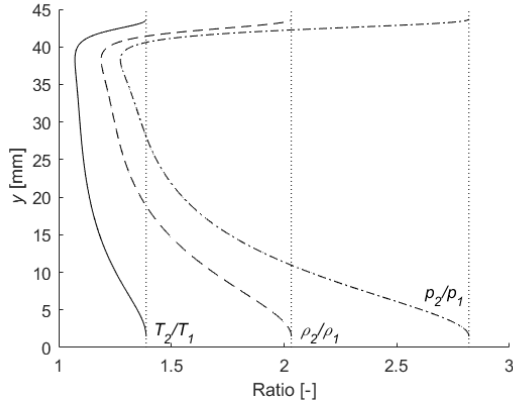For comparison, all physical quantities are calculated for a normal shock in a flow of $M_1 = 1.6$, such

Figure 4.11: Ratio of downstream and freestream values of static temperature, density and static pressure along the bow shock as a function of y. The dotted line is the value corresponding to a normal shock.
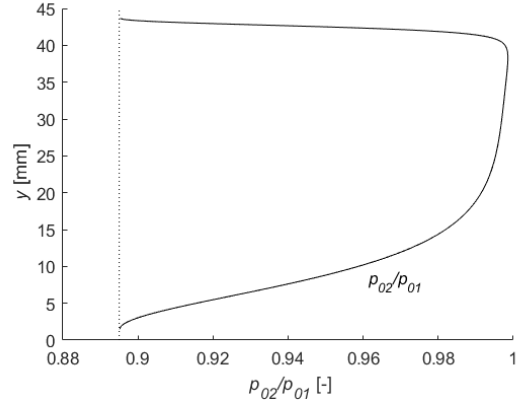
Figure 4.12: Ratio of total pressure and freestream value along the bow shock as a function of y. The dotted line is the value for a normal shock.

that the quantities as sketched in figure 4.9 to 4.12 are put into perspective. For a normal shock, $\theta = 0$, the quantities are independent of y and have the following values:

$$
\begin{aligned}
\mathrm{M}_2 &= 0.668 \\
\frac{T_2}{T_1} &= 1.388 \\
\frac{\rho_2}{\rho_1} &= 2.032 \\
\frac{p_2}{p_1} &= 2.820 \\
\frac{p_{02}}{p_{01}} &= 0.895
\end{aligned}
\tag{4.6}
$$

Comparing the quantities above in equation 4.6 with figures 4.9 to 4.12, it is clear that the maximum quantities near the wall approach the quantities for the normal shock wave. Furthermore, it can be seen that the loss through the bow shock is much lower than for a full normal shock, when comparing the total pressure loss ($\frac{p_{02}}{p_{01}} = 0.99$ for the oblique part of the bow shock and $\frac{p_{02}}{p_{01}} = 0.895$ for the normal part of the bow shock).

In reality, the bow shock is a 3D shock surface. However, in this case study of the bow shock from an experiment of Giskes [7], the bow shock positioned in the symmetry plane was used. When considering a 3D bow shock, there is a curvature of the bow shock in the third dimension. A flow at a certain distance from the symmetry plane will have a smaller normal component of the velocity on the bow shock due to the curvature compared to the 2D case. Due to this smaller normal component of the velocity, the shock wave will be weaker and as a result, the total losses will be smaller when considering the bow shock in 3D.

4.3.2 Bow Shock Reflections

Figure 4.13 shows that the bow shock is reflected at the wall opposite to the orifice. These types of reflection should be understood for the analysis of the flow field and the interaction of the jet with the supersonic crossflow. For that purpose, two types of shock reflections are considered.

In figure 4.14, an oblique shock is considered, originating at a slope discontinuity at the lower wall. This is called an incident shock wave. From the description of oblique shocks in section 2.2.2, it is known that a shock wave is formed at an angle of β_1 with respect to the incoming flow. The streamlines of the freestream with M_1 are deflected at an angle θ and the flow is decelerated to M_2. However, the
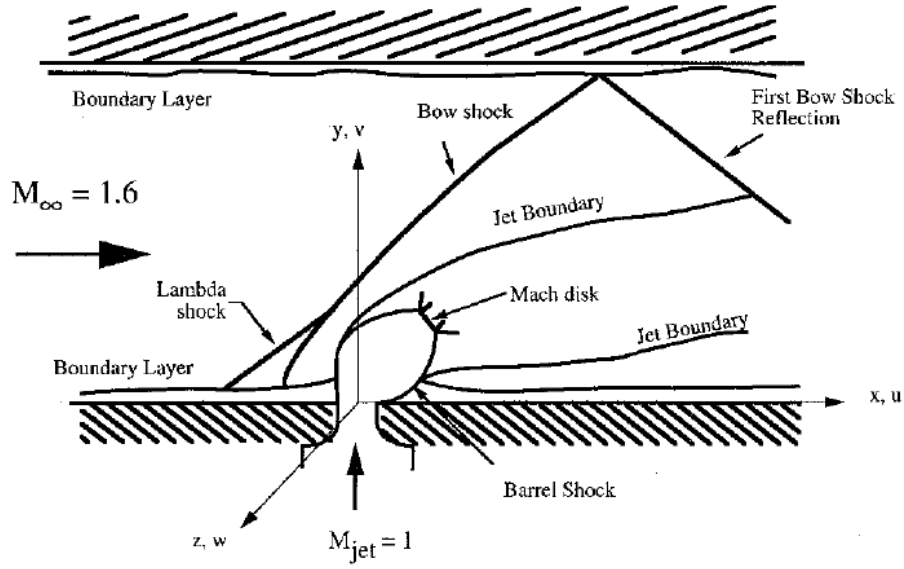
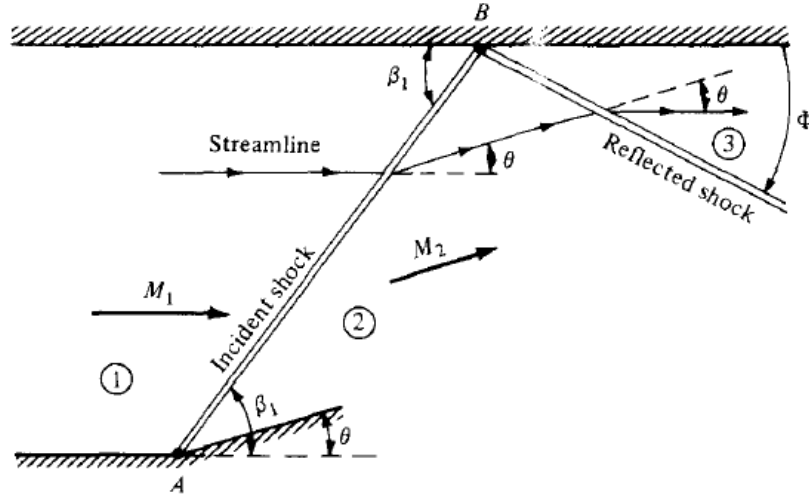Figure 4.13: Schematic of jet injection into supersonic crossflow including bow shock reflection [25].

Figure 4.14: Reflection of a shock wave with regular behaviour [6].

flow should be tangent everywhere along the upper wall. For that reason, the flow in region 2 has to be deflected, such that the flow becomes tangent to the upper wall. This is accomplished by nature by a reflected shock wave, originating from point B, the point at which the incident shock hits the wall. The strength of the reflected shock wave is weaker than the strength of the incident shock wave. As $M_1 > M_2$ and the deflection angle θ should be the same for both shocks, it requires the reflected shock to be weaker. Therefore, the angle of the shock with the upper wall Φ is not equal to β_1. The velocity in region 3, M_3, is again smaller and can be calculated from the knowledge of oblique shocks, such that every velocity and angle can be determined from M_1 and θ [6].

Another situation is given in figure 4.15. In this situation, M_1 is only slightly larger than the minimum Mach number that is required for having a straight, attached shock wave for a given deflection angle θ. In this case, the oblique shock equations give a solution for a straight, attached incident shock wave. The problem arises because of the Mach number decrease across the shock, such that M_2 may be too low for having a deflection θ through a reflected shock wave. In that case, the reflection as given in figure 4.14 is not possible. However, this is solved by nature, such that the situation of figure 4.15 appears. In this
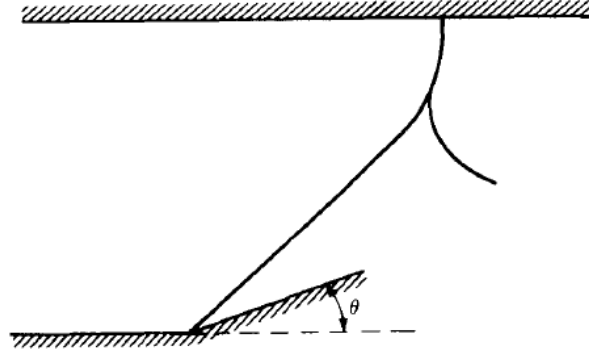
Figure 4.15: Mach reflection from the wall [6].

situation, the shock wave is curved near the upper wall, such that a partial normal shock, i.e. Mach stem, appears. Through this normal shock, streamlines are allowed to remain parallel to the wall downstream of the shock. At a certain distance from the wall, the oblique part of the incident shock is reflected. This reflected shock starts at the normal shock and propagates downstream. This reflection is called a Mach reflection. Calculations for this reflection are less straight-forward than for the case of figure 4.14, but numerical methods can determine the properties [6].

4.3.3 Behaviour Bow Shock

Ben-Yakar and Hanson [26] observed that the bow shock is not stationary, but its position oscillates as a result of the pulsating nature of the large-scale structures of the jet. This unsteady behaviour has been observed by Papamoschou et al. [30] too. In this research, the wrinkled behaviour of the shock wave was mentioned. Experiments by Giskes [7] and Lerink [31] confirm these observations. However, in the experiments of VanLerberghe [27], the bow shock appeared to be steady. This discrepancy in observations was not understood by VanLerberghe. It may be an unfortunate exception in the experiments and the analysis.

In their experiments of sonic jet injection of air into a supersonic crossflow, Gruber et al. [32] observed that the large-scale structures in the jet shear layer especially influence the near-wall behaviour of the bow shock. In this region, the curvature changes are severe and positional fluctuations are observed. However, the effects of the large-scale structures on the bow shock further away from the wall is weaker.

Experiments by Ben-Yakar and Hanson [26] give evidence of a strong dependency of the frequency of the bow shock fluctuations and the large-scale structures. It would be of interest to determine the correspondence of the fluctuation of the bow shock and the large-scale structures in the jet shear layer and whether there is a common frequency.
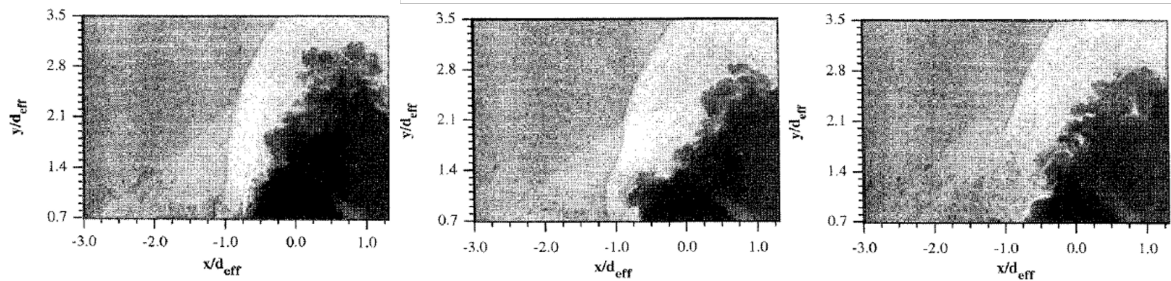
Figure 4.16: Interaction bow shock and large-scale shear layer structure in transverse injection of air at three moments in time [32].

In figure 4.16, the sonic jet injection of air into a supersonic crossflow is visualized with a planar laser-based visualization technique. d_{eff} is the jet diameter. Several features are shown. The bow shock has a standoff distance from the jet, which is on average $0.5D_j$. In addition, the bow shock's behaviour below

the point of intersection with the lambda shock upstream from the bow shock is strongly influenced by the large-scale structures formed in the jet shear layer. In the left-most image of figure 4.16, the normal shock part of the bow shock is shown, together with a small lift of the bow shock from the wall. In the middle image, the bow shock curves in upstream direction because of a large eddy at $y/D_j \approx 1$. In the right-most image, the bow shock is even lifted further from the wall than in the left-most image. This lifting appears to be a periodic feature. It is caused by a relatively thick boundary layer upstream of the orifice, which makes that the sonic line occurs further from the wall. Therefore, the boundary layer and jet fluid mix subsonically upstream of the jet orifice [32].

Next to the large-scale structures in the jet shear layer, the origin of the fluctuations can also be the result of the pressure fluctuations in the upstream boundary layer, the lambda shock in front of the bow shock, the recirculation zone and the pressure fluctuations in the jet itself [7][22][23].

4.4   Penetration of the Jet into the Crossflow

The purpose of the jet is to mix the fluid from the jet with the supersonic crossflow. In real applications, the jet fluid is a gaseous fuel. There are two important aspects of the sonic jet in the supersonic crossflow that determine the mixing efficiency. One aspect is the penetration and the other aspect is the mixing of the jet shear layer with the supersonic crossflow. The jet shear layer is elaborated on in section 4.5.

4.4.1   Investigation Parameters

For the penetration of the jet into the supersonic crossflow, several parameters are considered. These are flow, fluid and geometrical properties: the Mach number M, the temperature T, the density ρ, the pressure p, the specific heats c_p and c_v and the resulting ratio of specific heats $\gamma = c_p/c_v$, the viscosity of the gases μ, the heat conductance k, the molar weight of the gas $\mathcal{M}$ and the jet orifice diameter D_j [7]. A schematic overview is shown in figure 4.17.
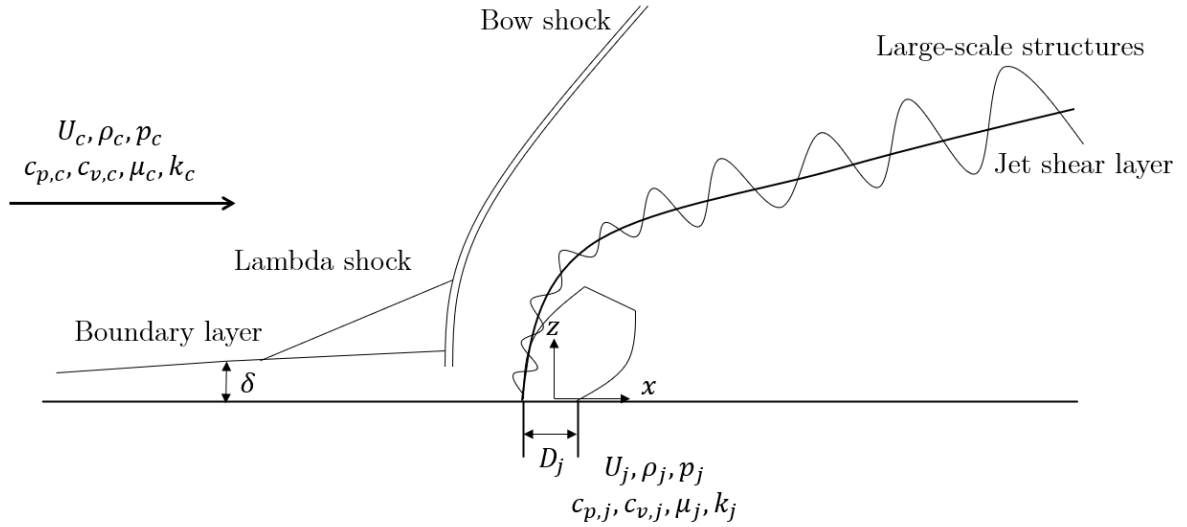
Figure 4.17: Schematic of jet penetration into supersonic crossflow in the symmetry plane.

From experiments, it is known that the penetration of the jet is found to be controlled primarily by the magnitude of the so-called **jet-to-crossflow momentum flux ratio** J [22][24][30][33], defined as:

$$J \equiv \frac{\rho_j U_j^2}{\rho_c U_c^2} \tag{4.7}$$

Here, the subscripts j and c correspond to the jet and the crossflow, respectively. The jet and crossflow are assumed to be ideal gases ($p = \rho RT$, $c_p = c_p(T)$ and $c_v = c_v(T)$), which result in the possibility of

rewriting equation 4.7:

$$J = \frac{\gamma_j p_j \mathrm{M}_j^2}{\gamma_c p_c \mathrm{M}_c^2} \tag{4.8}$$

In this expression, the static pressure p is used. Some other ratios are defined in the following, which are the velocity ratio $r_{j,c}$, the density ratio $s_{j,c}$ [34] and the pressure ratio $\eta_{j,c}$:

$$r_{j,c} \equiv \frac{U_j}{U_c} \tag{4.9}$$

$$s_{j,c} \equiv \frac{\rho_j}{\rho_c} \tag{4.10}$$

$$\eta_{j,c} \equiv \frac{p_j}{p_c} \tag{4.11}$$

These variables make that J can be rewritten to:

$$J = r_{j,c}^2 s_{j,c} \quad \text{or} \quad J = \eta_{j,c} \frac{\gamma_j \mathrm{M}_j^2}{\gamma_c \mathrm{M}_c^2} \tag{4.12}$$

For applications, it may be practical to use the stagnation or total pressure in the expression for the jet-to-crossflow momentum flux ratio [35]. Using the isentropic-flow relations, the expression for J becomes:

$$J = \frac{\gamma_j p_{0,j} \mathrm{M}_j^2 \left[1 + \frac{\gamma_c - 1}{2} \mathrm{M}_c^2\right]^{\frac{\gamma_c}{\gamma_c - 1}}}{\gamma_c p_{0,c} \mathrm{M}_c^2 \left[1 + \frac{\gamma_j - 1}{2} \mathrm{M}_j^2\right]^{\frac{\gamma_j}{\gamma_j - 1}}} \tag{4.13}$$

In chapter 3, a distinction was made between adapted (or pressure-matched) jets, nonadapted underexpanded jets and nonadapted overexpanded jets. Especially the first two types were taken into account in chapter 3. Papamoschou et al. [30] observed that the penetration of highly underexpanded jets is about the same as for adapted or pressure-matched jets. In the following, mainly underexpanded jets will be considered.

Parameter investigation of amongst others Papamoschou et al. [30], Schetz and Billig [36] and Portz et al. [37] shows that the scaled penetration height y/D_j depends on the following dimensionless parameters:

$$\frac{y}{D_j} = f\left(\frac{x}{D_j}, J, \frac{\delta}{D_j}, \mathrm{M}_c, \mathrm{M}_j, \eta_{j,c}, s_{j,c}, \frac{\mathcal{M}_j}{\mathcal{M}_c}, \frac{\mathrm{Re}_j}{\mathrm{Re}_c}\right) \tag{4.14}$$

In general, the penetration increases rapidly with increasing distance x/D_j, up to a certain distance, after which the penetration occurs more steadily [3].

It has been observed [23][25][30] that penetration strongly depends on the jet-to-crossflow momentum flux ratio J and this is the most important parameter for the penetration y/D_j. The penetration increases with increasing J [3][7][30][33]. As a result, the bow shock will be stronger for a larger J, i.e. a larger part of the bow shock will be normal. See also section 4.3. As a consequence, the total pressure loss will be larger for a larger value of J, which makes the process less efficient. So, the penetration increases with increasing J and so does the total pressure loss. For that reason, when designing a process, there is a balance between the desired J for transverse sonic jet injection into supersonic crossflow and the incurred losses.

The boundary layer thickness – scaled by the jet orifice diameter D_j – near the jet orifice is considered. According to experiments of hydrogen injection in supersonic crossflow of McClinton [38], an increase of the ratio δ/D_j increases the penetration. This was for a range of $1.25 \le \delta/D_j \le 6.25$. In addition, a study of Portz and Segal [37] showed that the effect of δ/D_j is significant for low supersonic Mach numbers. However, this effect decreases with increasing crossflow Mach number. Portz and Segal [37] observed that after J, δ/D_j has the strongest effect on the penetration. However, more recent experiments by Sun et al. [33] question this conclusion to be true in general, because the range of J used by Portz and Segal is rather small and for low values of J only. Therefore, the boundary layer thickness effect might not be significant for large values of J. Interestingly, in addition, many other studies such as [30][36] did not take the boundary layer thickness into account for the empirical relations they proposed. For example,

Gruber et al. [39] did not include δ/D_j into account for the equation too, but made sure that δ/D_j was equal to 1, such that it did not have an influence on the penetration equation when using a power-law function.

Furthermore, an increase of the crossflow Mach number M_c has a modest effect on the penetration: it results in an increased penetration. The reason is that when M_c increases, the local effective momentum flux ratio J_{eff} increases too [37]:

$$J_{\text{eff}} = \frac{\gamma_j p_j M_j^2}{\gamma_{c,2} p_{c,2} M_{c,2}^2} \tag{4.15}$$

In this equation, the subscript $c,2$ refers to the crossflow conditions downstream of the bow shock. If M_c increases, the bow shock becomes stronger. For that reason, the dynamic pressure downstream of the bow shock is smaller than upstream of the bow shock, which makes that locally $J_{\text{eff}} > J$. It is known that an increase of J or J_{eff} increases penetration and therefore, an increase of M_c results in increased penetration [37].

For considering constant J and M_j, $\eta_{j,c}$ and M_c are directly coupled, which makes that $\eta_{j,c}$ has a small influence on y/D_j too. It appeared that $s_{j,c}$ and M_j did not have a noticeable effect on the penetration [30]. However, the local behaviour can be altered by some parameters, although the overall penetration does not change. The density ratio $s_{j,c}$ and velocity ratio $r_{j,c}$ have an influence on the large-scale structures and the mixing behaviour of the jet [34].

Furthermore, Portz and Segal [37] observed a small dependence on the molecular weight ratio $\mathcal{M}_j/\mathcal{M}_c$ of the fluids in the jet and in the crossflow. Many other studies do not take this into account, which has to do with the small dependency and that $\mathcal{M}_j/\mathcal{M}_c = 1$ for many studies.

An even smaller effect on the penetration was observed by Portz and Segal [37] for the Reynolds number ratio Re_j/Re_c. This effect was to the power 3 smaller compared with the molecular weight ratio. As an illustration, the resulting penetration formula from Portz and Segal for $M_c = 1.6$ is shown with terms clustered, such that the relative strength is observed [37]:

$$\frac{y}{D_j} = 1.362 \left(J^{67.6} \left(\frac{x}{D_j} - 1.5 \right)^{32.9} \left(\frac{\delta}{D_j} \right)^{26.3} \left(\frac{Re_j}{Re_c} \right)^{-1} \left(\frac{\mathcal{M}_j}{\mathcal{M}_c} \right)^{2.98} \right)^{0.0084} \tag{4.16}$$

In this overview, the Reynolds number ratio is clearly the least contributing to the penetration. For that reason, in most studies, including [37], the effect of Re_j/Re_c was neglected.

In summary, the penetration of the jet y/D_j is determined by J and weakly by M_c; the other parameters have a negligible effect on the average penetration [30].

4.4.2   Analytical Derivations for Penetration of the Jet

Analytical derivations have been attempted for the description of a jet trajectory, for example by Schetz and Billig [36]. In their analysis, Schetz and Billig balanced forces over an infinitesimal part ds of the jet cross-section. For this analysis, gravity, average static pressure and drag force were considered. The following differential equation was derived for the angle of jet incidence α as function of the scaled distance along the jet axis $\bar{s} \equiv s/D_j$. The resulting differential equation is:

$$\frac{d\alpha}{d\bar{s}} = -\frac{C_D(\alpha) \sin^2(\alpha)}{2.5\pi} \frac{1}{J} \left(\frac{\rho}{\rho_c} \right) (2.25 + 0.22\bar{s})^3 \tag{4.17}$$

$$\begin{aligned} C_D(\alpha) &= 1.2 + (M_c \sin \alpha)^{7/2} & 0 \leq M_c \sin \alpha \leq 1 \\ C_D(\alpha) &= 1.06 + 1.14 \, (M_c \sin \alpha)^{-3} & M_c \sin \alpha \geq 1 \end{aligned} \tag{4.18}$$

In equation 4.17, the density ratio was assumed to be 1 and thereafter, a relation for the description of y/D_j and x/D_j can be obtained. In this expression, J again appears to be an important parameter. This corresponds with other observations, such as [30].

Although nice approaches were made, the physics appeared to be too complex for describing well by analytical derivations. However, in research, many experiments have been performed for determining properties and describing phenomena of jet injection into supersonic crossflow. In addition, many numerical simulations have been carried out over the past years. With the knowledge of these experiments and simulations, empirical relations for the jet penetration have been established.

4.4.3 Empirical Relations for Penetration of the Jet

In several studies, empirical relations were proposed. A general form of most empirical relations is given by Portz and Segal [37]:

$$\frac{y}{D_j} = c_1 J^{c_2} \left(\frac{x}{D_j} + c_3 \right)^{c_4} \left(\frac{\delta}{D_j} \right)^{c_5} \left(\frac{\mathcal{M}_j}{\mathcal{M}_c} \right)^{c_6} \tag{4.19}$$

In this equation, coefficients c_1 to c_6 can be functions of variables, specifically of M_c. Furthermore, the origin is in the center of the jet orifice. In the following, some experimental investigations are described, together with the resulting empirical relation for the penetration of the jet. Circular orifices will be considered. Note that different definitions of the penetration are possible: one can consider the location of the geometrical or mass center of the jet plume, or the location of the upper boundary of the jet shear layer (also called the **jet upper shear layer**). For example, Lee [9] used the following expression for the calculation of the penetration distance estimated with the cross-sectional center of mass of the hydrogen fuel in his numerical simulations:

$$y_{\mathrm{H}_2}(x) = \frac{\iint y \rho_{\mathrm{H}_2} \mathrm{d}y \mathrm{d}z}{\iint \rho_{\mathrm{H}_2} \mathrm{d}y \mathrm{d}z} \tag{4.20}$$

The following experimental investigations may have different definitions of the penetration depth.

Gruber et al. (1995) [40] investigated mixing and penetration characteristics for sonic injection, when considering circular transverse, circular oblique and elliptical transverse injectors. These experiments were for a supersonic crossflow of $\mathrm{M}_c = 2$ and the injectants were CO_2 and helium. The experiments were performed for $J = 1, 2$ and 3. The injection location was chosen to be at a point where the relative boundary layer thickness was $\delta/D_j = 1$. Planar Mie scattering was used for the study of the flow field. For the penetration profile, Gruber et al. proposed the following empirical relation:

$$\frac{y}{D_j} = 1.23 J^{0.656} \left(\frac{x}{D_j} \right)^{0.344} \tag{4.21}$$

In a later study, Gruber et al. (2000) [39] again investigated sonic transverse injection into supersonic crossflow with elliptical and circular orifices. The injectants were air and helium in a crossflow of air of $\mathrm{M}_c = 1.98$. Again, the jet injection was at the point where the relative boundary layer thickness was $\delta/D_j = 1$. Planar Rayleigh/Mie scattering was used for the examination of the 3D flow field. The results for air and helium as injectant were similar and the following relation was established for circular orifices. The upper boundary of the jet shear layer was used for the definition of the penetration:

$$\frac{y}{D_j} = 1.20 J^{0.656} \left(\frac{x}{D_j} + 0.5 \right)^{0.344} \tag{4.22}$$

This relation is also supported in [41]. The equation is only used in regions near the injectors, because otherwise, y/D_j would become improbably large with increasing x/D_j. Gruber et al. [41] found that the results of air and helium collapsed when dividing y/D_j and x/D_j by J. The shift of 0.5 is for the shifting of the penetration boundary to the upstream edge of the injection orifice.

In another research, McClinton [38] investigated the effect of the relative boundary layer thickness for a sonic transverse jet of hydrogen in a supersonic crossflow of air of $\mathrm{M}_c = 4.05$. All tests were run with $J \approx 1$. The boundary layer thickness to jet diameter ratio δ/D_j ranged from 1.25 to 6.50. This quantity was not experimentally but theoretically determined, from a theoretical model by Pinckney [42]. The data of experiments of McClinton [38] were combined with data from Rogers [43], which carried out experiments of hydrogen injection into a supersonic crossflow of air at $\mathrm{M}_c = 4.0$, at constant δ/D_j, $7 \le x/D_j \le 200$ and $0.5 \le J \le 2.0$. The combination gave the following empirical relation for the penetration of the jet upper shear layer [38]:

$$\frac{y}{D_j} = 4.20 J^{0.30} \left(\frac{x}{D_j} \right)^{0.143} \left(\frac{\delta}{D_j} \right)^{0.0574} \tag{4.23}$$

Furthermore, Rothstein and Wantuck [44] investigated injection of a sonic underexpanded jet into a supersonic crossflow. In this research, hydrogen was used as injectant and the supersonic crossflow

was $M_c = 1.5$. This argon-oxygen crossflow had a high temperature ($T = 1200$ K). The jet-to-crossflow momentum flux ratio J ranged from 5.9 to 38.6. The hydrogen penetration was measured using images, which were made by planar laser-induced fluorescence (PLIF) with the OH-molecule as target molecule. The resulting empirical relation for the upper boundary of the jet shear layer:

$$\frac{y}{D_j} = 2.173 J^{0.276} \left(\frac{x}{D_j}\right)^{0.281} \tag{4.24}$$

Portz and Segal [37] did experiments with injection of helium, hydrogen and argon, which were transversely injected into the supersonic flow of air. A Schlieren system was used for the visualization of the penetration. Experiments at a stagnation temperature T_0 of 1200 K and with a crossflow Mach number M_c of 1.3 to 3.6 were performed. The boundary layer thickness was measured at several locations, by measuring the stagnation pressure near the wall. For the experiments at $M_c = 1.6$, δ was 3.7 mm, so that for different sizes of D_j $0.8 \leq \delta/D_j \leq 3.7$. Furthermore, the jet-to-crossflow momentum flux ratio was $0.5 \leq J \leq 3.0$. For these experiments, the following empirical relation for the jet upper shear layer was determined:

$$\frac{y}{D_j} = 1.36 J^{0.568} \left(\frac{x}{D_j} - 1.5\right)^{0.276} \left(\frac{\delta}{D_j}\right)^{0.221} \left(\frac{\mathcal{M}_j}{\mathcal{M}_c}\right)^{-0.0251} \tag{4.25}$$

Comparing results of several experiments and relations from amongst others Schetz and Billig [36], Rogers [43] and McClinton [38], Portz and Segal [37] came up to a general equation in the form of equation 4.19, where the coefficients were a function of M_c. One observation to do so, was that the coefficient c_1 showed to have a strong correlation with M_c. The proposed relation is:

$$\frac{y}{D_j} = (1.049 M_c - 0.192) J^{-0.08 M_c + 0.615} \left(\frac{x}{D_j} - \frac{2.34}{M_c}\right)^{0.395 M_c - 0.823} \left(\frac{\delta}{D_j}\right)^{-0.067 M_c + 0.325} \left(\frac{\mathcal{M}_j}{\mathcal{M}_c}\right)^{-0.025} \tag{4.26}$$

Experiments at $M_c = 2.5$ validated this equation. However, if one would use $M_c = 1.6$ for the relation, c_4 becomes negative:

$$\frac{y}{D_j} = 1.486 J^{0.487} \left(\frac{x}{D_j} - 1.4625\right)^{-0.191} \left(\frac{\delta}{D_j}\right)^{0.219} \left(\frac{\mathcal{M}_j}{\mathcal{M}_c}\right)^{-0.025} \tag{4.27}$$

As a result of that, the location of the jet upper shear layer is not in the form of a power-law function with positive exponent anymore, but has an inversely proportional relation. As this behaviour is not expected, one can argue that this general relation in equation 4.26 cannot be applied for $M_c < 2.1$.

Finally, Sun et al. [33] did experiments with sonic jet injection of nitrogen into a supersonic flow of air at a stagnation temperature T_0 of 300 K and a stagnation pressure p_0 of 101325 Pa. The supersonic crossflow had a velocity of $M_c = 2.7$. Nanoparticle-based planar laser scattering (NPLS) was used and this recently-developed method is based on Rayleigh-Scattering. NPLS gave the possibility of measuring the boundary layer thickness with PIV velocity profile data. The jet-to-crossflow momentum flux ratio J ranged from 1.8 to 5.3. For the penetration of the jet, research was done into possible equations. The equation of Portz and Segal [37] was investigated, but the correctness of this equation was questioned for $J > 3$, because the experiments Portz and Segal investigated were not above a jet-to-crossflow momentum flux ratio J of 3. In the end, from the data, an equation similar to Rothstein and Wantuck [44] was obtained:

$$\frac{y}{D_j} = 2.933 J^{0.256} \left(\frac{x}{D_j}\right)^{0.161} \tag{4.28}$$

In table 4.1, the coefficients corresponding to equation 4.19 for all empirical relations discussed are given. In this overview, it is clear which parameters are more frequently used for empirical relations.

Figures 4.18, 4.19 and 4.20 show the relations as given in table 4.4 for $J = 1.0$, $J = 2.0$ and $J = 3.0$, respectively (except for Portz and Segal (gen.)). These plots help in getting an insight in the agreement or disagreement of the different empirical relations that are given in this section. In a later stadium, this

	c_1	c_2	c_3	c_4	c_5	c_6	M_c	J
Gruber et al. [40]	1.23	0.656	0	0.344	0	0	2	1, 2 and 3
Gruber et al. [39][41]	1.20	0.656	0.5	0.344	0	0	1.98	2.9
McClinton [38]	4.20	0.30	0	0.143	0.0574	0	4.0	1
Rothstein and Wantuck [44]	2.173	0.276	0	0.281	0	0	1.5	5.9 - 38.6
Portz and Segal [37]	1.36	0.568	-1.5	0.276	0.221	-0.0251	1.6	0.5 - 3.0
Portz and Segal [37] (gen.)	1.486	0.487	-1.4625	-0.191	0.219	-0.025	1.6	0.5 - 3.0
Sun et al. [33]	2.933	0.256	0	0.161	0	0	2.7	1.8 - 5.3

Table 4.1: Coefficients for c_1 to c_6 in equation 4.19 from several studies.

knowledge can be used for determining an empirical relation for penetration of the jet upper shear layer in the present research.

First of all, a general remark. The empirical relations are all determined for a fixed values of M_c. As penetration depends on M_c, some empirical relations at a relatively high M_c – such as McClinton [38] –, will structurally be off with respect to the others.

For $J = 1.0$ in figure 4.18, it appears that most relations do not correspond with each other. Gruber et al. and Portz and Segal are close, the same holds for Sun et al. and Rothstein and Wantuck. However, it is clear that there is little agreement in general.
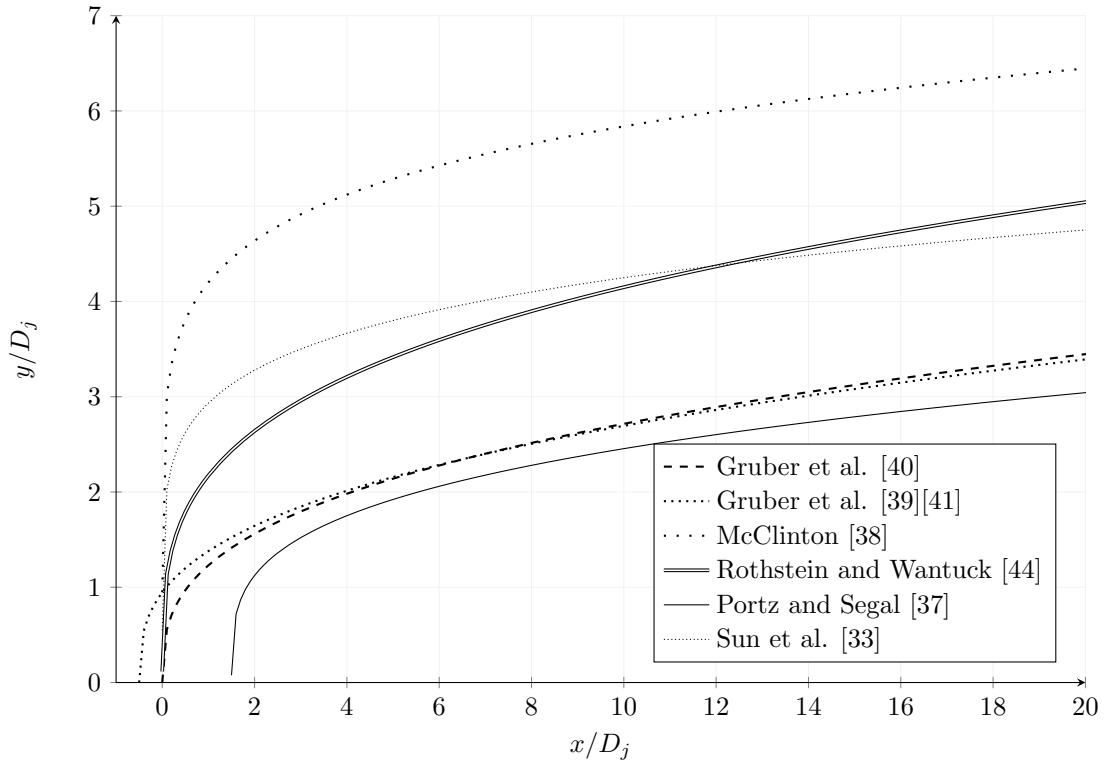
Figure 4.18: Empirical relations for the penetration for $J = 1.0$, $\delta/D_j = 1$ and $\mathcal{M}_j/\mathcal{M}_c = 1$.

The graphs for $J = 2.0$ in figure 4.19 show more agreement. All empirical relations except McClinton's are within a height of $2D_j$. Within this area, Portz and Segal's relation appears to give the lowest penetrations, whereas the relations of Sun et al. and Rothstein and Wantuck give the higher penetration. The relation of Gruber et al. is in between these two groups of lines.

When neglecting again McClinton's relation, it appears that the higher J, the better the agreement between the relations. In figure 4.20, the empirical relations for $J = 3.0$ are shown, which show the best agreement for the different empirical relations. Especially the relations of Gruber et al. and Rothstein and Wantuck show an excellent agreement.
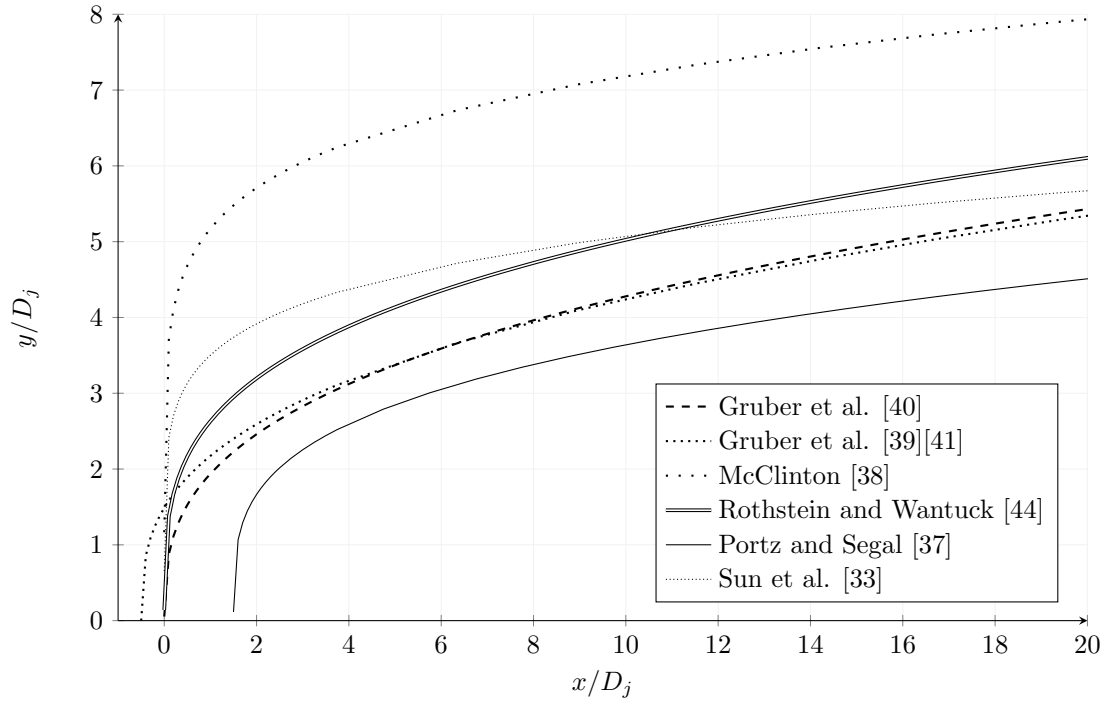
Figure 4.19: Empirical relations for the penetration for $J = 2.0$, $\delta/D_j = 1$ and $\mathcal{M}_j/\mathcal{M}_c = 1$.
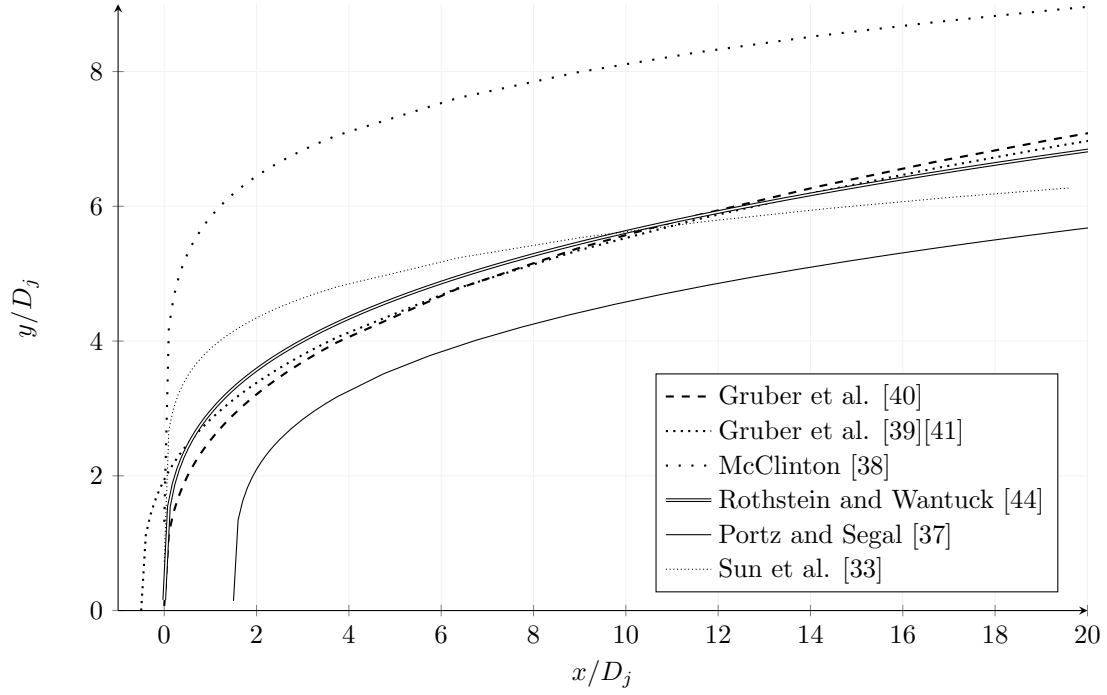

Figure 4.20: Empirical relations for the penetration for $J = 3.0$, $\delta/D_j = 1$ and $\mathcal{M}_j/\mathcal{M}_c = 1$.

It may depend on the case which empirical relation is the most suitable. This could be verified using experiments and examining which relation is the most suitable for the specific data set.

4.5 Behaviour of the Jet Shear Layer

An important feature of sonic jet injection into supersonic crossflow, is the behaviour of the jet shear layer. The jet shear layer is considered to be the fluid layer at the interface of the jet flow and the crossflow. The upper side of the jet shear layer is also called the jet upper shear layer. Figure 4.1 shows a schematic of the possible behaviour of the jet shear layer. In this jet shear layer, large-scale structures are present. These structures were also observed in figure 4.16. In this section, the large-scale structures will be analysed in more detail.

4.5.1 Large-Scale Coherent Structures in the Jet Shear Layer

The large-scale coherent structures have been studied for both subsonic and supersonic cases. Fric and Roshko [45] performed experimental studies for transverse jet injection into subsonic flow. Some of the phenomena that are visible in these analyses can also be observed in jet injection into supersonic flow [22]. In figure 4.21, an example of jet injection into subsonic flow is given. Focus will be on the vortices in the jet shear layer. It can be observed, that the roller structures become larger along the jet trajectory. These structures are essential in the mixing of the jet with the crossflow [22]. Mixing properties of the jet are elaborated in section 4.6.
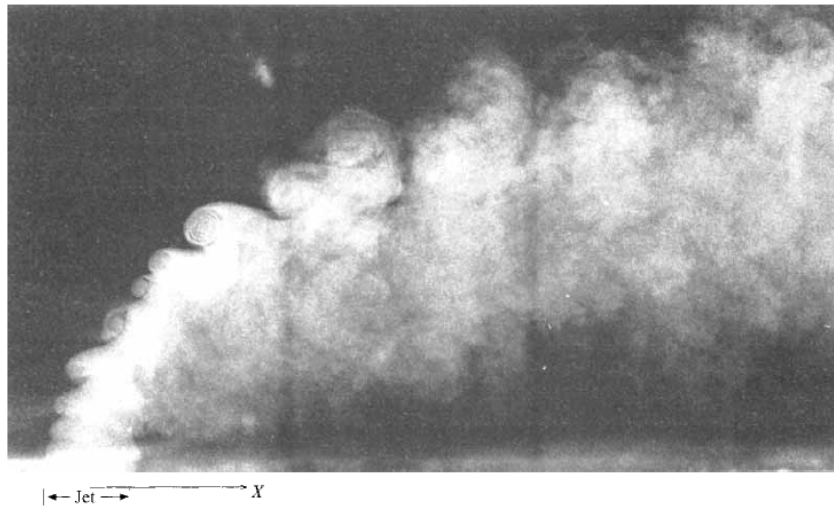

Figure 4.21: Jet shear layer of transverse jet injection into subsonic crossflow ($U_j/U_c = 4$), visualized by a smoke-filled jet [45].

Fric and Roshko argue that the found jet shear layer vortices are the result of the Kelvin-Helmholtz instability (see section 4.5.2 for an analysis of the Kelvin-Helmholtz instability). The Kelvin-Helmholtz instability being the origin of the vortices in the jet shear layer is also confirmed by numerical simulation of jet injection into subsonic flow by Yuan et al. [46]. These numerical simulations achieved quantitative agreement with experimental measurements. Yuan et al. observed that the vortices had a quasi-steady structure that oscillated around a fixed location. The behaviour, however, was not fully predictable.

In jet injection into supersonic flow, similar features are observed. In many studies, such as [22][26][34][39], large-scale eddies appear in measurements at the interface of the jet and the crossflow. The large-scale eddies are especially evolving at the upstream edge of the jet orifices and propagate in the upper boundary of the jet. The development of large-scale structures is strongly dependent on the Mach number [39].

Spreading of turbulent shear layers is also observed by Papamoschou and Roshko [47] for supersonic free shear layers. In their experiments, two fluids were flowing parallel to each other, such that these had an contact surface in common. The two flows had different velocities and could have different compositions. A schematic overview of the two parallel flows is shown in figure 4.22. In this figure, δ is the shear layer thickness and U_{conv} is the convective velocity.

The convective Mach number $\mathrm{M}_{\mathrm{conv}}$ for the case that $\gamma_1 = \gamma_2$ and $a_1 = a_2$ is expressed as [47]:
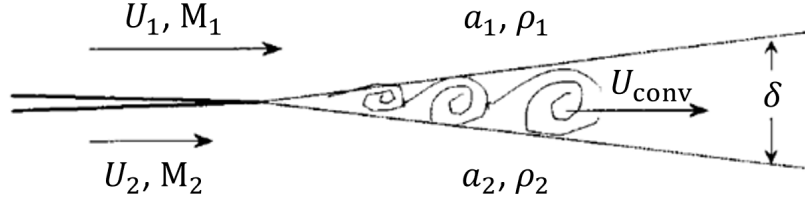
Figure 4.22: Schematic of shear layer between two parallel turbulent flows [48].

$$M_{conv} = \frac{M_1 + M_2}{2} \tag{4.29}$$

The growth rate was measured by Schlieren photography. The following expression was derived for the growth rate of the thickness of the shear layer, which holds for $U_1 \geq U_2 \Rightarrow r_{2,1} \leq 1$ [47]:

$$\frac{\delta}{x} = \frac{(1 - r_{2,1})(1 + \sqrt{s_{2,1}})}{1 + r_{2,1}\sqrt{s_{2,1}}} \tag{4.30}$$

This visual determined thickness depends on the velocity ratio $r_{2,1} = U_2/U_1$ and the density ratio $s_{2,1} = \rho_2/\rho_1$. This relation shows agreement with experimental data.

In the case of equal density, $\rho_1 = \rho_2$, the relation for the growth rate reduces to:

$$\frac{\delta}{x} = 2 \cdot \frac{1 - r_{2,1}}{1 + r_{2,1}} \tag{4.31}$$

Ben-Yaker and Hanson [26] observed that for jet injection into supersonic crossflow, the jet shear layer contains large-scale vortices. The eddies are formed as rollers periodically. This periodicity is found by some authors [23][27], but not endorsed by every other author [33]. Quantitative results were obtained in this study by high-speed imaging, by Schlieren images, which were taken with the possibility of having an interframing time down to 10 ns. A Xenon flashlamp was used as a light source. In the experiments, hydrogen was transversely injected at sonic speed into a nitrogen crossflow of $M_c = 3.38$, with $T_c = 1290$ K and $p_c = 32.4$ kPa, whereas $T_j = 246$ K and $p_j = 490$ kPa. As a result of that, the jet-to-crossflow momentum flux ratio J was 1.4 ± 0.1 and the boundary layer thickness was $\delta = 0.75$ mm near the orifice with diameter $D_j = 2.0$ mm.

The progress of the large-scale structures was measured by a cross-correlation method using a Fast Fourier Transform, based on the Schlieren images. In figure 4.23, Schlieren images are shown of a time sequence with an interframing time increment of 1 μm and an exposure time of 100 ns.

Figure 4.23 shows the convection of eddies and rollers. Ben-Yakar and Hanson [26] attribute these rollers to the Kelvin-Helmholtz instability (see section 4.5.2). The eddies start near the orifice of the jet and travel transversely, until around $x/D_j = 8$, where the eddies are convected in the same direction as the freestream [22]. The formation frequency of the eddies in the hydrogen appeared to be 568 kHz on average and being in the range between 513 and 663 kHz [26]. The frequency of this formation is related to the so-called preferred mode frequency f_j [49], which is characteristic for the large-scale eddies. Scaled with the jet velocity U_j and jet diameter D_j, the preferred mode Strouhal number equals:

$$St = \frac{f_j D_j}{U_j} \tag{4.32}$$

Many researchers confirmed this preferred mode and the Strouhal number varies in a broad range: $0.24 \leq St \leq 0.64$. However, higher values above 1 are obtained too [49].

A schematic of the eddies is shown in figure 4.24. In this figure, the jet upper shear layer is shown. λ is the spacing between the cores of the eddies and can be seen as the wavelength. a and b are the dimensions of an eddy [26].
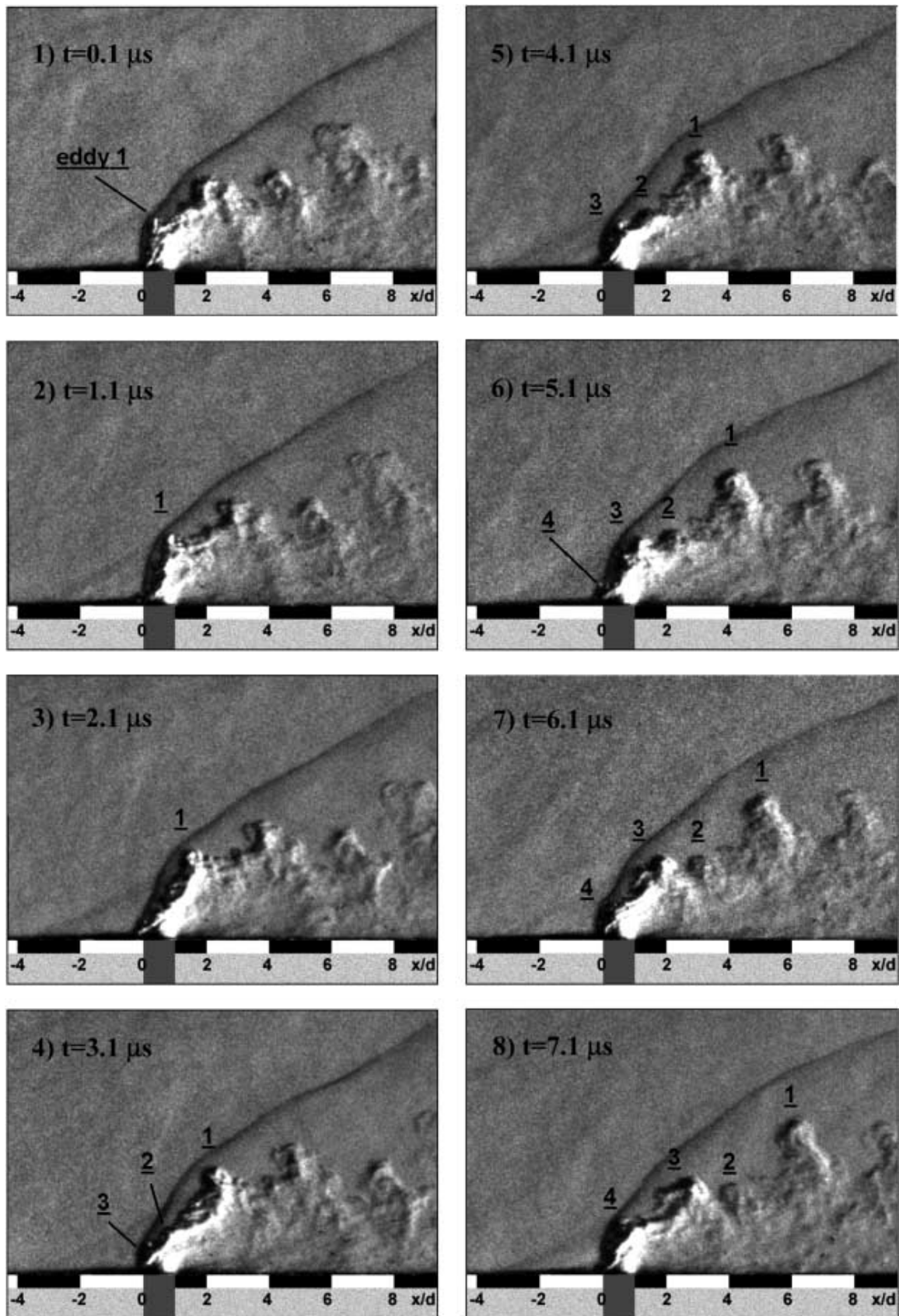
Figure 4.23: Schlieren images of sonic injection of hydrogen into a supersonic nitrogen crossflow, obtained by a high-speed-framing camera. $M_c = 3.38$, $T_c = 1290$ K, $p_c = 32.4$ kPa and $J = 1.4 \pm 0.1$ [26].
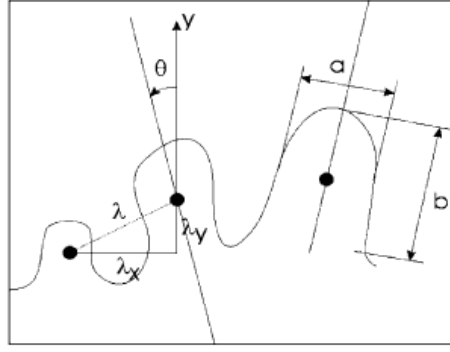
Figure 4.24: Schematic of the geometry of eddies in the jet shear layer [26].
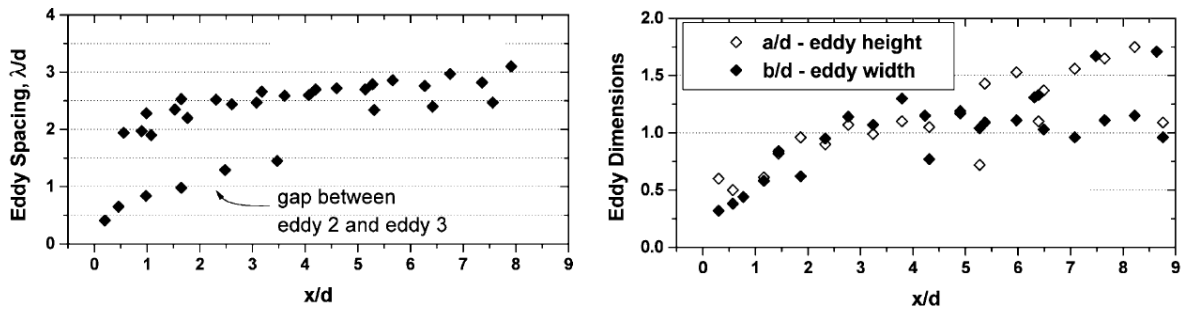

Figure 4.25: Eddy spacing and dimensions for the eddies in figure 4.23 [26].

Further investigation of the parameters in the experiments in figure 4.23 is considered in figure 4.25. This figure shows the eddy spacing versus x/D_j. As the eddies appear periodically, the eddy spacing can be seen as a measure of the wavelength λ. The outlying points are at the gap between eddy 2 and 3 (see figure 4.23), these are significantly different because of a secondary effect [26].

The size of the large-scale structures increases with x/D_j. It varies between $0.5D_j$ and $1.75D_j$. With increasing x/D_j, the eddies become elongated (b increases). The gap between the eddies λ slightly increases, but not much [26].

Ben-Yakar et al. [22] observed that the convection characteristics of the large-scale eddies depend on the injection fluid. In hydrogen large-scale structures propagated with a velocity closer to the freestream velocity than the large-scale structures in ethylene. According to Ben-Yakar et al, this is due to the different jet exit velocity, which is a result of different values for the speed of sound in hydrogen and in ethylene.

Rana et al. [23] arrived at the same conclusion as Ben-Yakar et al. [22], that the unsteady behaviour of the jet shear layer and the large-scale eddies mainly originate from the Kelvin-Helmholtz instabilities in that region. These structures appear specifically at the jet upper shear layer, which gives a good reason for Kelvin-Helmholtz instabilities being involved.

For that reason, in the next section, the Kelvin-Helmholtz instability is analysed for a simplified case, which can give insight into the working principles in a jet shear layer.

4.5.2 Kelvin-Helmholtz Instability of Jet Shear Layer

The Kelvin-Helmholtz instability is an instability that is commonly found in nature. It is sometimes found for example in clouds (figure 4.26) and occurs at the interface of two or more flows of different velocity.

The basic solution scheme of the Kelvin-Helmholtz instability is based on [50] and here extended with gravity and the effect of compressible flow. Surface tension will not be considered.

Figure 4.26: Kelvin-Helmholtz instability made visible by clouds [51].

4.5.2.1 Physics of Kelvin-Helmholtz Instability

The two-dimensional flow of two fluids is considered, which flows have a parallel velocity and share an interface. The upper fluid, fluid 1, occupies the space for which $z > 0$ and the lower fluid, fluid 2, occupies the space for which $z < 0$. Both fluids have a different density (ρ_1 and ρ_2), velocity in x-direction (U_1 and U_2) and pressure (p_1 and p_2). At the interface, there is a disturbance with a vertical displacement of $z = \zeta(x,t)$. In addition, there is gravity in negative z-direction. A sketch is shown in figure 4.27.
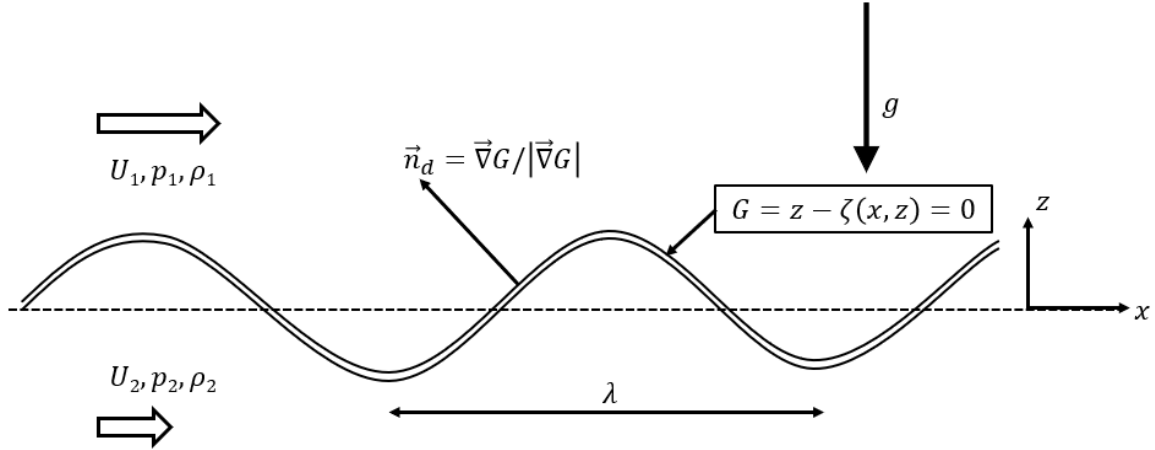
Figure 4.27: Schematic of two parallel flows in contact through an interface.

Bernoulli equation for the Kelvin-Helmholtz Instability

The problem is formulated by using the Bernoulli equation for inviscid, barotropic and irrotational flow subjected to a conservative force field [5]:

$$\frac{\partial \Phi}{\partial t} + \frac{1}{2}|\vec{u}|^2 + \int \frac{dp}{\rho} + F = \text{constant everywhere} \tag{4.33}$$

Applying gravity as only conservative external force results in:

$$\vec{f} = -\vec{\nabla}F \quad \Rightarrow \quad -g = -\frac{dF}{dz} \quad \Rightarrow \quad F = gz + C \tag{4.34}$$

Furthermore, for a barotropic flow of a calorically perfect gas (i.e. $p = c\rho^\gamma$), the integral can be evaluated as:

$$\int \frac{dp}{\rho} = c^{1/\gamma} p^{1-1/\gamma} \frac{1}{1-1/\gamma} = \frac{\gamma}{\gamma-1} \frac{p}{\rho} \tag{4.35}$$

$\Phi(x, z, t)$ is a velocity potential with the following definition:

$$\vec{u}(x, z, t) = \vec{\nabla} \Phi \tag{4.36}$$

For fluid 1, the velocity potential is $\Phi_1(x, z, t)$ and for fluid 2, the velocity potential is $\Phi_2(x, z, t)$. For the sake of generality, the following steps are for a general $\Phi(x, z, t)$. When substituting the relations in equation 4.33, Bernoulli's equation becomes:

$$\frac{\partial \Phi}{\partial t} + \frac{1}{2} |\vec{\nabla} \Phi|^2 + \frac{\gamma}{\gamma-1} \frac{p}{\rho} + gz = C \tag{4.37}$$

4.5.2.2   Kinematic and Dynamic Conditions for the Kelvin-Helmholtz Instability

The interface between the two fluids is considered (see figure 4.27). For an contact interface with velocity U_d between two fluids, an interface that is a stream surface, equation 2.10 yields:

$$u_{n_1} = 0 \quad \text{and} \quad u_{n_2} = 0 \quad \text{with} \quad u_n = (\vec{u} - \vec{u}_d) \cdot \vec{n}_d$$
$$p_1 = p_2$$
$$\vec{u}_{t_1} = \vec{u}_{t_2} \tag{4.38}$$
$$h_1 = h_2$$

The contact surface is described by the isocontour $G = 0$, where G is expressed as:

$$G = z - \zeta(x, t) \tag{4.39}$$

$\vec{\nabla} G$ is a vector perpendicular to isocontour $G = 0$ in the direction of increasing G. Therefore, the unit normal vector and unit tangential vector on the contact surface are:

$$\vec{n}_d = \frac{\vec{\nabla} G}{|\vec{\nabla} G|}$$
$$\vec{t}_d = \frac{\vec{e}_y \times \vec{\nabla} G}{|\vec{\nabla} G|} \tag{4.40}$$

which results in

$$\vec{n}_d = \frac{-\frac{\partial \zeta}{\partial x} \vec{e}_x + \vec{e}_z}{\sqrt{\left(\frac{\partial \zeta}{\partial x}\right)^2 + 1}}$$
$$\vec{t}_d = \frac{\vec{e}_x + \frac{\partial \zeta}{\partial x} \vec{e}_z}{\sqrt{\left(\frac{\partial \zeta}{\partial x}\right)^2 + 1}} \tag{4.41}$$

From $u_n = (\vec{u} - \vec{u}_d) \cdot \vec{n}_d = 0$ at $G = 0$, it follows that

$$\vec{u}_d \cdot \vec{n}_d = \vec{u} \cdot \vec{n}_d \tag{4.42}$$

The kinemetic condition is that the contact surface moves with the flow. Therefore, the total derivative of G is zero:

$$\frac{DG}{Dt} = 0 \quad \Rightarrow \quad \frac{\partial G}{\partial t} + \vec{u}_d \cdot \vec{\nabla} G = 0 \quad \Rightarrow \quad \frac{\partial G}{\partial t} + \vec{u} \cdot \vec{\nabla} G = 0 \quad \text{at} \quad G = 0 \tag{4.43}$$

With substitution of the velocity potential, the following kinematic condition is imposed:

$$\frac{\partial G}{\partial t} + \nabla \Phi \cdot \nabla G = 0 \quad \text{at} \quad G = 0 \tag{4.44}$$

which upon substitution of $G = z - \zeta(x,t)$ becomes:

$$\frac{\partial \zeta}{\partial t} + \frac{\partial \Phi}{\partial x}\frac{\partial \zeta}{\partial x} = \frac{\partial \Phi}{\partial z} \quad \text{at} \quad z = \zeta(x,t) \tag{4.45}$$

Equations 4.37 to 4.45 hold for both Φ_1 and Φ_2. So for the upper fluid ($z > 0$), the kinematic condition reads:

$$\frac{\partial \zeta}{\partial t} + \frac{\partial \Phi_1}{\partial x}\frac{\partial \zeta}{\partial x} = \frac{\partial \Phi_1}{\partial z} \quad \text{at} \quad z = \zeta(x,t)^{+} \tag{4.46}$$

and for the lower fluid ($z < 0$), the kinematic condition is:

$$\frac{\partial \zeta}{\partial t} + \frac{\partial \Phi_2}{\partial x}\frac{\partial \zeta}{\partial x} = \frac{\partial \Phi_2}{\partial z} \quad \text{at} \quad z = \zeta(x,t)^{-} \tag{4.47}$$

A seemed condition at the contact surface is the dynamic condition. For the dynamic condition, $p_1 = p_2$ at $z = \zeta(x,t)$. Substitution into equation 4.37 for both fluids results in the following dynamic condition:

$$\rho_1 \frac{\gamma_1 - 1}{\gamma_1}\left(\frac{\partial \Phi_1}{\partial t} + \frac{|\vec{\nabla}\Phi_1|^2}{2} + g\zeta - C_1\right) = \rho_2 \frac{\gamma_2 - 1}{\gamma_2}\left(\frac{\partial \Phi_2}{\partial t} + \frac{|\vec{\nabla}\Phi_2|^2}{2} + g\zeta - C_2\right) \quad \text{at} \quad z = \zeta(x,t) \tag{4.48}$$

If for both flows the same fluid is assumed, $\gamma_1 = \gamma$ and $\gamma_2 = \gamma$ will hold. Since $p_1 = p_2$ at the interface, it follows from the barotropic assumption that $\rho_1 = \rho_2$. Therefore, the dynamic condition reduces to:

$$\frac{\partial \Phi_1}{\partial t} + \frac{|\vec{\nabla}\Phi_1|^2}{2} - C_1 = \frac{\partial \Phi_2}{\partial t} + \frac{|\vec{\nabla}\Phi_2|^2}{2} - C_2 \quad \text{at} \quad z = \zeta(x,t) \tag{4.49}$$

Furthermore, the following holds far away from the interface:

$$\begin{aligned}
\vec{\nabla}\Phi_1 \to U_1 \vec{e_x} \quad \text{at} \quad z \to \infty \\
\vec{\nabla}\Phi_2 \to U_2 \vec{e_x} \quad \text{at} \quad z \to -\infty
\end{aligned} \tag{4.50}$$

4.5.2.3 Linearization

Now, the problem will be limited to infinitesimal disturbances with respect to the flow of two parallel uniform streams separated by a straight interface. It is assumed that the interface displacement is infinitesimal compared to other length scales. The velocity potential in the upper and that in the lower half-plane are expressed as

$$\begin{aligned}
\Phi_1(x,z,t) = U_1 x + \phi_1(x,z,t) \quad \text{and} \\
\Phi_2(x,z,t) = U_2 x + \phi_2(x,z,t),
\end{aligned} \tag{4.51}$$

respectively. Here ϕ_1 and ϕ_2 are infinitesimal compared to $U_1 x$ and $U_2 x$. By substitution of the velocity potentials, expressions for the kinematic and dynamic conditions are obtained in terms of ϕ_1 and ϕ_2. Because of linearization, the higher-order terms of ζ and ϕ will be neglected. This yields

$$\begin{aligned}
\frac{\partial \zeta}{\partial t} + \left(U_1 + \frac{\partial \phi_1}{\partial x}\right)\frac{\partial \zeta}{\partial x} = \frac{\partial \phi_1}{\partial z} \quad \text{at} \quad z = 0^{+} \Rightarrow \\
\frac{\partial \zeta}{\partial t} + U_1 \frac{\partial \zeta}{\partial x} = \frac{\partial \phi_1}{\partial z} + \text{h.o.t.} \quad \text{at} \quad z = 0^{+}
\end{aligned} \tag{4.52}$$

and similarly:

$$\begin{aligned}
\frac{\partial \zeta}{\partial t} + \left(U_2 + \frac{\partial \phi_2}{\partial x}\right)\frac{\partial \zeta}{\partial x} = \frac{\partial \phi_2}{\partial z} \quad \text{at} \quad z = 0^{-} \Rightarrow \\
\frac{\partial \zeta}{\partial t} + U_2 \frac{\partial \zeta}{\partial x} = \frac{\partial \phi_2}{\partial z} + \text{h.o.t.} \quad \text{at} \quad z = 0^{-}
\end{aligned} \tag{4.53}$$

For the dynamic condition, the constants are still to be eliminated. These constants are obtained by using Bernoulli's equation. The expression for the constant for undisturbed flow ($z \to \infty$ for flow 1 and $z \to -\infty$ for flow 2) becomes:

$$
\begin{aligned}
C_1 &= \frac{1}{2}U_1^2 \\
C_2 &= \frac{1}{2}U_2^2
\end{aligned}
\tag{4.54}
$$

Substitution of these constants and the velocity potential, while knowing that the main flow is undisturbed, results in the following dynamic condition:

$$
\frac{\partial \phi_1}{\partial t} + U_1 \frac{\partial \phi_1}{\partial x} + \frac{1}{2}\left(\frac{\partial \phi_1}{\partial x}\right)^2 + \frac{1}{2}\left(\frac{\partial \phi_1}{\partial z}\right)^2 = \frac{\partial \phi_2}{\partial t} + U_2 \frac{\partial \phi_2}{\partial x} + \frac{1}{2}\left(\frac{\partial \phi_2}{\partial x}\right)^2 + \frac{1}{2}\left(\frac{\partial \phi_2}{\partial z}\right)^2 \quad \text{at} \quad z = 0 \tag{4.55}
$$

$$
\frac{\partial \phi_1}{\partial t} + U_1 \frac{\partial \phi_1}{\partial x} + \text{h.o.t.} = \frac{\partial \phi_2}{\partial t} + U_2 \frac{\partial \phi_2}{\partial x} + \text{h.o.t.} \quad \text{at} \quad z = 0 \tag{4.56}
$$

Neglecting the higher order terms results in the following dynamic condition:

$$
\left(\frac{\partial \phi_1}{\partial t} + U_1 \frac{\partial \phi_1}{\partial x}\right)_{z=0^+} = \left(\frac{\partial \phi_2}{\partial t} + U_2 \frac{\partial \phi_2}{\partial x}\right)_{z=0^-} \tag{4.57}
$$

4.5.2.4 Normal Mode Analysis for Incompressible Flow

A sinusoidal disturbance of the interface is assumed in the form of

$$
\zeta(x,t) = \zeta_0 e^{i(kx-\omega t)} \tag{4.58}
$$

In this expression, k is the wave number and is restricted to real positive numbers, as k corresponds to an actual wavelength in physical space through [52]:

$$
\lambda = \frac{2\pi}{k} \tag{4.59}
$$

Further, ζ_0 is a real-valued constant and ω is the frequency of the temporal shape of the interface. This frequency may be a complex number in the form of [52]:

$$
\omega = \omega_r + i\omega_i \tag{4.60}
$$

If the imaginary part of ω is positive, then $e^{\omega_i t}$ grows exponentially in time. That is why a positive ω_i results in instability [52].

By convention, the real part (ω_r) of the final solution for ω is the representation of physical quantities. Therefore, the period of the waves can be determined by [52]:

$$
T = \frac{2\pi}{\omega_r} \tag{4.61}
$$

Combining the terms result in the Strouhal number, which expresses the nondimensional frequency:

$$
\text{St} = \frac{\omega}{ak} \tag{4.62}
$$

In this equation, St is the Strouhal number and a is the speed of sound. St can be a complex number, just like ω.

For an incompressible flow, the velocity potential has to satisfy the Laplace equation in two space dimensions:

$$
\nabla^2 \phi_i = 0, \quad i = 1, 2 \tag{4.63}
$$

The chosen expressions for ϕ_1 and ϕ_2 that satisfy this Laplace equation are [52]:

$$\phi_1(x, z, t) = \bar{\phi}_1(z)e^{i(kx - \omega t)}$$
$$\phi_2(x, z, t) = \bar{\phi}_2(z)e^{i(kx - \omega t)} \tag{4.64}$$

In this equation, $\bar{\phi}_i(z)$ is still an unknown function. By substituting equation 4.63, the following ordinary differential equation, which restricts $\bar{\phi}_i(z)$, is obtained:

$$\frac{d^2\bar{\phi}_i}{dz^2} = k^2\bar{\phi}_i \tag{4.65}$$

with general solution:

$$\bar{\phi}_j(z) = C_{1,j}e^{kz} + C_{2,j}e^{-kz} \tag{4.66}$$

This differential equation has to be satisfied for $\bar{\phi}_j(z)$. Accompanied with this second-order ordinary differential equation, two boundary conditions have to be satisfied, obtained by substituting ϕ_1 into equation 4.52 and utilizing that equation 4.50 holds [52]:

$$\bar{\phi}_1 \to 0 \quad \text{as} \quad z \to \infty$$
$$\frac{d\bar{\phi}_1}{dz} = i\zeta_0(kU_1 - \omega) \quad \text{at} \quad z = 0^+ \tag{4.67}$$

Similarly for ϕ_2:

$$\bar{\phi}_2 \to 0 \quad \text{as} \quad z \to -\infty$$
$$\frac{d\bar{\phi}_2}{dz} = i\zeta_0(kU_2 - \omega) \quad \text{at} \quad z = 0^- \tag{4.68}$$

Imposing the conditions of equation 4.67 and 4.68 then results in:

$$\bar{\phi}_1(z) = -\frac{i\zeta_0}{k}(kU_1 - \omega)e^{-kz}$$
$$\bar{\phi}_2(z) = \frac{i\zeta_0}{k}(kU_2 - \omega)e^{kz} \tag{4.69}$$

Now, the full expressions for ϕ_1 and ϕ_2 are known:

$$\phi_1(x, z, t) = -\frac{i\zeta_0}{k}(kU_1 - \omega)e^{-kz + i(kx - \omega t)}$$
$$\phi_2(x, z, t) = \frac{i\zeta_0}{k}(kU_2 - \omega)e^{kz + i(kx - \omega t)} \tag{4.70}$$

These expressions are substituted in equation 4.57, which results in:

$$(kU_1 - \omega)^2 = -(kU_2 - \omega)^2 \tag{4.71}$$

Rearranging and solving for ω results in:

$$\omega = \frac{k}{2}(U_1 + U_2) \pm i\frac{k}{2}|U_1 - U_2| \tag{4.72}$$

The layer is instable if the imaginary part of ω is positive and this holds if:

$$U_1 \neq U_2 \tag{4.73}$$

So for every case of two parallel flows with different velocities, the layer will become instable and appear as a Kelvin-Helmholtz instability, irrespective of the value of k. Time rate of growth depends linearly on $|U_1 - U_2|$ and linearly on $k = 2\pi/\lambda$. Thus the smaller λ, the faster the growth of the instability.

4.5.2.5   Normal Mode Analysis for Compressible Flow

In case of a compressible flow, the normal mode analysis becomes more complex. As the Bernoulli equation for compressible barotropic flow was used for two fluids with the same composition, this gave the same dynamic condition as for an incompressible flow. However, the velocity potential has to fulfill another condition than $\nabla^2 \phi_i = 0$ and this is the linearized unsteady Prandtl-Glauert equation [53]:

$$(1 - \mathrm{M}_i^2)\frac{\partial^2 \phi_i}{\partial x^2} + \frac{\partial^2 \phi_i}{\partial z^2} - \left(\frac{2\mathrm{M}_i^2}{U_i}\right)\frac{\partial^2 \phi_i}{\partial x \partial t} - \left(\frac{\mathrm{M}_j^2}{U_i^2}\right)\frac{\partial^2 \phi_i}{\partial t^2} = 0 \quad \text{for } i = 1, 2 \tag{4.74}$$

or rewritten with $\beta_i^2 = 1 - \mathrm{M}_i^2$:

$$\beta_i^2 \frac{\partial^2 \phi_i}{\partial x^2} + \frac{\partial^2 \phi_i}{\partial z^2} - \left(\frac{2\mathrm{M}_i^2}{U_i}\right)\frac{\partial^2 \phi_i}{\partial x \partial t} - \left(\frac{\mathrm{M}_i^2}{U_i^2}\right)\frac{\partial^2 \phi_i}{\partial t^2} = 0 \tag{4.75}$$

The speed of sound used for both Mach numbers is equal, because the temperature in both regions is equal, which is a result of the equal pressure, density and ratio of specific heats.

The same general expressions for $\zeta(x,t)$ and $\phi_i(x,z,t)$ are used as in equations 4.58 and 4.64, from which $\bar{\phi}_i(z)$ still has to be determined. The resulting linear second-order ordinary differential equation is obtained similar as for the incompressible case:

$$\frac{\mathrm{d}^2 \bar{\phi}_i}{\mathrm{d}z^2} = \left(k^2\beta_i^2 + \left(\frac{2\mathrm{M}_i^2}{U_j}\right)k\omega - \frac{\omega^2 \mathrm{M}_i^2}{U_i^2}\right)\bar{\phi}_i \quad \Rightarrow \tag{4.76}$$

$$\frac{\mathrm{d}^2 \bar{\phi}_i}{\mathrm{d}z^2} = k^2\left(1 - \left(\frac{U_i}{a_i} - \frac{\omega}{ka_i}\right)^2\right)\bar{\phi}_i \tag{4.77}$$

or when contracting the term in front of $\bar{\phi}_i(z)$ as ξ_i^2:

$$\frac{\mathrm{d}^2 \bar{\phi}_i}{\mathrm{d}z^2} = \xi_i^2 \bar{\phi}_i \tag{4.78}$$

with the boundary conditions as given in equation 4.67 and 4.68. The expressions for $\bar{\phi}_i$ result in, when solving equation 4.78:

$$\bar{\phi}_1(z) = -\frac{i\zeta_0}{\xi_1}(kU_1 - \omega)e^{-\xi_1 z}$$
$$\bar{\phi}_2(z) = \frac{i\zeta_0}{\xi_2}(kU_2 - \omega)e^{\xi_2 z} \tag{4.79}$$

with

$$\xi_1 = \sqrt{k^2\beta_1^2 + \left(\frac{2\mathrm{M}_1^2}{U_1}\right)k\omega - \frac{\omega^2 \mathrm{M}_1^2}{U_1^2}} = k\sqrt{1 - \left(\frac{U_1}{a_1} - \frac{\omega}{ka_1}\right)^2}$$
$$\xi_2 = \sqrt{k^2\beta_2^2 + \left(\frac{2\mathrm{M}_2^2}{U_2}\right)k\omega - \frac{\omega^2 \mathrm{M}_2^2}{U_2^2}} = k\sqrt{1 - \left(\frac{U_2}{a_2} - \frac{\omega}{ka_2}\right)^2} \tag{4.80}$$

The full equations for ϕ_1 and ϕ_2 are:

$$\phi_1(x,z,t) = -\frac{i\zeta_0}{\xi_1}(kU_1 - \omega)e^{-\xi_1 z + i(kx - \omega t)}$$
$$\phi_2(x,z,t) = \frac{i\zeta_0}{\xi_2}(kU_2 - \omega)e^{\xi_2 z + i(kx - \omega t)} \tag{4.81}$$

The full equations for ϕ_1, ϕ_2 and ζ are substituted into the dynamic condition given in equation 4.57. This results into:

$$\frac{\omega^2 - 2U_1 k\omega + U_1^2 k^2}{\xi_1(\omega)} = -\frac{\omega^2 - 2U_2 k\omega + U_2^2 k^2}{\xi_2(\omega)} \quad \text{at} \quad z = 0 \tag{4.82}$$

or

$$\frac{(\omega - U_1 k)^2}{k\sqrt{1 - \left(\frac{U_1}{a_1} - \frac{\omega}{ka_1}\right)^2}} = -\frac{(\omega - U_2 k)^2}{k\sqrt{1 - \left(\frac{U_2}{a_2} - \frac{\omega}{ka_2}\right)^2}} \quad \text{at} \quad z = 0 \tag{4.83}$$

When rewriting this equation with respect to the speed of sound, which for region 1 is equal to that for region 2:

$$\frac{\left(\frac{U_1}{a} - \frac{\omega}{ak}\right)^2}{\sqrt{1 - \left(\frac{U_1}{a} - \frac{\omega}{ak}\right)^2}} + \frac{\left(\frac{U_2}{a} - \frac{\omega}{ak}\right)^2}{\sqrt{1 - \left(\frac{U_2}{a} - \frac{\omega}{ak}\right)^2}} = 0 \quad \text{at} \quad z = 0 \tag{4.84}$$

or simplified:

$$\frac{(\mathrm{M}_1 - \mathrm{St})^2}{\sqrt{1 - (\mathrm{M}_1 - \mathrm{St})^2}} + \frac{(\mathrm{M}_2 - \mathrm{St})^2}{\sqrt{1 - (\mathrm{M}_2 - \mathrm{St})^2}} = 0 \quad \text{at} \quad z = 0 \tag{4.85}$$

St is a complex number and k is a positive real number. Solving this expression for ω explicitly, results in the following expression:

$$\mathrm{St} = \frac{1}{2}(\mathrm{M}_1 + \mathrm{M}_2) \pm i\sqrt{\sqrt{1 + (\mathrm{M}_1 - \mathrm{M}_2)^2} - \left(1 + \frac{1}{4}(\mathrm{M}_1 - \mathrm{M}_2)^2\right)} \tag{4.86}$$

or, rewritten with the introduction of a new term $\Delta \mathrm{M} = \mathrm{M}_1 - \mathrm{M}_2$:

$$\mathrm{St} = \frac{1}{2}(\mathrm{M}_1 + \mathrm{M}_2) \pm i\sqrt{\sqrt{1 + \Delta \mathrm{M}^2} - \left(1 + \frac{1}{4}\Delta \mathrm{M}^2\right)} \tag{4.87}$$

Comparing this solution to the solution for the incompressible case, the real parts of the Strouhal number are the same. Therefore, the same holds for the real part of the frequency. The imaginary part of the solution for the Strouhal number is different for the compressible case compared to that for the incompressible case. Thereby, in contrast to the incompressible case, the compressible case is not always unstable for $\mathrm{M}_1 \neq \mathrm{M}_2$. In figure 4.28, the two expressions for the imaginary part of the Strouhal number are shown.

Investigating figure 4.28 shows that the expression for incompressible flow is a linear approximation of the case of compressible flow around $\Delta \mathrm{M} = 0$. Thereby, it is shown that the compressible case is not always instable (i.e. $\Im(\mathrm{St}) > 0$) for $\Delta \mathrm{M} \neq 0$. If $\Delta \mathrm{M} > 2\sqrt{2} \approx 2.83$, the contact surface will be stable and for $0 < \Delta \mathrm{M} < 2\sqrt{2}$, the contact surface will be unstable. The maximal instability is found at $\Delta \mathrm{M} = \sqrt{3}$, for which $\Im(\mathrm{St}) = 0.5$.

Recapitulation of the definition of the Strouhal number shows that $\omega_i \propto ka \cdot \Im(\mathrm{St})$. This means that the division between stability and instability only depends on $\Delta \mathrm{M}$ and not on k. However, the larger k, the larger the imaginary part of the frequency ω_i will be, which makes the instability more severe. This means that the smaller the wave length λ, the more unstable the behaviour of the contact surface.

4.5.2.6 Extension for Fluids with Different Composition

The derivation thus far has been carried out for the case of two fluids that have the same composition. However, if the one fluid is for example air and the other fluid is hydrogen, some parameters cannot be equalized. The specific heats c_v and c_p can be different and then the same holds for the ratio of the specific heats γ and the specific gas constant R. As a result of that, the density ρ and speed of sound a also do not have to be equal for both fluids.

In that case, ρ and γ remain included in the dynamic condition and this results in the following equation as an equivalent of equation 4.84:

$$\rho_1 \frac{\gamma_1 - 1}{\gamma_1} \frac{\left(U_1 - \frac{\omega}{k}\right)^2}{\sqrt{1 - \left(\frac{U_1}{a_1} - \frac{\omega}{a_1 k}\right)^2}} + \rho_2 \frac{\gamma_2 - 1}{\gamma_2} \frac{\left(U_2 - \frac{\omega}{k}\right)^2}{\sqrt{1 - \left(\frac{U_2}{a_2} - \frac{\omega}{a_2 k}\right)^2}} = 0 \quad \text{at} \quad z = 0 \tag{4.88}$$

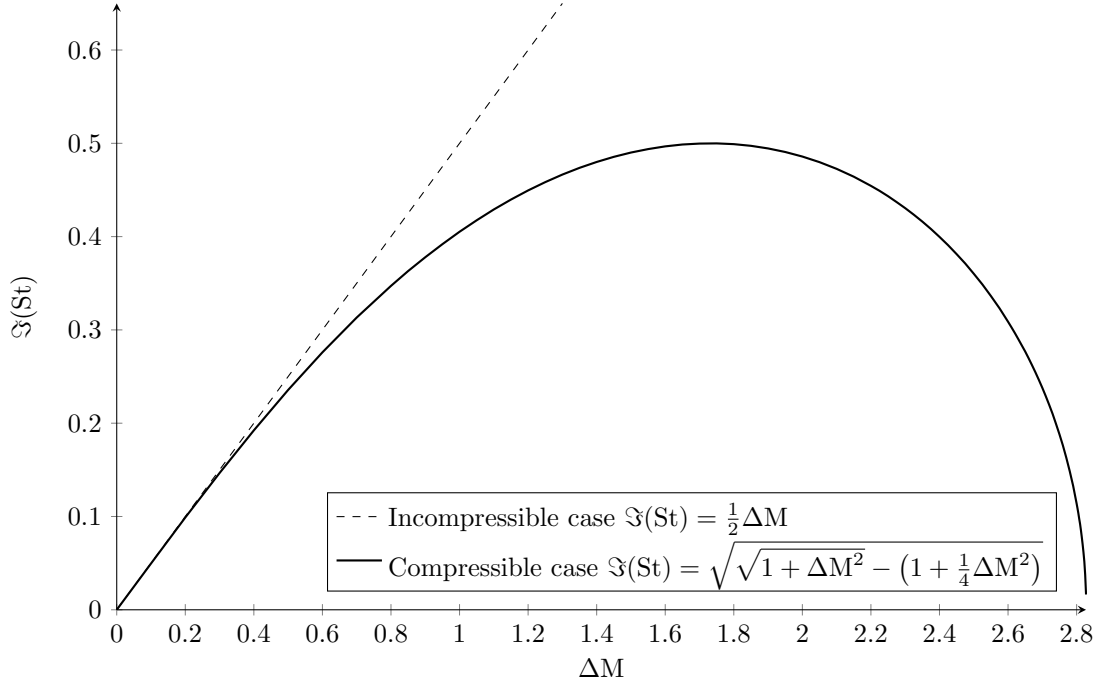This equation cannot be solved analytically, but a numerical solution can be obtained for ω.

Figure 4.28: Imaginary part of the Strouhal number versus the difference in Mach number ΔM.

4.5.2.7   Application

This above findings on of the Kelvin-Helmholtz instability can be applied to unstable jet shear layers and has the possibility of predicting and analyzing this behaviour. The analysis gives an expression for the physical frequency:

$$\omega_r = \frac{ka}{2}(M_1 + M_2) \tag{4.89}$$

or

$$f_r = \frac{a}{2\lambda}(M_1 + M_2) \tag{4.90}$$

which is the average of the two Mach numbers of the parallel flows, multiplied with the wave number k and the speed of sound a. For the application in supersonic flows, the compressible solution will be the appropriate solution.

However, the assumptions have to be taken into account and be weighed for their validity.

The most important assumption that might limit the use of the results is the assumption of having a two-dimensional parallel flow with semi-infinite regions, separated by a planar contact surface. Furthermore, the derivation is restricted to compressible, barotropic flows.

In jet injected crossflows, at a certain moment, the two flows will be parallel, with different velocities, which is comparable with the derivation. Furthermore, the compressibility effects of supersonic flows are taken into account in the derivation.

A difference comes up, because at the beginning, the jet flow is a cylindrical flow in another flow. Therefore, the effects are multidimensional and the far-field boundary conditions might not hold, because of the relatively small diameter of the jet flow. In addition, in the beginning, the jet flow is perpendicular to the crossflow and it is not bent directly into a parallel flow. Therefore, instability effects may already be present before having the conditions as assumed for the derivation in the present study.

However, it is worth analyzing the correspondence of the actual jet shear layer behaviour with the results of the derivation, because of the advantages this correspondence would have. Experimental images may be brought back to one period, such that the time-dependent behaviour of the fast large-scale structures can be investigated.

4.5.3 Analysis of Kelvin-Helmholtz Instabilities in Experiments

For the validation of the derivation of section 4.5.2, the best option would be to use an experiment from literature in which the behaviour of the large-scale eddies is documented. Ben-Yakar et al. [22] described the evolution of eddies in the jet shear layer over time, in which their experiments were exceptionally detailed compared to others. In the following analysis of the Kelvin-Helmholtz instability, the experiment of ethylene injection ($D_j = 2$ mm) into a nitrogen supersonic crossflow is taken.

For a couple of reasons, it is difficult to apply the equations from the derivation of section 4.5.2 to this experiment of Ben-Yakar et al. [22]. In the derivation, it was assumed that the fluids had the same composition, which is now not the case. However, the properties of ethylene and nitrogen have the same order of magnitude, which makes that the derived Kelvin-Helmholtz instability could give a result in the correct order of magnitude. For the different composition, the ratio of the specific heats γ, the specific gas constant R and the molecular mass $\mathcal{M}$ are the determining factors, which should be compared. For an ideal gas, $R = R_u/\mathcal{M}$, with R_u as the universal gas constant, which would give the same specific gas constant for ethylene and nitrogen. However, because of non-ideal effects in the flows, R is picked from literature.

Another difficulty arises when investigating the effect of the temperature. The crossflow has a temperature of 1290 K and the injectant a temperature of 263 K. For the Kelvin-Helmholtz instability, barotropic flow was assumed, which makes that $\rho_j = \rho_c$ (because of $p_j = p_c$) at the interface (for comparable fluids). When the specific gas constant R is in the same order of magnitude, then the temperature at the interface will be the same too. This temperature will probably be closer to T_c than to T_j, because of the larger amount of hot nitrogen compared to cold ethylene. The temperature at the interface will be somewhere in between these two values. A rough estimation is 1000 K. This determines the speed of sound, which makes the temperature rather important.

In the following table, the parameters of the injectant and the crossflow are summarized:

Parameter	Ethylene C_2H_4 (injectant)	Nitrogen N_2 (crossflow)
Static temperature T	263 K	1290 K
Velocity U	315 m/s	2360 m/s
Mach number M	1	3.38
Static pressure p	550 kPa	32.4 kPa
Density ρ	7.02 kg/m^3	0.0846 kg/m^3
Molecular mass $\mathcal{M}$	28 g/mol	28 g/mol
Specific gas constant R	296 J/kgK	286 J/kgK
Ratio of specific heats γ	1.27	1.4

Table 4.2: Parameters for the ethylene injectant and the nitrogen crossflow [22].

When comparing the last three parameters, they are in the same range of order of magnitude, which is an advantage for the comparability.

Another limitation is already mentioned in section 4.5.2.7, which is the orientation of the jet with respect to the crossflow. In the beginning, the jet is transversely oriented. Subsequently, the jet turns in the direction of the crossflow, which gives the situation of two parallel flows as analysed in section 4.5.2. For that reason, the frequencies and wavelengths are measured at a distance from the jet orifice, at the location where the jet and the crossflow appear to be more parallel.

Figure 4.29 shows Schlieren images of the ethylene injection into the nitrogen crossflow. The evolution of eddies is marked. In figure 4.30, the space-time trajectories of these eddies is tracked. From this figure, the following relevant parameters can be deduced. The wave length λ between the eddies is estimated as $\lambda = 3.5D_j = 7.0$ mm. The frequency of the shedding of the eddies is estimated as $f_r = 200$ kHz, or $\omega_r = 1.256 \cdot 10^6$ rad/s.

Equation 4.90 for the real frequency f_r obtained for the Kelvin-Helmholtz instability is rewritten to the following expression and values are substituted:

$$f_r = \frac{\sqrt{\gamma_{j,c} R_{j,c} T}}{2\lambda}(M_j + M_c) = \frac{\sqrt{1.33 \cdot 291 \cdot 1000}}{2 \cdot 7.0 \cdot 10^{-3}}(1 + 3.38) = 195 \text{ kHz} \qquad (4.91)$$
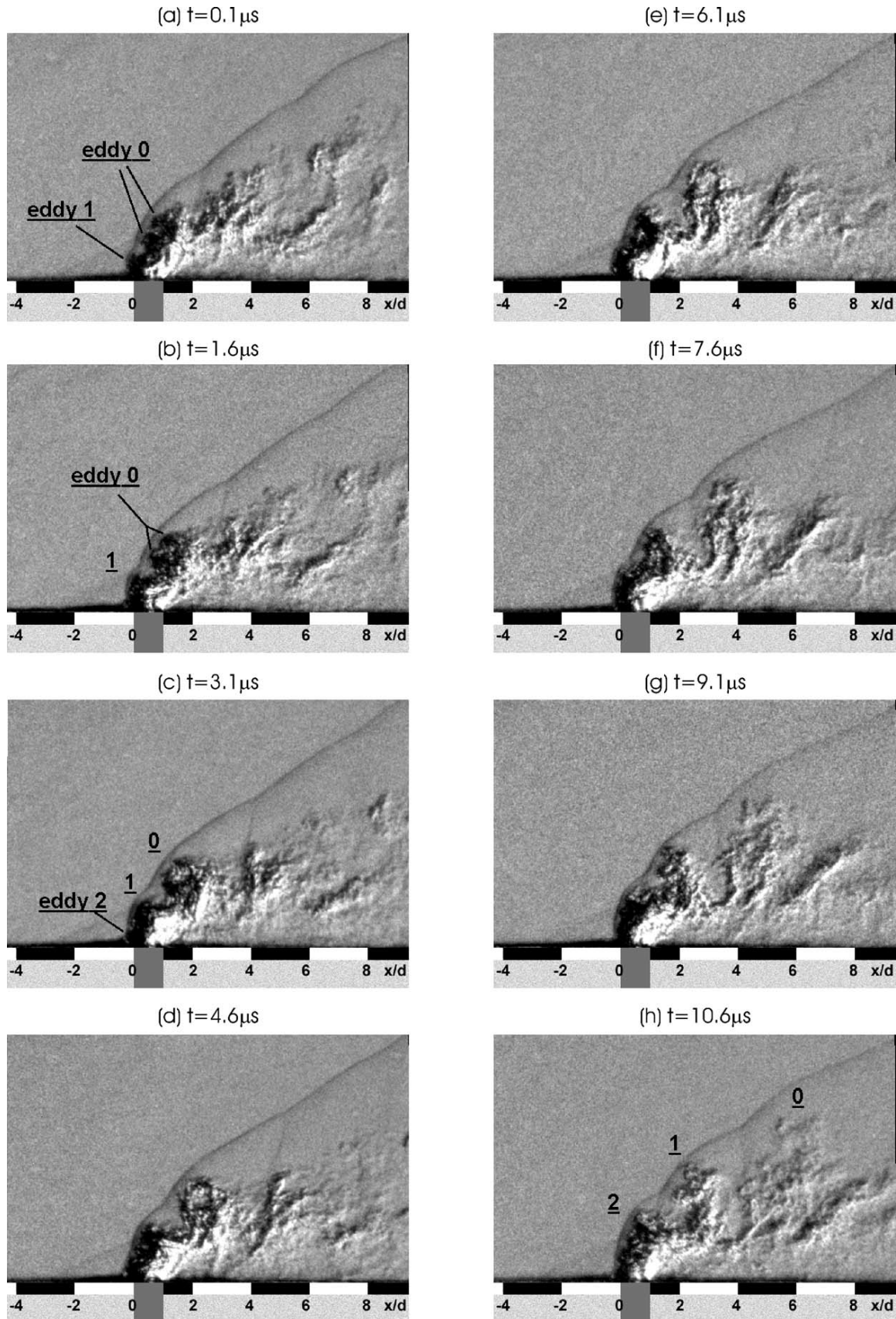
Figure 4.29: Schlieren images of sonic injection of ethylene into a supersonic nitrogen crossflow, obtained by a high-speed-framing camera ($\Delta t = 1.5$ μs). $M_c = 3.38$, $T_c = 1290$ K, $p_c = 32.4$ kPa and $J = 1.4 \pm 0.1$ [22].
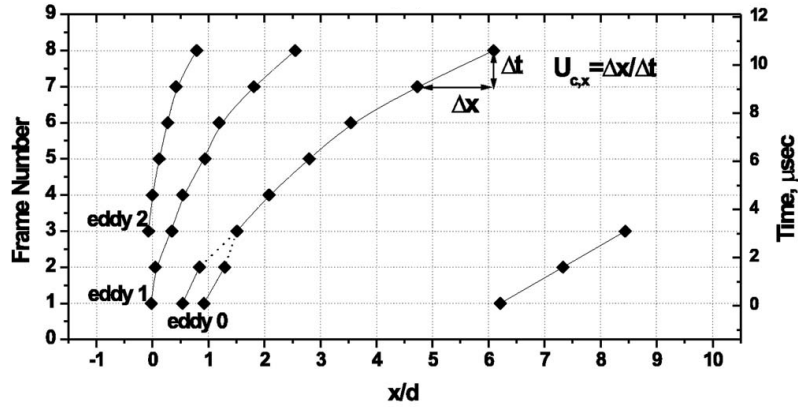
Figure 4.30: Space-time trajectories of the large-scale eddies of ethylene in the jet shear layer [22].

This calculated frequency of the large-scale structures is in the same order of magnitude as the frequency estimated from figure 4.30. Therefore, this gives an argument in favour of the validity of the derivation of the Kelvin-Helmholtz instability. Furthermore, it indicates that the large-scale structures are indeed largely the result of the Kelvin-Helmholtz instability.

4.6 Jet Plume Height and Bandwidth of Jet Upper Shear Layer

In the preceding sections, the jet shear layer and the penetration of the jet into the supersonic crossflow were analysed. The purpose of this jet injection is eventually having an adequate mixing of the jet and the supersonic crossflow. In applications, the jet fluid is fuel and the mixture with the crossflow of air should give a specific composition for efficient combustion. For that purpose, the thickness of the jet shear layer, i.e. the bandwidth of the jet upper shear layer mixing with the crossflow is important to analyze.

Figure 4.31 shows a Schlieren image of jet injection into a supersonic crossflow, in which the upper and lower boundaries of the **jet plume** – the height of the jet in vertical direction for a certain value of x – are marked with a black line. This front forms the contact surface between the crossflow and the jet. In the lower image, the data of a number of Schlieren images is processed and the colours show the variation of the boundaries of the jet plume. The higher the value of the colour in the colour scale, the more fixed the position of the jet shear layer had been found. The spreading of the location of the jet shear layer is found in most researches, which take this into account [22][33].

It depends on the definition of the penetration of the jet how the jet plume height can be defined. The jet plume height can be the distance from the **jet center line** – the line describing the center of the jet plume as function of x – to the jet upper shear layer in y-direction. Another option is omitting the jet center line and defining the jet plume height as the distance in y-direction between the upper and the lower boundary of the mixing area at a certain position x. Relations for this jet plume can be established. In section 4.5.2, an expression for the disturbance of the interface $\zeta(x,t)$ is derived, in which the disturbance height depends on the initial condition ζ_0 and the imaginary part of the frequency ω_i. In turn, ω_i depends on the Mach number difference ΔM, the speed of sound a and the wave number k.

The spreading of the jet upper shear layer is shown in figure 4.32. This spreading is called the bandwidth. The dots correspond with the position of the jet shear layer in the eight Schlieren images from [22]. It is clear that oscillatory structures are present, but in addition, from the near-field of the jet orifice onwards, the bandwidth steadily increases in streamwise direction. This bandwidth can be described largely by the Kelvin-Helmholtz instability, see section 4.6.1.

The mixing regions as described for the jet injection in still air (chapter 3) play an important role in the overall mixing of the jet with the crossflow. Thereby, the eddies and the instabilities in the jet shear layer
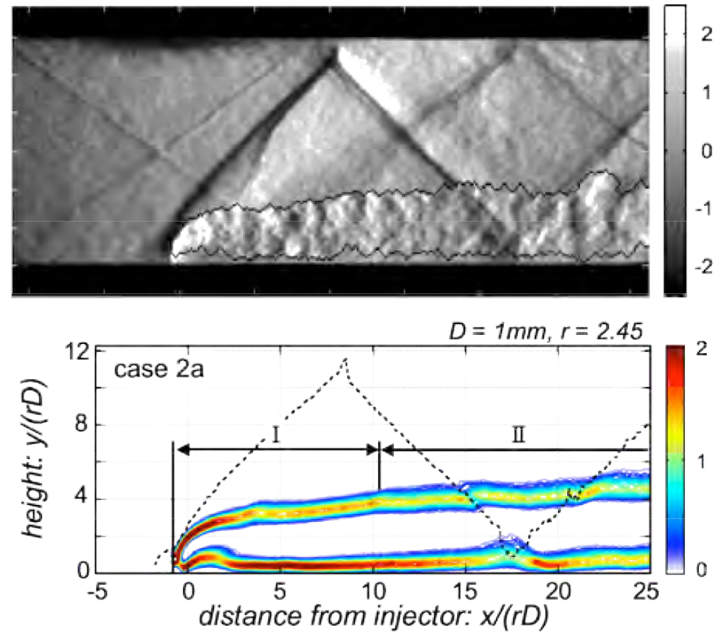
Figure 4.31: Schlieren image and processed view of helium injection into a supersonic crossflow of $M_c = 2$ [54].
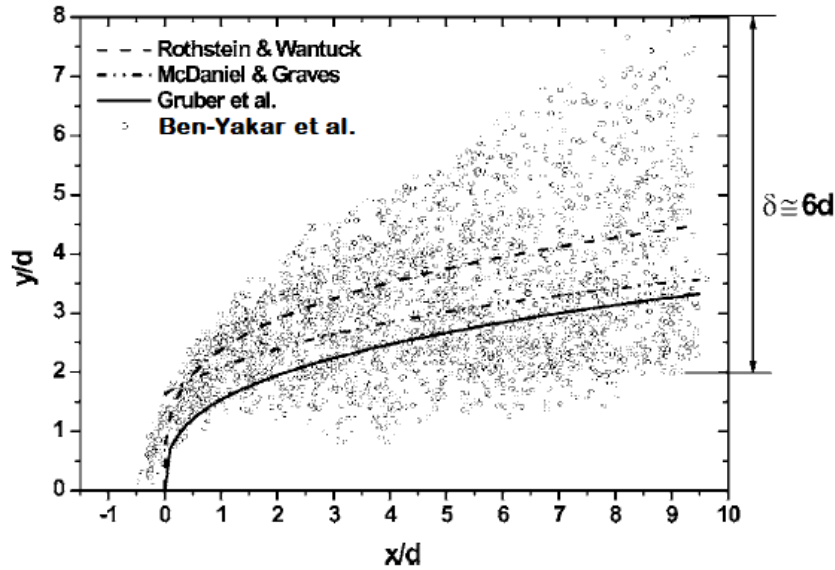

Figure 4.32: Transverse penetration data of ethylene jet injection. The dots are the position of the visually observable upper edge of the jet, when using eight Schlieren images ($M_c = 3.38$, $J = 1.4 \pm 0.1$). Rothstein & Wantuck's correlation is found to be the best for this experiment [22].

play an important role in the mixing. Especially the large-scale structures contribute significantly to the near-field mixing of the jet with the supersonic crossflow [27]. Small-scale turbulence also contributes to the mixing process [40]. Regions with high turbulent kinetic energy exist in the jet shear layer, specifically near the Mach disk. This leads to enhanced mixing [26].

It was already observed that penetration of the jet increases with increasing the ratio of jet-to-crossflow momentum flux J. In addition, the jet plume height increases too with increasing J [27]. In section 4.4, it was already mentioned that the penetration depends on J and not on the ratios within J, which are the density ratio s and the velocity ratio r. However, different combinations of s and r having the same J will result in different mixing. r has an influence on the Kelvin-Helmholtz instability (section 4.5.2),

because here the velocity difference is the driving mechanism for the instability. The influence of varying the ratio r and the ratio s is still subject of research [34].

It is important to consider the efficiency of mixing. For his numerical simulations of hydrogen injection into a supersonic crossflow of air, Lee [9] used the following definition for the mixing efficiency η_m:

$$\eta_m(x) = \frac{\oint \int Y_{\text{H}_2} \rho u \, \mathrm{d}y \mathrm{d}z}{\oint \int Y_{\text{H}_2}^r \rho u \, \mathrm{d}y \mathrm{d}z} \tag{4.92}$$

$$Y_{\text{H}_2}^r = \begin{cases} Y_{\text{H}_2}, & Y_{\text{H}_2} \leq Y_{\text{H}_2}^{\text{stoic}} \\ \left(\frac{1 - Y_{\text{H}_2}}{1 - Y_{\text{H}_2}^{\text{stoic}}} \right) Y_{\text{H}_2}^{\text{stoic}}, & Y_{\text{H}_2} > Y_{\text{H}_2}^{\text{stoic}} \end{cases} \tag{4.93}$$

Y_{H_2} is the mass fraction of H_2 in a hydrogen-air mixture and $Y_{\text{H}_2}^{\text{stoic}}$ is the stoichiometric mass fraction for a hydrogen-air mixture. Mixing efficiency increases in general with x/D_j. Penetration increases with J, but mixing becomes slower, which affects the mixing efficiency [9]. In many studies, the boundaries of the mixing region are not quantified, but it may be possible to determine these boundaries. In the next section, the same experiment as in section 4.5.3 is analysed, but now for the bandwidth of the jet upper shear layer.

4.6.1 Validation of the Kelvin-Helmholtz instability with respect to Bandwidth of the Jet Upper Shear Layer

The experiments by Ben-Yakar et al. [22] of ethylene injection into a nitrogen supersonic crossflow are used for the validation of the Kelvin-Helmholtz instability with respect to the bandwidth of the jet upper shear layer. The parameters and figures needed have been presented in section 4.5.3. Therefore, these will not be repeated here.

The disturbance equation is given as equation 4.58. When applying this equation to jet injection, the equation becomes the following, substituting $\omega = \omega_r + i\omega_i$:

$$\zeta(x, t) = \zeta_0 e^{i(kx - \omega_r t)} e^{\omega_i t} \tag{4.94}$$

For the bandwidth of the jet upper shear layer, the location of the envelope of the oscillating jet upper shear layer will be investigated. Therefore, the in-between oscillatory behaviour of the jet shear layer is neglected. For that purpose, the term $e^{i(kx - \omega_r t)}$ is neglected, as this is a combination of a sine and cosine. For the position of the envelope of the jet upper shear layer, $e^{i(kx - \omega_r t)}$ will be taken equal to 1.

In the equation for $\zeta(x, t)$, the terms ζ_0 and ω_i have to be determined. First, ω_i will be calculated. From section 4.5.2, it follows that for the case of a compressible flow, ω_i is expressed as:

$$\omega_i = \frac{2\pi a}{\lambda} \sqrt{\sqrt{1 + \Delta \text{M}^2} - \left(1 + \frac{1}{4} \Delta \text{M}^2 \right)} \tag{4.95}$$

With the findings from section 4.5.3, together with $\Delta \text{M} = 3.38 - 1 = 2.38$, $\omega_i = 227106$ rad/s is found. From figure 4.28, it can be seen that the jet shear layer is unstable at this value for ΔM, which indicates that Kelvin-Helmholtz instability phenomena arise.

Figure 4.32 is used for the validation. It is difficult to determine an appropriate reference line for the validation of the Kelvin-Helmholtz instability in the jet upper shear layer, because the jet initially penetrates in vertical direction, before it turns into the direction of the crossflow, where a parallel flow configuration is obtained. This parallel flow configuration is needed for application of the Kelvin-Helmholtz instability as derived in section 4.5.2. For good comparison, it is chosen to use a shift added to function of the jet upper shear layer. The shift is chosen to be $0.75D_j$ from the jet upper shear layer, such that at $x/D_t = 2$, the reference line and the data points of the upper boundary coincide. $x/D_t = 2$ is chosen, because at that point, the jet is turned sufficiently in the direction of the crossflow.

From figure 4.32, the bandwidth is determined by taking the position of the upper boundary of the area with dots, subtracting the penetration as described by Rothstein & Wantuck (equation 4.24) and $0.75D_j$ distance from the penetration added. In figure 4.33, the envelope of the jet upper shear layer is marked by red dots.
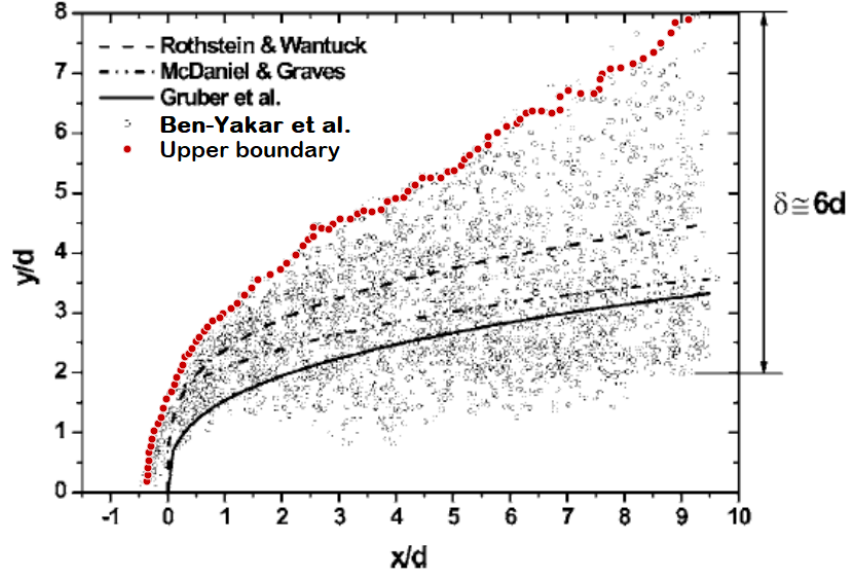
Figure 4.33: Transverse penetration of ethylene jet injection ($M_c = 3.38$, $J = 1.4 \pm 0.1$) [22]. The red dots are markers for the upper boundary of the jet upper shear layer.

The reference line is calculated by taking equation 4.24 and adding $0.75 D_j$ in the normal direction to equation 4.24:

$$\frac{y}{D_j} = 2.173 J^{0.276} \left(\frac{x}{D_j}\right)^{0.281}$$

$$\frac{\mathrm{d}\,(y/D_j)}{\mathrm{d}\,(x/D_j)} = 0.612 J^{0.276} \left(\frac{x}{D_j}\right)^{-0.719}$$

$$\vec{n}(x) = \frac{1}{\sqrt{\left(\frac{\mathrm{d}(y/D_j)}{\mathrm{d}(x/D_j)}\right)^2 + 1}} \begin{pmatrix} \frac{\mathrm{d}(y/D_j)}{\mathrm{d}(x/D_j)} \\ 1 \end{pmatrix} \tag{4.96}$$

$$\left(\frac{y}{D_j}\right)_{\text{jet}} = 2.173 J^{0.276} \left(\frac{x}{D_j} + 0.75 n_x(x)\right)^{0.281} + 0.75 n_y(x)$$

In figure 4.34, the envelope of the jet upper shear layer as determined from figure 4.33 is shown, together with penetration of the jet upper shear layer and the reference line of the jet upper shear layer for $x/D_t > 2$. The y/D_t of the reference line will be subtracted from the data points of the envelope of the jet upper shear layer for the analysis of the bandwidth of the jet upper shear layer.

In the next step, equation 4.94 is rewritten in terms of x instead of t. This is done by using that the propagation of the large-scale structures is according to the convective Mach number $M_{\text{conv}} = \frac{3.38+1}{2} = 2.19$. In this manner, x and t in the relation for the instability can be coupled:

$$t = \frac{x}{a M_{\text{conv}}} \tag{4.97}$$

Then substitution into equation 4.94 yields:

$$\frac{\zeta}{D_j}(x) = \frac{\zeta_0}{D_j} e^{\frac{\omega_i D_j}{a M_{\text{conv}}}\left(\frac{x}{D_j}\right)} \tag{4.98}$$

ζ_0/D_j is determined by substitution of a known value for the bandwidth of the jet upper shear layer. At $x/D_j = 9.0$, the distance between the envelope of the jet upper shear layer and the reference line is $\zeta/D_j = 2.7$. From these coordinates, it is derived that $\zeta_0/D_j = 0.135$.

Substitution of all found values into equation 4.98 results in the following expression for the bandwidth of the jet upper shear layer:
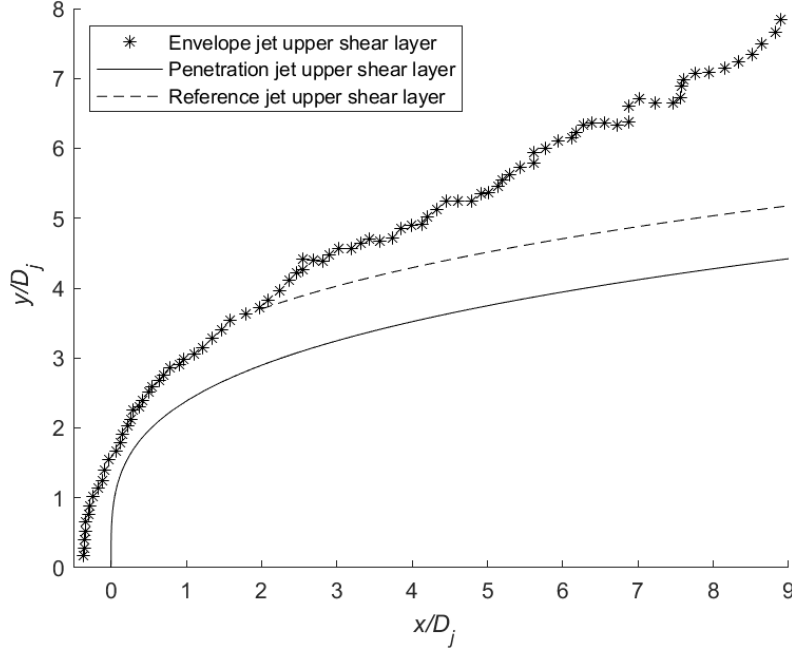
Figure 4.34: Transverse penetration of ethylene jet injection from figure 4.33 ($M_c = 3.38$, $J = 1.4 \pm 0.1$). The origin is positioned at the upstream side of the jet orifice. The envelope of the jet upper shear layer is denoted by $*$, the penetration of the jet upper shear layer is denoted by the solid line and the reference line is denoted by the dashed line.

$$\frac{\zeta}{D_j}(x) = 0.135 e^{0.333 \left(\frac{x}{D_j} \right)} \tag{4.99}$$

This equation plotted in figure 4.35, together with the data points of the envelope of the jet upper shear layer from figure 4.33 minus the reference line.

From figure 4.35, it can be seen that the results of the analysis of the Kelvin-Helmholtz instability fairly approximates the bandwidth of the jet upper shear layer. However, clearly, as there are uncertainties, which are mentioned in sections 4.5.2.7 and 4.5.3. In addition, there are more phenomena than the Kelvin-Helmholtz instability that contribute to the jet plume height (see section 4.1). However, the analysis of the Kelvin-Helmholtz instability provides a reasonable approximation for the macroscopic behaviour of the bandwidth of the jet upper shear layer.
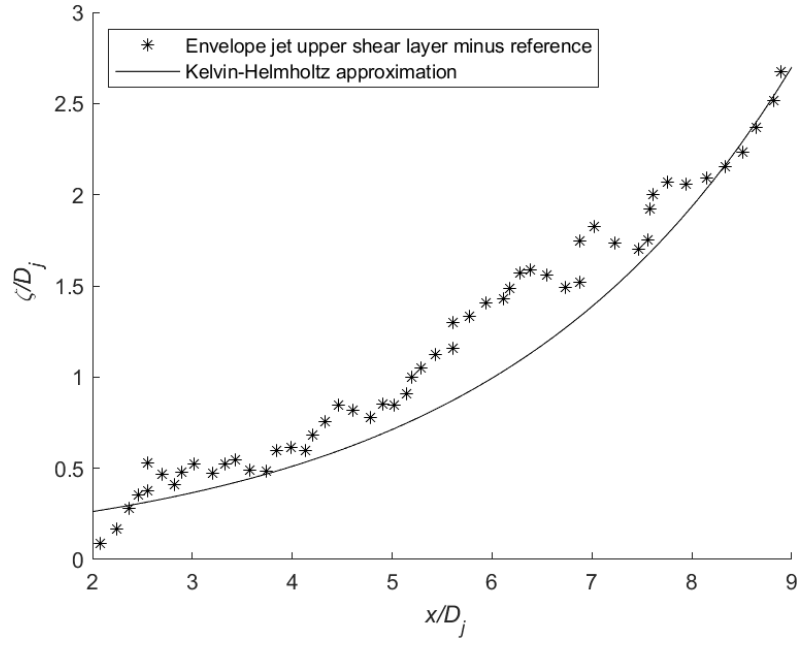
Figure 4.35: The upper boundary of the envelope of the jet upper shear layer minus the reference line ($M_c = 3.38$, $J = 1.4 \pm 0.1$). The domain for $x/D_t > 2$ is used for an appropriate application of the Kelvin-Helmholtz instability. The red dots in figure 4.33 minus the reference line are marked as $*$ and the approximation by the Kelvin-Helmholtz instability (equation 4.99) is the black line.

Chapter 5

Dual Jet Injection into Supersonic Crossflow

In chapter 4, single jet injection into a supersonic crossflow has been investigated. The observed features were described in detail. In the present study, the focus is on tandem dual jet injection into a supersonic crossflow. Therefore, the knowledge of single jet injection is used as a building block for dual jet injection. When the term dual jet injection is used, then a tandem configuration for dual jet injection is intended.

Figure 5.1 shows a schematic with features in tandem dual jet injection. Comparing figure 5.1 with figure 4.2 for single jet injection, similar features are observed, but also with some important differences. In figure 5.1, two jets are present and therefore, two bow shocks, one in front of each jet, are observed. Furthermore, it appears that the cascaded configuration has an influence on the penetration. Therefore, in the present chapter, these phenomena are investigated.
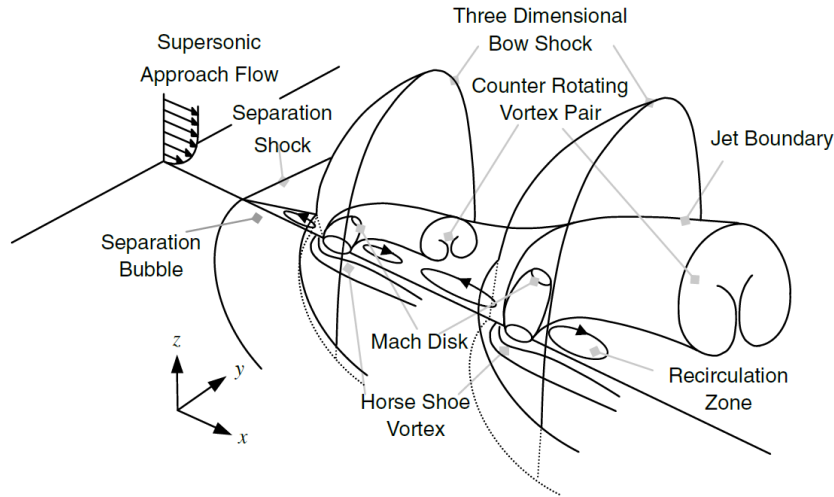

Figure 5.1: Schematic of tandem dual jet injection [9].

The focus is on the behaviour of the two bow shocks that appear upstream of each of the two jet orifices, as well as on the penetration of the rear, stronger, jet into the crossflow. These phenomena for dual jet injection are compared with features occurring in single jet injection. The question is whether dual jet injection improves the penetration of the jet compared to that in single jet injection, as well as as the dependence of the penetration on parameters of the flow.

The experimental and numerical studies into dual jet injection into a supersonic crossflow of De Maag [3][35], Landsberg [55] and Lee [9] are investigated. As an overview, the flow conditions for these studies are shown in table 5.1.

In the studies, a total diameter D_t is defined, which is used for appropriate scaling of variables [35][55]:

Conditions	De Maag [3][35]	Landsberg [55]	Lee [9]	Present study
M_c	1.6	2.623 - 5.272	2	1.55
p_c [kPa]	23.3 ± 2	44.24 - 99.48	146.6	25.66 ± 1
T_c [K]	194 ± 10	786.9 - 1143	1081	197 ± 3
u_c [m/s]	461 ± 10	1453 - 3483	1318	436.3 ± 10
M_j	1	1	1	1
Injection orientation	90°	45°	90°	90°
Injectant	Air	Hydrogen	Hydrogen	Air
D_t [mm]	2.23	2.01	3.18	2.23
D_1 [mm]	1	0.9	2.247	1
D_2 [mm]	2	1.8	2.247	2
J	1, 1.4, 2	1	1, 2	2.8, 3.8, 4.8
S	0 - 12	0 - 10	0 - 14	0 - 10

Table 5.1: Conditions for several studies into dual jet injection into a supersonic crossflow.

$$D_t \equiv \sqrt{D_1^2 + D_2^2} \qquad (5.1)$$

D_1 is the diameter of the jet orifice upstream and D_2 is that of the jet orifice downstream. Another important parameter is S, which is the distance between the center lines of the two orifices – the dimensionless **dual distance**. The absolute distance between the two center lines of the orifices, Δx, is scaled with D_t:

$$S = \frac{\Delta x}{D_t} \qquad (5.2)$$

In section 5.1, the behaviour of the two bow shocks in front of the jets is considered and in section 5.2, the penetration of the two jets into the supersonic crossflow.

5.1 Bow Shocks in Front of the Two Jets

In section 4.3, the behaviour of the bow shock in front of a single jet was observed and detailed. The same behaviour is observed in simulations and experiments for tandem dual jet injection, but in that case, a bow shock appears in front of each jet. Therefore, two bow shocks are present (see figure 5.1).

A single jet induces a strong bow shock – i.e. a bow shock with a large normal part –, which will cause blockage effects in the crossflow. Downstream of the bow shock, the momentum of the crossflow is lower, which allows the jet to penetrate more easily into the crossflow [55]. This phenomenon is utilised in tandem dual jet injection, in order to improve the penetration (see section 5.2).

In the experiments of De Maag, the bow shocks are clearly present in the Schlieren images (figure 5.2). The downstream bow shock is stronger than the upstream bow shock. At a certain position, the two bow shocks merge. It is observed, that this behaviour is different for different values of J, S and M_c [3]. In the following, it is investigated on which parameters the behaviour of the two bow shocks depends.

First of all, the Mach number of the crossflow is an important parameter for the behaviour of the two bow shocks. The inclination of the oblique part of the bow shock is determined by M_c, as described in section 4.3. However, the downstream bow shock does not always have the same slope of its oblique part as the upstream shock, as observed in experiments of De Maag [3]. This is due to the slowing down of the crossflow by the upstream bow shock, which makes that the slope of the downstream bow shock is larger than the slope of the upstream bow shock.

The crossflow downstream of the upstream bow shock recovers after a certain distance, which makes that the two bow shocks behave identically for equally sized jets, such as in Lee's study [9] for large S (see figure 5.3). If S is large enough, the two jets behave as two independent single jets, because of the disappearance of the effect of the presence of the quasi-stagnant region that is present right downstream of a bow shock [55]. However, when decreasing S, the two bow shocks interact. Due to the smaller local crossflow Mach number right downstream of the upstream bow shock, the slope of the downstream bow
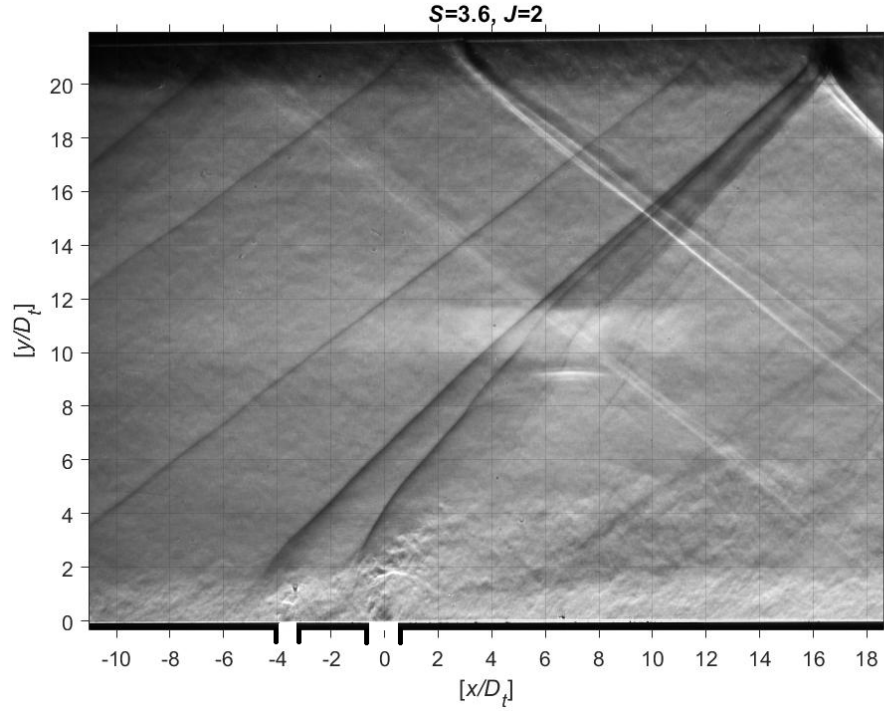
Figure 5.2: Schlieren image of dual injection of air into a supersonic air crossflow by De Maag [3]. The crossflow is from left to right and injection is at the bottom wall at $x/D_t = -3.6$ and $x/D_t = 0$. The bow shock in front of each of the two jets is recognizable by the two dark curves starting around $x/D_t = -3.6$ and $x/D_t = 0$, respectively. Conditions: $J = 2$, $S = 3.6$, $\mathrm{M}_c = 1.6$, $p_c = 24$ kPa and $T_c = 194$ K.

shock is larger, i.e. the smaller S becomes, the steeper the downstream bow shock becomes. At a certain point, S becomes small enough for the two bow shocks to merge [3]. That is why the dual distance S is important for the behaviour of the bow shocks.

It is observed in studies (e.g. [3][9]), that a higher J gives a larger penetration of the jet into the crossflow, which is also the case for single jet injection. As a result, the normal part of the bow shock is larger for larger J and therefore, the part of the bow shock near the jet orifice is stronger. This means that the flow downstream of the bow shock is slowed down to subsonic speed. The stronger a part of the bow shock, the lower the flow speed downstream of the bow shock.

Assuming J equal for both orifices, it can be observed that the larger the jet orifice, the larger the mass flow, the larger the perturbation and therefore, the stronger the bow shock [9][55]. In numerical simulations by Landsberg [55], the mass flow of the downstream jet was four times the mass flow of the upstream jet, but nevertheless, the strength of the bow shocks is comparable. This is in contrast with the results of the numerical simulations by Lee [9], in which equally sized jet orifices were used, because in Lee's results, the bow shock in front of the upstream jet is stronger. Concluding, the diameter of the jet orifice has an effect on the strength of the bow shock and the larger the diameter of the orifice, the stronger the bow shock.

Summarizing, the strength of the bow shocks depends on the crossflow Mach number M_c, the dual distance S, the jet-to-crossflow momentum flux ratio J, and the mass flow of each jet – which for equal conditions can be characterized by the ratio of the two orifice diameters [55].

Under certain conditions, the two bow shocks merge. The point at which the two shocks merge is called the **merger point** of the bow shocks. De Maag [3] suggests that whether or not the bow shocks merge or remain spatially separated has an influence on the penetration of the jet. Therefore, it is necessary to investigate the merger point as a function of the relevant parameters, which will be pursued in the present study.
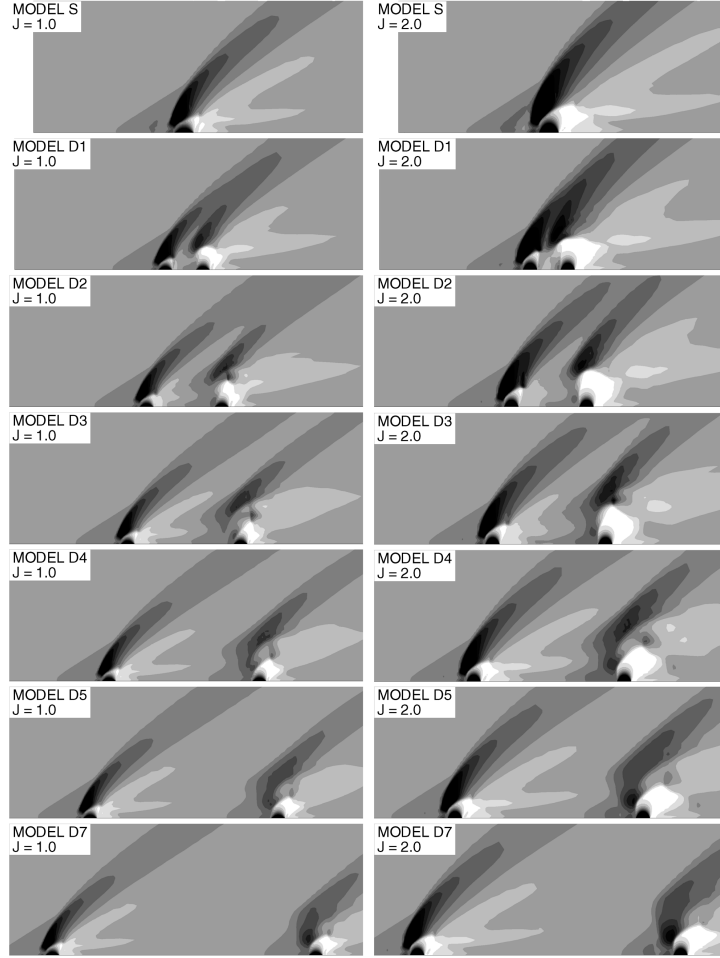
Figure 5.3: Contour plots of the pressure field near the jet orifices in numerical simulations by Lee [9]. The darker the region, the higher the pressure (maximum pressure is $6.7p_c$). Conditions are: $M_c = 2$, $p_c = 146.6$ kPa, $T_c = 1081$ K, $D_1 = 2.2468$ mm, $D_2 = 2.2468$ mm. For the simulations left, $J = 1$ and for the simulations right, $J = 2$. Model S is single jet injection and Model DN corresponds with $S = 2N$.

5.2 Penetration of Two Jets into Crossflow

The penetration of a single jet into a supersonic crossflow is detailed in section 4.4. The behaviour and mathematical description of tandem dual jet injection into a supersonic crossflow is comparable with single jet injection, but it is more complicated because of the interaction between the two jets. The governing parameter of dual jet injection, in addition to those for single jet injection, is the dual distance S. In addition, in section 4.4, it was investigated that J has the largest effect on the penetration for single jet injection, and – although not often quantified – also the crossflow Mach number M_c. Therefore, in this section, the influence of S, J and M_c on the penetration is investigated.

Landsberg [55] investigated dual jet injection of hydrogen into a supersonic crossflow of air numerically, from which the conditions are shown in table 5.1. In figure 5.4, the penetration of the jet in terms of the hydrogen center of mass is shown for several values of S and for two values for M_c (2.623 and 5.272), both for $J = 1$. From the figure, it becomes clear that two jets, i.e. dual jet injection, increases the transversal penetration compared to single jet injection for the same equivalent diameter D_t. This phenomenon is caused by the blockage effect of the upstream jet, which causes the value of the local J to increase. As a result, the downstream jet penetrates deeper into the crossflow [55].

In the top subfigure of figure 5.4, it is shown that the dual distance S has an optimum value with respect to distance of penetration for that conditions. For $S = 4$, the largest penetration is provided and for larger and smaller values of S, the penetration is smaller. In the bottom subfigure of figure 5.4,
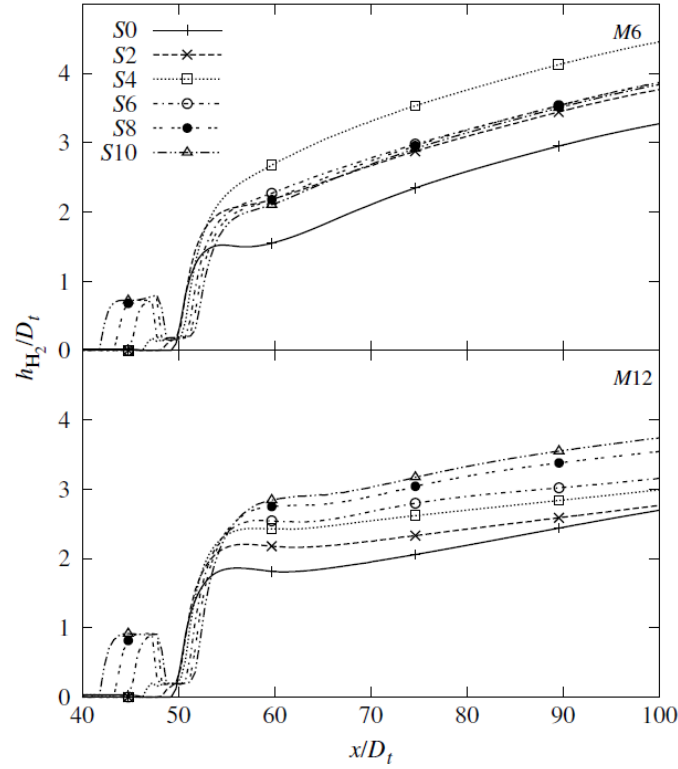
Figure 5.4: Results from numerical simulations of dual jet injection of hydrogen into a supersonic crossflow of air by Landsberg [55]. Presented is the penetration height of the hydrogen center of mass h_{H_2}/D_t versus x/D_t. Conditions in top figure (M6): $M_c = 2.623$, $p_c = 99.48$ kPa, $u_c = 1453$ m/s and $T_c = 786.9$ K. Conditions in bottom figure (M12): $M_c = 5.272$, $p_c = 44.24$ kPa, $u_c = 3483$ m/s and $T_c = 1143$ K. Conditions for both figures: $D_1 = 0.9$ mm, $D_2 = 1.8$ mm, $J = 1$ and $S \in [0 : 10]$. The downstream orifice is located at $x/D_t = 50$.

the penetration increases for every S up to $S = 10$. The only difference between the top figure and the bottom figure is the Mach number of the crossflow. Landsberg elaborates that the quasi-stagnant region downstream of the leading jet creates the conditions under which the rear jet can penetrate deeper. At a certain position downstream of the leading jet, the flow is reattached and is supersonic again, which means that the quasi-stagnant region is bounded between the leading jet and the reattachment point. The optimal penetration is obtained in that quasi-stagnant region. If the rear jet is located downstream of reattachment, penetration is decreased. In the top subfigure of figure 5.4 for $M_c = 2.623$, it can be observed that this reattachment occurs for $S > 4$, but this point is not observed in the bottom subfigure. Landsberg suggests that the reattachment location in the bottom subfigure with $M_c = 5.272$ is delayed, such that the maximum penetration is obtained for larger S. This is caused by the stronger bow shock as a result of the higher Mach number of the crossflow [55].

Another observation is that the far-field penetration for $M_c = 2.623$ is in general higher than for $M_c = 5.272$, whereas for the near-field penetration, it is the other way around. Landsberg explains that this is caused by vertical momentum losses induced by the stronger barrel shock for the case of $M_c = 5.272$, compared to the case of $M_c = 2.623$. This is a result of the larger underexpansion of the fuel. In the end, absolute penetration decreases with increasing crossflow Mach number.

Lee [9] also investigated dual jet injection of hydrogen into a supersonic crossflow of air numerically. In his research, $M_c = 2$ and $J = 1.0$ and 2.0 were used, together with dual distances of $S \in [0 : 14]$. For further conditions, see table 5.1. Figure 5.5 shows the transversal penetration of the hydrogen center of mass z_{H_2}/D_t of tandem dual jet injection for single jet and dual jet injection for four values of S, and both for $J = 1.0$ and $J = 2.0$.
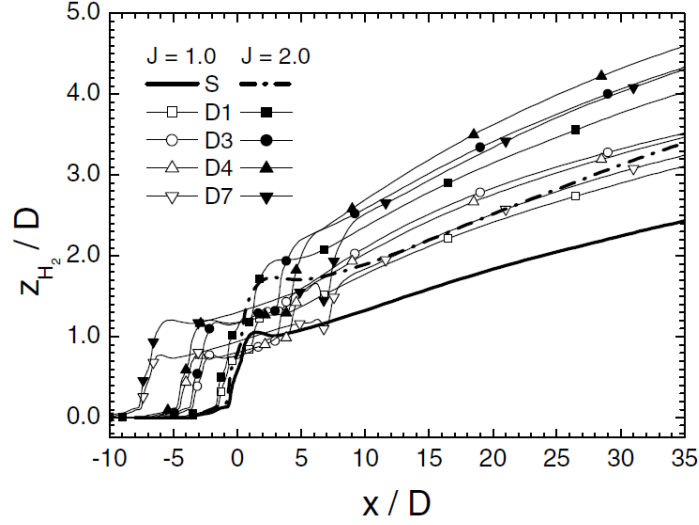
Figure 5.5: Results from numerical simulations of dual jet injection of hydrogen into a supersonic crossflow of air by Lee [9], corresponding to figure 5.3. Presented are penetration heights of the hydrogen center of mass z_{H_2}/D_t versus x/D_t. Conditions are: $M_c = 2$, $p_c = 146.6$ kPa, $T_c = 1081$ K, $D_1 = 2.247$ mm, $D_2 = 2.247$ mm, $J = 1$ and 2 and $S \in [0:14]$. Model S is single jet injection and Model DN corresponds with $S = 2N$. The upstream orifice is located at $x/D_t = -N$ and the downstream orifice is located at $x/D_t = N$.

From figure 5.5, it can be seen that similar to the investigation in section 4.4, penetration increases with increasing J. Furthermore, Lee [9] explains that there is a strong relationship between the penetration and S, which was also observed by Landsberg [55]. Similar to the results of Landsberg [55], the penetration for dual jet injection is larger than for single jet injection. The optimal value for S for maximum penetration is around $S = 6$ (D3) for $J = 1.0$ and around $S = 8$ (D4) for $J = 2.0$. Based on these findings, Lee suggests that for every J, there will be a different optimal value of S for maximal penetration.

De Maag [3][35] investigated tandem dual air jet injection into a supersonic crossflow of air in an experimental set-up. The wind tunnel inlet was at ambient conditions and the crossflow Mach number was $M_c = 1.6$. Jet injection was investigated for $J = 1.0$, 1.4 and 2.0 and for $S \in [0:11]$. The further conditions are provided in table 5.1.

The penetration of the jet upper shear layer from the rear jet was investigated by Schlieren images, which were captured at a frequency of 1000 frames per second. This is not fast enough for investigating the propagation of structures, because that would require a 1000 times faster rate of capturing. Therefore, time-averaged penetration of the jet upper shear layer was found by manual determination of the position of the jet upper shear layer from graphical results. This was a rather labour-intensive work, therefore, the number of Schlieren images that was used for determining the data of the location of the jet upper shear layer was limited to four. De Maag used the following fit for the time-averaged location of the upper shear layer [35]:

$$\frac{y}{D_t} = a \left(\frac{x}{D_t} - c \right)^b \tag{5.3}$$

For some specific dual distances S, a fit with similarity coordinates involving J was obtained, such as for $S = 4.5$ (see figure 5.6 and figure 5.7):

$$\frac{y}{J^{0.65} D_t} = 2.8 \left(\frac{x}{J^{1.5} D_t} + 0.42 \right)^{0.18} \tag{5.4}$$

Figure 5.7 shows that the data for the different values of J collapse well in a band around the location given by equation 5.4. Therefore, scaling of the fit for the jet upper shear layer by a power-law function
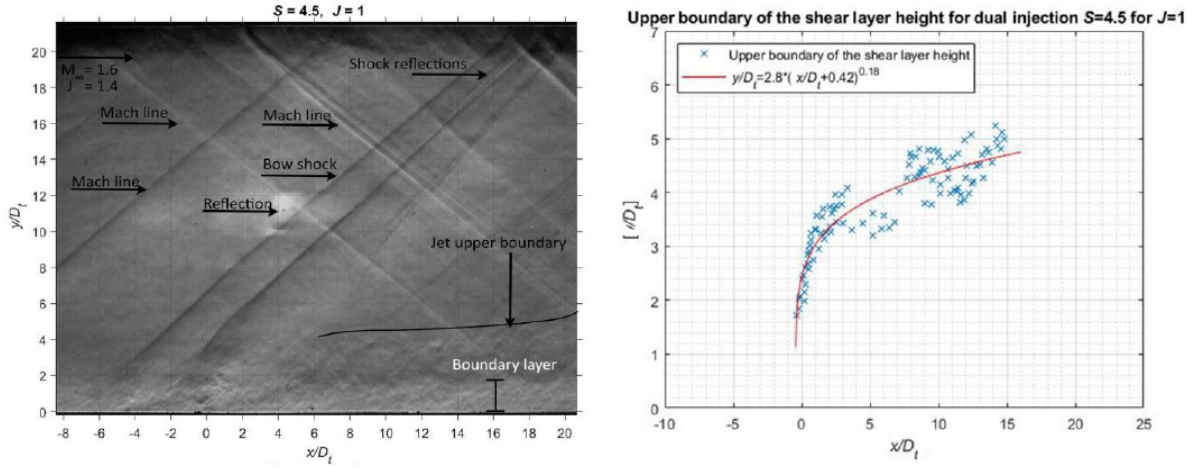
Figure 5.6: Schlieren image for tandem dual jet injection of air in a $M_c = 1.6$ supersonic crossflow of air. $D_1 = 1$ mm, $D_2 = 2$ mm, $J = 1.0$ and $S = 4.5$. Left: Schlieren image. Right: Corresponding data set for the jet upper shear layer from the main orifice, employing four consecutive frames with $\Delta t = 1$ ms. The corresponding fit is included [35].
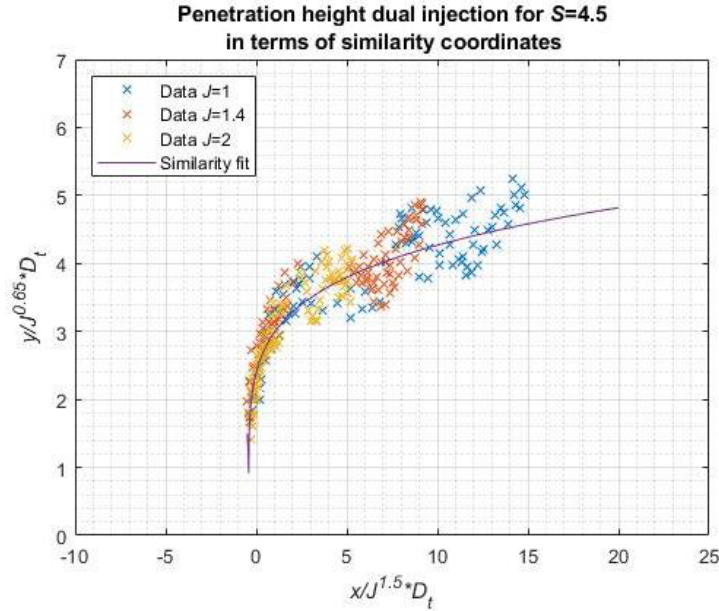

Figure 5.7: Results from experiments of tandem dual jet injection of air in a supersonic crossflow of air by De Maag [35], for the conditions $J \in [1, 1.4, 2]$, $S = 4.5$ and $M_c = 1.6$. Presented are the data of the location of the jet upper shear layer and the fit of equation 5.4 in terms of similarity coordinates.

of J appears to be appropriate to use.

De Maag showed in his results that around $x/D_t = 5$, there is a dip in the penetration for some conditions. This dip was also found in some results from Landsberg [55] and Lee [9]. De Maag demonstrated that splitting of the domain and using a separate fit for each domain would improve the fit of the location of the upper shear layer significantly. Nevertheless, the fit as proposed previously is applied to all conditions, but with the notion that splitting the domain or sophisticating the fit would improve the result.

Furthermore, De Maag calculated the average penetration of the jet upper shear layer as described by the fit. For every fit, he calculated the average penetration y_{avg}/D_t for the domain $0.5 \leq x/D_t \leq 15$ in the following manner:

$$\frac{y_{avg}}{D_t} \equiv \frac{1}{14.5} \int_{0.5}^{15} \frac{y\,(x/D_t)}{D_t} d\frac{x}{D_t} = \frac{1}{14.5} \frac{a}{1+b} \left[(15-c)^{1+b} - (0.5-c)^{1+b} \right] \tag{5.5}$$
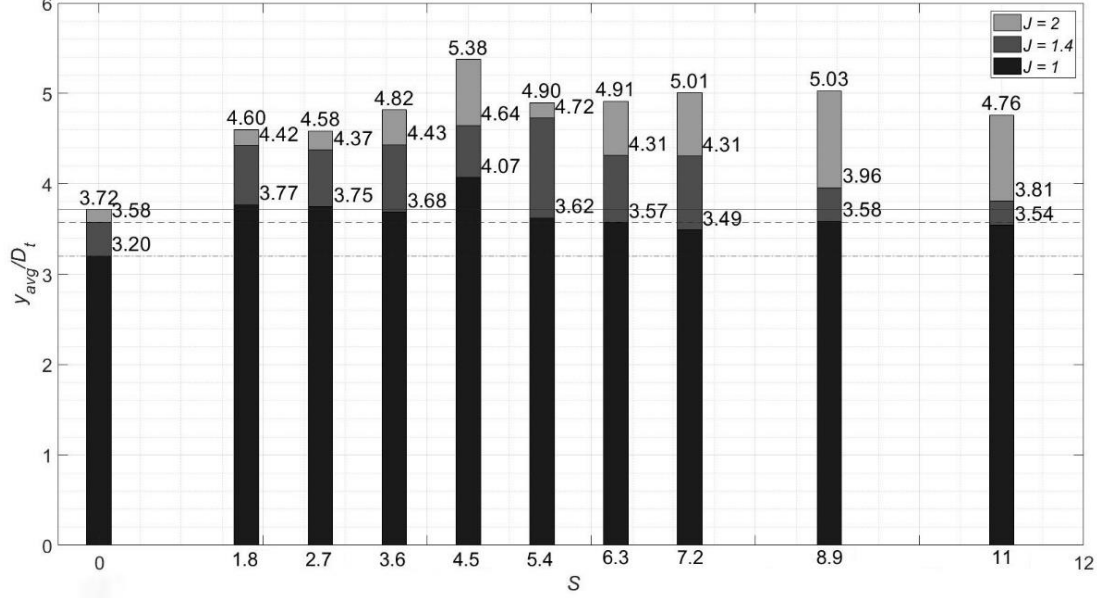

Figure 5.8: Results from experiments by De Maag [35]. Average penetration height versus dual distance $S \in [1.8 : 11]$, calculated from equation 5.5, using the fits of the data obtained from Schlieren images for tandem sonic jet injection in a $M_c = 1.6$ supersonic air stream, which was based on data for $0.5 \leq x/D_t \leq 15$. $D_1 = 1$ mm, $D_2 = 2$ mm. $J = 1, 1.4$ and 2.

In equation 5.5, the coefficients a, b and c correspond to the coefficients in the fit given in equation 5.3. The result of the values for y_{avg}/D_t are shown in figure 5.8.

De Maag excluded the results for $S = 4.5$ in his further analysis, because the results were not in line with the expectation based on the results for all other values of S, which may be due to the injection block for $S = 4.5$ having a different plenum compared to the plenum of the other injection blocks. When disregarding the results for $S = 4.5$ in figure 5.8, the maximum penetration for each J is investigated. For $J = 1.0$, the maximum y_{avg}/D_t was found around $S = 1.8$, with a percentage increase compared to single jet injection of 18%. For $J = 1.4$, the maximum y_{avg}/D_t is the clearest and was found at $S = 5.4$, with a percentage increase of 32%. Finally, for $J = 2.0$, the maximum y_{avg}/D_t was found to be somewhere between $S = 7.2$ and $S = 8.9$, with a percentage increase of 34%. As shown in the results of Lee [9], the penetration increases for increasing J and the optimal value for S at which the maximum penetration is obtained, also increases with increasing J.

In the three studies that were considered in the present study, only De Maag [35] showed a derivation of relations by finding fits (equation 5.3). For some values of S, these fits were scaled in terms of J, but an appropriate scaling for S was not found. Having an insight in the scaling of S would be advantageous and give a more precise insight into the optimal S for maximum penetration. Therefore in the present study, the scaling in terms of S of the penetration of the jet upper shear layer will be a focus point.

Chapter 6

Schlieren and Imaging Techniques

The supersonic flow phenomena that are detailed in the preceding chapters have to be made visible during experiments. A proven method for visualization of fluid structures, is the use of **Schlieren** (English: streaks) techniques. The first scientist that used an optical method for Schlieren was Robert Hooke (1635-1703) and it has been advanced until the present time [56]. In this chapter, the basics of Schlieren techniques and the capture of images of the visualisation are investigated.

6.1   Schlieren Techniques

Schlieren techniques are used for visualization of generally invisible, transparent, flow structures, by visualization of the density gradients in the flow. These density gradients show the flow behaviour qualitatively [56].

The speed of light in vacuum is well-known as $c_0 = 3.8 \cdot 10^8$ m/s, but in a medium, light can be slowed down by interaction with the matter. For a homogeneous medium, light propagates uniformly through the medium and can be uniformly slowed down by interaction with the matter to the speed c. However, if a medium is inhomogeneous, then light can be nonuniformly slowed down by interaction with the matter, such that the light speed c becomes position dependent. A measure for this feature is the refractive index n [56]:

$$n = \frac{c_0}{c} \tag{6.1}$$

The effect of refraction of the light is used to visualize the density gradients. For gases, such as air – used in the present study –, the following equation can be applied [56]:

$$n - 1 = \kappa\rho \tag{6.2}$$

This equation is the relationship between the gas density ρ and the refraction index n, in which κ is the so-called **Gladstone-Dale coefficient**. This coefficient depends on the medium, the conditions of the surroundings and the illumination [56]. For air at standard conditions ($T = 288$ K), κ is around $2.33 \cdot 10^{-4}$ m^3/kg [3].

The refractive index n depends on temperature, gas density, gas composition and the wavelength of illumination, shown by equation 6.2. As an illustration, when light from a Sodium-D spectral line passes air at 273 K and 1 bar environmental pressure, the refractive index is $n = 1.000292$. This illustrates the small numbers that are worked with for $(n-1)$. As a result, an increase of the density by some orders of magnitude, will hardly increase n [56].

Figure 6.1 shows the effect of the refraction of light through an inhomogeneous medium. The Schlieren object has a density gradient in y-direction and as a result, the light is refracted at the Schlieren refraction angle ε. This angle is small and therefore approximately equal to $\partial y/\partial z$. Figure 6.2 visualizes the refraction of a light ray, for which $n_2 < n_1$, such that the upper ray travels faster with velocity $c_2 = c_0/n_2$ than the lower ray with velocity $c_1 = c_0/n_1$ [7].

After a mathematical derivation, for which the reader is referred to Giskes [7], the following differential equations for $\vec{x} = (x = x(t), y = y(t), z = t)^T$ are obtained [7]:
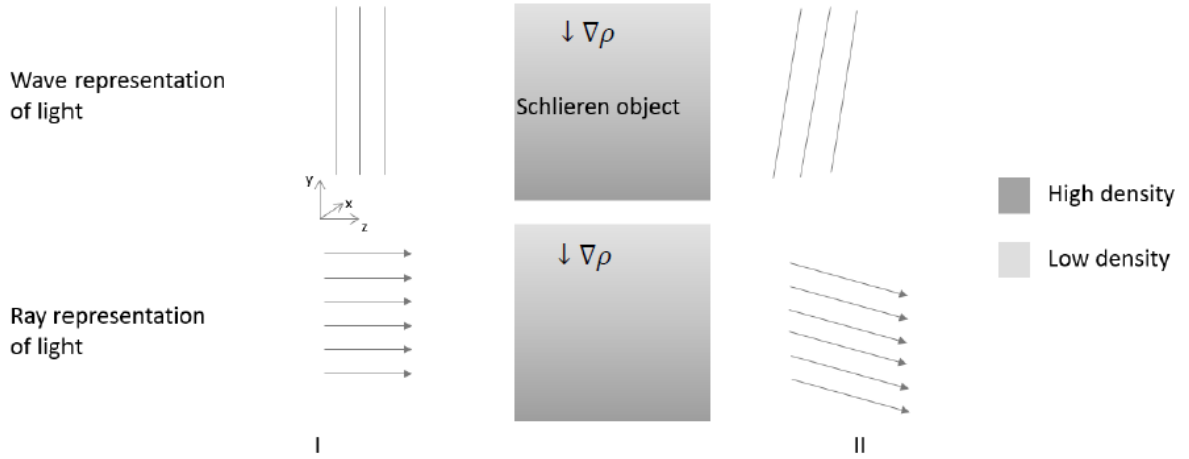
Figure 6.1: Reflection of light rays passing a Schlieren object with a density gradient in y-direction [7].

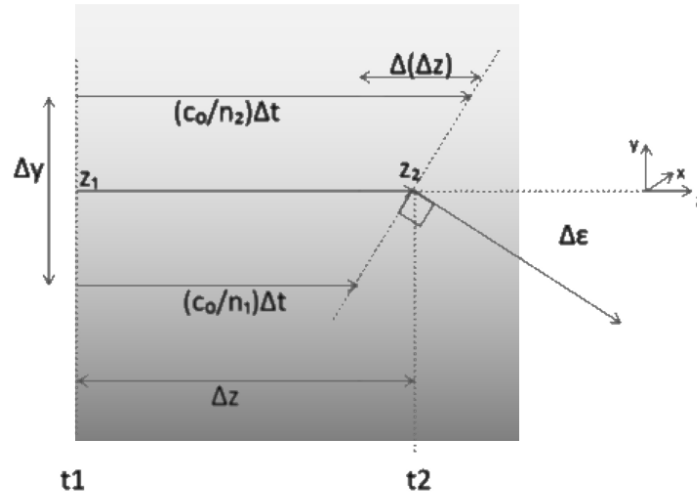Figure 6.2: Schematic of a finite volume with a density gradient in y-direction, in which refraction of light occurs at an angle $\Delta \varepsilon$ [7].

$$\frac{\mathrm{d}^2 \vec{x}}{\mathrm{d}t^2} = \frac{\mathrm{d}\vec{\varepsilon}}{\mathrm{d}t} = \frac{\kappa}{1 + \kappa\rho} \vec{\nabla}\rho \approx \kappa \vec{\nabla}\rho \tag{6.3}$$

These differential equations show that the change in the deflection of the light rays is governed by the components of the density gradients of the medium.

Up to now, the basic principles of Schlieren techniques have been described. For visualization of the flow using this technique, an optical set-up is needed. Figure 6.3 shows a schematic configuration of a Schlieren set-up. From a point light source, light rays are converged to parallel rays by Lens 1. Subsequently, the rays pass a Schlieren object, which can be an air flow with a density gradient. As a result of the density gradient in the Schlieren object, rays are refracted at an angle ε. The subsequent Lens 2 converges the rays such that the unrefracted rays would converge into a focal point. After converging, the rays diverge again and are projected on a screen or on a chip in a camera. As a result of the refraction of the rays in the Schlieren object, these rays will not converge into the focal point and will therefore show a distortion in the projection, i.e. a Schliere. However, this streak is not clearly projected. In order to improve the projection, a knife is used [56].
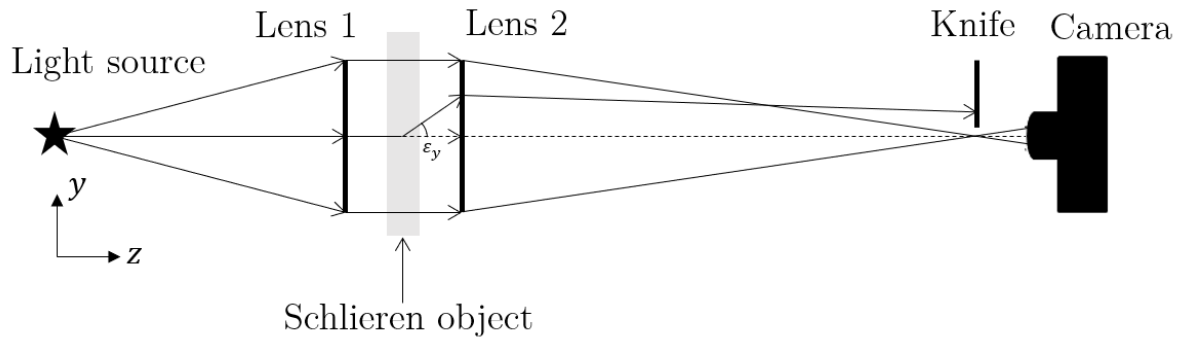
Figure 6.3: Schematic of a Schlieren set-up after [7].

A knife is placed near the focal point of the unrefracted light rays. The knife-edge intercepts the rays that do not pass through the focal point, i.e. these light rays are not projected. As a result, shadows are shown in the projection, which represent the density gradients as a result of flow structures [56].

The knife-edge can have different configurations. A horizontally oriented knife-edge blocks rays from vertical density gradients, such that these structures are more emphasized in the projection. The horizontal density gradients are emphasized using a vertical knife-edge. A combination of both – a circular cutoff by a knife – emphasizes the density gradients in both directions equally. Figure 6.4 shows an example of the use of different configurations of the knife [56].
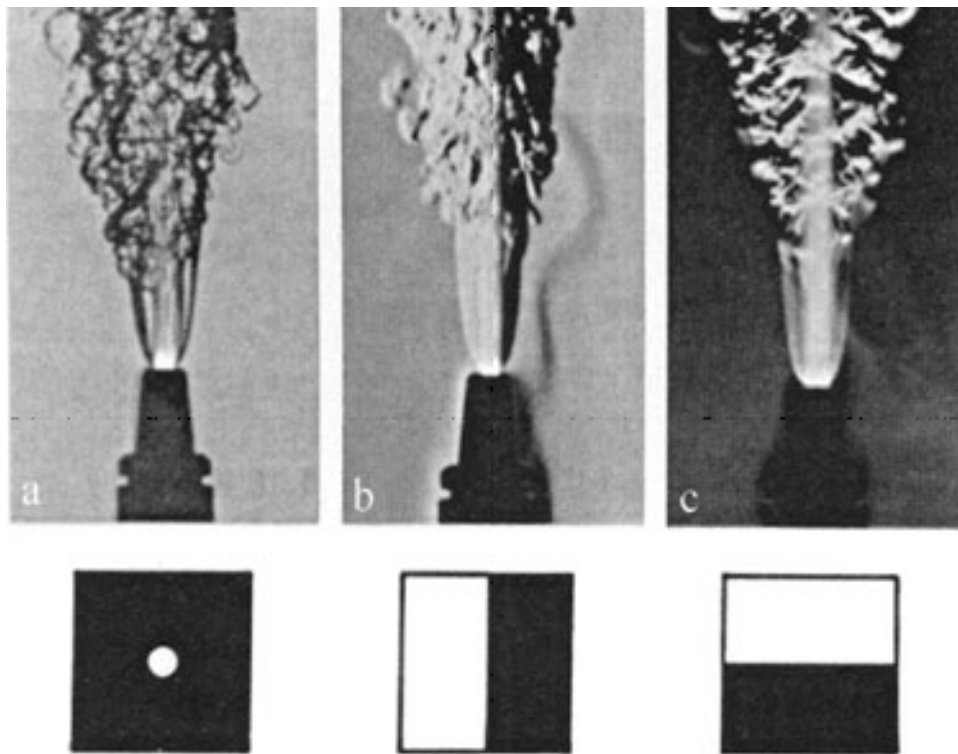

Figure 6.4: Schlieren images of a turbulent flame with different knife-edge configurations. a) Circular cutoff by a knife. b) Vertically oriented knife-edge. c) Horizontally oriented knife-edge [56].

In the following, a horizontally oriented knife is used. The knife-edge is placed at the focal point of the light rays. Figure 6.5 shows a schematic of the effect of the knife. On the left, the half of the light source slit is blocked by the knife. This represents the unrefracted light that passes through the focal point. On the right, a representation of a refracted light source slit is shown. Due to the density gradient,

the light rays are refracted upwards. As a result, relatively less light is cut off for the Schlieren structures compared to the original image. Therefore, the Schlieren structures as projected are lighter than the overall image. On the other hand, a density gradient can also refract light rays downwards resulting in more light rays being cut off by the knife than in case of the unrefracted light rays. In that case, the Schlieren structures as projected are darker than the overall image.
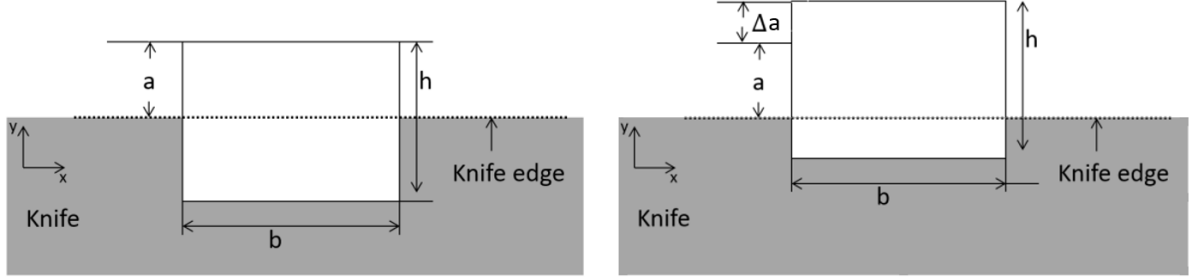

Figure 6.5: Schematic of the technique of the cutoff by the knife-edge at the focal point. Left: The knife blocks a part of the light source slit for the case that no Schlieren refraction is present. Right: The knife blocks a part of the light source slit, which is smaller than left due to Schlieren refraction [7].

In figure 6.5, b and h are the width and height of the light source slit, respectively. a is the part of h that is not blocked by the knife and Δa is the part of h for a Schlieren object that is not blocked by the knife subtracted by a. Two quantities are important to define. The cutoff ratio is equal to the ratio a/h and the contrast C is equal to the ratio $\Delta a/a$ [3]. The latter is the difference between the illumination of the Schlieren objects and the unrefracted illumination, as fraction of the unrefracted illumination. Refraction by the density gradients results in the fixed quantity $\Delta a = \varepsilon_y f_2$, in which f_2 is the focal point of Lens 2. Therefore, only the quantity a can adjust the cutoff and the contrast, and this is done by moving the knife-edge [56].

In literature, a cutoff ratio of 50% is recommended, but deviation from this percentage could emphasize other elements of the Schlieren object. The cutoff determines the contrast in the image and also the illumination by the light source. It is important, that the illumination is strong enough, because otherwise, the image would become too dark. On the other hand, the cutoff should not be too small, because that would affect the contrast. Therefore, a delicate optimum for the cutoff has to be determined [56]. This is often accomplished in a trial-and-error process [3].

In the present section, the parts of figure 6.3 between the light source and the camera were investigated. The Schlieren images are captured by a camera, which use also depends on the light source. In the next section, the imaging techniques with respect to the light source and the camera are detailed.

6.2   Imaging Techniques

The projections as achieved by Schlieren techniques have to be captured, such that the results can be analysed. For that purpose, an appropriate camera is needed. Nowadays, digital cameras with an appropriate lens are used. In the Schlieren set-up, light rays propagating towards the camera pass a lens, an aperture, a shutter and will then meet a photosensitive chip with sensors that capture a photograph. Electronics and software control the camera, its attributes and the saving of the photographs [7]. Figure 6.6 shows a schematic of the camera configuration.

For taking a photograph, the shutter has to be open so that the photosensitive chip is illuminated. Subsequently, when the shutter is closed, illumination of the photosensitive chip stops and the photograph is saved. Then, the shutter opens again and the photosensitive chip is illuminated again. In successive photographing, the frame rate of the camera is important. This is expressed in frames per second (fps). Every inter-photo frame time exist of a period in which the shutter is open and a period in which the shutter is closed, see also figure 6.7. In standard cameras, the time that the shutter is open is equal to the exposure time T_e, during which the photosensitive chip is exposed to light [7].
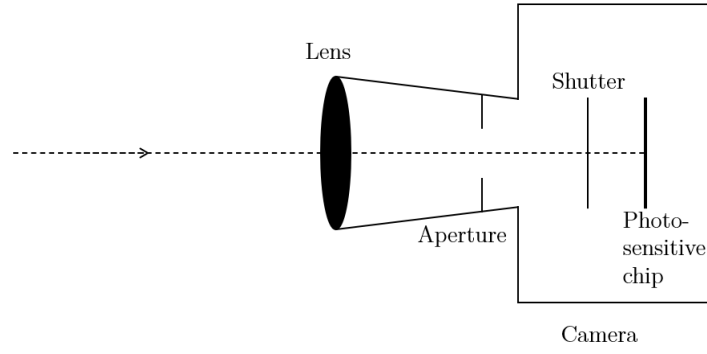
Figure 6.6: Schematic of a digital camera with a light ray propagating into the camera, based on [7].
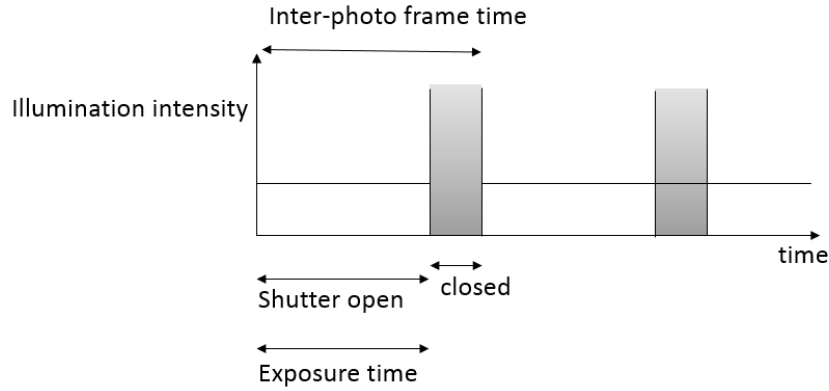

Figure 6.7: Continuous illumination of the photosensitive chip as function of time, including the shutter control [7].

When photographing stationary structures, the exposure time is not a large problem. However, in the case of fastly propagating structures, the exposure time becomes more important, because the projections intercepted by the photosensitive chip will possibly not be unambiguous when dealing with moving structures. Imagine flow structures moving at Mach number M, propagating in one direction. It can be calculated how many pixels an element of the flow has travelled during the exposure time T_e [3]:

$$\frac{\text{pixels travelled}}{\text{exposure}} = a\text{M}T_e\rho_{\text{pix}} \tag{6.4}$$

In equation 6.4, a is the speed of sound in m/s and ρ_{pix} is the pixel density in pixels/m. If the number of pixels travelled during exposure time is less than 1, then the photograph is focused well and does not have blurs due to motion. Therefore, the exposure time T_e has to be small enough [3].

The exposure time depends on the frame rate, and the larger the frame rate, the smaller the exposure time. Therefore, the frame rate has to be increased in order to obtain images without blurs due to motion. However, for flow structures in high-speed wind tunnels, the frame rate has to be large, tending to 1 million fps. Most cameras do not achieve this speed combined with high-quality images [7].

A solution is in the use of the light source. The light source was up to now a continuously illuminating object. However, if the illumination is pulsed, then the time that the photosensitive chip is exposed to the light can be reduced. The time that the shutter is open is then still too long for continuous illumination, but if the time of the illumination itself is reduced, then the problem with the exposure time is solved [7]. The exposure time is then equal to the pulse width T_p of the pulsed illumination [3]. This principle is shown in figure 6.8.

Giskes [7] used a LED with a pulse width of $T_p = 130$ ns. De Maag [3] improved the light source by using a Vertical-Cavity-Surface-Emitting-Laser (VCSEL) that had a pulse width of $T_p = 100$ ns and which pulse width could be reduced to $T_p = 10$ ns. Therefore, the quality of the images has been im-
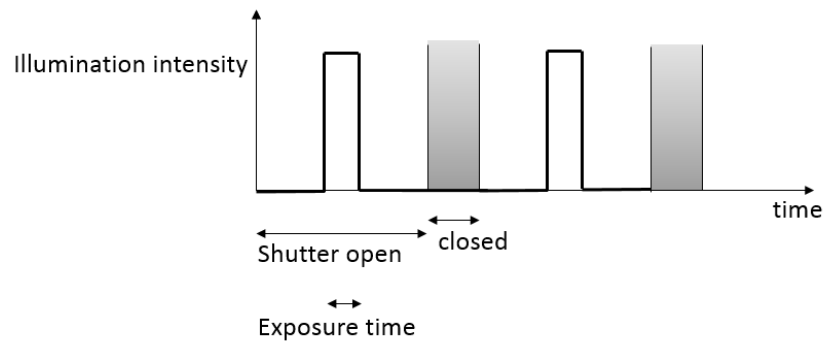
Figure 6.8: Pulsed illumination of the photosensitive chip as function of time, including the shutter control [7].

proved, because of the absence of motion blurs [3]. With this technique, a camera with a limited frame rate can capture high-quality images without motion blurs.

The Schlieren and imaging techniques as described in this chapter are used in the present study and discussed further in the methodology in chapter 7.

Chapter 7

Methodology

In the preceeding chapters, flow phenomena in supersonic flows (chapter 2), jet behaviour in still air (chapter 3), single jet injection into supersonic crossflow (chapter 4), tandem dual jet injection into supersonic crossflow (chapter 5), and the Schlieren techniques (chapter 6) have been described extensively. In the present chapter, the method for addressing the research questions from section 1.1 is described.

The wind tunnel set-up for injection and Schlieren are described. Thereafter, the analysis methods are described for the analysis of the behaviour of bow shocks and the behaviour of jets. For the latter, a semi-automatic algorithm is programmed, which will be described in detail.

7.1 Wind Tunnel Set-up

The experiments have been carried out in the supersonic wind tunnel facility, which is located at the University of Twente and operated by the Engineering Fluid Dynamics group. This air indraft wind tunnel is run by a 96 kW Kaeser Omega pump [3], which generates a sub-atmospheric pressure at the downstream part of the wind tunnel, such that air is drawn from the inlet through the wind tunnel. A picture of the wind tunnel is shown in figure 7.1.
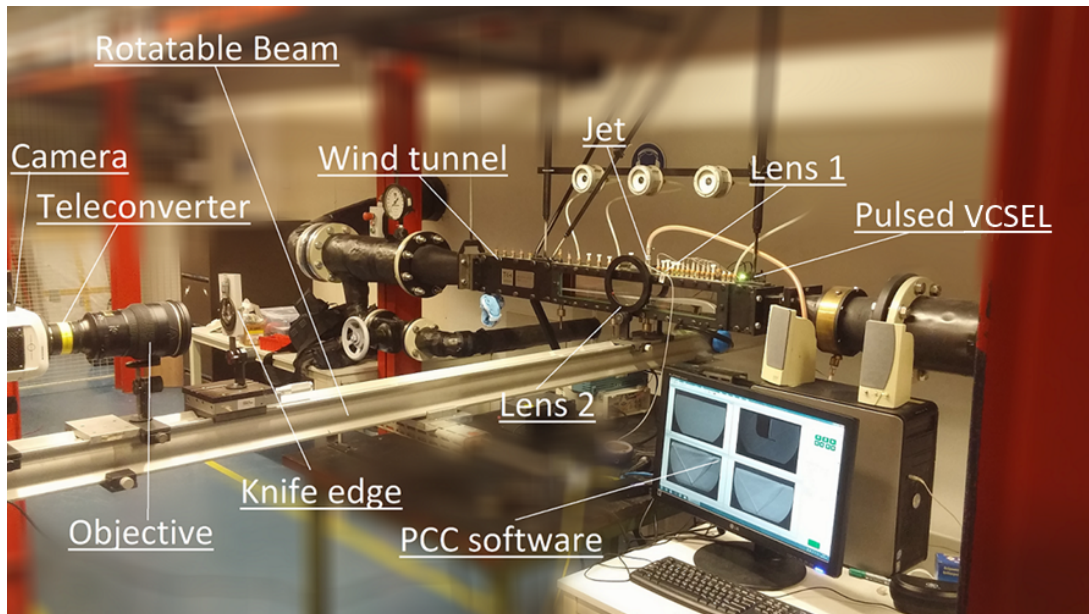

Figure 7.1: Supersonic wind tunnel and Schlieren set-up at the University of Twente [3].

The gray lower wall provides the nozzle-diverging profile, which is adjustable by adjustment bolts. The air is drawn through a throat, at which sonic speed is reached. Downstream of the throat, the diverging cross-sectional area of the gray lower wall makes the flow in the wind tunnel to accelerate

further to supersonic speeds. At the test section, the rectangular cross-section of the wind tunnel has a width of 45 mm and a height of 47.9 ± 0.5 mm. A schematic overview of the wind tunnel is shown in figure 7.2. In reality, the flow is from right to left and the injection is at the top, but for the sake of convention, the resulting measurement images are mirror-imaged, such that the flow is depicted from left to right and the injection is at the bottom.
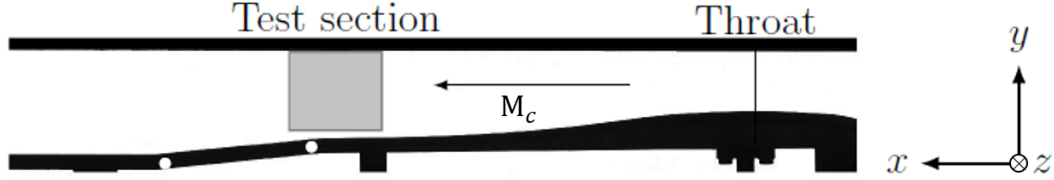

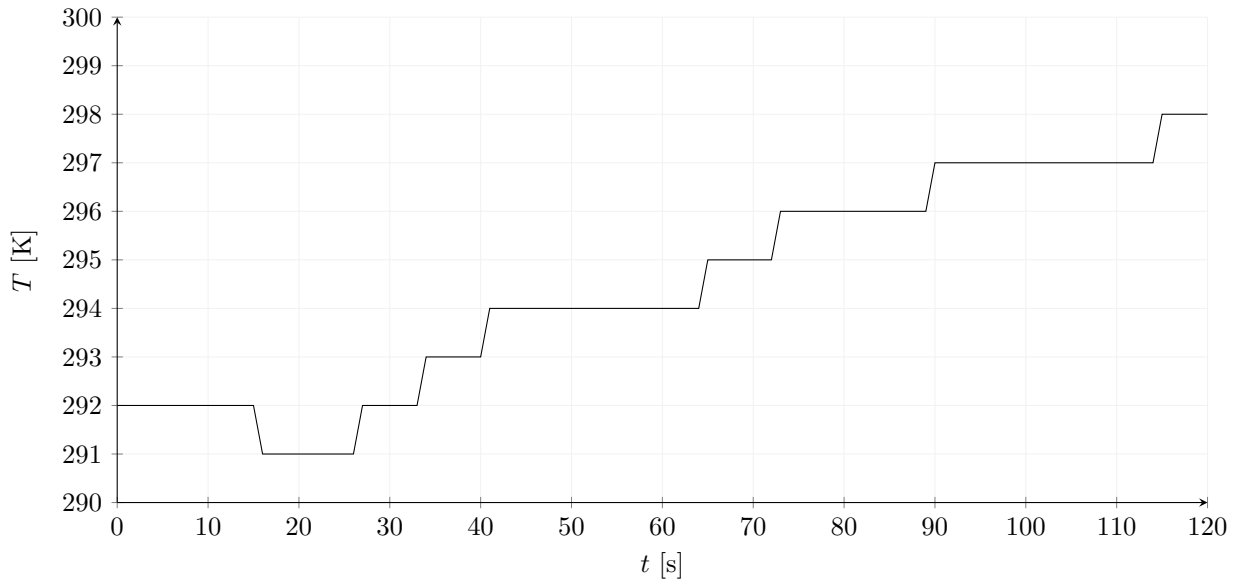Figure 7.2: Schematic of the supersonic wind tunnel at the University of Twente [57].

Figure 7.3: Total temperature at the inlet of the wind tunnel versus time, tracked with a resolution of 1 K.

Disadvantageous for this wind tunnel is, that the inlet of the wind tunnel is in the same room as the pump. This pump generates a significant amount of heat, which increases the temperature in the machine chamber in time despite the air conditioning that is present. The total temperature in the flow in the wind tunnel is determined by measuring the temperature at the inlet. If this total temperature increases during the experiment, then the static temperature in the wind tunnel also increases, which has an effect on other parameters. Therefore, the total temperature at the inlet should remain constant. During the experiments, the total temperature was monitored and it appeared that the temperature is approximately constant for the first 30 seconds, which is long enough for a measurement. Figure 7.3 shows a graph of the temperature at the inlet over time, measured by a thermocouple, which tracked the temperature with a resolution of 1 K. It can be seen that the temperature decreases somewhat at the start, which is due to the colder air from the air conditioning that is drawn to the inlet. However, within a margin of 1 K, the total temperature remains the same during each of the measurements. The conditions in the test section of the wind tunnel are shown in table 7.1.

$T_{0,c}$	292 ± 2	K
$p_{0,c}$	101.325 ± 1	kPa
M_c	1.55 ± 0.02	
a_c	281.5 ± 2.5	m/s
u_c	436.3 ± 10	m/s
T_c	197 ± 3	K
p_c	25.66 ± 1	kPa
γ_c	1.4	

Table 7.1: Conditions in test section for injection into supersonic crossflow. The first three parameters are experimentally measured and the other parameters are derived from relevant relations for a calorically perfect gas.

7.2 Set-up Injection Block

For addressing the research questions, sonic injection into supersonic crossflow experiments are carried out. For that purpose, compressed air is injected into the supersonic crossflow via orifices in an injection block. Compressed air is supplied via rubber hoses that are airtightly connected to G1/4 gas connections. Within the whole injection block, everything is airtight by seal o-rings, such that the total pressure of the outcoming jet can be measured precisely.

As is dealt with tandem dual tandem injection, several configuration parameters have to be chosen. The diameters of the two orifices are D_1 (upstream) and D_2 (downstream). Based on mass conservation, an equivalent diameter D_t is defined for appropriate scaling and enabling comparison with literature:

$$D_t \equiv \sqrt{D_1^2 + D_2^2} \tag{7.1}$$

The distance between the two center lines of the orifices S, the dimensionless **dual distance**, is Δx, scaled with D_t:

$$S = \frac{\Delta x}{D_t} \tag{7.2}$$

Schlieren images are used for visualization of the flow, in order to get an insight in the behaviour of the jet and the bow shocks due to the injection. For the jet, it is the purpose to visualize both the behaviour of the full jet and the behaviour of the jet upper shear layer and the jet lower shear layer (lower side of the jet plume). Furthermore, it is investigated at which conditions the bow shock in the front of the upstream jet and the one in front of the downstream jet merge or remain spatially separated and whether there is a correlation with the behaviour of the jet.

In the present study, the results for penetration are compared with the results of De Maag [3][35], Landsberg [55] and Lee [9]. De Maag [3][35] investigated the jet upper shear layer for dual jet injection with dual distances $S = 1.8, 2.7, 3.6, 4.5, 5.4, 6.3, 7.2, 8.9$ and 11 and orifice diameters $D_1 = 1$ mm and $D_2 = 2$ mm, that make together an equivalent diameter of $D_t = \sqrt{5} \approx 2.24$. In his research, De Maag used jet-to-crossflow momentum flux ratios $J = 1, 1.4$ and 2.

De Maag showed in his results [35], that an interesting range of S is around $S = 5$, because within this range, maximum average penetration is obtained for both $J = 1$ and $J = 1.4$. The maximum for $J = 2$ is less clear because of outlying points that pollute the data. It appeared that the injection blocks of $S = 4.5$ and $S = 6.3$ were different from the other injection blocks, which may have caused outlying points. As the dual distance S around $S = 5$ appeared to be the most interesting, the focus of the present research will be on dual distances concentrated around $S = 5$.

The brass injection block for the present study exists of two parts: a base and a top-piece block, see figure 7.4. The base is used in all measurements, but different top-piece blocks are used, for the varying distance between the two orifices. The base and top-piece block are bolt-connected. For preventing leakage of compressed air, a seal o-ring is placed between the two parts in the plena. Figure 7.4 presents the injection block. In figure 7.5, a schematic of the injection block is shown. The technical drawings are shown in appendix A.
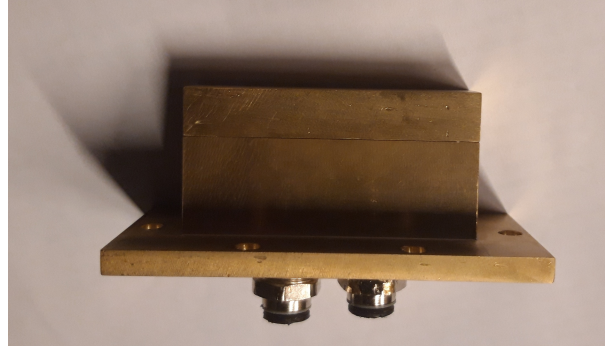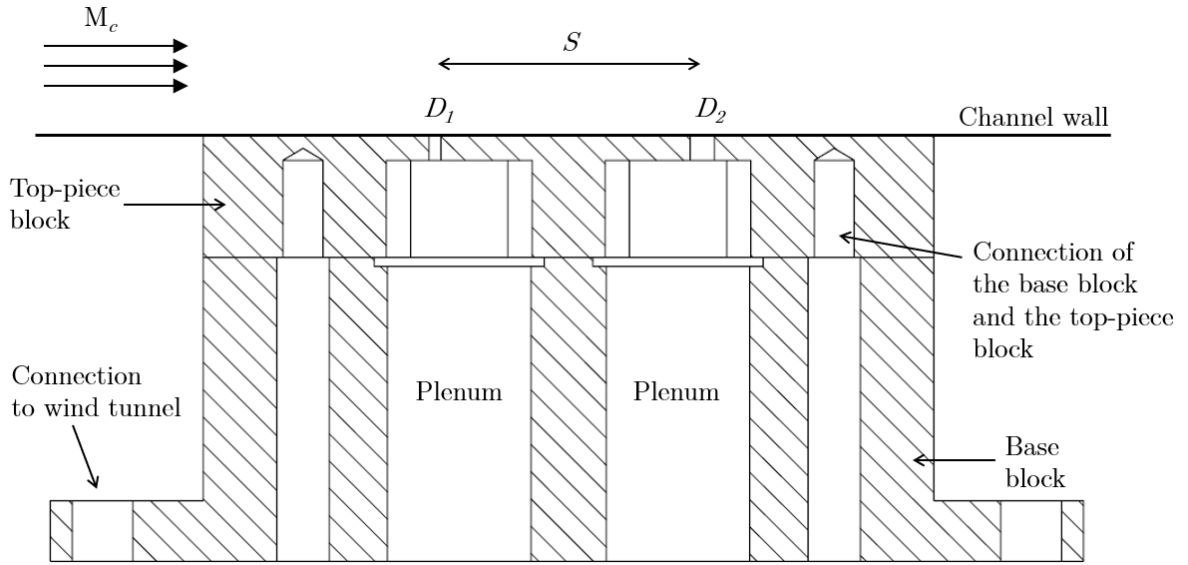
Figure 7.4: Picture of the total injection block.

Figure 7.5: Schematic of the injection block.

For the variation of S, 11 top-piece blocks are used. The interior of these blocks are identical, the only difference is the position of the channels to the orifices. This is done for warranting a good comparison between the blocks and to prevent having outlying measurement data, such as De Maag [35] shows in his research for a top-piece block that was manufactured differently.

The orifices of the top-piece block have a sharp edge, such that the underexpanded jets have a pure expansion fan. Because of the underexpansion, the Mach number at the exit of the orifice is precisely $M_j = 1$. Furthermore, the surface of the block that is in contact with the crossflow, has a surface roughness of $R_a = 0.4$ μm and a flatness tolerance that is minimized.

In table 7.2, the different values for S for the 10 dual jet top-piece blocks are shown. The diameters of the upstream and downstream jet orifices are $D_1 = 1$ mm and $D_2 = 2$ mm, respectively. In addition, a top-piece block with a single orifice is used for the comparison of results for a single jet with results for dual jet injection. This single jet top-piece block has an orifice diameter equal to the equivalent diameter: $D_1 = D_t = 2.23$ mm.

S [-]	3.59	4.04	4.48	4.93	5.38	5.83	6.28	7.17	8.52	9.87
Δx [mm]	8	9	10	11	12	13	14	16	19	22

Table 7.2: Top-piece blocks: dual distances S.

For the experiments, the jet-to-crossflow momentum flux ratio J is chosen to be $J = 2.8$ and $J = 3.8$.

In addition, some experiments at $J = 4.8$ are performed. These conditions are chosen, such that data can be added to the data of De Maag, which together gives a good overview of the penetration of dual jet injection for lower values of J ([35]) and higher values of J (present study). The value of J is calculated employing equation 4.13. In order to tune the value of J, the parameters in this equation for J have to be adjusted. However, the Mach number is fixed due to the fixed configuration of the wind tunnel as well as for reasons of comparability. Also, the pressure of the air inlet of the wind tunnel is hard to increase, because it is the ambient pressure. Therefore, the adjustment of the value for J is reached by an adjustment in the total pressure in the plena of the injection block. The total pressure is measured by a GE Druck DPI 104 pressure sensor.

In addition, the atmospheric pressure is obtained from a nearby weather station and the total temperature of the air is measured using a thermocouple. The parameters related to the jets are summarized in table 7.3.

$T_{0,j}$	292 ± 2	K
$p_{0,j}$	$330,443 \pm 5$	kPa
M_j	1	
J	$2.8, 3.8$	
a_j	312.7 ± 1.5	m/s
u_j	312.7 ± 1.5	m/s
T_j	243 ± 2	K
p_j	53.5 ± 1	kPa
γ_j	1.4	

Table 7.3: Parameters of the jet for injection into supersonic crossflow. The first three parameters are measured. The other parameters have been derived from relevant relations for a calorically perfect gas.

7.3 Schlieren Set-up

The flow structures in the flow within the wind tunnel are made visible using a Schlieren system. An overview photograph is shown is figure 7.1 and a schematic overview is shown in figure 7.6. The light source that is used, is a Vertical-Cavity-Surface-Emitting-Laser (VCSEL) from Tyson Technology, manufactured by the Optical Sciences group at the University of Twente. The VCSEL has a wavelength $\lambda = 808$ nm and a power of $P = 4.5$ W, emitted from a laser surface of 1.19×1.19 mm. Furthermore, the pulse time T_p is 100 ns. In figure 7.7, an image of the light source is shown and in figure 7.8, a peak power beam profile of the light source is shown. For more information about the light source, the reader is referred to [3].
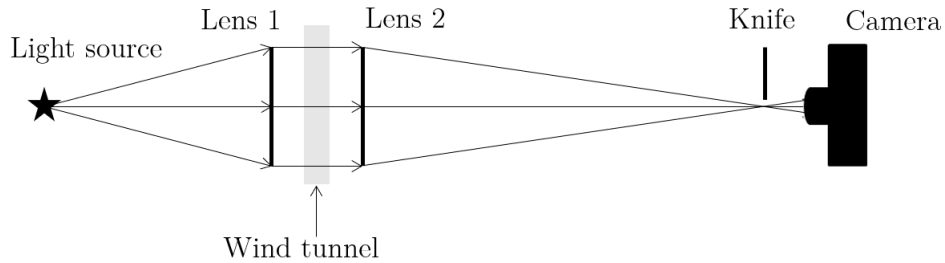

Figure 7.6: Schematic overview of the Schlieren set-up.

The pulsed light is converged through lens 1 with a focal point $f = 0.5$ m and then travels in a parallel light beam through the wind tunnel. Subsequently, lens 2 converges the light beam with a focal point $f = 1.0$ m and the light beam is partly cut off by a horizontally oriented knife edge. The light beam ends in the Phantom V611 camera. Attached to the camera is the Nikon TC-20 E AF-S Teleconverter II and on that teleconverter, the Nikkor AF-S 200 mm f2.0 ED VR. This set-up was also used by De Maag [3].
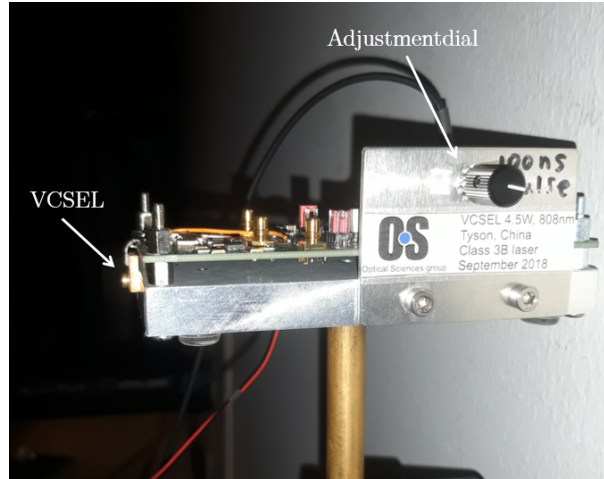
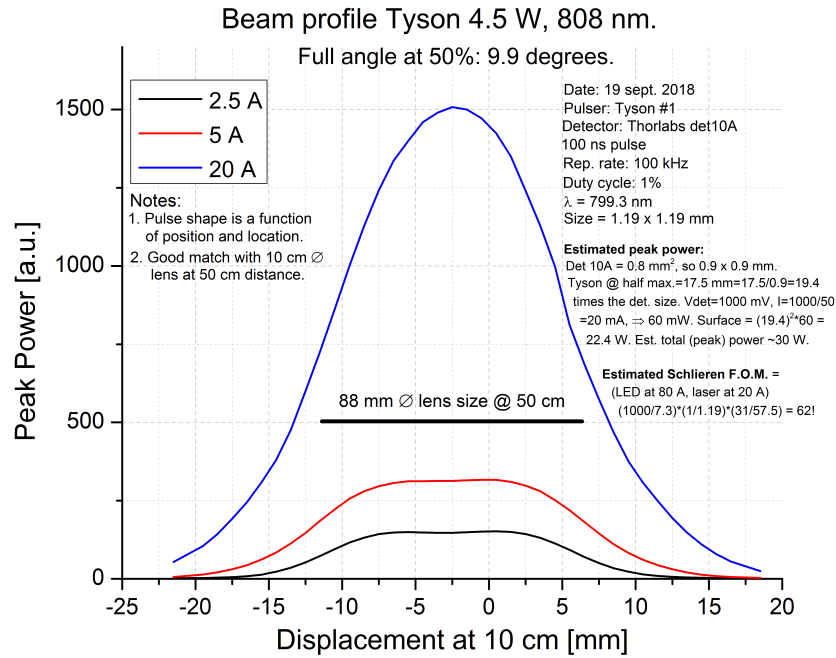Figure 7.7: Picture of the VCSEL light source used in the experiments.

Figure 7.8: Peak power beam profile of the VCSEL light source [3].

During measurements, the room is dark, such that the only light that is captured by the camera is the light beam from the VCSEL. The VCSEL is connected to a pulse generator that has frequency of 1.0 kHz, such that 1000 frames per second can be captured. This frame rate is not large enough for capturing time series that could show structures in the flow propagating in time, because that would need a time step, not of 1 ms, but one in the order of magnitude of 1 μs [22]. The exposure time of the camera is large: 990 μs. Thus, the light beam with a pulse width T_p of 100 ns is easily captured, as between the frames, a time step of 1 ms is set.

7.4 Analysis of the Experiments

The frames recorded by the camera are captured by the software Panthom Camera Control® (PCC) version 3.4 from Phantom™. From this array of frames, images are extracted (as an example, figure 7.9). These images are mirror-imaged, such that the crossflow is from left to right and the injection is at the bottom of the picture, by convention. Subsequently, after binarization a Hough transform is used for detecting the upper and lower wall of the wind tunnel, using MATLAB R2020a® (figure 7.10). By rotation of the image, a possible tilt is corrected and subsequently, the image is cropped in vertical direction using the detection of the upper and lower wall. In horizontal direction, it is manually determined to what limits the image is cropped. The result of the editing of the image in figure 7.9 is shown in figure 7.11. The determined mirroring, rotation and cropping is applied to all images of the same measurement, in order to be consistent. This step can be justified, as the camera and wind tunnel do not move and therefore, the wind tunnel position is for all images of the same measurement session identical.
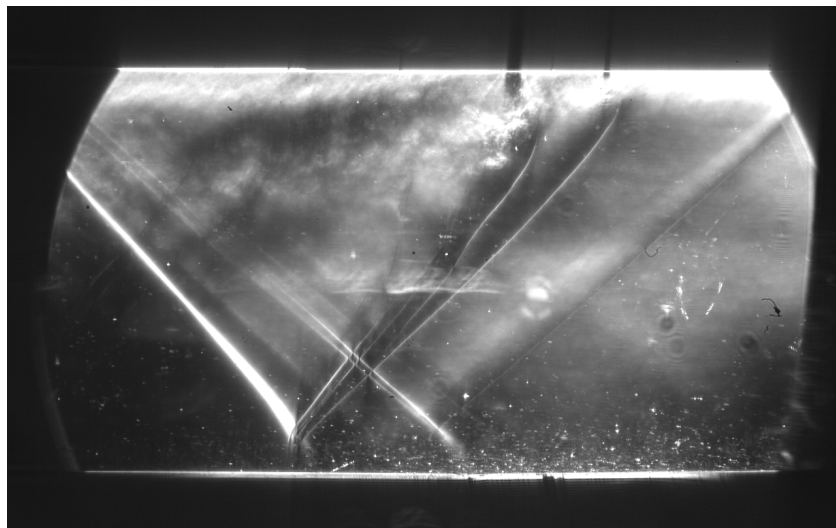

Figure 7.9: Original Schlieren image, directly obtained from the PCC software ($J = 3.8$, $S = 4.93$ and $M_c = 1.55$). The flow is from right to left, the jets are at the top of the picture.
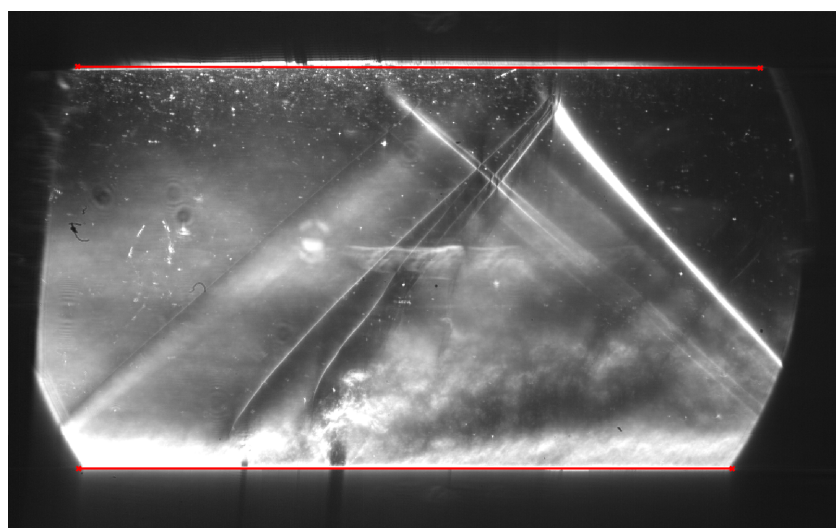

Figure 7.10: Mirroring of figure 7.9 and indication of the upper and lower wind tunnel walls using a Hough transform. The red lines are the upper and lower wall as detected ($J = 3.8$, $S = 4.93$ and $M_c = 1.55$). The flow is from left to right, the jets are at the bottom of the picture.
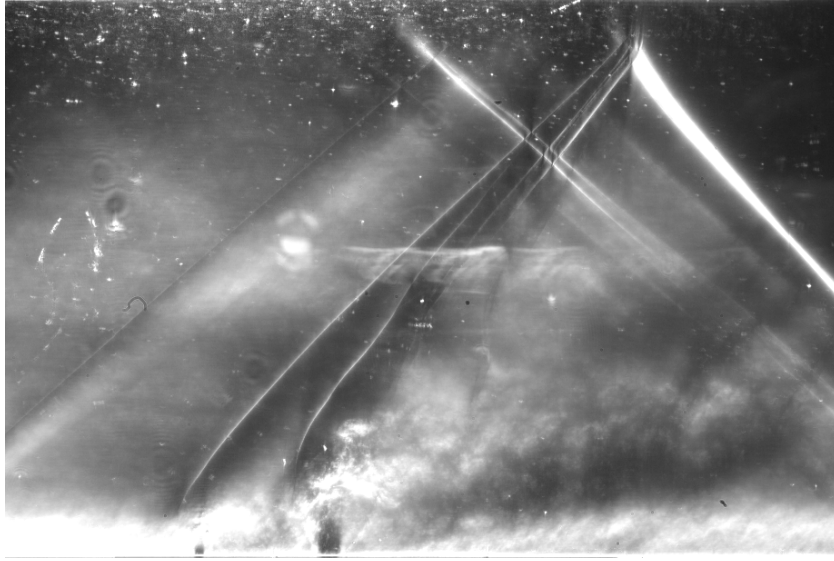
Figure 7.11: Corrected Schlieren image from figure 7.9 after mirroring, rotation and cropping ($J = 3.8$, $S = 4.93$ and $\mathrm{M}_c = 1.55$). The flow is from left to right, the jets are at the bottom of the picture.

Up to this point, the processed images are used as starting point for all analysis steps.

7.4.1   Behaviour Bow Shock

For dual jet injection, the behaviour of the bow shock is investigated from the Schlieren images, in order to analyse whether or not the two bow shocks merge. Also determined is the dependency on J and S. Whether the bow shocks merge or remain spatially separated may have an influence on the penetration of the jet.

The downstream bow shock fluctuates significantly, because of the large-scale structures of the downstream jet. That is why the merger point of the two bow shocks fluctuates too. In order to get a good view of the point of merging, 20 images are used for determining the merger point.

The data acquisition procedure is as follows:

1. The height of the wind tunnel is used for obtaining a conversion factor from pixels to mm.

2. The downstream jet orifice exit center is selected and set as the origin of the coordinate system.

3. For every image, the merger point of the bow shocks is determined manually.

The result of the determination of the merger point for one case is shown in figure 7.12. The fluctuation is visible (blue asterisks) and therefore, a mean value is indicated by a red asterisk. The resulting data sets for all experiments will be analysed in section 8.1.

7.4.2   Behaviour Jet

For analysis of the behaviour of the jet in the crossflow, several steps are taken. The purpose is to have a largely automated analysis algorithm that can handle a significant number of images for each measurement. De Maag [35] showed an excellent study into the jet upper shear layer, but his method of using only 4 images for the analysis could be more robust, by using more images. However, in that study, the images are all processed manually, which was rather labour intensive. That is why in the present study, it is purposed to create a less labour intensive processing of the images. Then one is able to increase the number of images per measurement to process easily and render the analysis more robust.

Lerink [31] suggests to make an automatic algorithm using MATLAB's Image Processing Toolbox for detection of the jet upper shear layer. In his study, Lerink shows a method of image processing that could be a building block for an automatic algorithm that detects the jet. Furthermore, Lerink recommendates to make a binary mask that covers non-relevant parts of the images such that the relevant flow features
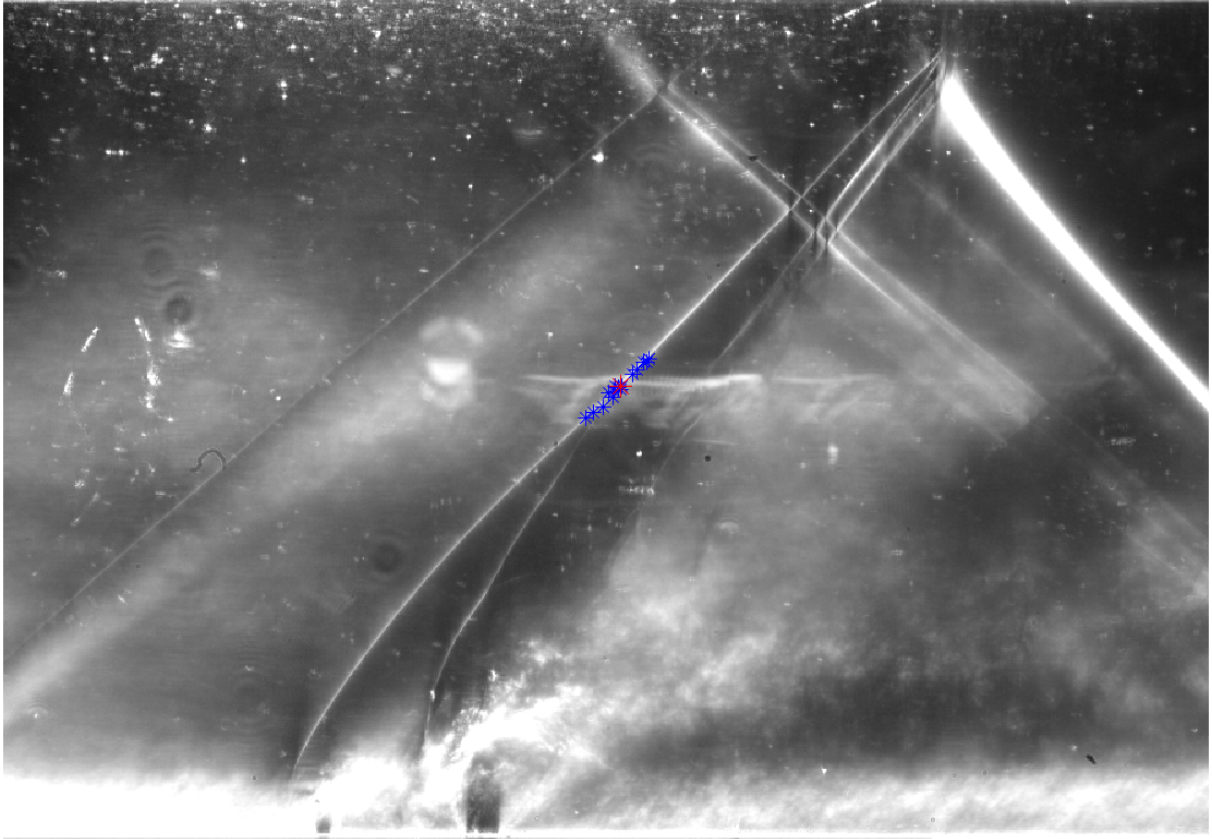
Figure 7.12: Analysis of the bow shocks merger point for 20 images. The blue asterisks indicate the merger point for the individual images and the red asterisk indicates the mean position of the merger point ($J = 3.8$, $S = 4.93$ and $M_c = 1.55$).

are emphasized, in this case the jet upper shear layer. This selection of images could then be subjected to the image processing proposed above. In the present research, the recommendation of automation and emphasizing relevant parts of an image for processing is followed.

Furthermore, Kouchi et al. [54] propose a method of detection of the full jet. However, this method cannot be fully applied, because in contrast to Kouchi et al., the present study does not produce images at small time steps. Still, the method they propose can partly be used and will be applied for the determination of the window (section 7.4.2.1).

In the present study, the following procedure is used for determining the jet behaviour:

- Determination window (section 7.4.2.1)

    - Identification of the orifices and the approximate height of the boundary layer.

    - Identification of the shock waves and areas that may pollute the image processing data.

    - Determination of the window (a binary mask) in which the jet is captured from the original image, using 5 images.

- Jet determination (section 7.4.2.2)

    - Processing of 20 images for the identification of the jet structures.

    - Per image individually determination of the jet upper shear layer and the jet lower shear layer, followed by correction of this data.

- Analysis results (section 7.4.2.3)

    - Identification of flow structures.

  – Find fits for:
      * Jet upper shear layer.
      * Jet center line.
      * Jet lower shear layer.
  – Determine the average penetration of the jet upper shear layer into the crossflow.
  – Possible generalizations of the individual measurements by a study of scaling.

The procedure is programmed in MATLAB R2020a$^{\circledR}$ and all three parts are saved individually after processing, such that the process can be redone or optimized in parts.

7.4.2.1 Determination Window

The purpose of the determination of the window is to select a part of the original image that contains the jet and neglects most of the disturbing elements in the image.

As an input, the process requires a number of Schlieren images (5 in the present study) and the height of the wind tunnel. The output is a binary mask that is used as window, the position of the orifices, the boundary layer height, the position of the shocks and the conversion factor from position in pixels to position in mm. The procedure is as following:

1. The orifices are identified by manual clicking. Using this data, the preparation for the window determination is performed. A selection from the original image is extracted for further processing, which is bounded in vertical direction by the middle of the image and the bottom of the image, and bounded in horizontal direction by the right side of the image and 80 pixels to the left of the upstream orifice. This frame is used for the further analysis of the jet behaviour.

2. The approximate height of the boundary layer is clicked. The boundary layer would give a significant amount of noise in the determination of the jet and therefore, a binary mask is applied to the boundary layer downstream of the orifices. This is achieved by utilising an approximating asymptotic function, below which the image is masked. The function is defined as:

$$y(x) = b \left(1 + \frac{1}{\frac{b}{3000} \left(x_{orifice} + 40 - x \right) - 1} \right) \tag{7.3}$$

In this equation, $y(x)$ is the vertical position in pixels, x is the horizontal position in pixels, b is the boundary layer height in pixels and $x_{orifice}$ is the x-position of the downstream orifice in pixels. The function has a root at $x = x_{orifice} + 40$ and approaches b for large x. By this means, the boundary layer is masked without affecting the jet.

3. The purpose of the next step is to detect which areas in the image are the most deviating in time, because one of these areas is the jet plume. 5 images are subsequently processed in the following standardization method [54]:

   (a) A possible linear gradient of the intensity in the image is corrected. A linear plane ($f(x, y) = c_1 x + c_2 y + c_3$) is used as fit for the intensity plot of the image and subsequently, the linear plane is subtracted from the original image. Figure 7.13 is the original image and figure 7.14 is the corrected result.

   (b) The function `imfilter` with convolution settings is used with a window size of 10×10 for generation of a blurred version of the image, which is in the next step subtracted from the image. In this manner, the stationary elements in the image (light reflection of the lens, partly shock waves) are filtered out.

   (c) Points with outlying intensity values are filtered out.

   (d) Local contrast is increased by the function `localconstrast`, using an edge threshold of 0.3 and a strong enhancement.
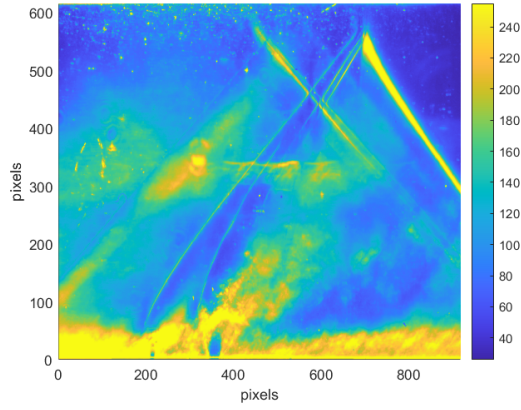
Figure 7.13: Color image of the light intensity of the original Schlieren image ($J = 3.8$, $S = 4.93$ and $M_c = 1.55$).
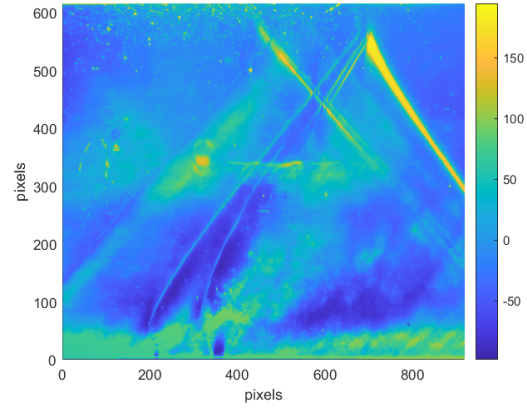

Figure 7.14: Color image of the light intensity of the with linear plane corrected Schlieren image ($J = 3.8$, $S = 4.93$ and $M_c = 1.55$).

(e) The mean intensity μ of the image is calculated and subtracted from the image, such that the resulting image has a mean of 0. Subsequently, the standard deviation σ of the intensity of the image is calculated. The image intensity values are divided by σ, in order to get a standardized imaged ($\mu = 0$ and $\sigma = 1$) [54]. Figure 7.15 shows a result.
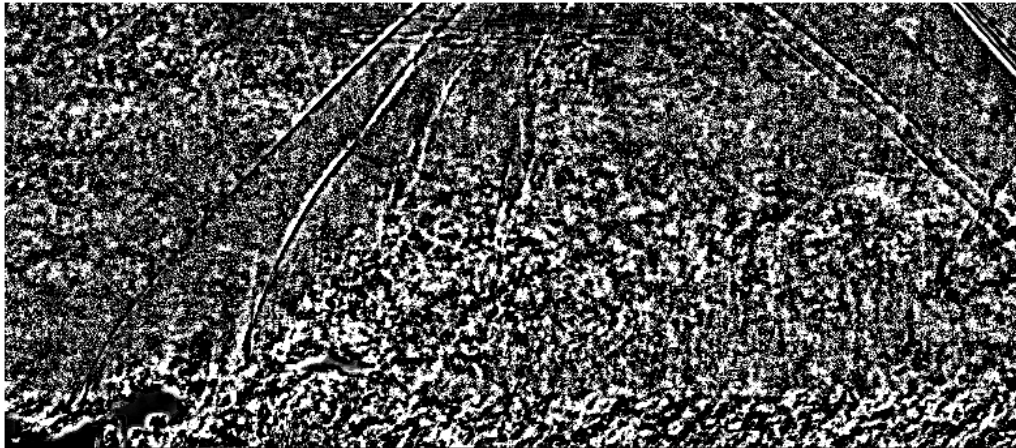

Figure 7.15: Standardized intensity image, with $\mu = 0$ and $\sigma = 1$ ($J = 3.8$, $S = 4.93$ and $M_c = 1.55$).

4. The next step in the procedure of the window determination is finding the most deviating areas in the images. One standardized image is used as a reference. The reference image is subtracted from all other images and remaining are 4 difference images, which emphasize the moving structures (i.e. the boundary layer and the jet plume).

   The Sobel filter is used for detecting the jet region [54]. The threshold that is needed for this filter varies per part of the image. Therefore, the images are cut in horizontal direction into 4 parts, making it possible having a larger threshold around the jet orifice than further downstream. The result of the filter is a binary image for all four parts of the images, and these parts are put together to one image. This is done for all 4 difference images and these binary images are added together and subsequently binarized again. The intermediate result is a binary image in which the moving structures in the image are recognizable (figure 7.16).

5. The granular structures in the image are turned into a solid area by using a sequence of dilatation, hole-filling and erosion. The solid area is aimed to overlap the full jet structures, such that it can be used as the upper boundary of the binary mask for further analysis. Some structures (bow shock,
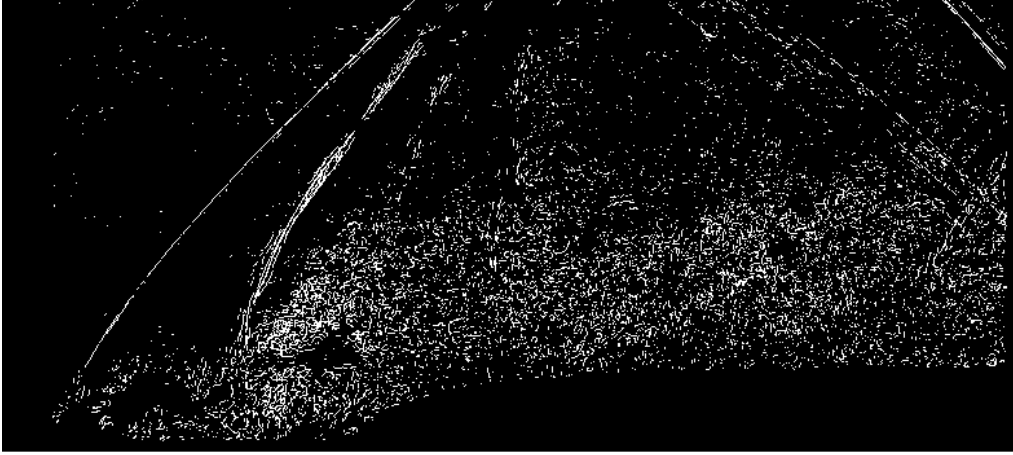
Figure 7.16: Binary image of jet injection, combined from four binarized difference images ($J = 3.8$, $S = 4.93$ and $M_c = 1.55$).

recompression shock, etc.) can pollute this solid area. For that purpose, shocks can be selected in the image. These white parts are accordingly erased. Figure 7.17 shows the result of shock selection.

Figure 7.17: Visualization of the selection of shock waves for having a correct window determination. The selected parts are marked in red and numbered ($J = 3.8$, $S = 4.93$ and $M_c = 1.55$).

After having erased the shock patterns in the binary image, the dilatation–hole-filling–erosion steps are repeated. From the resulting binary image, the largest area is selected (figure 7.18).
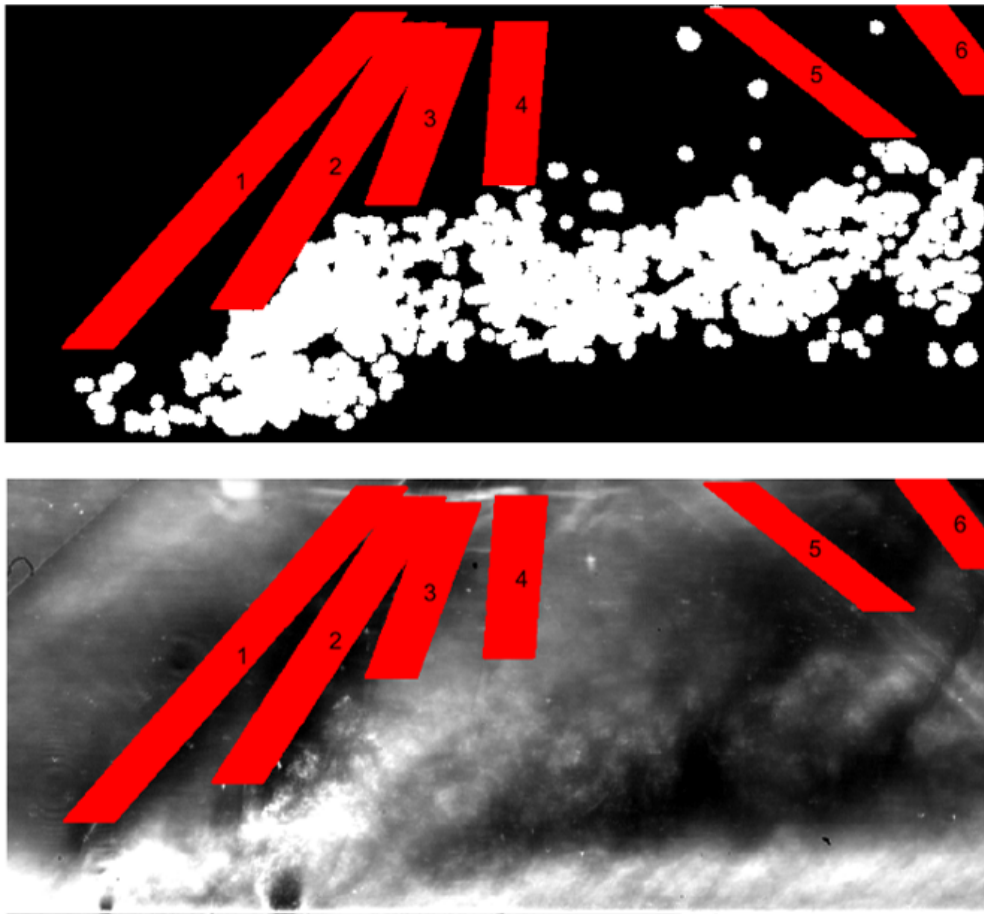

Figure 7.18: Selection of the largest area (yellow), from which the upper boundary is used for the fit of equation 7.5 ($J = 3.8$, $S = 4.93$ and $M_c = 1.55$).

6. The upper y-coordinates of the largest area are selected and a function is fitted, which becomes the upper boundary of the window for the jet determination. The initial function is a power function:

$$g(x) = c_1(x + c_3)^{c_2} + c_4 \tag{7.4}$$

The function above is corrected with a linear or constant term added, depending on the relative largest positive peak $(x_{peak}, y_{peak} - g(x))$ that towers the highest above the function $g(x)$:

$$f(x) = \begin{cases} c_1(x + c_3)^{c_2} + c_4 + (y_{peak} - g(x_{peak}))\frac{x+25}{x_{peak}+25} & x \le x_{peak} \\ c_1(x + c_3)^{c_2} + c_4 + (y_{peak} - g(x_{peak})) & x > x_{peak} \end{cases} \tag{7.5}$$

The resulting window (binary mask) is shown in figure 7.19 and is used in the whole further analysis of the behaviour of the jet.

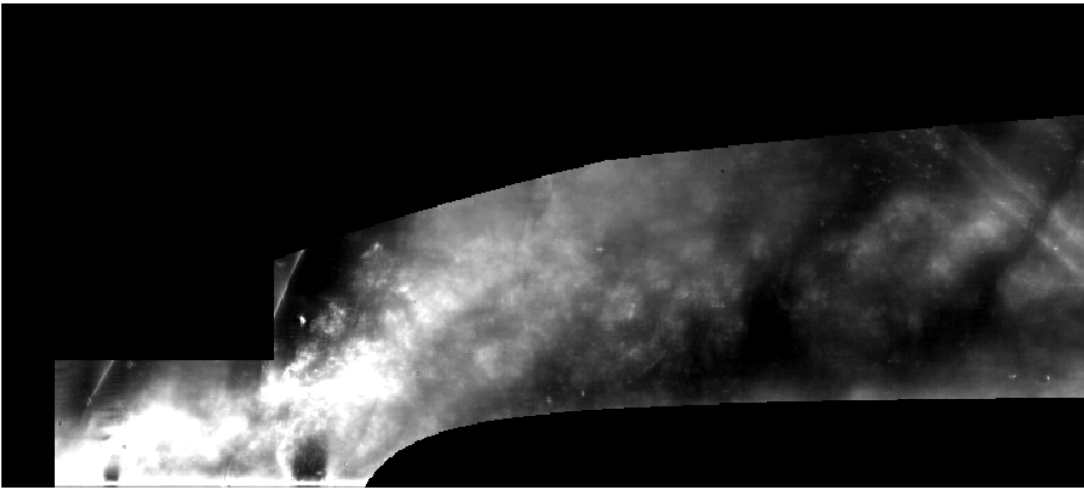Figure 7.19: Schlieren image overlaid by the final determined window (binary mask), which is used for further analysis of the behaviour of the jet ($J = 3.8$, $S = 4.93$ and $M_c = 1.55$).

7.4.2.2   Jet Determination

The purpose of the jet determination processing is to detect the jet structures within the determined window.

As an input, the process requires a number of Schlieren images (20 in the present study), the determined window (binary mask), and the position of the shocks (see figure 7.17). The output for every Schlieren image is 3 sets of coordinates: Coordinates of the full jet structures, the jet upper shear layer, and the jet lower shear layer.

The following procedure is applied to every Schlieren image individually, for which the binary mask is always applied:

1. Local contrast is increased by the function `localcontrast`, using an edge threshold of 0.3 and a strong enhancement.

2. The image is divided into 5 parts – because of the variation of the light intensity and dominance of the jet structures, such that the jet determination is optimal –, and every part is processed in the following manner (see figure 7.20) [31]:
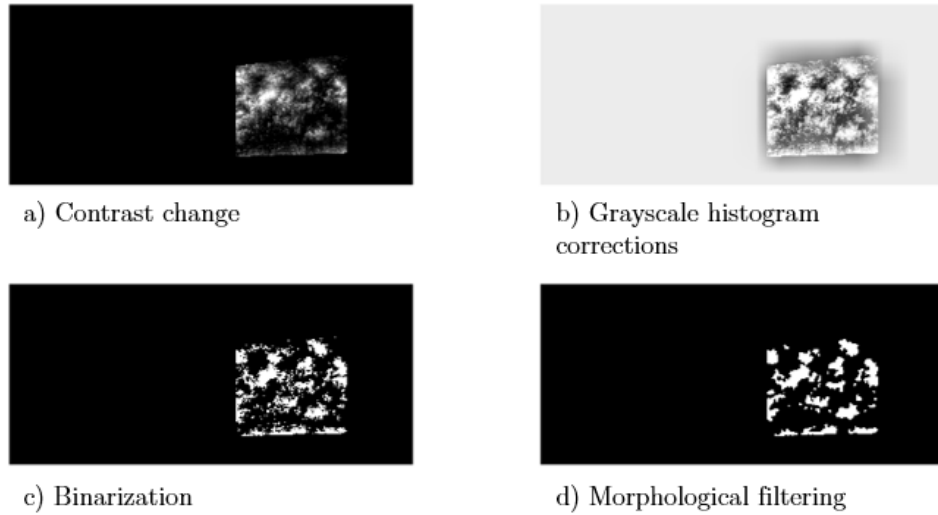

Figure 7.20: Intermediate steps for the jet determination for $J = 3.8$, $S = 4.93$ and $\mathrm{M}_c = 1.55$. The processing steps here shown are for one partial window. a) Contrast change using `imadjust`. b) Grayscale histogram corrections using `histeq` and `adapthiseq`. c) Binarization using `imbinarize`. d) Morphological filtering using `bwmorph`.

(a) Firstly, the function `imadjust` changes the contrast of the image part, with automatic contrast limits and the value for the shape of the curve describing the relationship of input and output values of 1.5 (figure 7.20a).

(b) Next, the grayscale Schlieren image is transformed by the function `histeq`, such that the histogram of the output grayscale image has approximately a uniformly distributed shape.

(c) Subsequently, the function `adapthiseq` is used for enhancing the local contrast, such that amplification of noise is avoided. The number of tiles setting divides the image in $8{\times}16$ parts and a contrast enhancement limit of 0.4 ± 0.05 is used (figure 7.20b).

(d) In the next step, the image is binarized using the function `imbinarize`, for which a locally adaptive image threshold is used. A sensitivity of 0.36 ± 0.04 is applied (figure 7.20c).

(e) For the filtering of noisy 1's in the binary image, the function `bwmorph` is used. Majority is applied – the majority in a 3-by-3 area has to be 1, then all become 1, otherwise, every pixel is 0 –, such that the dominant structures in the binary image remain as spots (figure 7.20d).

The steps above are applied to all 5 parts of the image separately. Subsequently the 5 parts are put together. This compound binary image is used for the further processing.

3. The binary image is transformed into a set of coordinates of all pixels with a value of 1. Previously determined shock waves are erased from the set of coordinates.

4. The coordinates are taken together as spots using the function `bwboundaries`. If the center of a spot is within 10 pixels from the window boundary, then this spot is erased from the set of coordinates, because it is plausible that this spot is an undesired side-effect of the processing steps.

5. The set of coordinates of the remaining spots is the final result of this process and represent the plume of the jet (see figure 7.21).
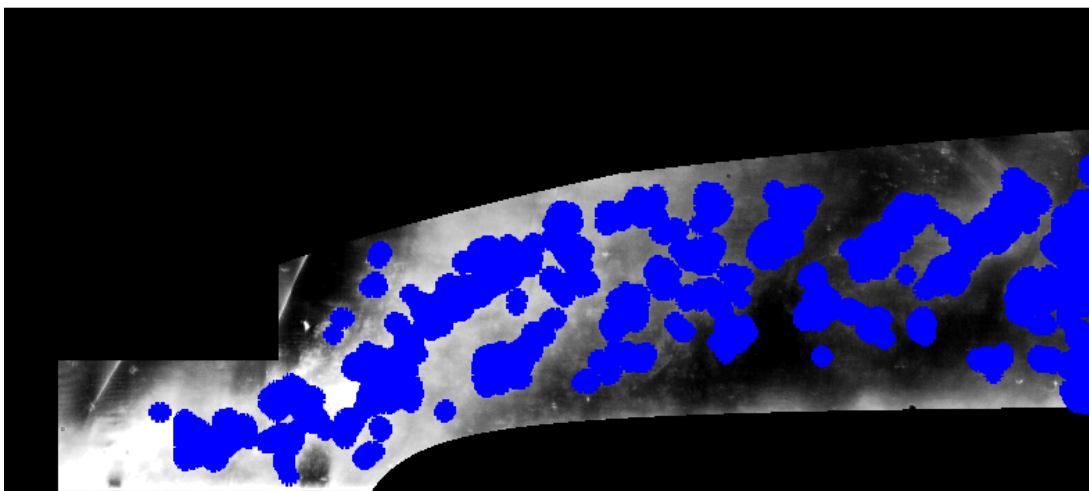
Figure 7.21: Jet plume determination for one image ($J = 3.8$, $S = 4.93$ and $\mathrm{M}_c = 1.55$).

From this set of coordinates, the upper and lower boundary of the plume for every x-coordinate are determined and stored as sets of coordinates. As it is possible that the upper boundary of the plume determined in this manner is fanciful, this set of coordinates is corrected by filtering points that are far away from of the moving median or moving average. The same is done for the lower boundary of the plume. An example of the result of the filtering is shown in figure 7.22.

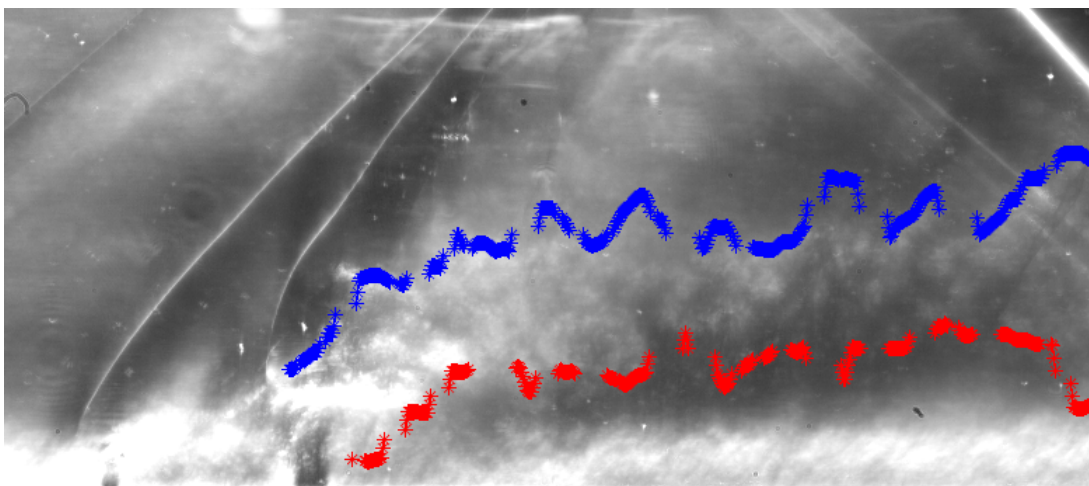Figure 7.22: Jet upper shear layer (blue) and jet lower shear layer (red) determined after correction for one image ($J = 3.8$, $S = 4.93$ and $\mathrm{M}_c = 1.55$).

The sets of coordinates of all 20 Schlieren images are stored and are used for the analysis of the results.

7.4.2.3   Results Analysis

In this step, the data sets obtained in the previous steps are combined and functions are found for the description of the jet upper shear layer, the jet lower shear layer and the jet center line.

In figure 7.23, the jet behaviour is visualized by an iso-incidence plot. The incidence is indicated by the colour. From these colours, it becomes clear which structures within the jet plume are often detected at that certain position by the jet determination for different Schlieren images. For example, around the jet orifice, the incidence is high, because of largely stationary structures, such as the barrel shock.
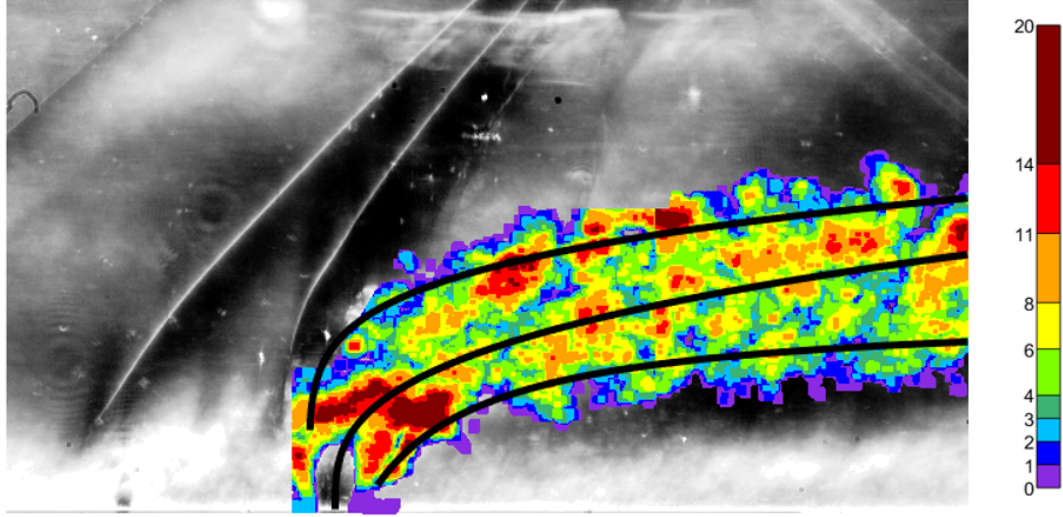

Figure 7.23: Iso-incidence plot for the jet analysis, together with a fit for the jet upper shear layer (up), the jet center line (mid) and the jet lower shear layer (down) ($J = 3.8$, $S = 4.93$ and $M_c = 1.55$).

In section 4.4, several functions for describing the jet were proposed and analysed. In general, power-law functions are used for both the jet upper shear layer and the jet center line. For the jet upper shear layer, the same fit as Gruber et al. [39] and De Maag [3] is used:

$$\frac{y}{D_t} = c_1 \left(\frac{x}{D_t} - c_3 \right)^{c_2} \tag{7.6}$$

This fit will be denoted as the **fit without shift** for the jet upper shear layer. In order to investigate whether the penetration depth could be described better by adding a constant term, the following fit is used for the same data of the jet upper shear layer:

$$\frac{y}{D_t} = c_1 \left(\left(\frac{x}{D_t} - c_3 \right)^{c_2} + c_4 \right) \tag{7.7}$$

This fit will be denoted as the **fit with shift** for the jet upper shear layer. For the two fits, the data of the jet upper shear layer for $-1.0 < x/D_t < 15$ is used.

For the jet center line, another fit is used, for the range $0 < x/D_t < 15$. The center of the plume starts at the center of the downstream orifice, which is the origin of the coordinate system. Therefore, the following fit is used:

$$\frac{y}{D_t} = d_1 \left(\frac{x}{D_t} \right)^{d_2} \tag{7.8}$$

Furthermore, a fit for the jet lower shear layer is sought. In the first place, the jet moves upwards and thereafter, the plume spreads out. As a consequence, a function that would fit the jet lower shear layer, is a challenge. An appropriate approximation for the range $0.5 < x/D_t < 15$ is the following rational function:

$$\frac{y}{D_t} = \frac{e_1\left(\left(\frac{x}{D_t}\right) - e_2\right)}{\left(\frac{x}{D_t}\right)^2 + e_3\left(\frac{x}{D_t}\right) + e_4} \tag{7.9}$$

The fits are found using a least-squares algorithm. For checking the quality of the fits, the coefficient of determination, R^2, is used:

$$R^2 = 1 - \frac{\sum_i (f(x_i) - y_i)^2}{\sum_i (\bar{y} - y_i)^2} \tag{7.10}$$

The variable $\bar{y}$ is the mean of the data, calculated by $\bar{y} = \frac{1}{n}\sum_{i=1}^{n} y_i$, $f(x)$ is the fit and (x_i, y_i) are the data.

One characterization of a jet injection experiment is the penetration. De Maag's definition [35] for the average penetration will be used in the present study:

$$\frac{y_{avg}}{D_t} \equiv \frac{1}{x_{up}/D_t - x_{down}/D_t} \int_{x_{down}/D_t}^{x_{up}/D_t} \frac{y\left(x/D_t\right)}{D_t} d\left(\frac{x}{D_t}\right) \tag{7.11}$$

The range $0.5 \leq x/D_t \leq 15$ is chosen ($x_{up}/D_t = 15$ and $x_{down}/D_t = 0.5$). The lower boundary is chosen to be $x/D_t = 0.5$ because at that point, the jet is bulged out enough for a good description by the chosen fit. The upper boundary is chosen to be $x/D_t = 15$ because for larger distance, reflected shocks will intersect the jet plume, which makes that the structures are harder to be identified. Furthermore, the range is large enough for determining the average penetration.

From the analysis described above, relations can be generalized in terms of scalings of J and S. An approach to match the empirical equations to the general equations will be detailed in section 8.2.2.2.

Chapter 8

Results and Discussion

In this chapter, the results of the experiments described in chapter 7 are analysed and discussed. In section 8.1, the results of the behaviour of the bow shocks are described and discussed, and in section 8.2, the results of the behaviour of the jet are described and discussed.

8.1 Results Behaviour Bow Shocks

This section describes the observations and results of the behaviour of the two bow shocks that form in dual jet injection. In section 8.1.1, some observed features are described and compared with literature. Subsequently in section 8.1.2, the analysis of the merger point of the two bow shocks is given. Finally, concluding remarks are provided in section 8.1.3.

8.1.1 Observations

In the experiments with dual jet injection, two bow shocks are formed, one in front of each of the two jets. These two bow shocks, as described in section 4.3, have a nearly normal part near the jet orifice and an oblique part further from the orifice away from the wall. Near the upper wall, the oblique part of the bow shock turns again into a normal shock, the so-called Mach stem, due to the phenomenon of shock reflection. The features as described are shown in figure 8.1.

In section 4.3.3, the behaviour of the bow shock with respect to its position – whether this shock wave oscillates or not – was analysed. Most studies (e.g. [7][26]) found that the bow shock position is not stationary. Gruber et al. [32] showed that the large-scale structures within the jet upper shear layer cause the pulsating character of the oscillation of the bow shock. These studies were for single jet injection. In the present study, a similar behaviour has also been observed for dual jet injection. In figure 8.2, the bow shocks near the orifices are shown for a number of random moments in time. It is found, that the upstream bow shock oscillates only within a small bandwidth. However, the downstream bow shock moves more intensively due to the large-scale structures in the jet upper shear layer of the downstream jet. It is thought, that the large-scale structures are more dominant in the jet downstream than in the jet upstream because the mass ratio $\dot{m}_{downstream}/\dot{m}_{upstream} = 4/1$ implies that the jet downstream is more intense.

The position of the upstream bow shock is more volatile because of the interaction with the boundary layer upstream of the orifice and feedback through the subsonic flow region. The position of the downstream bow shock fluctuates because of the interaction with the main jet.

Time-averaged, the downstream bow shock has a larger normal shock part than the upstream bow shock, which is due to the larger orifice diameter i.e. larger mass flow. In addition, the downstream bow shock has a larger normal part because of the more prominent bulging of the underexpanded jet. Near the upstream jet, the flow is slowed down, which gives the downstream jet the space to bulge out more.

Starting from dual jet injection with $D_1 = 1$ mm and $D_2 = 2$ mm with the total pressure $p_{0,j}$ that is the same for both jets, it is observed that the position of the bow shock is dependent on the Mach number of the crossflow M_c, the jet-to-crossflow momentum flux ratio J and to a smaller extent on the dual jet distance S. A larger crossflow Mach number results in a smaller inclination of the oblique part of

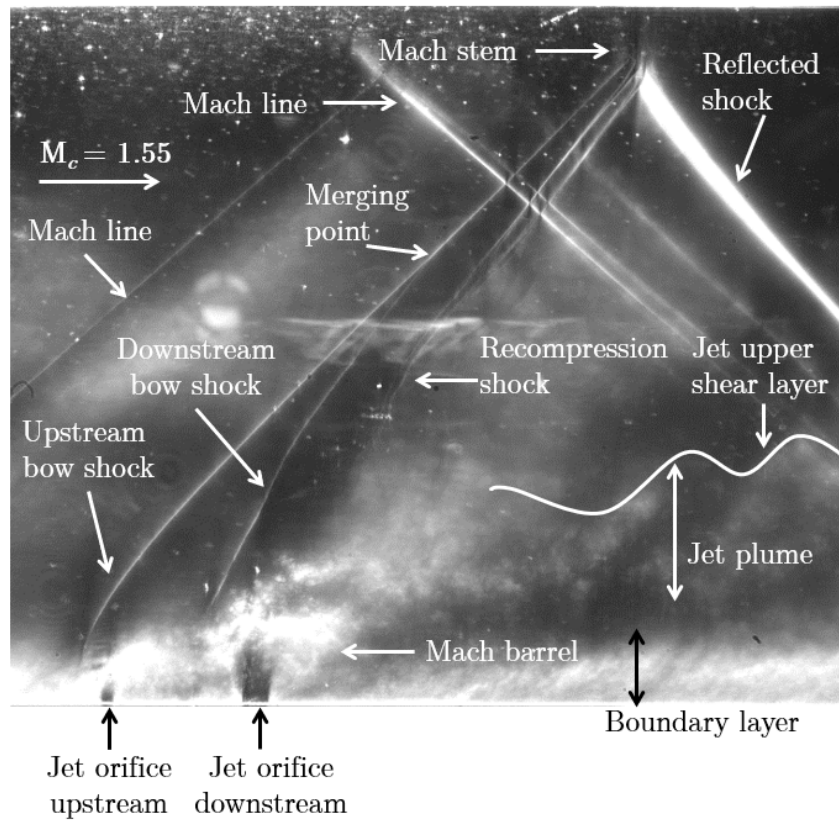Figure 8.1: Features of dual jet injection into a supersonic crossflow ($J = 3.8$, $S = 4.48$ and $M_c = 1.55$) shown in original Schlieren image.
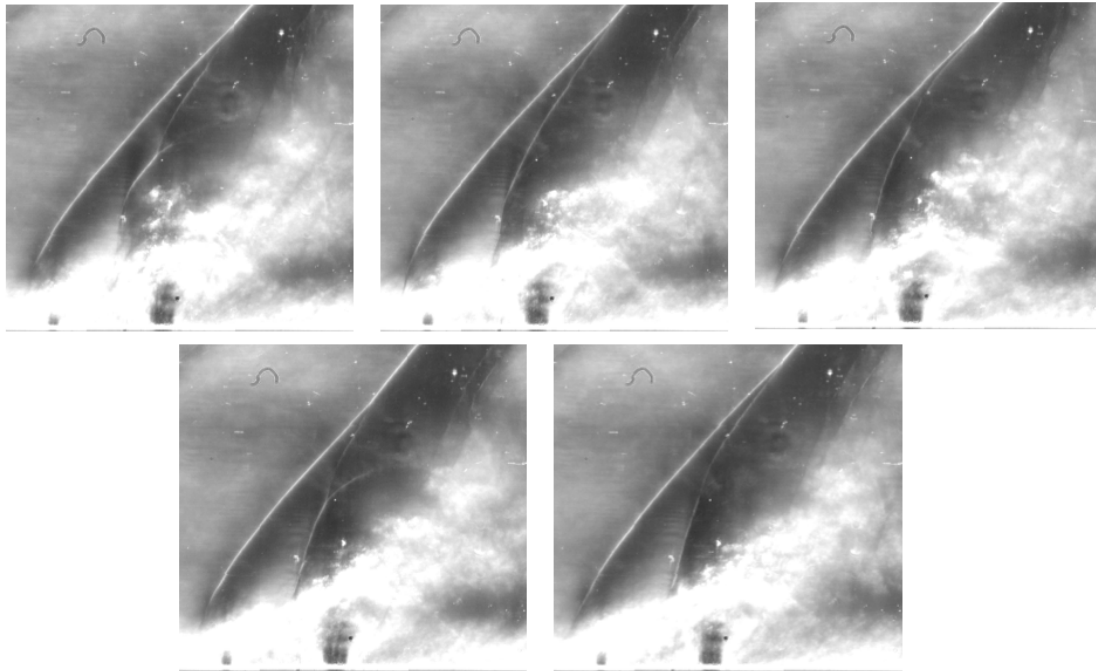

Figure 8.2: Cutout of the original Schlieren images for visualizing the bow shocks at five random moments in time. Especially the downstream bow shock fluctuates in position and so does the merger point of the two bow shocks. ($J = 3.8$, $S = 3.59$ and $M_c = 1.55$).
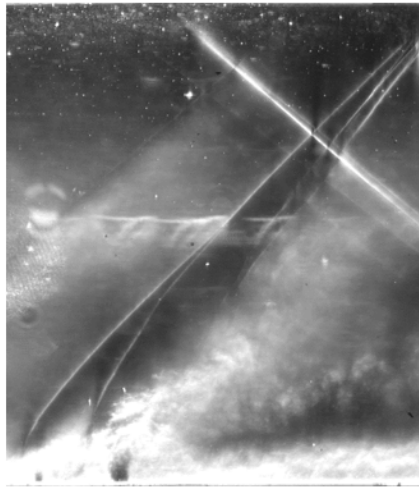
a) $J = 2.8$, $S = 3.59$ b) $J = 3.8$, $S = 3.59$

Figure 8.3: Original Schlieren images of the full wind tunnel height showing bow shocks for two different J's. The bow shocks merge earlier for larger J. a) Experiment for $J = 2.8$, $S = 3.59$ and $M_c = 1.55$. b) Experiment for $J = 3.8$, $S = 3.59$ and $M_c = 1.55$.

a) $J = 3.8$, $S = 3.59$ b) $J = 3.8$, $S = 4.48$

c) $J = 3.8$, $S = 5.38$ d) $J = 3.8$, $S = 9.87$

Figure 8.4: Original Schlieren images of the full wind tunnel height showing bow shocks for four different values of S. The bow shocks merge earlier for smaller S. a) Experiment for $J = 3.8$, $S = 3.59$ and $M_c = 1.55$. b) Experiment f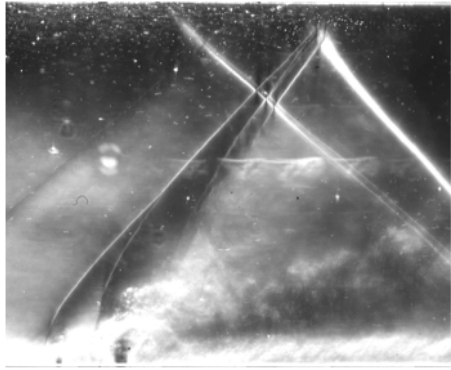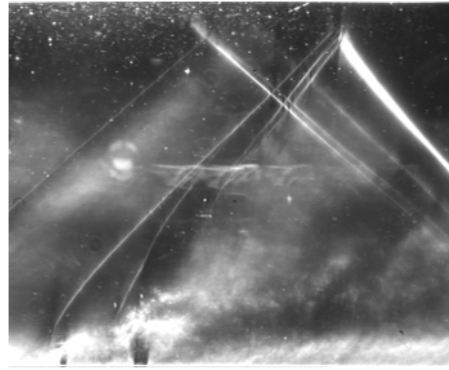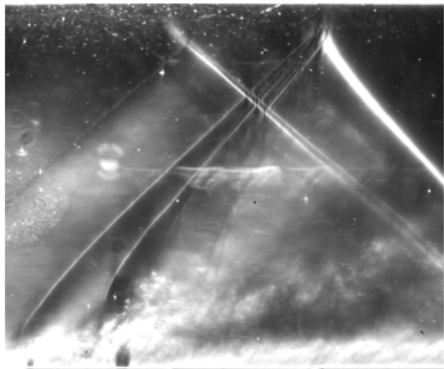or $J =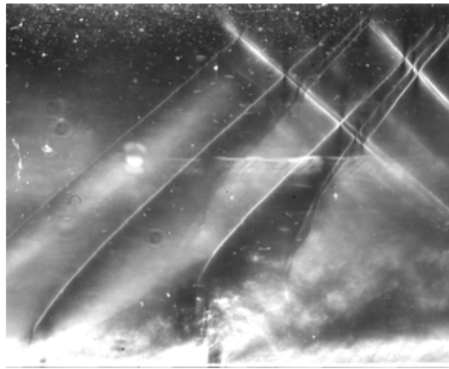 3.8$, $S = 4.48$ and $M_c = 1.55$. c) Experiment for $J = 3.8$, $S = 5.38$ and $M_c = 1.55$. d) Experiment for $J = 3.8$, $S = 9.87$ and $M_c = 1.55$.

the bow shock and a stronger effect of the normal part of the bow shock. S gives a large contribution to the effect, whether or not the two bow shocks merge or remain spatially separated. A larger J results in a more extensive bulging of the jet and therefore a larger normal part of the bow shock. For comparison, Schlieren images of the bow shocks for several experiments at the same S but different J are shown in figure 8.3 and Schlieren images of the bow shocks for several experiments at the same J but different S are shown in figure 8.4.

8.1.2   Merger Point of the Bow Shocks

A further feature observed in the Schlieren images of the bow shocks, is that the two bow shocks merge at some point which depends on the specific combination of S and J. The point at which this occurs is called the merger point $(\xi, \eta) = (x/D_t, y/D_t)$. As observed in figure 8.3 and figure 8.4, the position of this merger point is dependent on both J and S, and presumably, this merger point position also depends on M_c, because the bow shock position does depend on M_c.

It is observed, that for larger J, the merger point is closer to the jet orifice, and that for larger S, the merger point is further away from the jet orifice. Above a certain value of S, the bow shocks do not merge, i.e. remain spatially separated at least within the height of the wind tunnel. This value is dependent on J.

All experiments are performed for $M_c = 1.55 \pm 0.02$, and the correlation between the position of the merger point and J and S is investigated.

Because of the fluctuating character of especially the downstream bow shock, the position of the merger point is not stationary. For getting an average value, the data of 20 Schlieren images is used for obtaining the data. In figure 8.5, all data sets for the position of the merger point are shown for $J = 2.8$ and $J = 3.8$. For one value of S, a measurement for $J = 4.8$ added to the data sets. Remarkably, for every experiment, the merger point is located on the upstream bow shock (see also figure 7.12).
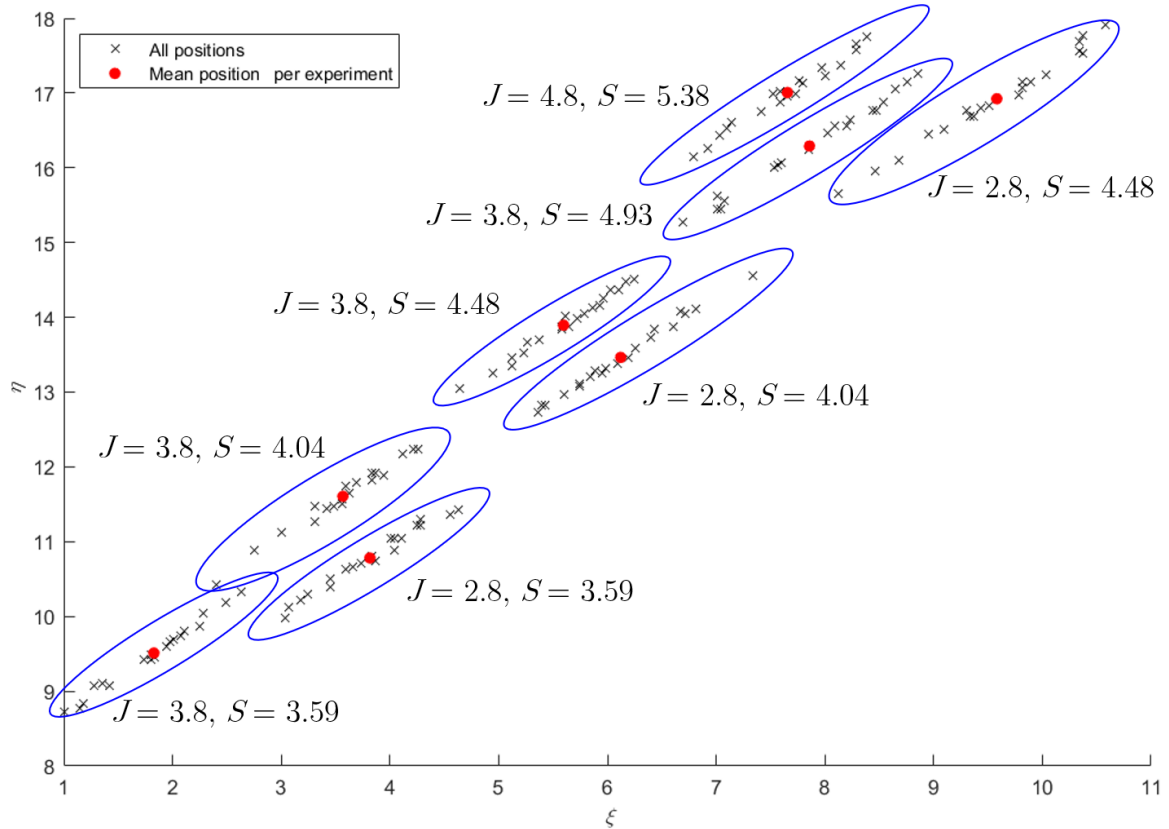

Figure 8.5: Position of merger point for several values of J and S, $M_c = 1.55$.

For investigating the correlation between the position of the merger point and J and S, separate equations are sought for the horizontal coordinate ξ and the vertical coordinate η.

In figure 8.6, the values of ξ and η are plotted against S. Included in this figure is the mean value of ξ and of η as the red dot. In figure 8.7, figure 8.6 is transformed by taking the logarithmic values. In the logarithmic plots, the results for constant J show a linear relation between $\log(\xi)$ and $\log(S)$, and between $\log(\eta)$ and $\log(S)$. As a result of that, the functions for describing $\xi = \xi(J, S)$ and $\eta = \eta(J, S)$ are in the following form:

$$
\begin{aligned}
\xi(J, S) &= f_1(J) \cdot S^{c_1} \\
\eta(J, S) &= f_2(J) \cdot S^{c_2}
\end{aligned}
\tag{8.1}
$$

The functions f_1 and f_2 are a function of J. There are not many different J's, which makes deriving a general function not very accurate. However, it is attempted to find an expression for $f_1(J)$ and $f_2(J)$, using the data for $J = 2.8$, $J = 3.8$ and $J = 4.8$. In figure 8.8, the logarithmic values of the scaled positions ξ and η are plotted against the logarithmic values of J, with ξ and η are scaled by $S^{4.229}$ and $S^{1.827}$, respectively. These power coefficients are derived from the fits in figure 8.7. Figure 8.8 reveals a linear relation between the logarithm of the scaled position and the logarithm of J. As a result, it has been concluded that a power-law fit for J may is appropriate. Therefore, the general fits for the position ξ and η are:

$$
\begin{aligned}
\xi(J, S) &= c_1 J^{c_2} S^{c_3} \\
\eta(J, S) &= c_4 J^{c_5} S^{c_6}
\end{aligned}
\tag{8.2}
$$

The two functions of J and S are fitted separately using the least-squares method. All data sets available are used; not only the mean positions. This results in the following equations:

$$
\begin{aligned}
\xi(J, S) &= 0.114 J^{-1.864} S^{4.229} \\
\eta(J, S) &= 1.924 J^{-0.572} S^{1.827}
\end{aligned}
\tag{8.3}
$$

The fit for ξ has an R^2 value of 0.952 and the fit for η has an R^2 value of 0.962. These values are both very acceptable. The equation is valid for $2.8 \leq J \leq 4.8$, $3.59 \leq S \leq 5.38$, $M_c = 1.55$ and a upper bound $\eta \leq 19.3$ (height of the wind tunnel minus the height of the boundary layer). It has to be noted that because of the small number of data and the small range because of the fixed values of S and the wind tunnel height, the equations found may not be valid for J and S exceeding the ranges. In figure 8.9, all positions of the merger point of the bow shocks, scaled by power functions of J and S, are given. It appears that for most of the measurements, the scaling is appropriate, as the mean values are almost all inside the black circle with radius 0.05. There is one relative outlier, which is the measurement for $(J = 3.8, S = 3.59)$. For this measurement, the point the nearest to the jet orifice is obtained. It may be that as a result of other effects, the fit is not appropriate near $\xi = 0$.

Further research could confirm the findings and investigate meticulously to what extent bow shocks remain spatially separated or merge and at which point they merge.

8.1.3   Concluding Remarks Behaviour Bow Shock

From the relations found in equation 8.3, some practical concluding remarks can be given. The wind tunnel has a height of $21.4 D_t$, which makes that the relations are limited applicable. In the preceding section, it was mentioned that $\eta_{\max} = 19.3$ because of the wind tunnel height and the boundary layer. If this maximum is set, then a relation for S depending on J can be derived from equation 8.3, which expresses the maximum value for S for a certain J for which the bow shocks merge. Above this limiting value of S, the bow shocks remain spatially separated. This pivoting value for S, S_{pivot}, is expressed as:

$$
S_{pivot} = 3.53 J^{0.313}
\tag{8.4}
$$

In the next sections on the results of the behaviour of the jet, it is investigated whether S_{pivot} has an effect on the behaviour of the jet.
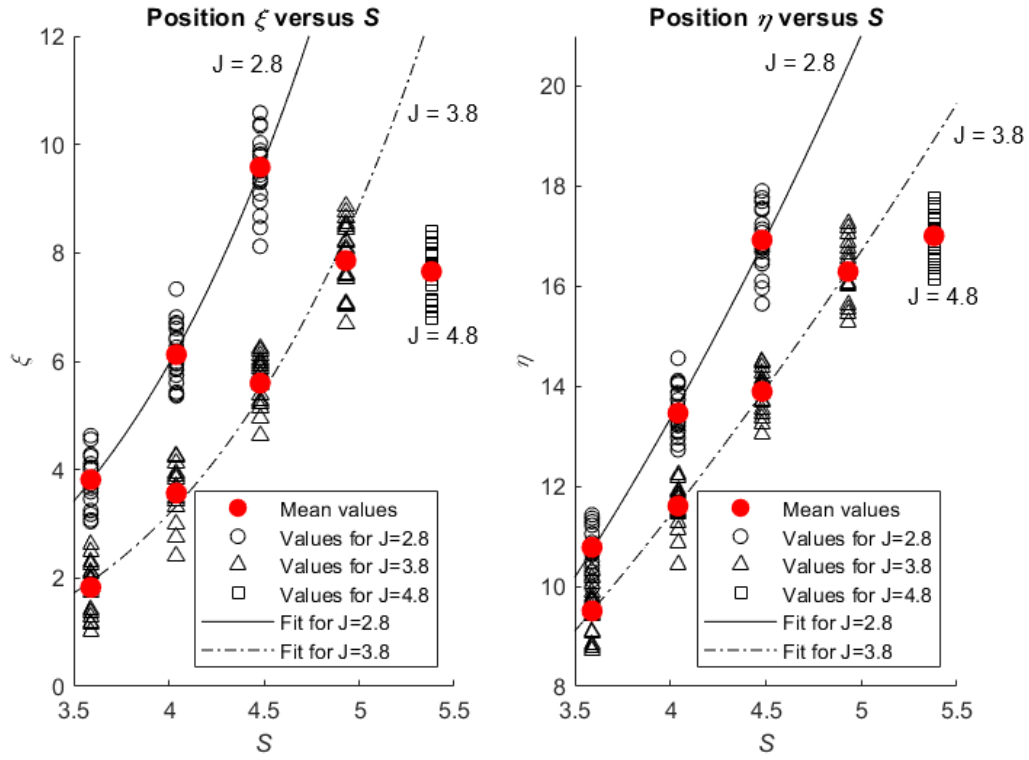
Figure 8.6: Position of the merger point for several values of J and S and $M_c = 1.55$, together with fits for equation 8.1.
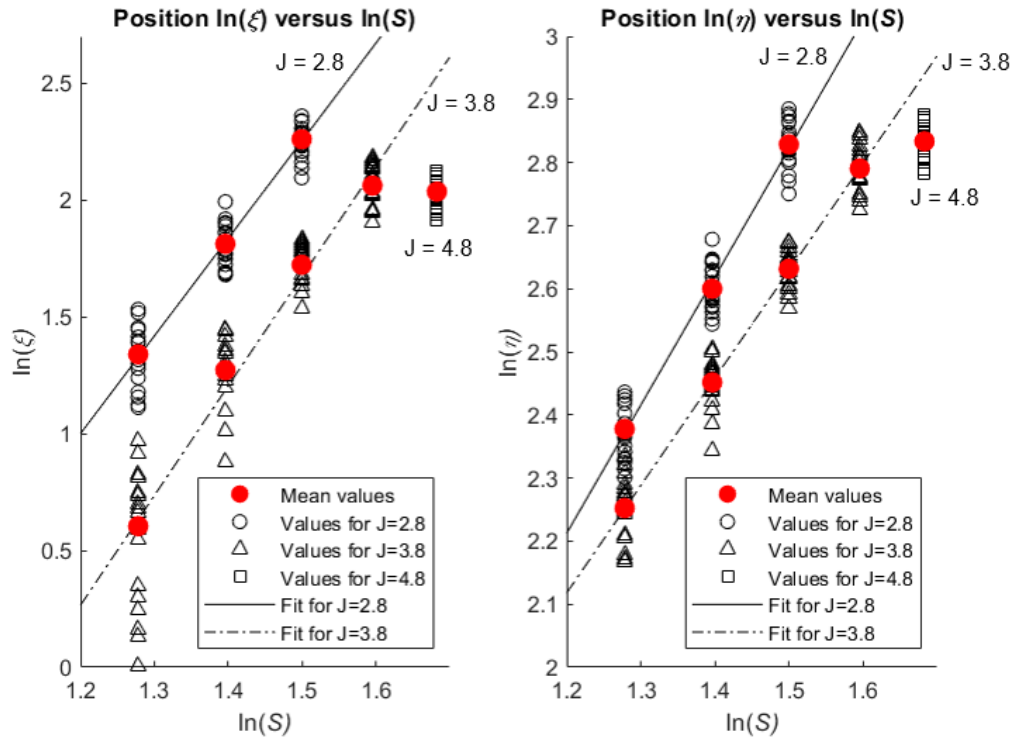
Figure 8.7: Logarithm of position of the merger point for a number of values of J and S and $M_c = 1.55$, together with fits for equation 8.1.
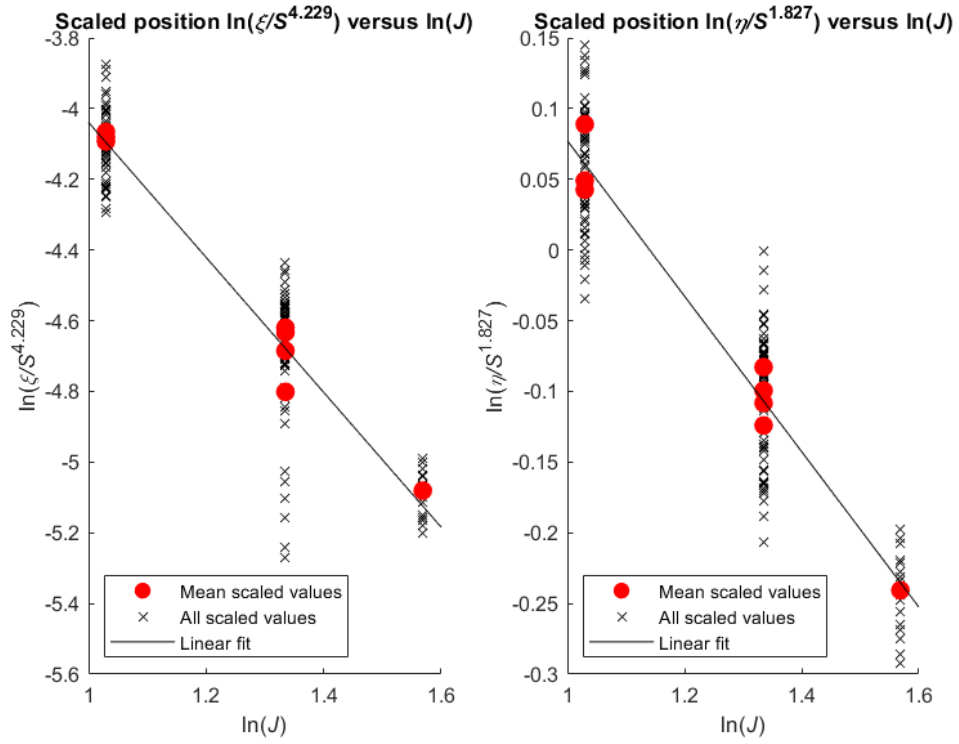
Figure 8.8: Position of the merger point scaled by a power of S for a number of values of J, $M_c = 1.55$. Included are fits from equation 8.2.
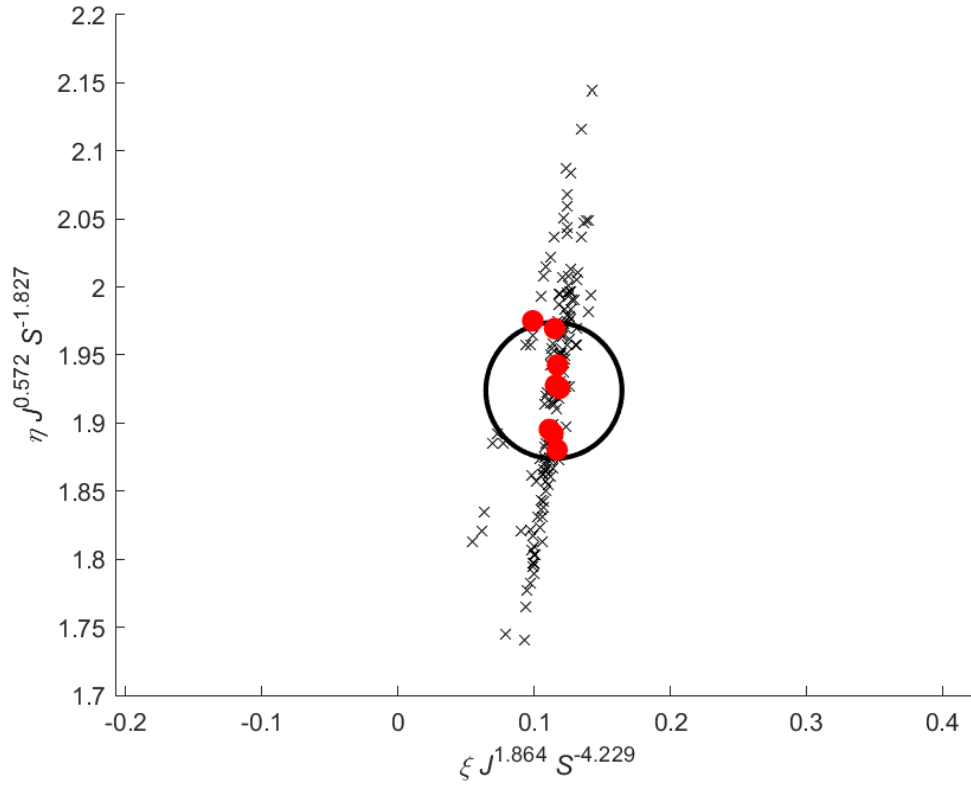
Figure 8.9: Position of the merger point scaled by powers of J and S according to equation 8.3 at $M_c = 1.55$. The crosses are scaled values of all measurements and the red dots are the scaled mean values per combination (J, S). The larger black circle is centered at $(0.114, 1.924)$ and has radius 0.05.

8.2   Results Behaviour Jet

The results of the behaviour of the jet are investigated, which is the focus point in the present study. Several phenomena are analysed, quantified, and subsequently discussed. In section 8.2.1, Schlieren images of the results together with graphic results are given. Subsequently, in section 8.2.2 to 8.2.5, the behaviour of the jet is discussed, quantified by relations for the position of the jet upper shear layer and jet lower shear layer as well as the jet center line. Using these equations, the penetration of the jet into the crossflow is quantified. All these results are investigated for a certain range of S for $J = 2.8$, $J = 3.8$ and $J = 4.8$. This leads to identifying relations for the behaviour of the jet depending on J and on S. The focus is on the jet-to-crossflow momentum ratios $J = 2.8$ and $J = 3.8$.

In section 8.2.2, the results for the jet upper shear layer are elaborated on. Sections 8.2.3 and 8.2.4 present the results of the analysis for the jet center line and jet lower shear layer, respectively. Finally, concluding remarks on the behaviour of the jet are given in section 8.2.5.

8.2.1   Visual Results for Behaviour Jet

In this section, Schlieren images are presented from the experiments described in chapter 7. From every experiment, one out of the 20 images taken is extracted and shown in figure 8.10 to 8.12. The results for $J = 2.8$ are shown in figure 8.10 and the results for $J = 3.8$ are shown in figure 8.11. Two experiments for $J = 4.8$, which have dual distances $S = 0$ and $S = 5.38$, respectively, are shown in figure 8.12. In the center of each Schlieren image, light reflection due to the reflection of the lens appears. In addition, some contamination is present in the images (dust particles and fingerprint). However, these irregularities do not affect the results.

In chapter 5, several studies were considered on a parameter study of the behaviour of especially the rear jet. In the present section, it is investigated whether the results show similar behaviour to that found in literature.

In the Schlieren images, the horizontal domain extends approximately from $-9 \leq x/D_t \leq 20$, which is similar to the images taken by De Maag [3][35], taken in the same facilities. The results of Lee [9] and especially Landsberg [55] consider a larger domain, $-10 \leq x/D_t \leq 35$ and $-10 \leq x/D_t \leq 50$, respectively. Therefore, in their studies, the behaviour of the jet further downstream has more focus. In the present study, the focus is on the near-field behaviour of the injection.

A qualitative analysis of the results in figures 8.10 to 8.12 shows that, similar to described in section 5.2, dual jet injection ($S > 0$) features a stronger penetration than single jet injection ($S = 0$). Furthermore, at constant J, the variation of penetration with S has a maximum at a certain value of S. This is in line with the expectations [9]. Whether the value of S at which the maximum penetration is obtained increases with increasing J – as observed in the study of De Maag [35] – is not clear from this qualitative analysis and is investigated in the quantitative analysis in the present section.

Another parameter that had an effect on the behaviour of the jet is the jet-to-crossflow momentum ratio J. In line with literature, penetration increases with increasing J, which is seen in results for constant S, with increasing from $J = 2.8$, 3.8 and 4.8.

In section 4.5.2, the Kelvin-Helmholtz instability for the jet upper shear layer was analysed. In the present experimental study, the focus is not on this phenomenon, which would require a more detailed study. However, when investigating the behaviour of the jet qualitatively, it is observed in many Schlieren images, that roller structures in the jet upper shear layer are present. As an example, figure 8.10a shows a possibly periodic behaviour of the jet upper shear layer as expected from the derivation in section 4.5.2. This behaviour is not observed equally clear in all Schlieren images. A further experimental in-depth study into this phenomenon is recommended (see chapter 10).

Figures 8.13 to 8.16 are so-called iso-incidence plots, based on 20 Schlieren images in which the jet plume is determined for the domain $-1 \leq x/D_t \leq 15$ (for the procedure, see section 7.4.2.2). The closer the colour is towards dark red, the larger the incidence in the plot. As a result, the more stationary, more dominant and frequently occurring structures in the jet can be recognized by their colour. Most figures show the barrel shock clearly, with a large value of the incidence, indicating that the barrel shock is largely a stationary structure.

a) $J = 2.8$ and $S = 0$

b) $J = 2.8$ and $S = 3.59$

c) $J = 2.8$ and $S = 4.04$

d) $J = 2.8$ and $S = 4.48$

e) $J = 2.8$ and $S = 4.93$

f) $J = 2.8$ and $S = 5.38$

g) $J = 2.8$ and $S = 5.83$

h) $J = 2.8$ and $S = 6.28$

Figure 8.10: Results of jet injection into a supersonic ($\mathrm{M}_c = 1.55$) crossflow for $J = 2.8$ at eleven values of S. The frame extends from $x/D_t = -9$ to $x/D_t = 20$ in horizontal direction.

a) $J = 2.8$ and $S = 7.17$

b) $J = 2.8$ and $S = 8.52$

c) $J = 2.8$ and $S = 9.87$

Figure 8.10: Results of jet injection into a supersonic ($M_c = 1.55$) crossflow for $J = 2.8$ at eleven values of S. The frame extends from $x/D_t = -9$ to $x/D_t = 20$ in horizontal direction. *(Continued)*

a) $J = 3.8$ and $S = 0$

b) $J = 3.8$ and $S = 3.59$

c) $J = 3.8$ and $S = 4.04$

d) $J = 3.8$ and $S = 4.48$

Figure 8.11: Results of jet injection into a supersonic ($M_c = 1.55$) crossflow for $J = 3.8$ at eleven values of S. The frame extends from $x/D_t = -9$ to $x/D_t = 20$ in horizontal direction.

a) $J = 3.8$ and $S = 4.93$

b) $J = 3.8$ and $S = 5.38$

c) $J = 3.8$ and $S = 5.83$

d) $J = 3.8$ and $S = 6.28$

e) $J = 3.8$ and $S = 7.17$

f) $J = 3.8$ and $S = 8.52$

g) $J = 3.8$ and $S = 9.87$

Figure 8.11: Results of jet injection into a supersonic ($M_c = 1.55$) crossflow for $J = 3.8$ at eleven values of S. The frame extends from $x/D_t = -9$ to $x/D_t = 20$ in horizontal direction. *(Continued)*

a) $J = 4.8$ and $S = 0$ b) $J = 4.8$ and $S = 5.38$
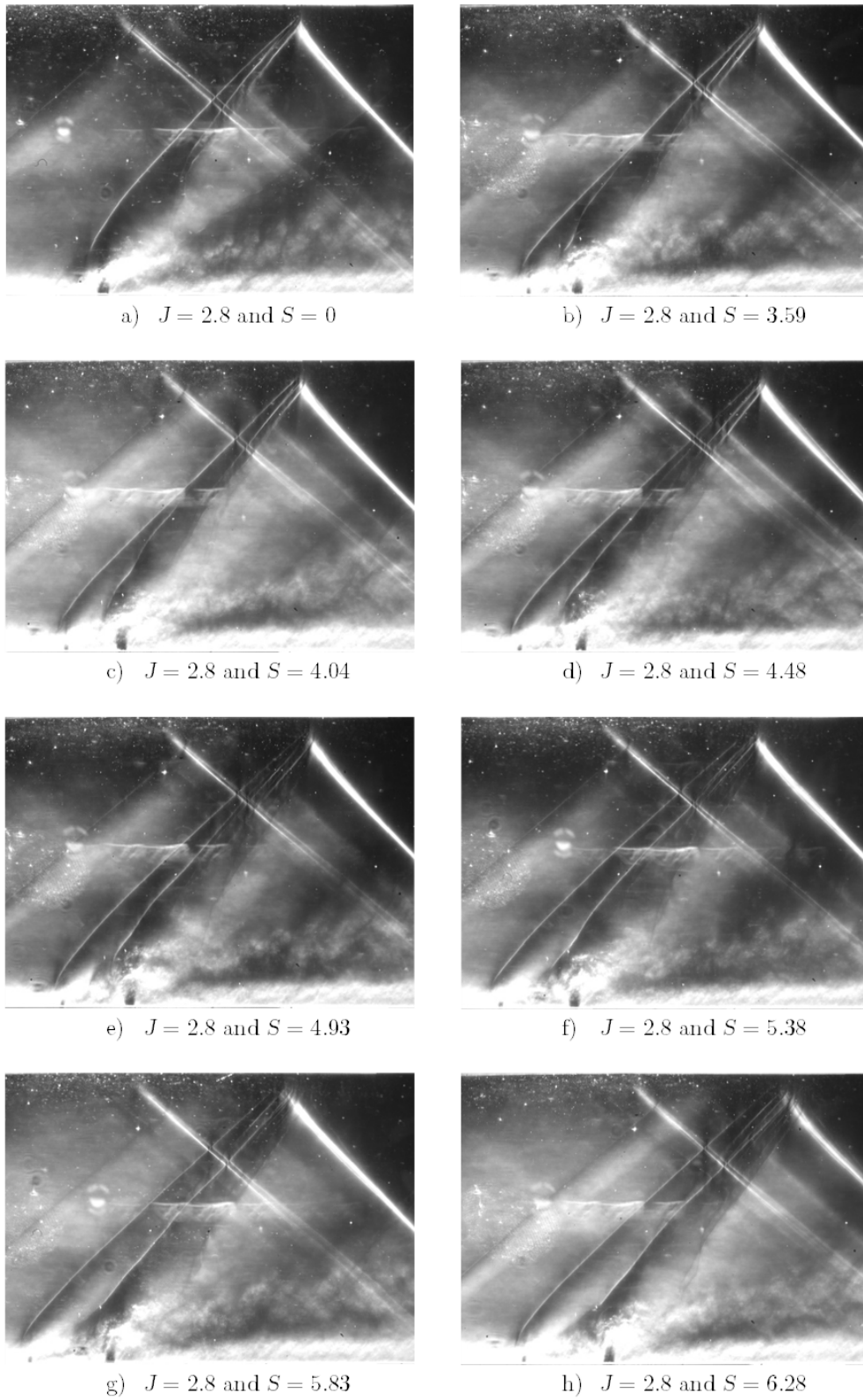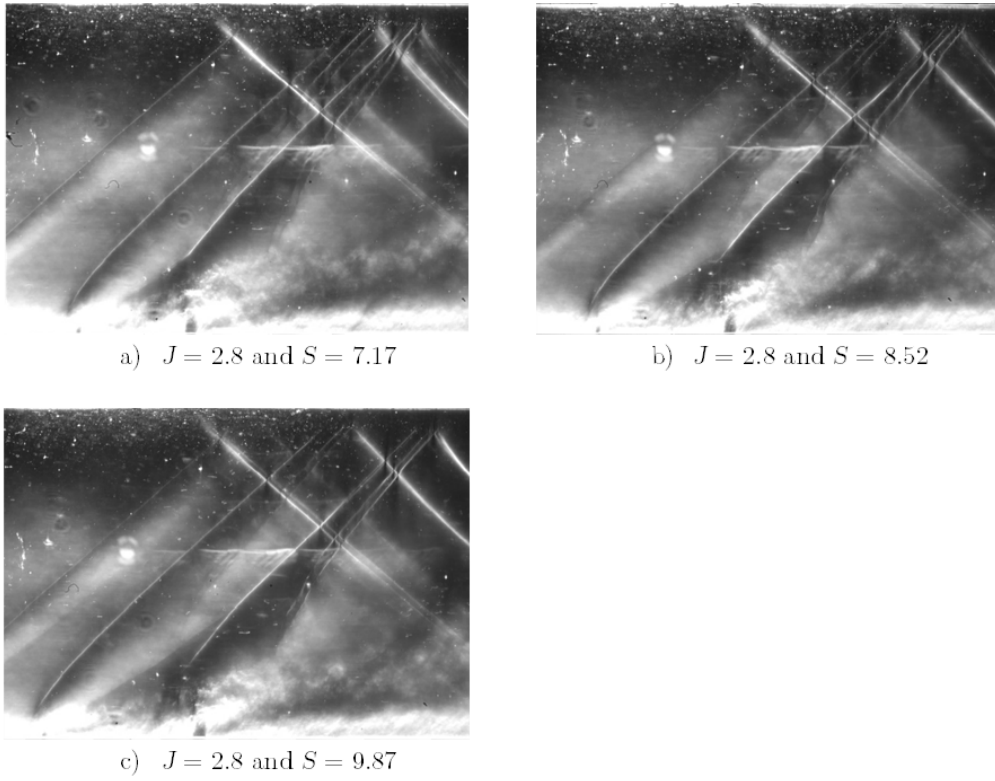
Figure 8.12: Results of jet injection into a supersonic ($M_c = 1.55$) crossflow for $J = 4.8$ at two values of S. The frame extends from $x/D_t = -9$ to $x/D_t = 20$ in horizontal direction.
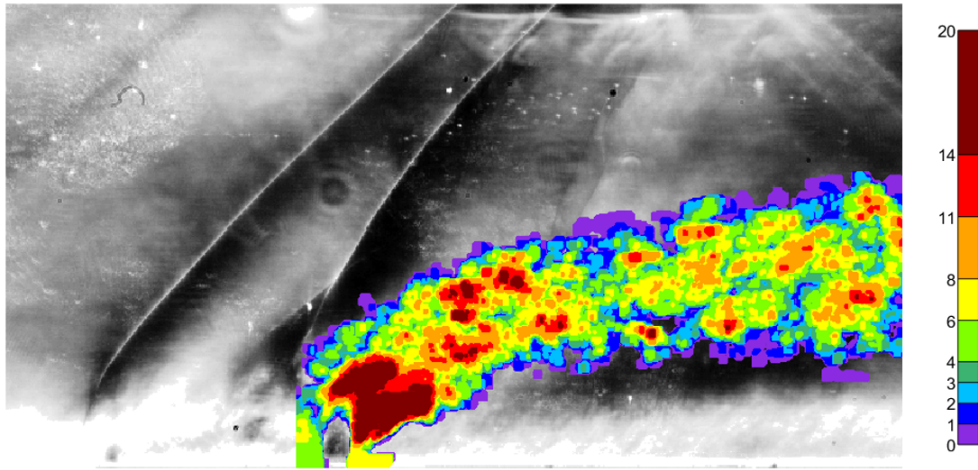
Figure 8.13: Iso-incidence plot for jet plume, based on 20 Schlieren images ($J = 2.8$, $S = 5.83$ and $M_c = 1.55$). Cut-out for $-7 \leq x/D_t \leq 15$ from an enhanced Schlieren image. The jet plume is shown for $-1 \leq x/D_t \leq 15$.
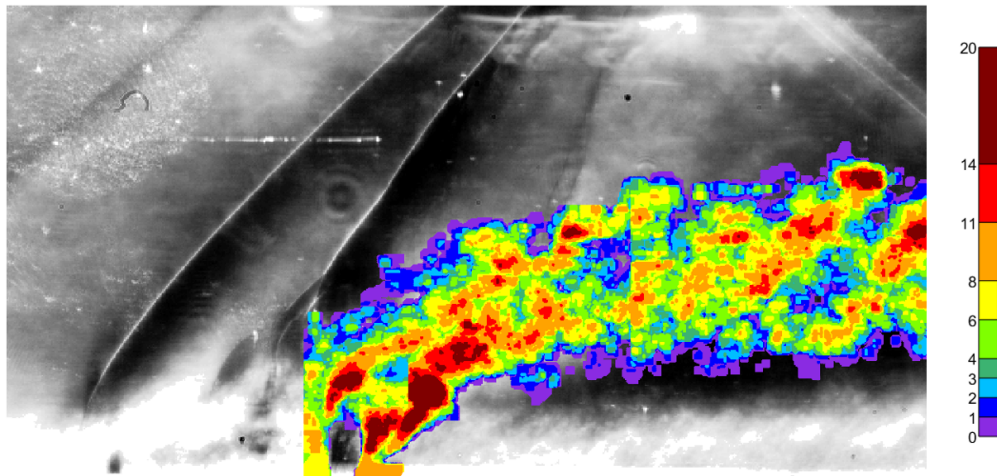
Figure 8.14: Iso-incidence plot for jet plume, based on 20 Schlieren images ($J = 3.8$, $S = 5.83$ and $M_c = 1.55$). Cut-out for $-7 \leq x/D_t \leq 15$ from an enhanced Schlieren image. The jet plume is shown for $-1 \leq x/D_t \leq 15$.
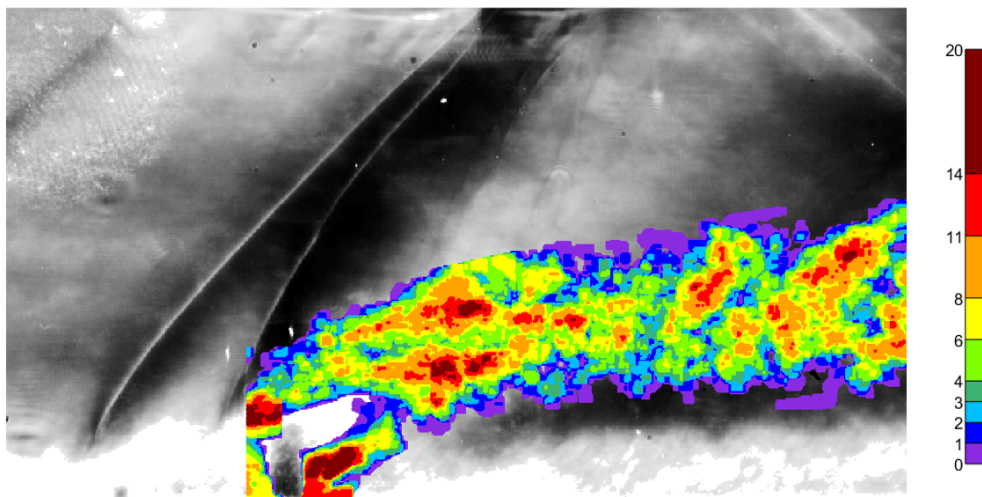
Figure 8.15: Iso-incidence plot for jet plume, based on 20 Schlieren images ($J = 2.8$, $S = 4.04$ and $M_c = 1.55$). Cut-out for $-8 \leq x/D_t \leq 15$ from an enhanced Schlieren image. The jet plume is shown for $-1 \leq x/D_t \leq 15$.
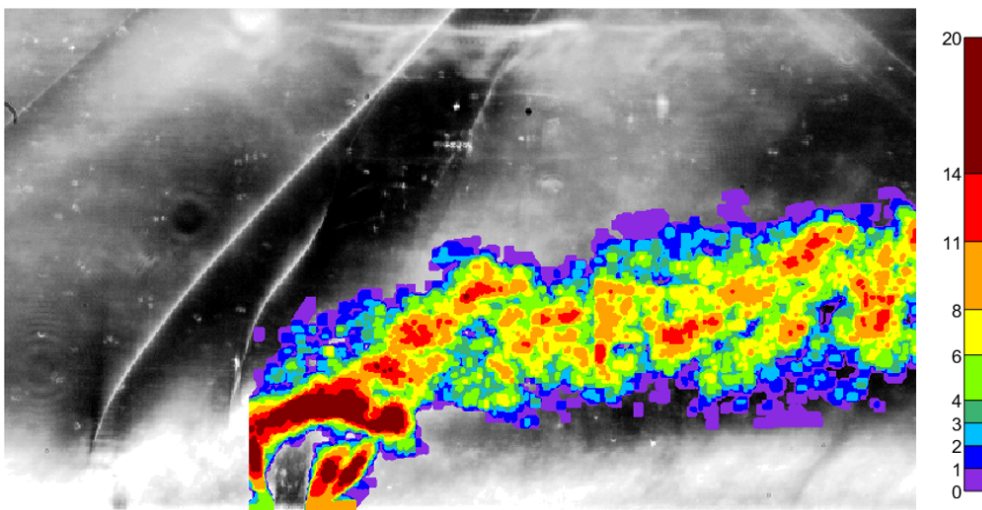
Figure 8.16: Iso-incidence plot for jet plume, based on 20 Schlieren images ($J = 3.8$, $S = 4.04$ and $M_c = 1.55$). Cut-out for $-8 \leq x/D_t \leq 15$ from an enhanced Schlieren image. The jet plume is shown for $-1 \leq x/D_t \leq 15$.

Figure 8.13 and figure 8.14 have the same dual distance S, but a different value of J. The same holds for figure 8.15 and figure 8.16. The effect of J on the jet is found in these figures: The general behaviour of the jet for different values of J appears to be similar, but for larger values of J, the size of the barrel shock increases and the jet penetrates deeper into the crossflow.

Two characteristic cases for the behaviour of the jet are shown in figure 8.13 and figure 8.16, respectively. In figure 8.13, the jet plume height increases steadily with increasing x/D_t, but in figure 8.16, the jet plume height for increasing x/D_t has a less steady behaviour. In both figures, but especially in figure 8.16, the jet upper shear layer shows a dip in the penetration in the neighbourhood of the location of the recompression shock. This dip was also observed by De Maag [35].

The general time-averaged characteristics of the jet upper shear layer and its penetration can be described by equation 7.6 (fit without shift) or equation 7.7 (fit with shift), but a more accurate description could be provided by splitting the domain [35] or using an even more sophisticated fit.

For finding the expressions for the location of the jet upper shear layer, jet center line and the jet lower shear layer, three different data sets are used (see section 7.4.2.3). In figure 8.17, the data sets for the plume (blue), the jet upper shear layer (green) and the jet lower shear layer (yellow) are shown, together with the corresponding fits. This figure shows how the data points for the jet upper shear layer and jet lower shear layer and the corresponding fits are positioned in the jet. Note that in figure 8.17, the fit without shift is used for the jet upper shear layer.
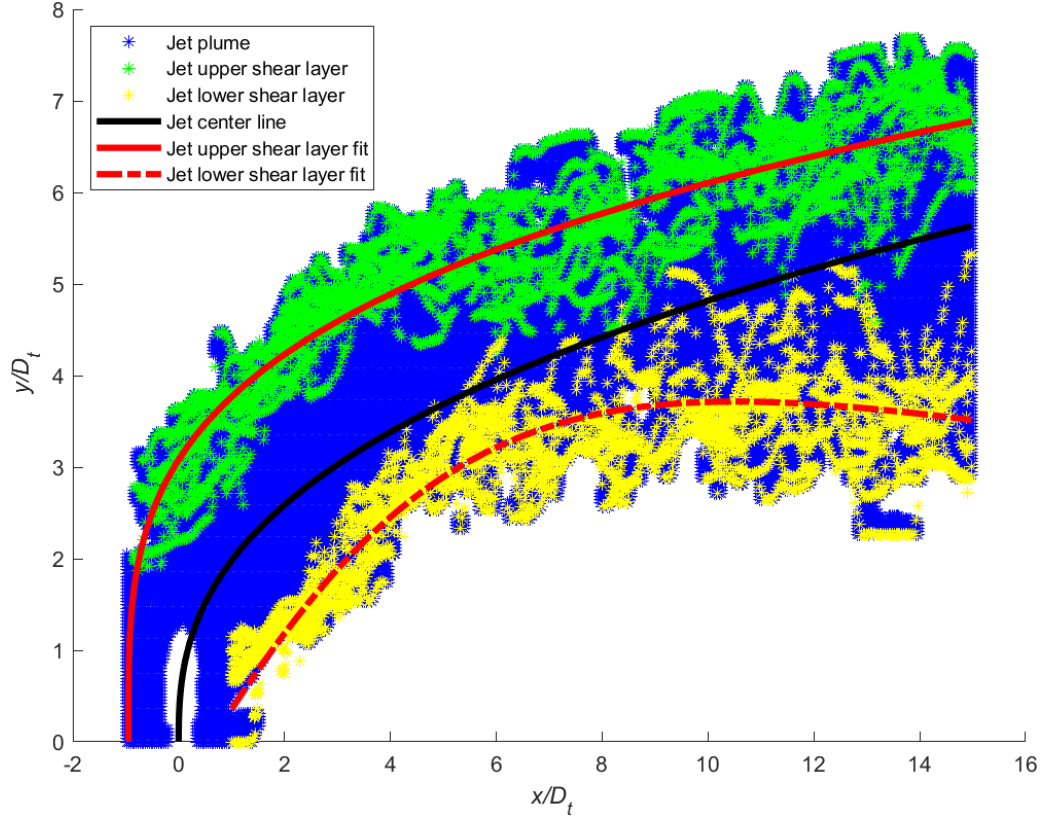
Figure 8.17: Jet plume (blue) with the data from 20 Schlieren images for the jet upper shear layer (green) and the jet lower shear layer (yellow). Note the stretching of the vertical axis. Included are fits for the jet center line (black), the jet upper shear layer (red solid) and the jet lower shear layer (red dash-dotted). $J = 2.8$, $S = 5.83$ and $M_c = 1.55$, see also figure 8.13.

It is observed that the jet upper shear layer has a variation in the bandwidth of the data around the fit. Near the jet orifice, the bandwidth is smaller than further downstream. For an investigation of the bandwidth of the jet upper shear layer, see section 8.2.2.3.

The far outliers for especially the jet lower shear layer are due to uncertainties in the acquisition of the data. In fact, the jet lower shear layer is not a normal shear layer such as the jet upper shear layer, but a combination of the two shear layers at the lower side of the jet, which feature a cross-section of the mushroom-shaped counter rotating vortex pair (see figure 5.1). That is the reason that it is harder to determine the lower side of the plume accurately and the reason behind the occurrence of outliers.

Summarizing, the general behaviour of the jet is in line with the observations in literature (chapter 4 and 5). The next sections detail the quantitative results of the jet upper shear layer, jet center line and jet lower shear layer.

8.2.2 Results for the Jet Upper Shear Layer

From the results shown in figures 8.10 to 8.12, it is clear that the jet has an initial bulging in upstream direction that causes a larger penetration height, i.e. the downstream jet penetrates deeper into the crossflow with decreasing slope. This is seen for all combinations of J and S considered. As elaborated in section 4.4, power functions are appropriate functions for describing the jet upper shear layer. This type of fits are used in the following.

In section 8.2.1, visual results of the jet behaviour have been presented and the behaviour of the jet was discussed qualitatively. In this section for the jet upper shear layer, fits for its position are found in section 8.2.2.1. Generalizations for S and J, and discussion are found in section 8.2.2.2. Subsequently, the bandwidth of the jet upper shear layer is investigated in section 8.2.2.3. Some concluding remarks are provided in section 8.2.2.4.

8.2.2.1 Quantification of the Location of the Jet Upper Shear Layer

An adequate penetration of the jet upper shear layer is important for a good mixing of the jet and the supersonic crossflow. Therefore, it is important to determine the penetration. For that purpose, least-squares fits of the location of the jet upper shear layer are found. The same procedure is performed for the fit without shift and for the fit with shift. For the fit without shift (equation 7.6), table 8.1 shows the values of the coefficients corresponding to $J = 2.8$ and $J = 3.8$, both for a number of values of S, together with the coefficient of determination (R^2) and the average penetration y_{avg}/D_t, as calculated by equation 7.11.

J	S	0	3.59	4.04	4.48	4.93	5.38	5.83	6.28	7.17	8.52	9.87
	c_1	2.602	3.303	3.854	3.642	3.805	3.362	3.128	3.764	3.533	3.919	3.357
	c_2	0.229	0.228	0.167	0.216	0.189	0.252	0.279	0.203	0.244	0.164	0.215
2.8	c_3	-0.555	-0.871	-0.538	-0.506	-0.508	-0.853	-0.950	-0.533	-0.505	-0.500	-0.180
	R^2	0.75	0.81	0.74	0.83	0.77	0.74	0.84	0.78	0.80	0.71	0.72
	$\frac{y_{avg}}{D_t}$	4.10	5.26	5.35	5.58	5.52	5.62	5.56	5.63	5.73	5.41	5.08
	c_1	2.887	3.670	4.092	4.231	4.247	4.374	3.708	3.682	4.863	4.403	3.965
	c_2	0.224	0.207	0.168	0.184	0.194	0.173	0.257	0.272	0.148	0.194	0.184
3.8	c_3	-0.758	-0.509	-0.543	-0.577	-0.612	-0.645	-1.168	-0.887	-0.433	-0.606	-0.499
	R^2	0.72	0.76	0.74	0.71	0.81	0.76	0.80	0.79	0.69	0.76	0.74
	$\frac{y_{avg}}{D_t}$	4.54	5.52	5.71	6.10	6.24	6.17	6.34	6.42	6.49	6.48	5.70

Table 8.1: Parameters of the fit for $y/D_t = c_1 \left(x/D_t - c_3\right)^{c_2}$, with $J = 2.8$ and $J = 3.8$ and $S \in [0 : 9.87]$. Data for the range $-1.0 \leq x/D_t \leq 15$ is used. The average penetration y_{avg}/D_t is calculated by equation 7.11.

Table 8.1 shows that the found fits are acceptable when looking at the coefficient of determination (R^2). It is investigated, whether the location of the jet upper shear layer can be described better by adding a constant term to the fit – the fit with shift. This shift makes that the power function is able to describe the bulging out behaviour of the jet better (equation 7.7). The results of a least-squares fit with shift are given in table 8.2 for $J = 2.8$ and $J = 3.8$, both for 11 values of S.

Comparing the results for $J = 2.8$ and $J = 3.8$ for both fits, shown in table 8.1 and table 8.2, respectively, some similarities and some differences become apparent. The average penetration y_{avg}/D_t is approximately the same for both fits at equal conditions. The differences are mostly within a margin of 0.02. Graphical results of the average penetration for all conditions, calculated by the fits in table 8.1 and table 8.2, are shown in figure 8.18 and figure 8.19, respectively. These figures show the average penetration for the fits of equation 7.6 and equation 7.7, respectively. For additional information, the average penetration for $J = 4.8$ combined with $S = 0$ and $S = 5.38$ is included in both figures.

Both figure 8.18 and figure 8.19 give an indication of the way how the average penetration depends on S and J. In De Maag's study [35], it was found that for a constant J, the average penetration had a maximum for a certain value of S, see figure 5.8. Due to the resolution in S, the precise maximum is hard to find, but the trend is clear. All found penetration depths for dual jet injection exceed that for single

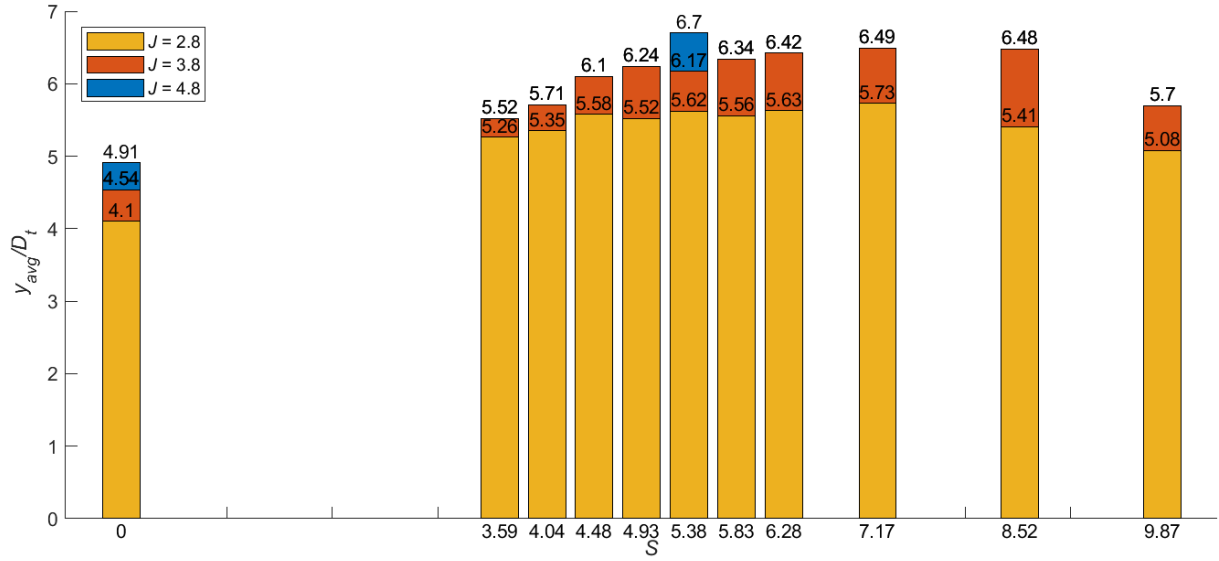Figure 8.18: Average penetration y_{avg}/D_t versus dual distance S calculated using $y/D_t =$ $c_1 \left(x/D_t - c_3 \right)^{c_2}$, for $J \in [2.8, 3.8, 4.8]$ and $M_c = 1.55$.
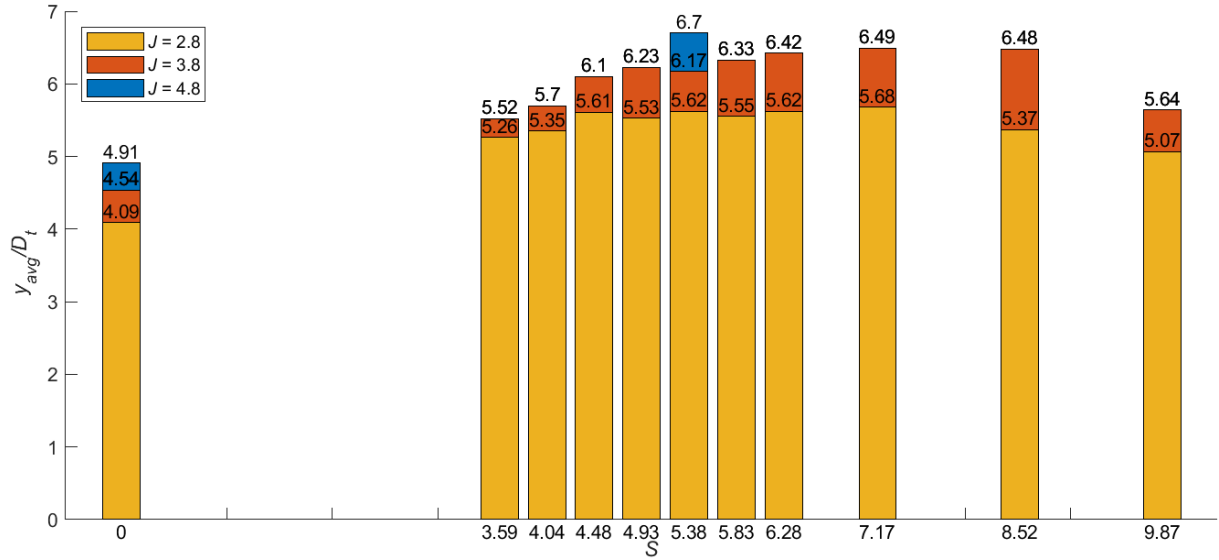

Figure 8.19: Average penetration y_{avg}/D_t versus dual distance S calculated using $y/D_t =$ $c_1 \left((x/D_t - c_3)^{c_2} + c_4 \right)$, for $J \in [2.8, 3.8, 4.8]$ and $M_c = 1.55$.

J	S	0	3.59	4.04	4.48	4.93	5.38	5.83	6.28	7.17	8.52	9.87
2.8	c_1	1.475	1.948	1.833	2.162	1.869	2.734	1.615	1.494	1.631	1.359	2.660
	c_2	0.354	0.320	0.330	0.360	0.346	0.281	0.409	0.399	0.431	0.395	0.265
	c_3	-0.696	-0.681	-0.744	-0.819	-0.631	-0.645	-0.618	-0.332	-0.639	-0.489	-0.288
	c_4	0.721	0.787	0.961	0.508	0.951	0.294	1.143	1.555	1.073	1.736	0.229
	R^2	0.76	0.80	0.76	0.85	0.77	0.74	0.84	0.79	0.81	0.71	0.71
	$\frac{y_{avg}}{D_t}$	4.09	5.26	5.35	5.61	5.53	5.62	5.55	5.62	5.68	5.37	5.07
3.8	c_1	1.881	1.431	1.399	2.875	2.196	2.330	1.218	2.402	2.285	1.983	1.049
	c_2	0.309	0.419	0.398	0.259	0.333	0.292	0.472	0.345	0.312	0.360	0.520
	c_3	-0.765	-0.776	-0.564	-0.711	-0.642	-0.646	-0.245	-0.536	-0.757	-0.528	-0.625
	c_4	0.534	1.490	1.842	0.434	0.872	0.849	2.644	0.676	0.953	1.209	2.463
	R^2	0.72	0.78	0.76	0.70	0.81	0.76	0.79	0.79	0.72	0.76	0.77
	$\frac{y_{avg}}{D_t}$	4.54	5.52	5.70	6.10	6.23	6.17	6.33	6.42	6.49	6.48	5.64

Table 8.2: Parameters of the fit for $y/D_t = c_1 \left((x/D_t - c_3)^{c_2} + c_4\right)$, with $J = 2.8$ and $J = 3.8$ and $S \in [0 : 9.87]$. Data for the range $-1.0 \leq x/D_t \leq 15$ is used. The average penetration y_{avg}/D_t is calculated by equation 7.11.

jet injection ($S = 0$). Somewhere in the range of $S = 5$ to $S = 7$, the maximum penetration is obtained. This is also observed in figure 8.18 and figure 8.19, but it appears that the maximum penetration is at a larger S for larger J.

Several differences are observed when comparing the fit results. It appears that, in general, the fits with shift have an approximately equal (margin of 0.01) or better coefficient of determination compared to the fits without shift. 5 out of 22 fits have a significantly better value of R^2 for the fit with shift.

Due to the extra degree of freedom c_4 in equation 7.7, the function is in all fits shifted in y-direction. That is why in general the values of c_2 are larger and the values for c_1 are lower for the fit with shift, compared to the fit without shift.

The differences between the two fits are made clear in figure 8.20 and figure 8.21. The two fits are shown in blue (fit without shift) and red (fit with shift). In figure 8.20, the two fits are coinciding almost everywhere. This behaviour is not a coincidence, it is recognizable for many other conditions.

However, in figure 8.21, the two fits do not fully coincide, i.e. the red fit has a larger slope in the function than the blue fit. Judging by the coefficient of determination, the red fit (fit with shift) has a better representation of the location of the jet upper shear layer.

Over the whole, both fits do almost coincide, though the fit with shift has a better representation.

In section 8.1, the results for the behaviour of the bow shocks in front of the two jets was analysed. As a result of the analysis, the question was raised whether there is a correlation between the merger point of the two bow shocks on the one hand, and penetration and the behaviour of the jet on the other hand. No clear change in behaviour of the jet is observed around the pivoting point whether the two bow shocks merge or remain spatially separated, despite the focus on the dual distances of the injection blocks around $S = 5$ in this study – corresponding to the pivoting value of S for which the bow shocks merge or not (for $J = 2.8$, $S_{pivot} = 4.87$, and for $J = 3.8$, $S_{pivot} = 5.36$). The merger point of the bow shocks is for the analysed conditions at significant higher values of y/D_t than penetration of the jet occurs. As a result, direct influence of the merger point is less likely. The largest increase of penetration with increasing S is observed up to S_{pivot}, but it is premature that this has a correlation with the merger point of the two bow shocks.

In the next section, a similarity analysis is performed for the fits of the location of the jet upper shear layer with respect to S. For the two fits, the same procedure is executed subsequently. Subsequently, the two scaled fits are compared and it is concluded, which fit is the preferred one. Finally, it is attempted to find a generalized expression of the location of the jet upper shear layer as function of x/D_t, S and J.

Figure 8.20: Two different fits for the location of the jet upper shear layer. The jet upper shear layer for every Schlieren image individually is marked with its own colour. The jet center line is drawn in black. ($J = 2.8$, $S = 5.83$ and $\mathrm{M}_c = 1.55$).
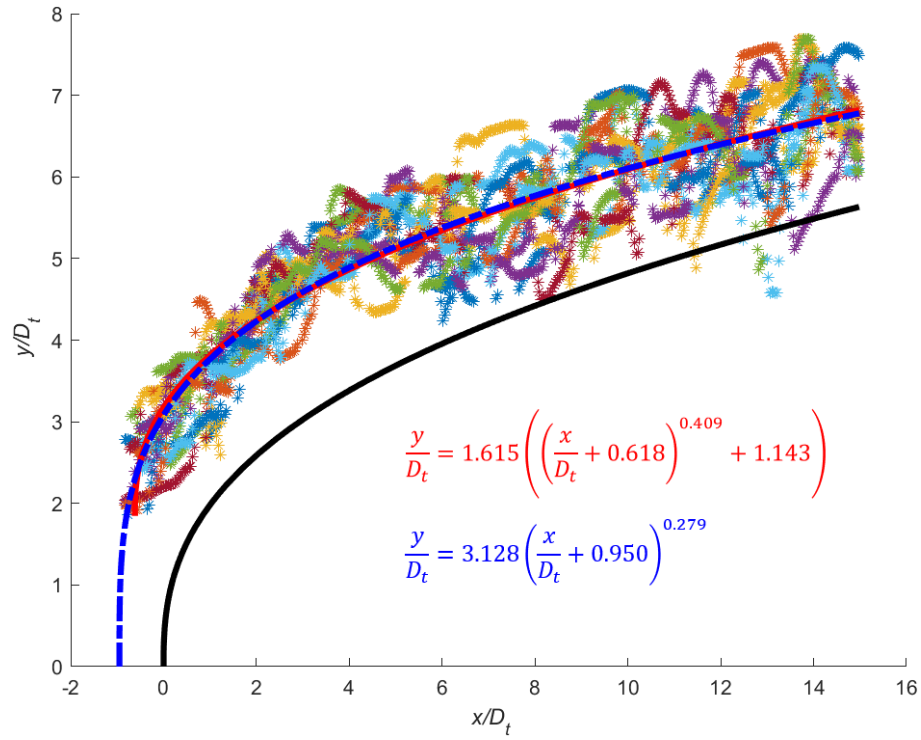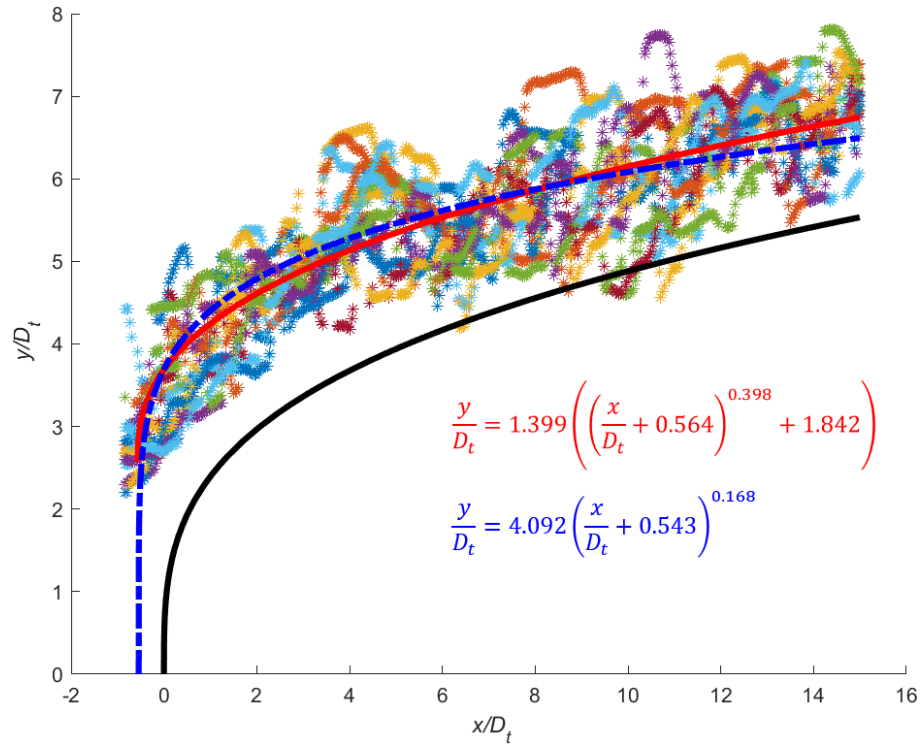

Figure 8.21: Two different fits for the location of the jet upper shear layer. The jet upper shear layer for every Schlieren image individually is marked with its own colour. The jet center line is drawn in black. ($J = 3.8$, $S = 4.04$ and $\mathrm{M}_c = 1.55$).

8.2.2.2   Scaling of the Location of the Jet Upper Shear Layer

Scaling of $y/D_t = c_1 (x/D_t - c_3)^{c_2}$

It is attempted to find similarities between the fits for a constant J, in order to find a single relation for the penetration y/D_t for different S. The fit without shift: $y/D_t = c_1 (x/D_t - c_3)^{c_2}$ (equation 7.6) is considered first. Then the same procedure is followed for the fit with shift: $y/D_t = c_1 ((x/D_t - c_3)^{c_2} + c_4)$ (equation 7.7). The idea is to fix coefficients that are similar for all values of S and keep variables that change with S free. When analysing the results in the tables of coefficients, in general, c_2 and c_3 are approximately in the same range for all fits of the same type and for the same J. Furthermore, c_1 appears to be a function of S.

For both $J = 2.8$ and $J = 3.8$, appropriate values for the coefficients of the fit of equation 7.6 that appear to be independent of S are chosen, based on the coefficients from table 8.1 and a trial-and-error process. When having fixed these coefficients, the least-squares method is executed again for finding the most appropriate fit. It is demanded that the coefficient of determination R^2 does not drop too much. A maximum drop of 0.05 is set, such that the fits still have a coefficient of determination in the range of $0.65 \leq R^2 \leq 0.85$.

The following coefficients are chosen to be constant:

J	2.8	3.8
c_2	0.20	0.19
c_3	-0.55	-0.78

Table 8.3: Fixed coefficients for $y/D_t = c_1 (x/D_t - c_3)^{c_2}$, based on the results of table 8.1.

When applying the fixed coefficients of table 8.3 and recalculating the least-squares fit for the two values of J, the coefficients, dependent on S, are shown in table 8.4, together with the coefficient of determination and the average penetration.

J	S	0	3.59	4.04	4.48	4.93	5.38	5.83	6.28	7.17	8.52	9.87
	c_1	2.761	3.530	3.602	3.745	3.722	3.781	3.772	3.787	3.862	3.636	3.388
2.8	R^2	0.73	0.81	0.74	0.81	0.77	0.73	0.82	0.77	0.75	0.71	0.67
	$\frac{y_{avg}}{D_t}$	4.10	5.25	5.35	5.57	5.53	5.62	5.61	5.63	5.74	5.40	5.03
	c_1	3.100	3.774	3.894	4.158	4.252	4.210	4.320	4.331	4.431	4.410	3.871
3.8	R^2	0.69	0.74	0.74	0.70	0.80	0.76	0.76	0.72	0.72	0.75	0.73
	$\frac{y_{avg}}{D_t}$	4.55	5.53	5.71	6.10	6.24	6.18	6.34	6.35	6.50	6.47	5.68

Table 8.4: Parameters of the fit for $y/D_t = c_1 (x/D_t - c_3)^{c_2}$, with $J = 2.8$ and $J = 3.8$ and $S \in [0 : 9.87]$. Data for the range $-1.0 \leq x/D_t \leq 15$ is used and the coefficients from table 8.3 are applied. The average penetration y_{avg}/D_t is calculated by equation 7.11.

When comparing the results in table 8.1 with those in table 8.4, some interesting differences and similarities appear. The average penetration determined for the fits are all very similar (within a margin of 0.05), except for one condition ($J = 3.8$ and $S = 6.28$), which has a larger difference. A graphical representation of this data is shown in figure 8.22.

The coefficients of determination for the fits in table 8.4 are lower or equal to the coefficients of determination for the fits in table 8.1. This was as expected, because in table 8.1, the best fit for that specific data set was sought, whereas in this section, a generalized solution is sought. However, the coefficients of determination are mostly within the range of a maximum drop of 0.05, which is assumed to be acceptable. In addition, all values of R^2 are still within the range of $0.67 \leq R^2 \leq 0.82$.

A generalization for $y/D_t = c_1 (x/D_t - c_3)^{c_2}$ is sought. The behaviour of the penetration as a function of S, in terms of c_1, appears to have a lower limit for $S = 0$ (single jet injection), and with increasing S, a maximum is found. The same correlation is found in the values of the average penetration, both in the present study and in [35]. The following generalized fit is found to describe the penetration of the jet upper shear layer as a function of S:
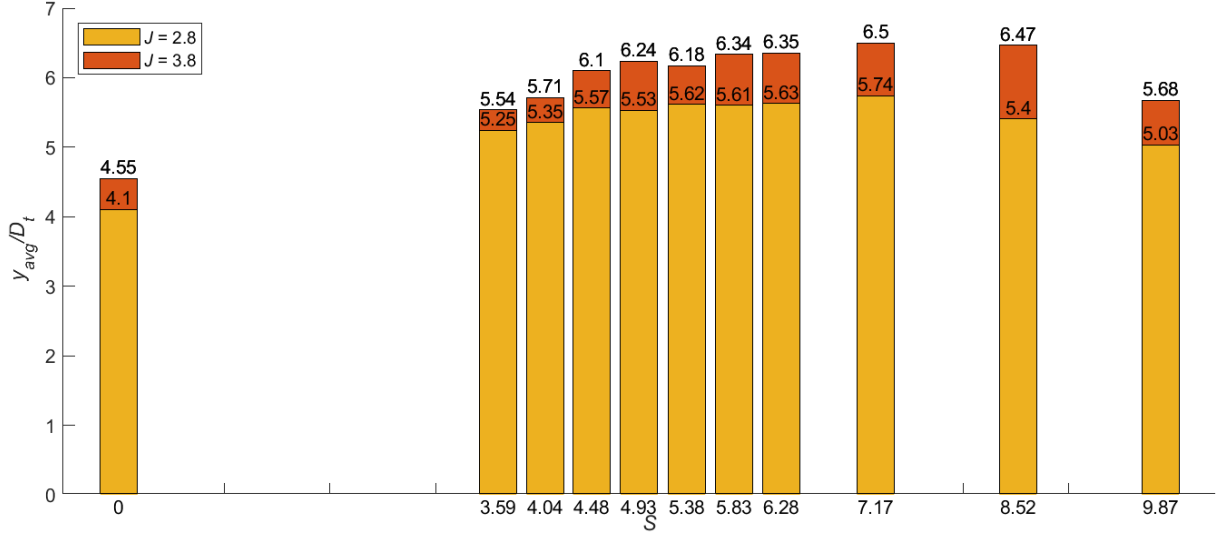
Figure 8.22: Average penetration y_{avg}/D_t versus dual distance S calculated for $y/D_t = c_1 \left(x/D_t - c_3 \right)^{c_2}$, for $J \in [2.8, 3.8]$ and $\mathrm{M}_c = 1.55$. The adjusted coefficients from table 8.3 and table 8.4 are used.

$$\frac{y}{D_t} = c_1(S) \left(\frac{x}{D_t} - c_3 \right)^{c_2} \tag{8.5}$$

Or, using similarity coordinates:

$$\frac{y}{D_t c_1(S)} = \left(\frac{x}{D_t} - c_3 \right)^{c_2} \tag{8.6}$$

In equation 8.5, coefficient $c_1(S)$ is expressed as:

$$c_1(S) = k_1 + k_4 \exp\left(-\frac{1}{2} \left(\frac{S - k_2}{k_3} \right)^2 \right) \tag{8.7}$$

Equation 8.7 contains a Gaussian distribution function. This function is chosen, because the average penetration as a function of S shows a similar behaviour. This was also observed in the results of De Maag [35].

In the expression for c_1, the new coefficients k_1 to k_4 are used. k_2 is equal to the value of S for which the maximum penetration occurs. k_3 is the so-called standard deviation of the Gaussian distribution function and k_1 and k_4 are amplification factors to be determined. The resulting function for c_1 is therefore a Gaussian distribution function with an asymptotic limit of k_1, and a maximum at $S = k_2$ of $c_1 = k_1 + k_4$. The full equation then becomes:

$$\frac{y}{D_t} = \left(k_4 \exp\left(-\frac{1}{2} \left(\frac{S - k_2}{k_3} \right)^2 \right) + k_1 \right) \left(\frac{x}{D_t} - c_3 \right)^{c_2} \tag{8.8}$$

The data sets for the location of the jet upper shear layer for every S at constant J are used for determining the coefficients k_1, k_2, k_3 and k_4; the other coefficients are initially fixed.

The least-squares method is applied to the data set of the data points for all values of S of the location of the jet upper shear layer, once for $J = 2.8$ and once for $J = 3.8$. A least-squares method provides a fit for y/D_t as a function of x/D_t and S. The following function is found as optimal fit for the data for $J = 2.8$:

$$\frac{y}{D_t} = \left(1.137 \exp\left(-\frac{1}{2} \left(\frac{S - 6.366}{3.191} \right)^2 \right) + 2.761 \right) \left(\frac{x}{D_t} + 0.55 \right)^{0.20} \tag{8.9}$$

The function $y/(D_t c_1(S))$, in which y/D_t is divided by c_1 in order to obtain similarity coordinates – similar to equation 8.6 –, has a coefficient of determination of 0.739, which is acceptable and in the same

range as the values of R^2 for the individual fits. It is logical that the value of R^2 for the generalized equation is lower than the mean of the values of R^2 of the individual fits, because a compromise has to be found for 11 conditions of S and the generalized fit cannot be as good as the individual fits. However, the result is still acceptable and provides insight into possibilities for scaling by S.

For $J = 3.8$, a similar expression is found:

$$\frac{y}{D_t} = \left(1.432 \exp\left(-\frac{1}{2}\left(\frac{S - 6.952}{2.893}\right)^2\right) + 3.100\right)\left(\frac{x}{D_t} + 0.78\right)^{0.19} \tag{8.10}$$

Also for this function for $y/(D_t c_1(S))$, an acceptable coefficient of determination of 0.715 is obtained, which is also in the range of the values of R^2 obtained for the individual fits.

As an overview, figure 8.23 shows the behaviour of $c_1(S)$ and table 8.5 shows the coefficients for the fit for $J = 2.8$ and $J = 3.8$.
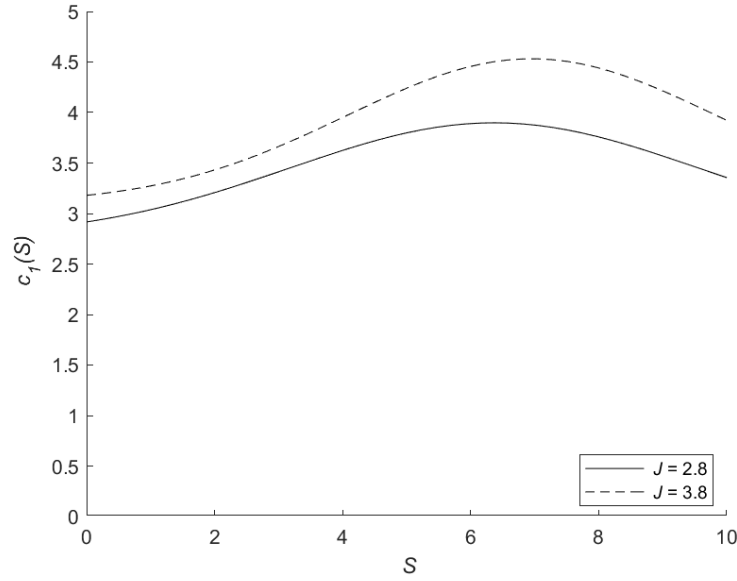

Figure 8.23: Plot of the expressions for $c_1(S)$, found for $J = 2.8$ and $J = 3.8$, as shown in equation 8.9 and equation 8.10, respectively.

J	2.8	3.8
c_2	0.20	0.19
c_3	-0.55	-0.78
k_1	2.761	3.100
k_2	6.366	6.952
k_3	3.191	2.893
k_4	1.137	1.432
R^2	0.739	0.715

Table 8.5: Coefficients for the fit of data for the location of the jet upper shear layer: $y/D_t = \left(k_4 \exp\left(-\frac{1}{2}\left((S - k_2)/k_3\right)^2\right) + k_1\right)(x/D_t - c_3)^{c_2}$, see equation 8.9 and equation 8.10.

The quality of the scaling is further investigated as following. Figure 8.25 and figure 8.27 show scalings of the fits, using the coefficients from table 8.3 and table 8.4. The fits are scaled by $c_1(S)$ (equation 8.7 with the coefficients from table 8.5). Figure 8.25 and figure 8.27 show that the similarity analysis of the fits is appropriate.

Further investigation is done by a similarity analysis of the data sets for the location of the jet upper shear layer. Figure 8.24 and figure 8.26 show the points in the jet upper shear layer for all measurements for $J = 2.8$ and $J = 3.8$, respectively, scaled by $c_1(S)$. For both values of J, a reasonable cloud of data
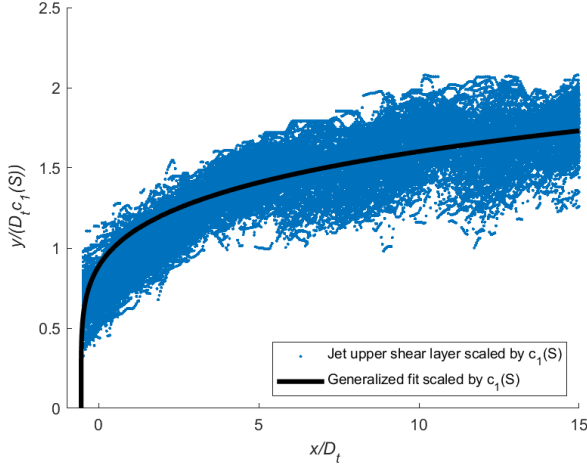
points is obtained around the scaled fit.

Figure 8.24: Location of the jet upper shear layer (blue) and the generalized fit (black), both scaled by $c_1(S)$ for $J = 2.8$, $S \in [0 : 9.87]$, $\mathrm{M}_c = 1.55$. The data stem from 20 Schlieren images per (J, S) combination.

Figure 8.25: Fits for the location of the jet upper shear layer from table 8.3 and table 8.5 (red), and the generalized fit (black), both scaled by $c_1(S)$ for $J = 2.8$, $S \in [0 : 9.87]$, $\mathrm{M}_c = 1.55$.
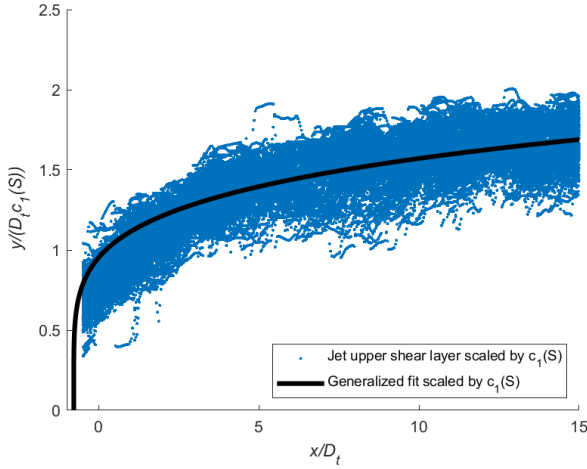
Figure 8.26: Location of the jet upper shear layer (blue) and the generalized fit (black), both scaled by $c_1(S)$ for $J = 3.8$, $S \in [0 : 9.87]$, $\mathrm{M}_c = 1.55$. The data stem from 20 Schlieren images per (J, S) combination.
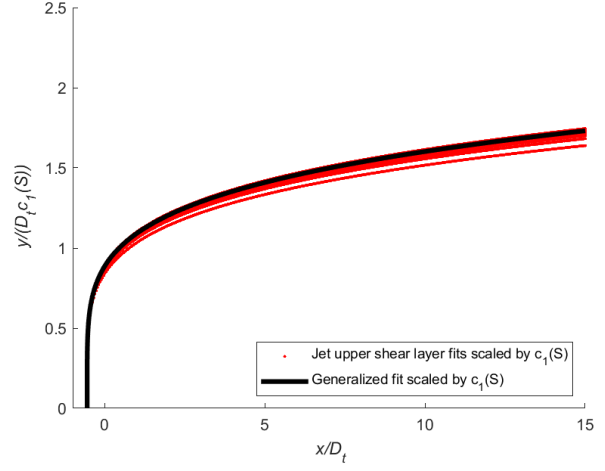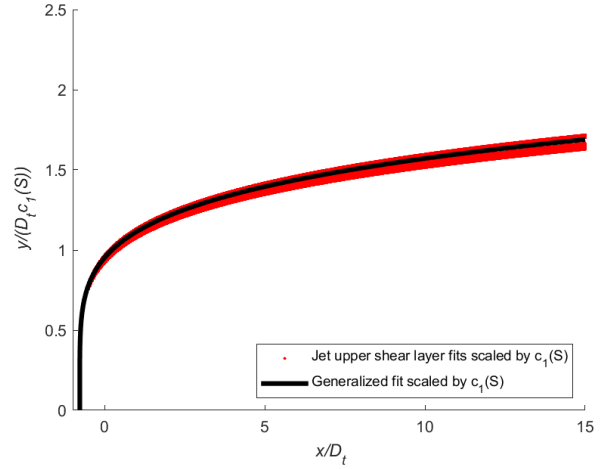

Figure 8.27: Fits for the location of the jet upper shear layer from table 8.3 and table 8.5 (red), and the generalized fit (black), both scaled by $c_1(S)$ for $J = 3.8$, $S \in [0 : 9.87]$, $\mathrm{M}_c = 1.55$.

The scaling of the y-coordinate with $\left(k_4 \exp\left(-\frac{1}{2} \left((S - k_2)/k_3 \right)^2 \right) + k_1 \right)$ appears to be appropriate for the values of S that are measured. A theoretical investigation is performed in the following for validation of the results. Imagine the two tandem jet orifices ($D_1 = 1$ mm and $D_2 = 2$ mm) with a total diameter of $D_t = 2.23$ mm. If the dual distance $S = 0$, then the two orifices are combined to one orifice with diameter D_t. This was elaborated before.

When increasing S, the downstream jet will at first be positioned in the so-called quasi-stagnant zone (see section 5.1), and will subsequently be in the zone of reattaching supersonic flow. The larger S, the more time the flow has to recover to supersonic conditions. When imagining $S \to \infty$, the crossflow in front of the downstream jet has the same conditions as the crossflow in front of the upstream jet [9].

In that case, the two jets behave as two independent jets that have no influence on each other. The penetration of the main jet is then equal to that of single jet injection with an orifice diameter of 2 mm. This diameter is smaller than D_t and consequently, the penetration for $S \to \infty$ is smaller than the penetration for $S = 0$. As a result, c_1 has to be equal to k_1 for $S \to \infty$. This condition was not investigated, but it should be done in order to describe the behaviour of the location of the jet upper shear layer for the full domain of $0 \leq S \leq \infty$ correctly.

Still some questions remain, such as: How large is the difference between the penetration for $S = 0$ and for $S \to \infty$? What is the behaviour of the penetration depth for $S > 10$ and for what value of S do the two jets behave as two jets that do not affect each other? Moreover, is it actually possible to combine the results of the location of the jet upper shear layer for single jet injection and dual jet injection, or is this behaviour fundamentally different, such that these conditions should be treated separately? When having more knowledge about this behaviour for especially $S > 10$, a more robust proposal for a scaling can be formulated for the full domain. However, for the domain $0 \leq S \leq 10$, the scaling by $\left(k_4 \exp\left(-\frac{1}{2} \left((S - k_2)/k_3 \right)^2 \right) + k_1 \right)$ appeared to be very appropriate.

In the next section, the same scaling process is performed for $y/D_t = c_1 \left((x/D_t - c_3)^{c_2} + c_4 \right)$ and subsequently, the results of both scalings are compared.

Scaling of $y/D_t = c_1 \left((x/D_t - c_3)^{c_2} + c_4 \right)$

The same procedure as for the fit without shift is applied to the fit with shift. Again, similarities between coefficients for different values of S at constant J are sought. After a trial-and-error process, c_2, c_3 and c_4 are found to be in the same range for all values of S at a constant J. For both $J = 2.8$ and $J = 3.8$, the values for these coefficients are fixed, requiring that the coefficient of determination does not decrease too much. The same norms as for the fit without shift are used, which means that a maximum drop of 0.05 for the coefficient of determination is allowed and the coefficients of determination have to be in the range of $0.65 \leq R^2 \leq 0.85$.

The following coefficients are chosen to be constant:

J	2.8	3.8
c_2	0.35	0.32
c_3	-0.70	-0.68
c_4	0.80	0.80

Table 8.6: Fixed coefficients for $y/D_t = c_1 \left((x/D_t - c_3)^{c_2} + c_4 \right)$, based on the results of table 8.2.

When applying the fixed coefficients of table 8.6 to the fit with shift and recalculating the least-squares fit for both $J = 2.8$ and $J = 3.8$, the resulting coefficients dependent on S, together with the coefficients of determination and the average penetration are listed in table 8.7.

J	S	0	3.59	4.04	4.48	4.93	5.38	5.83	6.28	7.17	8.52	9.87
	c_1	1.444	1.853	1.885	1.970	1.951	1.979	1.964	1.981	2.016	1.887	1.777
2.8	R^2	0.75	0.80	0.75	0.84	0.76	0.73	0.84	0.79	0.78	0.70	0.67
	$\frac{y_{avg}}{D_t}$	4.10	5.26	5.35	5.59	5.53	5.61	5.57	5.62	5.72	5.35	5.04
	c_1	1.674	2.037	2.105	2.247	2.297	2.277	2.339	2.359	2.390	2.390	2.093
3.8	R^2	0.71	0.77	0.76	0.69	0.81	0.75	0.78	0.75	0.72	0.76	0.76
	$\frac{y_{avg}}{D_t}$	4.54	5.52	5.71	6.09	6.23	6.17	6.34	6.40	6.48	6.48	5.68

Table 8.7: Parameters of the fit for $y/D_t = c_1 \left((x/D_t - c_3)^{c_2} + c_4 \right)$, with $J = 2.8$ and $J = 3.8$, for $S \in [0 : 9.87]$. Data for the range $-1.0 \leq x/D_t \leq 15$ is used and the coefficients from table 8.6 are applied. The average penetration y_{avg}/D_t is calculated using equation 7.11.

Table 8.2 and table 8.7 are compared with each other. The average penetration as calculated shows for both tables similar behaviour and the values deviate within the range of 0.04 from each other. In figure 8.28, a graphical representation of the average penetration is shown.
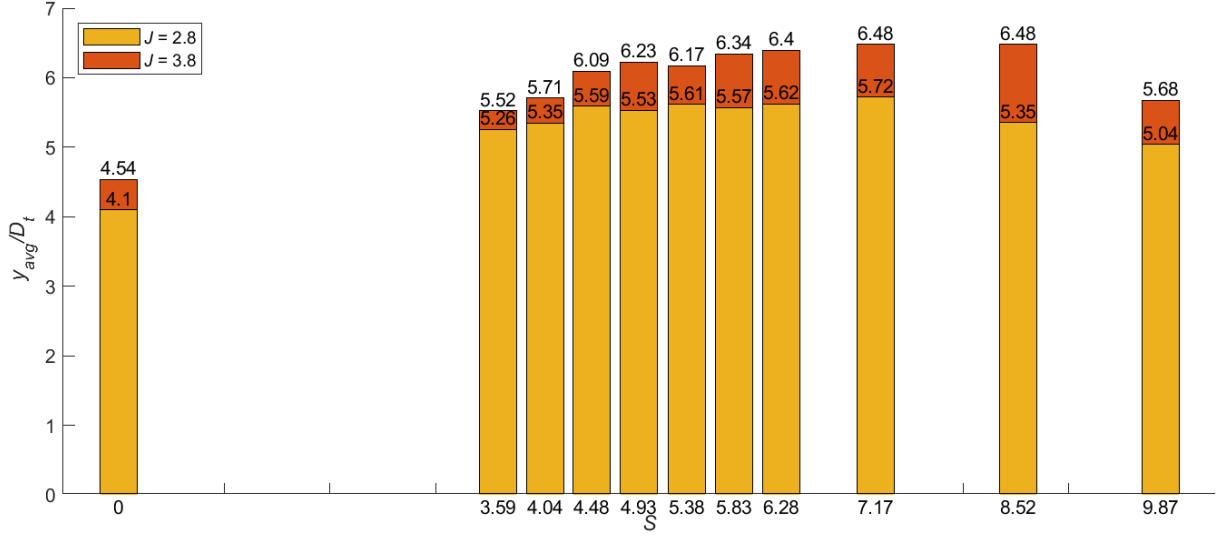
Figure 8.28:   Average penetration y_{avg}/D_t versus dual distance S calculated for $y/D_t = c_1 \left((x/D_t - c_3)^{c_2} + c_4\right)$, for $J \in [2.8, 3.8]$ and $\mathrm{M}_c = 1.55$. The adjusted coefficients from table 8.6 and table 8.7 are used.

As expected, the coefficients of determination in table 8.7 are lower or equal compared to the values in table 8.2. The largest drop is 0.04 (for $J = 2.8$, $S = 9.87$ and $J = 3.8$, $S = 6.28$), so all R^2 values of the fits are within the allowed range. No clear trends are observed in the degradation of the coefficients of determination and all values of R^2 are within the range $0.67 \leq R^2 \leq 0.84$.

The next step is to find a generalization for $y/D_t = c_1 \left((x/D_t - c_3)^{c_2} + c_4\right)$, valid for all S. At constant J, c_2, c_3 and c_4 are fixed and only c_1 is a function of S. The same function for c_1 as used for the fit without shift is applied to the fit with shift, resulting in:

$$\frac{y}{D_t} = \left(k_4 \exp\left(-\frac{1}{2} \left(\frac{S - k_2}{k_3} \right)^2 \right) + k_1 \right) \left(\left(\frac{x}{D_t} - c_3 \right)^{c_2} + c_4 \right) \tag{8.11}$$

The function for $c_1(S)$ containing a Gaussian distribution function with coefficients k_1 to k_4 are applied similar to the fit without shift: k_2 is the value of S at which the penetration is maximal, k_3 is the standard deviation of the Gaussian distribution and k_1 and k_4 are amplification factors.

The full data sets for the jet upper shear layer for every S at constant J are used for the fit of equation 8.11, with c_2, c_3, c_4 fixed and k_1, k_2, k_3 and k_4 to be determined. A least-squares method is used for the fit of y/D_t as a function of x/D_t and S. The result for $J = 2.8$ is:

$$\frac{y}{D_t} = \left(0.598 \exp\left(-\frac{1}{2} \left(\frac{S - 6.370}{3.209} \right)^2 \right) + 1.444 \right) \left(\left(\frac{x}{D_t} + 0.70 \right)^{0.35} + 0.80 \right) \tag{8.12}$$

This scaled equation has an acceptable coefficient of determination of 0.744, which is in the same range as values of R^2 for the individual fits.

Similarly, for $J = 3.8$, the following expression is obtained:

$$\frac{y}{D_t} = \left(0.781 \exp\left(-\frac{1}{2} \left(\frac{S - 6.954}{2.914} \right)^2 \right) + 1.674 \right) \left(\left(\frac{x}{D_t} + 0.68 \right)^{0.32} + 0.80 \right) \tag{8.13}$$

Also this generalized function has an acceptable coefficient of determination, which is equal to 0.733. Again, this is in the same range of the values of R^2 for the individual fits.

As an overview, the expressions of $c_1(S)$ for $J = 2.8$ and $J = 3.8$ are shown in figure 8.29 and the coefficients and values of R^2 of the generalized functions are shown in table 8.8.

Also for this generalized fit, the quality of the scaling is further investigated in figure 8.31 and figure 8.33. These figures show scalings of the functions from table 8.6 and table 8.7, with the functions divided
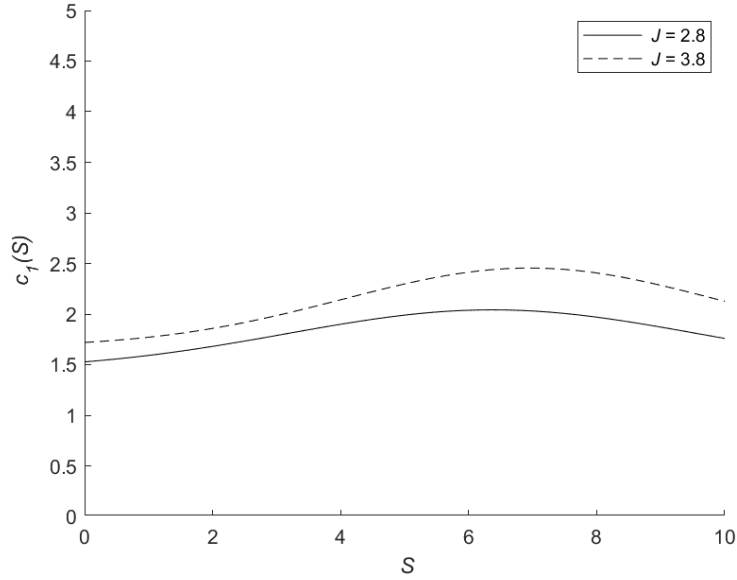
Figure 8.29: Plot of the expressions for $c_1(S)$, found for $J = 2.8$ and $J = 3.8$, as shown in equation 8.12 and equation 8.13, respectively.

J	2.8	3.8
c_2	0.35	0.32
c_3	-0.70	-0.68
c_4	0.80	0.80
k_1	1.444	1.674
k_2	6.370	6.954
k_3	3.209	2.914
k_4	0.598	0.781
R^2	0.744	0.733

Table 8.8: Coefficients for $y/D_t = \left(k_4 \exp\left(-\frac{1}{2}\left((S - k_2)/k_3\right)^2\right) + k_1\right)\left((x/D_t - c_3)^{c_2} + c_4\right)$, from equation 8.12 and equation 8.13.

by $c_1(S)$, such that every fit should collapse on $y/(D_t c_1(S)) = (x - c_3)^{c_2} + c_4$. Figure 8.31 and figure 8.33 show that the scaling for both $J = 2.8$ and $J = 3.8$ turns out to be appropriate.

Furthermore, the data sets for the jet upper shear layer are scaled in a similar manner as the fits. As a result, a reasonable cloud of points is obtained around the fit for $S = 0$ in both figure 8.30 and figure 8.32.

In the next section, the results for the fits with and without shift are compared.

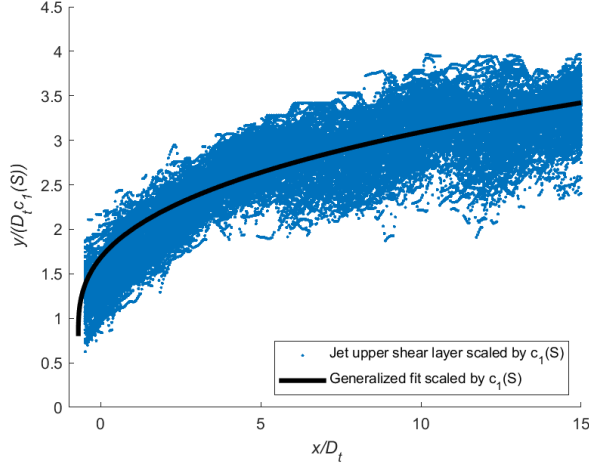Figure 8.30: Location of the jet upper shear layer (blue) and the generalized fit (black), both scaled by $c_1(S)$ for $J = 2.8$, $S \in [0 : 9.87]$, $M_c = 1.55$. The data stem from 20 Schlieren images per (J, S) combination.

Figure 8.31: Fits for the location of the jet upper shear layer from table 8.6 and table 8.8 (red), and the generalized fit (black), both scaled by $c_1(S)$ for $J = 2.8$, $S \in [0 : 9.87]$, $M_c = 1.55$.

Figure 8.32: Location of the jet upper shear layer (blue) and the generalized fit (black), both scaled by $c_1(S)$ for $J = 3.8$, $S \in [0 : 9.87]$, $M_c = 1.55$. The data stem from 20 Schlieren images per (J, S) combination.
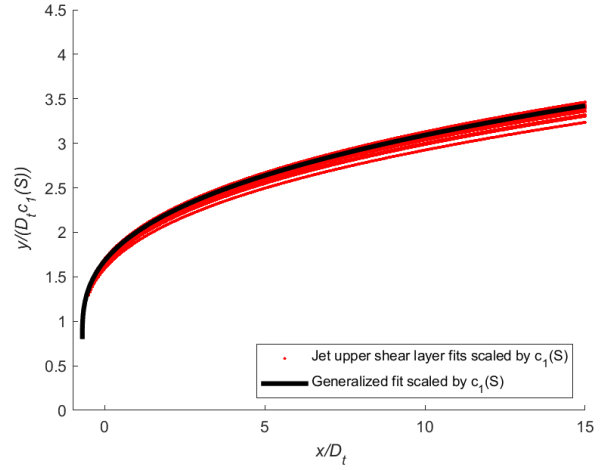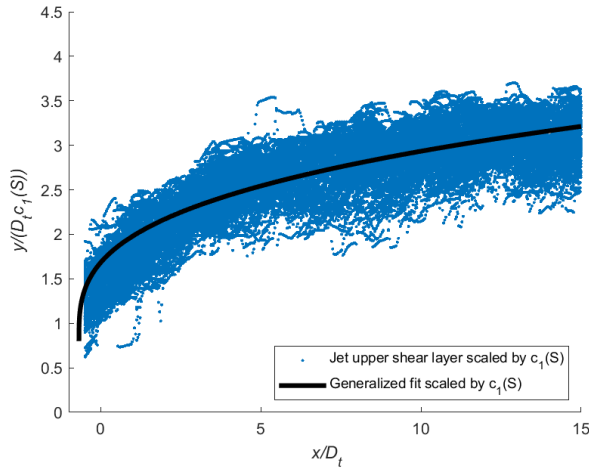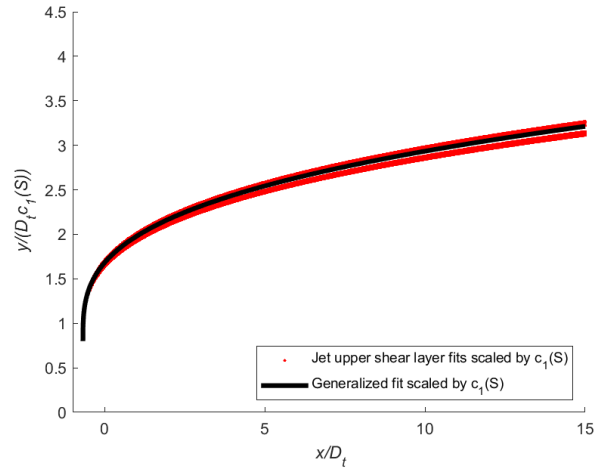

Figure 8.33: Fits for the location of the jet upper shear layer from table 8.6 and table 8.8 (red), and the generalized fit (black), both scaled by $c_1(S)$ for $J = 3.8$, $S \in [0 : 9.87]$, $M_c = 1.55$.

Comparison of the scalings

In the preceding sections, the fits for the location of the jet upper shear layer with and without shift were investigated and scaled. In this study, a relevant question is whether the fit with shift improves the description of the location of the jet upper shear layer significantly.

First of all, it should be realized that the fit with shift has an extra degree of freedom, that can give a larger range for the values of the coefficients than would be the case for the fit without shift. Figure 8.20 shows that the appearance of both fits is similar, but having different coefficients. As a result, it is important to consider that similarities between fits are less straight-forward without a thorough analysis (compare table 8.2 with table 8.6). With respect to this, in case the two fits have equal quality, the fit without shift would in general be more convenient.

When having a closer look at the coefficients c_2, c_3 and c_4 of the fit without shift and the fit with shift, it appears that the coefficients of the fit with shift do not change much with J. Therefore, the

coefficients c_2, c_3 and c_4 appear to be independent of J for the fit with shift. This does not hold for the fit without shift, because in that case, c_3 has larger changes with J. Therefore, a scaling for J could possibly be obtained easier for the fit with shift than for the fit without shift.

Next, the results of the scalings are investigated. From table 8.5 and table 8.8, it can be seen that certain coefficients have about the same values for both generalized fits. At constant J, the values for k_2 and k_3 are (almost) equal for both fits. In addition, the coefficient c_3 is for all fits in the range $-0.78 \leq c_3 \leq -0.55$. These three coefficients determine the position of x/D_t and S at which characteristics of the penetration (maximum penetration, spreading of the penetration around maximum value, origin) are obtained. Therefore, it is as expected that k_2, k_3 and c_3 are in the same range. The other coefficients (c_2, c_4, k_1 and k_4) are different for the two fits, but provide similar behaviour.

In figure 8.20 and figure 8.21, characteristic examples were shown for the two fits. From these figures, it was concluded that sometimes the two fits collapse, and that sometimes the fit with shift provides a better description of the location of the jet upper shear layer than the fit without shift. The same conclusion follows from the coefficients of determination in the preceding sections, from which a summarizing overview is given in table 8.9.

		$y/D_t = c_1 \left(x/D_t - c_3\right)^{c_2}$	$y/D_t = c_1 \left(\left(x/D_t - c_3\right)^{c_2} + c_4\right)$
	Range before generalization	$0.705 \leq R^2 \leq 0.843$	$0.713 \leq R^2 \leq 0.850$
$J = 2.8$	Range after generalization	$0.669 \leq R^2 \leq 0.815$	$0.674 \leq R^2 \leq 0.837$
	$R^2_{generalized}$ for $y/(D_t c_1)$	0.738	0.744
	Range before generalization	$0.693 \leq R^2 \leq 0.813$	$0.701 \leq R^2 \leq 0.807$
$J = 3.8$	Range after generalization	$0.693 \leq R^2 \leq 0.800$	$0.692 \leq R^2 \leq 0.807$
	$R^2_{generalized}$ for $y/(D_t c_1)$	0.715	0.733

Table 8.9: Coefficients of determination for the fit without shift and the fit with shift, for both $J = 2.8$ and $J = 3.8$. The range of R^2 for the individual fits and the value of R^2 for the generalized fits are given.

The summary in table 8.9 shows that in general, the fit with shift has a better coefficient of determination for the ranges of all fits both before and after generalization. Furthermore, it appears that the individual fits show on average a smaller drop in the R^2 values for the fit with shift compared to the drop of the values of R^2 for the fit with shift (see tables 8.1 and 8.4, and tables 8.2 and 8.7). This shows that the fit with shift has a more robust behaviour.

For further investigation, for every fit and every value of J, the values of y/D_t are divided by the corresponding function. The result should be 1 for points on the curve, and a cloud around 1 is formed, corresponding to the data points that are not on the curve. Figure 8.34 shows a box plot of this scaling and gives an indication of the spreading of the cloud. Table 8.10 shows the corresponding characteristic values. The data sets for both $J = 2.8$ and $J = 3.8$ contain around $60 \cdot 10^3$ data points.

	$J = 2.8$		$J = 3.8$	
	Fit without shift	Fit with shift	Fit without shift	Fit with shift
Minimum	0.465	0.453	0.371	0.388
Lower adjacent	0.656	0.665	0.682	0.691
25th percentile	0.907	0.912	0.917	0.922
Median	0.998	1.001	1.003	1.006
75th percentile	1.074	1.077	1.075	1.076
Upper adjacent	1.323	1.320	1.308	1.306
Maximum	1.691	1.438	1.357	1.340

Table 8.10: Numerical values of the box plot of figure 8.34.

A median close to 1 and the smallest box and whiskers are characteristics of the best scaling. All fits have a median close to 1, with a margin of 0.06 maximally. It appears that the 75th percentile and the upper adjacent are approximately equal for the fits for a specific J, but that the 25th percentile and lower adjacent improve for the fit with shift compared to the fit without shift. In addition, at the upper side in the case of $J = 2.8$, there are less outliers for the fit with shift than for the fit without shift.
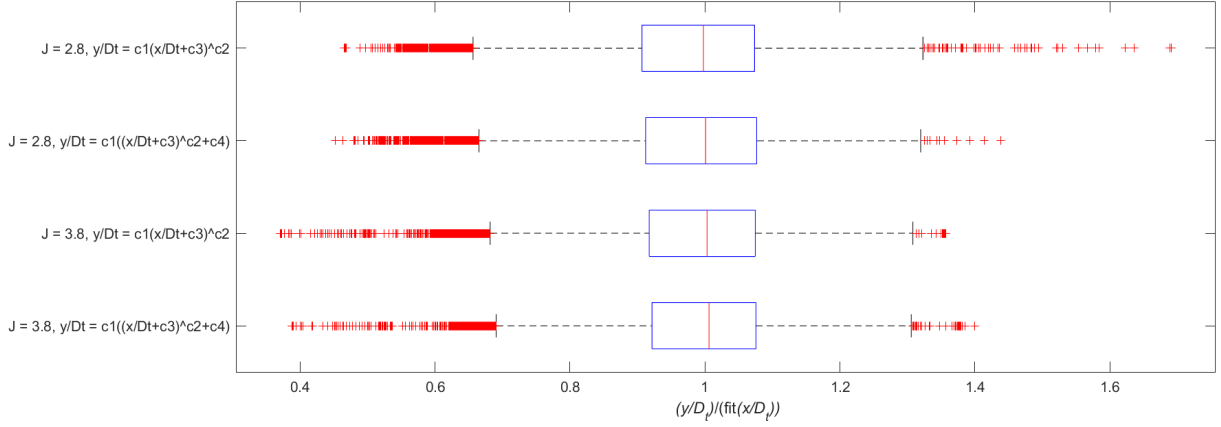
Figure 8.34: Boxplots of the scaling of the data by the generalized equation. The center of the jet upper shear layer is scaled to 1. Dual distance $S \in [0 : 9.87]$, $J \in [2.8, 3.8]$ and $M_c = 1.55$ are used. A box with the 25th and 75th percentile is used and whiskers covering $\pm 2.7\sigma$. The median is the red line inside the box and the outliers are marked as a red +-sign.

Summarizing, the fits with shift achieve a better collapse of the cloud of points.

   Taking everything into consideration, it is concluded that the fit with shift (equation 7.7) has a significantly and consistently better performance than the fit without shift (equation 7.6). The advantages outweigh the disadvantages. Therefore, it is recommended to use the fit with shift. However, with the side note that parameter control is important in order to keep similarities between coefficients for fits with different conditions in sight, which is important for similarity analyses.
   The next section elaborates on a scaling in terms of J of the location of the jet upper shear layer.

Generalization of $y/D_t = c_1 \left((x/D_t - c_3)^{c_2} + c_4 \right)$ for x/D_t, J and S

The fit with shift appeared to have the best performance for describing the location of the jet upper shear layer. Another advantage of this fit is that the coefficients c_2, c_3 and c_4 for $J = 2.8$ and for $J = 3.8$, although determined independently, are almost equal. Therefore, it is worthwhile investigating whether a function could be found for y/D_t as function of x/D_t in which J is included as variable.

   First, generic values for c_2, c_3 and c_4 are determined. Starting from the coefficients in table 8.8, a trial-and-error process was performed. Rounded numbers were preferred if appropriate. In the end, the following equation was determined:

$$\frac{y}{D_t} = c_1(J, S) \left(\left(\frac{x}{D_t} + 0.68 \right)^{0.333} + 0.80 \right) \tag{8.14}$$

   which means that $c_2 = 0.333$, $c_3 = -0.68$ and $c_4 = 0.80$. c_1 is a function of S – as shown in the preceding sections – and appears to be a function of J as well. The equation for $c_1(J, S)$, based on the preceding sections, is:

$$c_1(J, S) = k_1(J) + k_4(J) \exp \left(-\frac{1}{2} \left(\frac{S - k_2(J)}{k_3(J)} \right)^2 \right) \tag{8.15}$$

   In the equation above, k_1 to k_4 may be a function of J. In the next step, the least-squares method is applied for finding the coefficients k_1 to k_4 in $c_1(J, S)$ for $J = 2.8$ and for $J = 3.8$ separately. The resulting equations for $c_1(J = 2.8, S)$ and $c_1(J = 3.8, S)$ are:

$$c_1(J = 2.8, S) = 1.392 + 0.693 \exp \left(-\frac{1}{2} \left(\frac{S - 6.365}{3.569} \right)^2 \right) \tag{8.16}$$

$$c_1(J = 3.8, S) = 1.598 + 0.801 \exp\left(-\frac{1}{2}\left(\frac{S - 6.951}{3.044}\right)^2\right) \tag{8.17}$$

The equation for $y/(D_t c_1(J = 2.8, S))$ has a coefficient of determination of $R^2 = 0.743$ and the equation for $y/(D_t c_1(J = 3.8, S))$ has a coefficient of determination of $R^2 = 0.733$. Both data sets consist of results for $S \in [0 : 9.87]$, $M_c = 1.55$ and the domain $-0.5 \le x/D_t \le 15$. These values for R^2 are a little lower or equal compared to previously determined values for R^2 for equation 8.12 and equation 8.13, respectively. However, that is logical, because a compromise had to be found for the values of c_2 and c_3, which would hold for both values of J. Still, the values of R^2 are quite acceptable.

Only for two values of J, results were obtained for a full range of eleven values of S, which renders much uncertainty to an expression for the jet upper shear layer as a function of J. However, still an attempt is made to formulate such an expression.

From literature and preceding results, it is likely that the coefficients k_1 to k_4 that depend on J are in the form of power-functions. Therefore, it is attempted to come up with an expression for c_1, in which the coefficients are replaced by a power-function of J: $k_i = b_{2i-1}J^{b_{2i}}$. Substitution results in:

$$c_1(J, S) = b_1 J^{b_2} + b_7 J^{b_8} \exp\left(-\frac{1}{2}\left(\frac{S - b_3 J^{b_4}}{b_5 J^{b_6}}\right)^2\right) \tag{8.18}$$

Based on the coefficients of equation 8.16 and equation 8.17, the coefficients of equation 8.18 can be calculated directly. The resulting function $c_1(J, S)$ then evolves as:

$$c_1(J, S) = 0.874 J^{0.452} + 0.425 J^{0.474} \exp\left(-\frac{1}{2}\left(\frac{S - 4.732 J^{0.288}}{6.103 J^{-0.521}}\right)^2\right) \tag{8.19}$$

The terms expressing $b_1 J^{b_2}$ and $b_7 J^{b_8}$ appear to have a ratio that is approximately fixed, equal to 2. Therefore, equation 8.19 is rewritten and simplified to:

$$c_1(J, S) = 0.432 J^{0.461}\left(2 + \exp\left(-\frac{1}{2}\left(\frac{S - 4.732 J^{0.288}}{6.103 J^{-0.521}}\right)^2\right)\right) \tag{8.20}$$

This is the final expression for $c_1(J, S)$. Substitution of $c_1(J, S)$ in the expression for y/D_t results in a description of the location of the jet upper shear layer as a function of x/D_t, J and S:

$$\frac{y}{D_t}\left(\frac{x}{D_t}; J, S\right) = 0.432 J^{0.461}\left(2 + \exp\left(-\frac{1}{2}\left(\frac{S - 4.732 J^{0.288}}{6.103 J^{-0.521}}\right)^2\right)\right)\left(\left(\frac{x}{D_t} + 0.68\right)^{0.333} + 0.80\right) \tag{8.21}$$

In the following, the quality of equation 8.21 is investigated and compared to the previously determined functions for y/D_t for $J = 2.8$ (equation 8.16) and $J = 3.8$ (equation 8.17).

Figure 8.35 shows the data for $J \in [2.8, 3.8]$, $S \in [0 : 9.87]$ and $M_c = 1.55$, as $y/(D_t c_1(J, S))$ plotted versus x/D_t. In the same figure, equation 8.21 divided by $c_1(J, S)$ (equation 8.20) is plotted. Similar to the results shown in figure 8.30 and figure 8.32, a cloud of points is obtained around the fit. The coefficient of determination for this full data set is $R^2 = 0.739$, which is approximately the mean of the coefficients of determination for the individual fits of $y/(D_t c_1(J = 2.8, S))$ and $y/(D_t c_1(J = 3.8, S))$ (equation 8.16 and equation 8.17, respectively). Therefore, this generalized equation $y/D_t(x/D_t, J, S)$ is equally acceptable as the individual fits, for $J \in [2.8, 3.8]$.

If equation 8.21 would also describe the location of the jet upper shear layer for other values of J than $J \in [2.8, 3.8]$, then it could be validated, whether the scaling in terms of J is appropriate for a wider range of J. Fortunately, in addition to the experiments for $J = 2.8$ and $J = 3.8$, two experiments for $J = 4.8$ have been performed ($S = 0$ and $S = 5.38$, respectively), which could validate further whether the scaling is appropriate.

Figure 8.36 shows the location of the jet upper shear layer for $J = 4.8$ and $S = 0$ and figure 8.37 shows the location of the jet upper shear layer for $J = 4.8$ and $S = 5.38$. In the two figures, equation 8.21 is plotted with the corresponding combination of values for J and S. For the two conditions, it appears that the function describes the location of the jet upper shear layer qualitatively well.
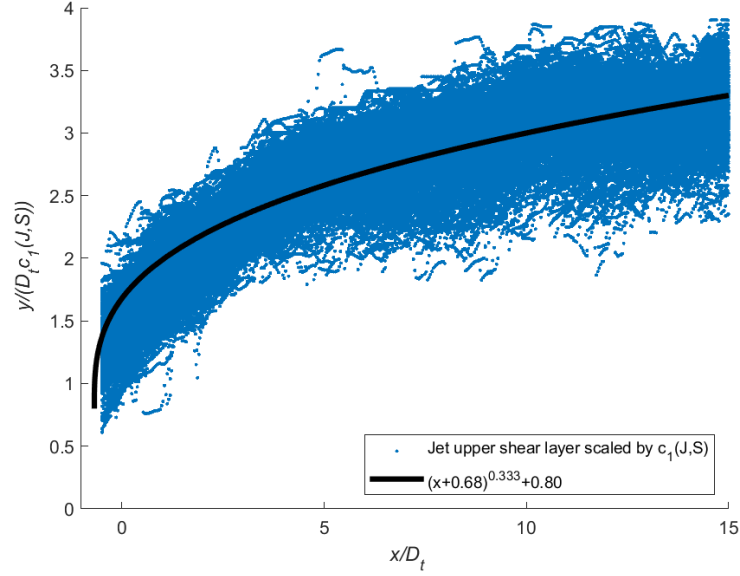
Figure 8.35: Location of the jet upper shear layer (blue) and the generalized fit (black), both scaled by $c_1(J, S)$ (equation 8.20) for $J = [2.8, 3.8]$, $S \in [0 : 9.87]$, $M_c = 1.55$. The data stem from 20 Schlieren images per (J, S) combination.
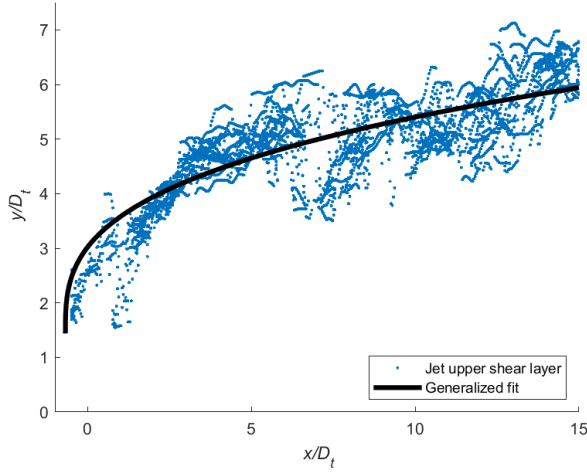
Figure 8.36: Location of the jet upper shear layer (blue) and the generalized fit (black), for $J = 4.8$, $S = 0$, and $M_c = 1.55$. Data is from 20 Schlieren images.
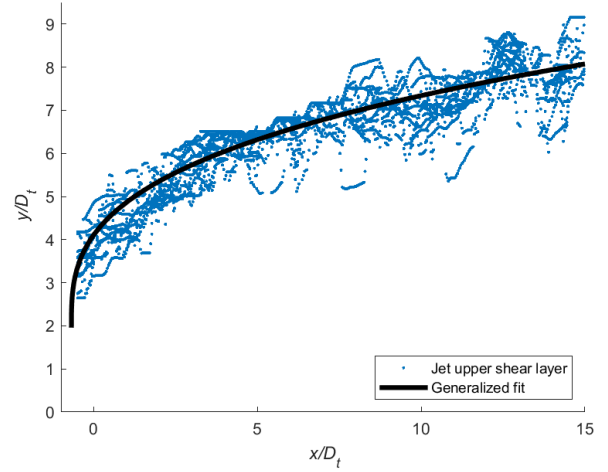
Figure 8.37: Location of the jet upper shear layer (blue) and the generalized fit (black), for $J = 4.8$, $S = 5.38$, and $M_c = 1.55$. Data is from 20 Schlieren images.

In addition, the quantitative quality of the fit is investigated. For the two values of S, the value for c_1 as used in the equation for y/D_t is determined, by calculating c_1 using equation 8.20 and by taking the least-squares fit of $y/D_t = c_1((x/D_t + 0.68)^{0.333} + 0.80)$. These results are shown in table 8.11.

Conditions		Based on least-squares		Based on equation 8.21	
		c_1	R^2	$c_1(J, S)$	R^2
$J = 4.8$	$S = 0$	1.804	0.680	1.800	0.680
	$S = 3.8$	2.424	0.842	2.447	0.840

Table 8.11: Results for the analysis of the quality of equation 8.21 applied to the jet shear layer for the conditions: $J = 4.8$, $S \in [0, 5.38]$ and $M_c = 1.55$.

It appears that the value of c_1 in equation 8.21 closely approaches the value of c_1 based on the least-squares fit. In addition, the coefficients of determination are also almost equal for the two methods. The value of R^2 for $J = 4.8$ with $S = 0$ is rather low ($R^2 = 0.68$). However, this is in line with the observed results for single jet injection for other values of J. The value of R^2 for $J = 4.8$ with $S = 5.38$ on the other hand, is much higher and very acceptable ($R^2 = 0.84$).

For further investigation, figure 8.28 combined with the results for $J = 4.8$ is displayed in figure 8.38. This figure includes the average penetration for $J = 2.8$, $J = 3.8$ and $J = 4.8$ calculated employing equation 8.21 and equation 7.11. This figure shows that the fit describes the average penetration of the jet upper shear layer adequately.
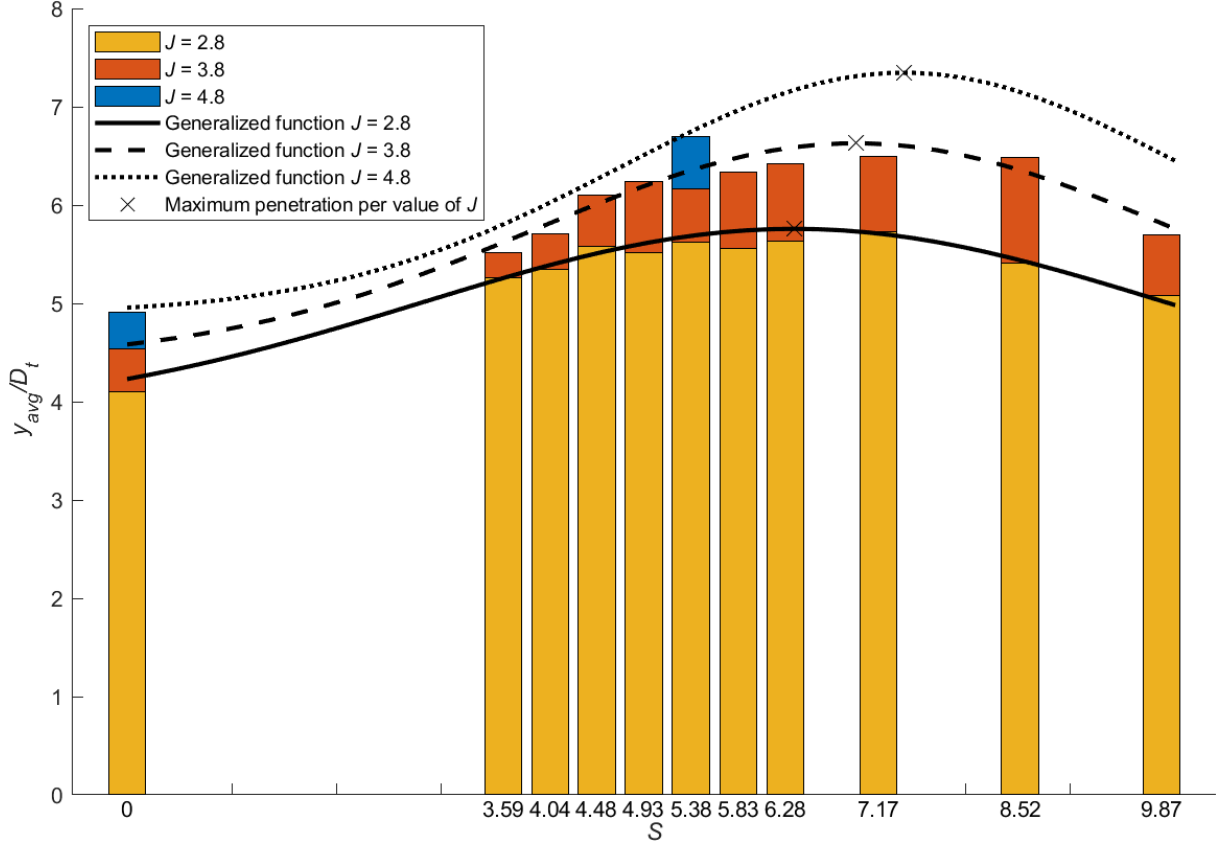
Figure 8.38: Average penetration from figure 8.28, together with the results for $J = 4.8$ and the average penetration as calculated from equation 8.21 and equation 7.11. The optimal value of S at constant J for maximal penetration is $S_{optimal}(J) = 4.732 J^{0.288}$.

Concluding, equation 8.21 describes the location of the jet upper shear layer for $J = 4.8$ and $S \in [0, 5.38]$ very well. This is an indication that with equation 8.21, a relation is obtained that can be applied to a wide range of parameters.

One characteristic of the penetration for dual jet injection is that an optimal value of S can be obtained. In line with Lee's [9] results, the optimal value for S in equation 8.21 increases with J. The optimal value for S for maximal penetration at a certain value of J using the generalized function for y/D_t is determined by $b_3 J^{b4}$:

$$S_{optimal}(J) = 4.732 J^{0.288} \qquad (8.22)$$

Up to now, only $J \in [2.8, 3.8, 4.8]$ was used for the application of equation 8.21. As an example, it is investigated whether trends as found in literature can validate the behaviour of equation 8.21. The study of De Maag [35] uses conditions that are the closest to the present study ($M_c = 1.6$) for a similar

range for S, but then for $J = [1, 1.4, 2]$. Therefore, the generalized function cannot be applied entirely, but the trends can be investigated. In the experiments of De Maag [35], the value of S for maximal penetration is not very clear for $J = 1$ and $J = 2$ (when neglecting the results for $S = 4.5$, see section 5.2), but for $J = 1.4$, it is clear that the maximum in penetration is obtained around $S = 5.4$ (see figure 5.8). Equation 8.22 shows the maximum penetration to be at $S(J = 1.4) = 5.21$, which is in line with the result from De Maag [35]. Further remarks are provided in section 8.2.2.4.

In the preceding sections, the cases for S approaching 0 and infinity with respect to the location of the jet upper shear layer were discussed. These findings also apply to the generalized function $y/D_t(x/D_t; J, S)$ (equation 8.21). In addition, this function also shows the similarity behaviour as a function of J that was observed in literature and in the preceding sections:

- Penetration increases with increasing J.

- The value of S for which the maximum penetration is obtained increases with increasing J.

- The relative spreading of the larger penetration as obtained for dual jet injection decreases with increasing J.

The generalized function $y/D_t(x/D_t; J, S)$ is appropriate for all experiments performed in the present study. However, further validation of the fit in equation 8.21 and possibly tuning of specifically the coefficients b_1 to b_6 might be advantageous, in order to investigate the validity of the function for other conditions of J and S. For that purpose, in the domain of J, investigation of the location of the jet upper shear layer for especially $J < 2.8$ and $J > 3.8$, and in the domain of S, investigation of the location of the jet upper shear layer for $S < 3.5$ and $S > 10$ would give more insight into the validity of equation 8.21. Investigation of the effect of D_1 and D_2 – the diameters of the jet orifices – can be performed and can validate the present study further.

8.2.2.3 Bandwidth of the Jet Upper Shear Layer

In the preceding sections, the penetration depth of the jet upper shear layer was researched thoroughly. In the following, the bandwidth of the jet upper shear layer is explored.

The bandwidth of the jet upper shear layer is important, because it is a measure of the thickness of this shear layer and therewith of its mixing behaviour, as described in sections 4.5 and 4.6. The larger the bandwidth of the shear layer, the more volatile the shear layer is and the faster the mixing occurs. Therefore, a large bandwidth is desired for better mixing of the flow as an addition to large penetration depth.

Two characteristic cases are investigated in figure 8.39 and figure 8.40. In the top subfigure, the location of the jet upper shear layer is shown geometrically and in the bottom subfigure, the fit with shift is subtracted from the data of the location of the jet upper shear layer, such that the cloud of data points is centered around the x/D_t-axis. In the subfigures, the full data set of the jet upper shear layer for one condition is displayed as blue asterisks, and the upper and lower boundary for each value of x/D_t is marked by red and yellow asterisks, respectively. The dotted line is the fit with shift for the location of the jet upper shear layer. The upper and lower dashed lines are the medians of the data for $\delta/D_t > 0$ and for $\delta/D_t < 0$, respectively, which show the core of the jet upper shear layer. Furthermore, the medians of the data of the upper and lower boundary (red and yellow asterisks, respectively) are determined to be the upper- or lower-side bandwidth ($\delta_{BW,up}/D_t$ and $\delta_{BW,down}/D_t$, respectively). The difference between $\delta_{BW,up}/D_t$ and $\delta_{BW,down}/D_t$ is the bandwidth δ_{BW}/D_t of the jet upper shear layer and this quantity is the most important to specify.

Figure 8.39 shows a jet upper shear layer with a certain bandwidth that is approximately constant over the full length. The one-sided medians are around $|\delta/D_t| = 0.4$ and the one-sided boundary medians are around $|\delta/D_t| = 0.75$. It is observed that the bandwidth does not increase significantly with x/D_t. On the other hand, figure 8.40 shows another phenomenon. Observing $x/D_t \geq 6$, the bandwidth increases with x/D_t and a constant value for the bandwidth is not appropriate as a characterization. A (linear) dependency on x/D_t would give a better representation and this is in line with literature about a shear layer for parallel flows (see section 4.5). However, this is out of scope of this exploration, and therefore, only the simple determination of the bandwidth is applied.
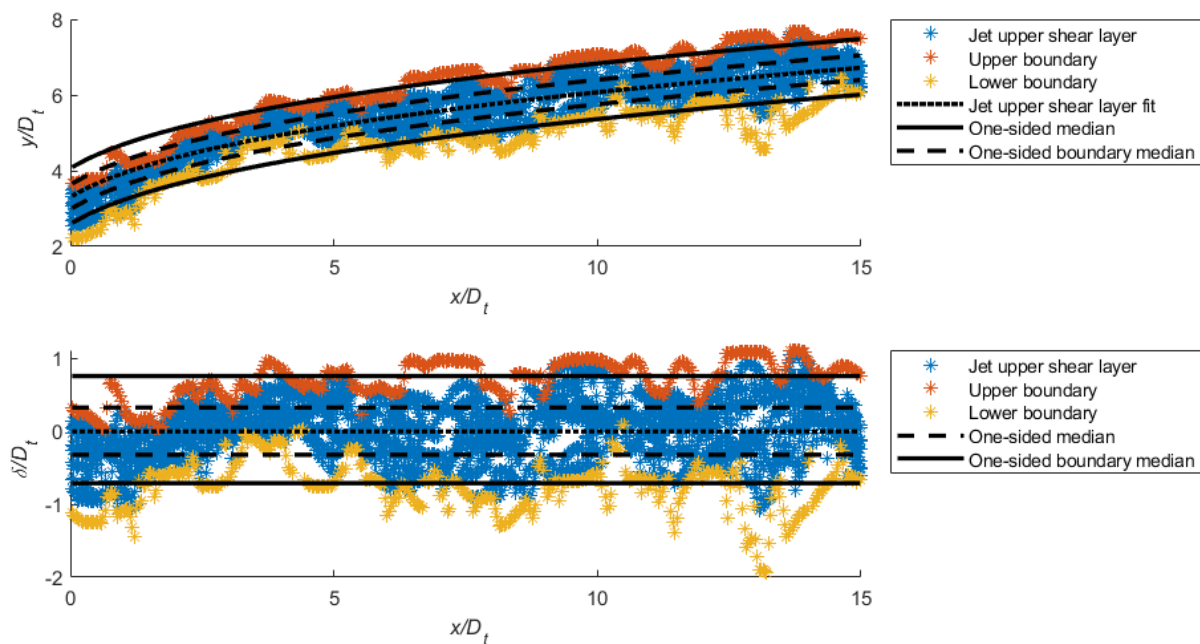
Figure 8.39: Data of the jet upper shear layer for $J = 2.8$, $S = 5.83$ and $\mathrm{M}_c = 1.55$. Top figure: The fit for the location of the jet upper shear layer for the corresponding condition is dotted. The one-sided medians are determined by using only the data of the upper or lower regions and calculating the median (dashed). The median of the points on the boundary gives a good indication of the (approximately constant) one-sided bandwidth (solid). Bottom figure: Data and median values of the jet upper shear layer are subtracted by the corresponding fit with shift.
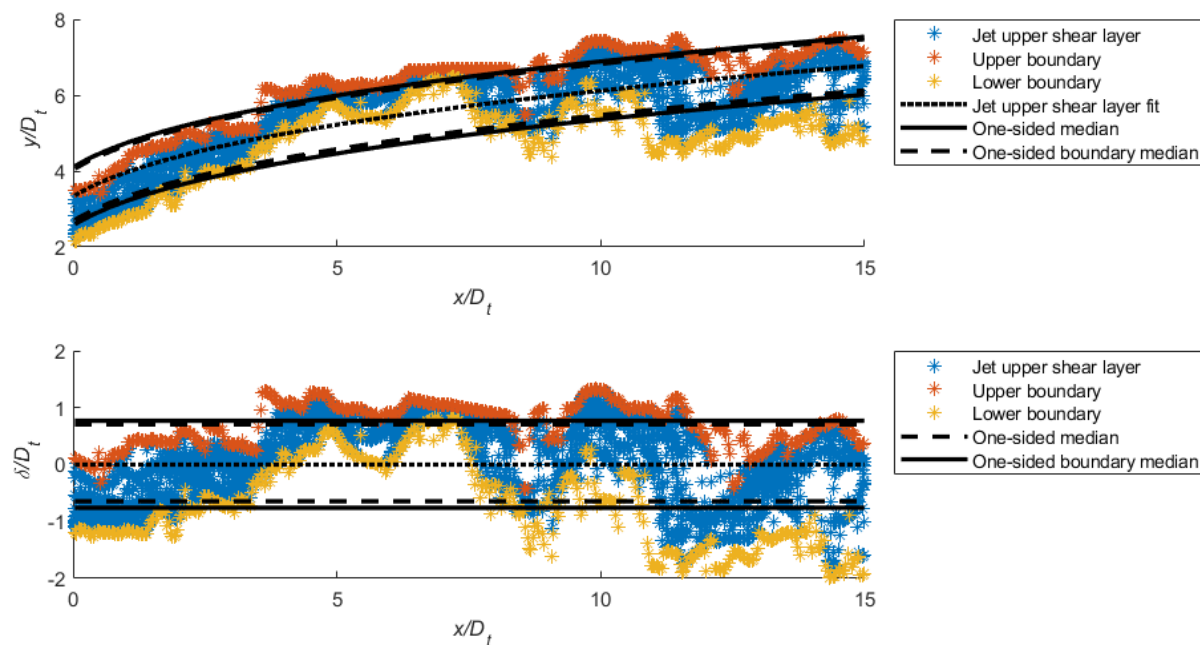
Figure 8.40: Data of the jet upper shear layer for $J = 2.8$, $S = 5.38$ and $\mathrm{M}_c = 1.55$. Top figure: The fit for the location of the jet upper shear layer for the corresponding condition is dotted. The one-sided medians are determined by using only the data of the upper or lower regions and calculating the median (dashed). The median of the points on the boundary does not give a good indication of the one-sided bandwidth (solid). Bottom figure: Data and median values of the jet upper shear layer are subtracted by the corresponding fit with shift.
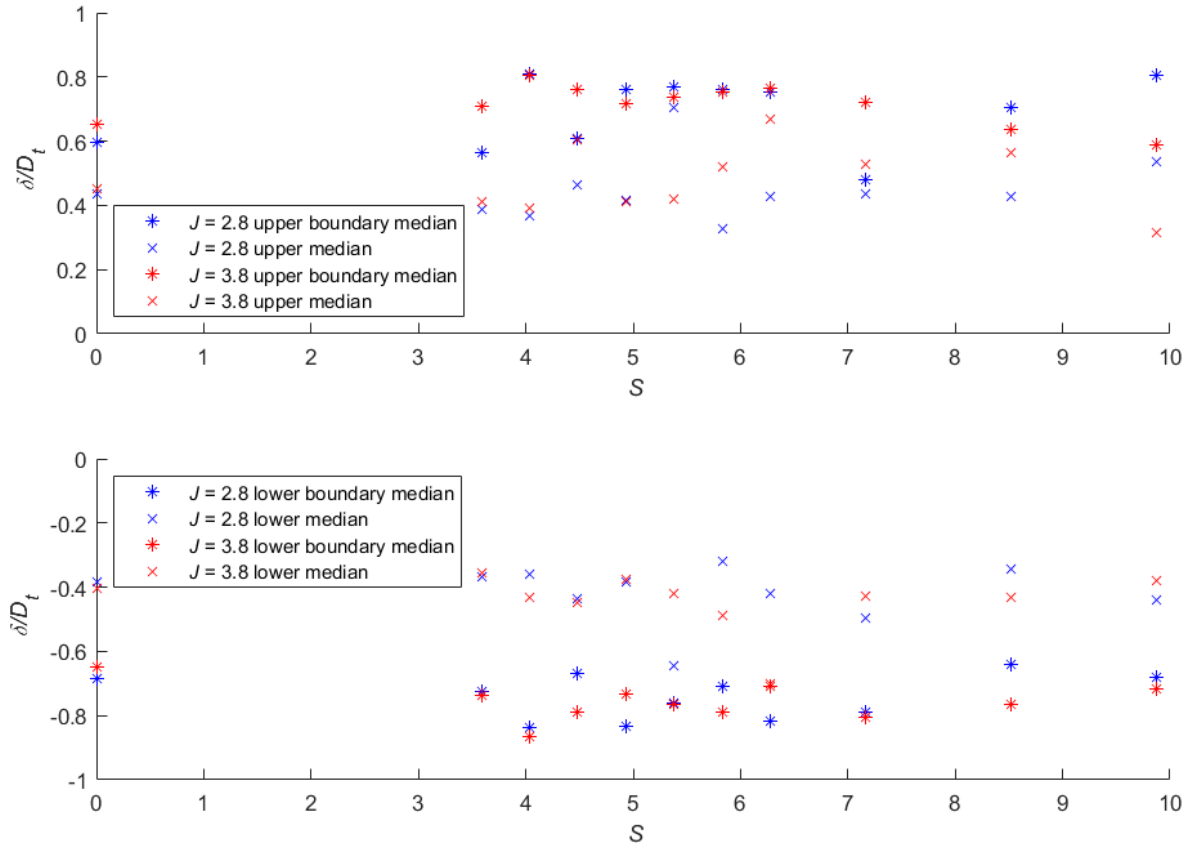
Figure 8.41: The one-sided medians and one-sided boundary medians δ/D_t are shown as function of S for $J = 2.8$ and $J = 3.8$ and $\mathrm{M}_c = 1.55$. The results are obtained from data sets such as in figure 8.39.

Figure 8.42: The full bandwidth and jet upper shear layer core δ/D_t are shown as function of S for $J = 2.8$ and $J = 3.8$ and $\mathrm{M}_c = 1.55$. The difference between the upper and lower values in the two subfigures from figure 8.41 is taken for finding the results in this plot.

Figure 8.41 shows the results for the upper- and lower side of the bandwidth ($\delta_{BW,up}/D_t$ and $\delta_{BW,down}/D_t$) and the core of the jet upper shear layer and figure 8.42 shows the results 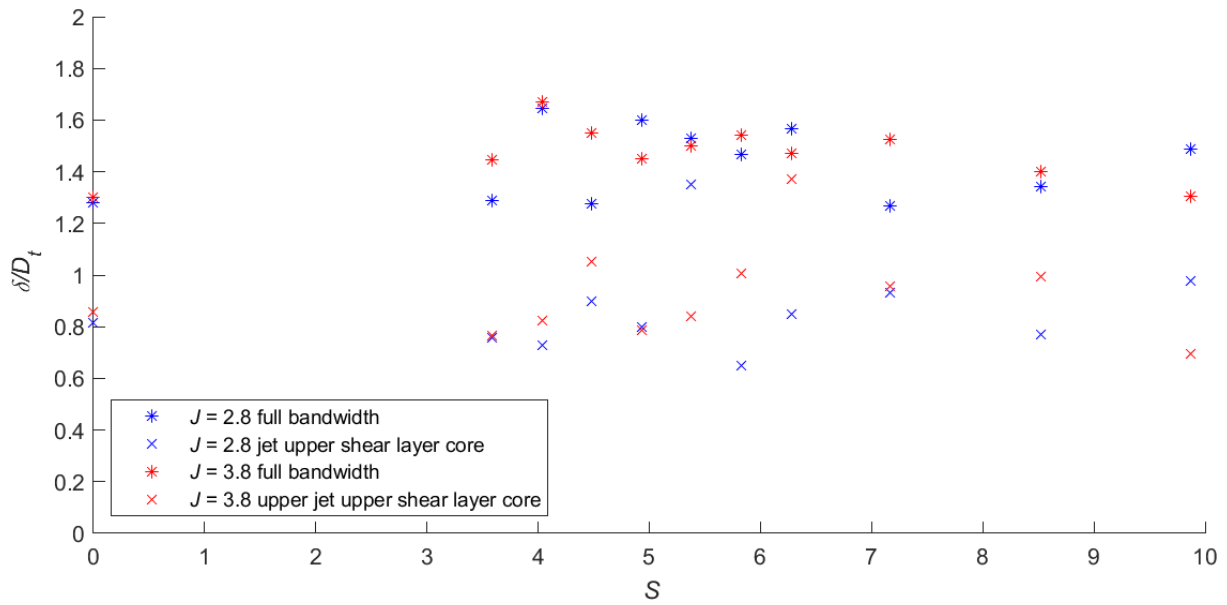for the bandwidth δ_{BW}/D_t and core of the jet upper shear layer, which are combinations of the two subfigures of figure 8.41. These results are for all conditions of $J = 2.8$ and $J = 3.8$, $M_c = 1.55$ and $S \in [0 : 9.87]$. As described for figure 8.39 and figure 8.40, these results are not all appropriate for an accurate quantification of the bandwidth, but it shows the effect of dual jet injection compared to single jet injection. The bandwidth is over the whole range of S larger for dual jet injection than for single jet injection. This is an important observation, because this means that the jet upper shear layer is more volatile, resulting in a better mixing behaviour for dual jet injection than for single jet injection.

It is possible that the results have a small bias for the lower boundary median, because the correction steps for the jet upper shear layer correct lower outlying data (see section 7.4.2.2). Therefore, the lower boundary median may be a bit closer to 0 than the upper boundary median. However, the difference is rather small and this does not affect the difference between the results for single jet injection and dual jet injection, as for both the same procedure is applied.

Further research into the variability of the bandwidth δ_{BW}/D_t would contribute to more insight into the mixing behaviour of the jet, in combination with the penetration.

8.2.2.4 Concluding Remarks on Behaviour Jet Upper Shear Layer

Concluding remarks on the penetration of the jet upper shear layer are given below.

- Behaviour of the jet upper shear layer as observed in the present study is comparable with the results of De Maag [3][35], Lee [9] and Landsberg [55]. The jet upper shear layer shows a dip around $x/D_t = 5$. Further downstream, the jet penetrates further into the crossflow. Furthermore, time-dependent behaviour of the jet upper shear layer, that appears to be periodic, is observed, which indicates the possibility of the presence of the Kelvin-Helmholtz instability in this shear layer.

- The penetration depth can be described by a fit without shift ($y/D_t = c_1(x/D_t - c_3)^{c_2}$) or a fit with shift ($y/D_t = c_1((x/D_t - c_3)^{c_2} + c_4)$). The fit with shift provides a better description of the penetration and it is recommended to use this expression. However, it should be noted that the coefficients c_1 through c_4 can exhibit a larger variation, while also similarity is more difficult to identify.

- Similarity analysis shows that the penetration at constant J can be scaled by the function $c_1(S) = k_4 \exp\left(-\frac{1}{2}\left(\frac{S-k_2}{k_3}\right)^2\right) + k_1$, because c_1 is the only coefficient that is clearly not only a function of J, but also a function of S. Coefficients of determination (R^2) for this scaling are in the same order of magnitude as the R^2 of the fits for individual combinations of J and S (around $R^2 = 0.74$).

- Further similarity analysis shows that the location of the jet upper shear layer can be described by the following function for $y/D_t(x/D_t; J, S)$, valid for $J \in [2.8, 3.8]$, $S \in [0 : 9.87]$, $M_c = 1.55$:

$$\frac{y}{D_t}\left(\frac{x}{D_t}; J, S\right) = 0.432 J^{0.461}\left(2 + \exp\left(-\frac{1}{2}\left(\frac{S - 4.732 J^{0.288}}{6.103 J^{-0.521}}\right)^2\right)\right)\left(\left(\frac{x}{D_t} + 0.68\right)^{0.333} + 0.80\right)$$

(8.23)

This equation is also validated for the conditions $J = 4.8$, $S \in [0, 5.38]$, $M_c = 1.55$, and has a coefficient of determination ($R^2 = 0.739$), which is assessed to be acceptable.

- At a given S, average penetration increases with increasing J. Furthermore, penetration for tandem dual jet injection is larger than for single jet injection. The dimensionless dual distance S has an optimal value at which the penetration averaged over $0.5 \leq x/D_t \leq 15$ is maximal. This optimal value of S (which is equal to $4.732 J^{0.288}$) increases with increasing J.

- The relation for the time-averaged location of the jet upper shear layer as described by equation 8.23, is also applied to $J \in [1.0, 1.4, 2.0]$ for comparison with the results of De Maag [35]. Therefore, figure 8.43 shows De Maag's results of the average penetration of the jet upper shear layer together with the average penetration as calculated from substituting equation 8.23 in equation 7.11.
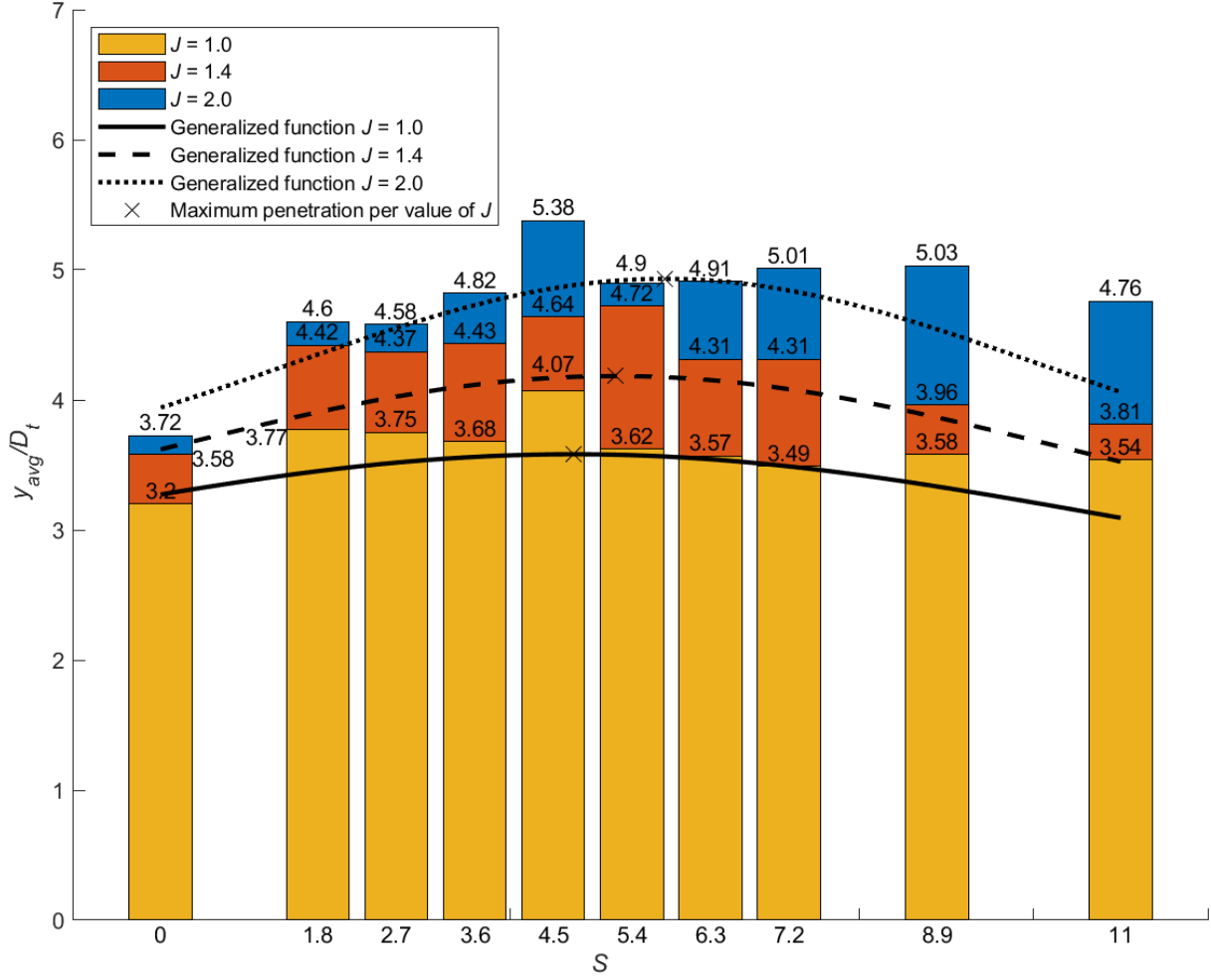
Figure 8.43: Average penetration ($0.5 \leq x/D_t \leq 15$) from results of De Maag [35], together with average penetration as calculated from equation 8.23. The optimal value of S at constant J for maximal penetration is based on $S_{optimal} = 4.732 J^{0.288}$. The result for $S = 4.5$ is discarded in De Maag's analysis.

De Maag discarded the results in $S = 4.5$, because these deviate substantially from the trend indicated by the results for the other values of S. This is possibly due to a different plenum in the injection block, compared to the plena in the other injection blocks (see section 5.2). The generalized fit, equation 8.23, describes some trends of the results of De Maag, such as the maximum average penetration for $J = 1.4$ around $S = 5.4$. However, for some results such as the ones for larger values of S, the generalized fit differs substantially in amplitude. This can have a number of reasons. First, the extrapolation of the generalized fit from values of $J \in [2.8, 3.8]$ to much smaller values of J can cause the deviation. Also, the Mach number of the study of De Maag was somewhat higher than the Mach number in the present study ($M_c = 1.6$ and $M_c = 1.55$, respectively). In addition, the method of data acquisition of De Maag was different. In his study, the location of the jet upper shear layer was determined manually from four Schlieren images, while in the present study, a semi-automatic algorithm with larger data acquisition is applied to 20 Schlieren images. Furthermore, the focus of the present study is on a range of $3.59 < S < 6.28$. The location of the jet upper shear layer for this range of S has a more dominant contribution to the generalized fit, whereas De Maag used a wider range of values of S, up to $S = 11$, with less focus on possible maxima at lower values of S. These differences might cause the differences between the generalized fit and the results of De Maag [35].

- The bandwidth of the jet upper shear layer is larger for dual jet injection than for single jet injection, which indicates an enhancement of the mixing behaviour for dual jet injection compared to single jet injection.

8.2.3   Results for the Jet Center Line

In this exploration, the results for the jet center line are presented. Figure 8.17 shows the jet plume, together with the different characteristics of the plume, amongst others the jet center line. The location of the jet center line is determined from the least-squares fit of the data of the plume for $0 \leq x/D_t \leq 15$ in the form:

$$\frac{y}{D_t} = d_1 \left(\frac{x}{D_t}\right)^{d_2} \tag{8.24}$$

For the conditions used in the analysis of the jet upper shear layer, the jet center line has been determined. Table 8.12 shows the coefficients of the fit for the location of the jet center line for $J = 2.8$ and $J = 3.8$ and $S \in [0 : 9.87]$.

	S	0	3.59	4.04	4.48	4.93	5.38	5.83	6.28	7.17	8.52	9.87
	d_1	1.748	2.081	2.492	2.178	2.074	2.089	1.981	2.064	1.966	1.895	2.078
$J = 2.8$	d_2	0.299	0.345	0.263	0.329	0.363	0.348	0.386	0.354	0.382	0.370	0.322
	$\frac{y_{avg}}{D_t}$	3.09	4.03	4.10	4.08	4.17	4.07	4.17	4.07	4.10	3.86	3.84
	d_1	1.908	2.215	2.395	2.487	2.434	2.344	2.263	2.410	2.527	2.195	1.945
$J = 3.8$	d_2	0.309	0.353	0.309	0.295	0.327	0.339	0.368	0.344	0.327	0.381	0.387
	$\frac{y_{avg}}{D_t}$	3.44	4.36	4.32	4.36	4.55	4.49	4.59	4.66	4.73	4.57	4.10

Table 8.12: Parameters of the fit for $y/D_t = d_1 (x/D_t)^{d_2}$, with $J = 2.8$ and $J = 3.8$, $S \in [0 : 9.87]$ and $M_c = 1.55$. Data for the range $0 \leq x/D_t \leq 15$ is used. The average penetration y_{avg}/D_t is calculated employing equation 7.11.
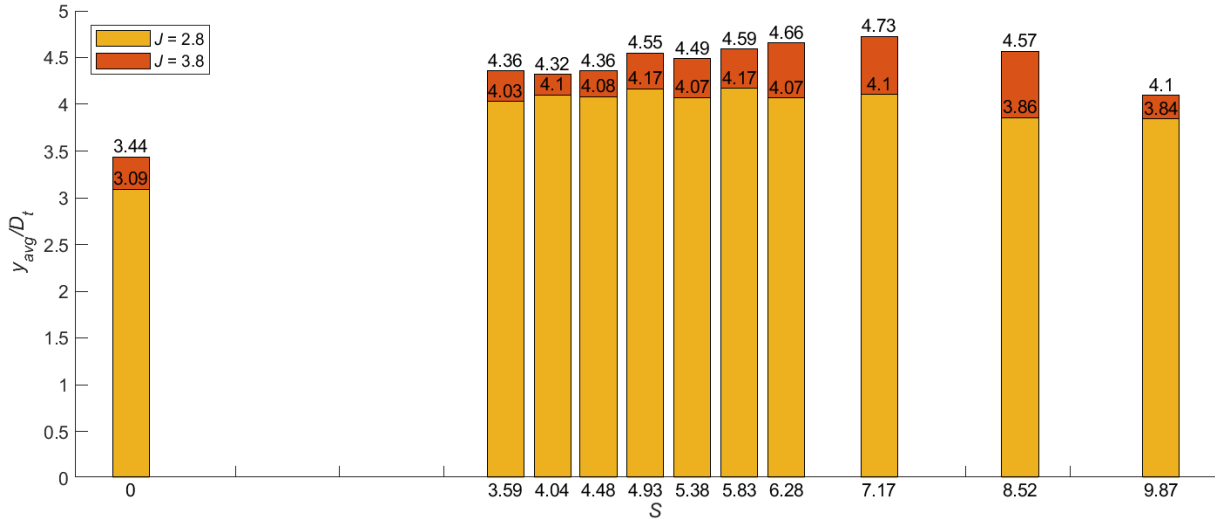

Figure 8.44: Average penetration of the jet center line, calculated from equation 7.11, for $J \in [2.8, 3.8]$, $S \in [0 : 9.87]$ and $M_c = 1.55$.

For the jet center line, similar behaviour is observed as for the jet upper shear layer. In figure 8.44, it is observed that penetration of the jet center line increases with increasing J. Investigation of figure 8.17 learns that the jet center line has a smaller offset than the jet upper shear layer, and a comparable slope. Although the behaviour is similar, the differences between the jet center line for different values of S are rather small. Figure 8.45 shows the jet center lines for $J = 2.8$ at five values of S. It appears that the jet center line is the smallest for single jet injection – as expected. The jet center line for dual jet injection is for all S significantly at a higher location than for single jet injection. At the same moment, the jet center line for dual jet injection does not differ much for a large range of values of the dual distance S. This is observed in figure 8.45 as well as in figure 8.44, which shows the average penetration for the jet center line. In figure 8.44, especially for $J = 3.8$, a progression comparable with that for the jet upper
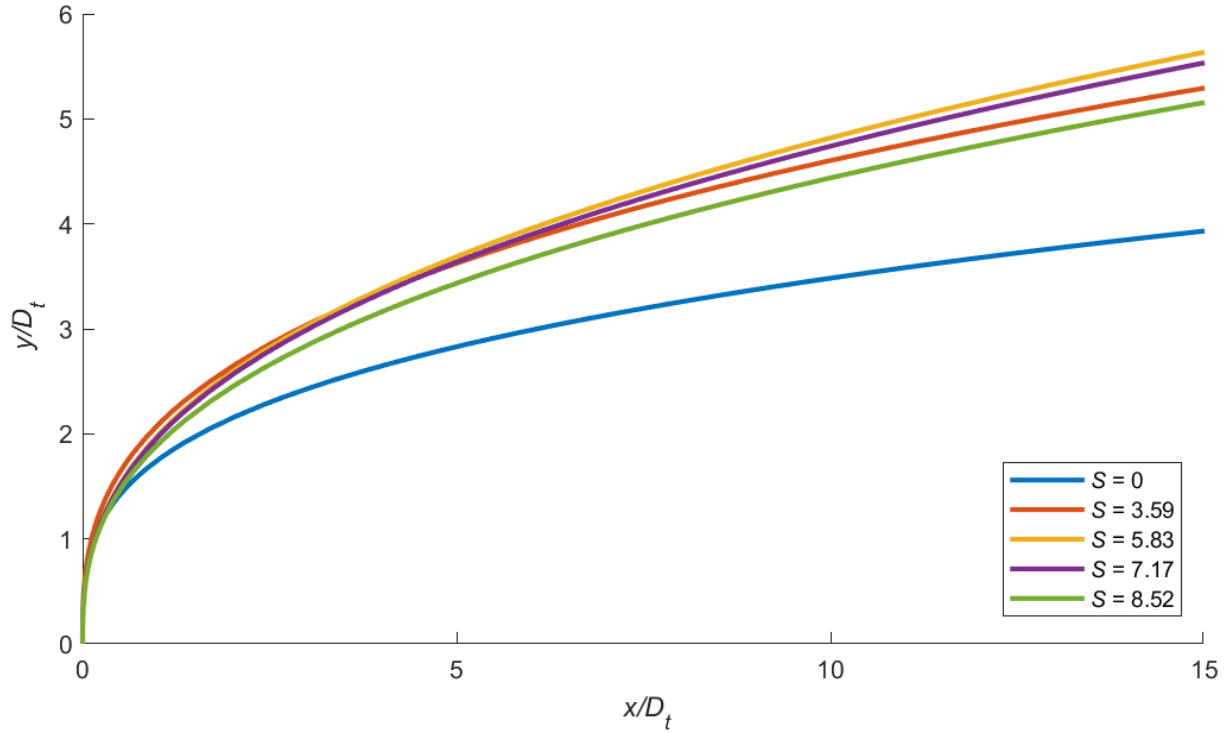
Figure 8.45: Results for the fits for the jet center line for $J = 2.8$, $M_c = 1.55$ and some values of S showing the behaviour of the jet center line as function of S.

shear layer is visible, but then with smaller differences. As a result of the smaller differences, inaccuracies in the average penetration that can be about ± 0.05 may dominate. Therefore, the progression with S is not very clear for the jet center line and especially for $J = 2.8$.

Figure 8.44 shows that the jet center line penetration does not differ very much as function of S. Therefore, the difference in location between the jet upper shear layer and the jet center line – the upper part of the height of the plume – varies with S in the same manner as the jet upper shear layer. This suggests that the spreading of the plume scales especially with the jet upper shear layer, because the penetration of the jet upper shear layer has clear differences for different values of S.

8.2.4 Results for the Jet Lower Shear Layer

The phenomenon that is in the present study called the **jet lower shear layer**, is in fact not a shear layer similar to the jet upper shear layer. It is a combination of the two shear layers at the lower side of the mushroom-shaped counter rotating vortex pair (see figure 5.1) of the jet plume. More precisely, the jet lower shear layer as determined and used is the lower side of the jet plume, observed in the Schlieren images.

In this section, it is attempted to characterize the jet lower shear layer. Data acquisition is performed as described in section 7.4.2.2 and an example of the result of this acquisition is shown in figure 8.17. The data feature more outliers compared to the data of the jet upper shear layer, which is caused by more complex behaviour of the interacting vortex pair. Therefore, a fit of the jet lower shear layer is presumably not a law of nature, but an adequate approximation.

Figure 8.17 shows that the jet lower shear layer has its origin around $x/D_t = 1$. In many conditions, a certain distance downstream, a maximum is observed for the jet lower shear layer. Downstream of the maximum, y/D_t decreases slightly. In section 7.4.2.3, a rational function was proposed to use for a fit:

$$\frac{y}{D_t} = \frac{e_1\left(\left(\frac{x}{D_t}\right) - e_2\right)}{\left(\frac{x}{D_t}\right)^2 + e_3\left(\frac{x}{D_t}\right) + e_4} \tag{8.25}$$

This fit contains four coefficients, i.e. four degrees of freedom. Due to the quotient in the function, the coefficients may be very large, because they compensate each other. The exorbitant values for the coefficients are undesired, because a combination of simpler coefficients might give a similar result. However, when the coefficients are determined to be large, then this is the result of the least-squares fit, which is assumed to be the best fit. A more thorough analysis would provide more insight whether there are similarities between fits, such as is performed for the jet upper shear layer. Table 8.13 shows an overview of the coefficients for the fits of the jet lower shear layer.

J	S	0	3.59	4.04	4.48	4.93	5.38	5.83	6.28	7.17	8.52	9.87
	e_1	$1.46 \cdot 10^6$	121	200	153	194	136	90.4	133	128	91.4	$8.68 \cdot 10^3$
	e_2	0.62	0.93	1.08	0.86	0.88	0.91	0.61	1.16	0.72	0.63	0.73
2.8	e_3	$4.39 \cdot 10^5$	12.3	37.9	24.6	30.9	21.8	3.29	19.7	13.6	7.72	$2.18 \cdot 10^3$
	e_4	$9.76 \cdot 10^5$	89.0	54.3	79.4	102	75.2	95.9	67.6	104	90.3	$3.19 \cdot 10^3$
	R^2	0.78	0.85	0.82	0.77	0.82	0.76	0.82	0.81	0.79	0.76	0.75
	e_1	$1.49 \cdot 10^6$	1130	$1.35 \cdot 10^6$	293	$3.33 \cdot 10^6$	537	165	216	183	543	83.8
	e_2	0.50	1.10	1.03	1.12	0.93	0.91	0.79	0.82	0.71	0.88	0.78
3.8	e_3	$4.02 \cdot 10^5$	218	$3.31 \cdot 10^5$	66.6	$7.86 \cdot 10^5$	107	21.1	35.6	26.1	100	3.97
	e_4	$9.49 \cdot 10^5$	324	$2.03 \cdot 10^5$	42.9	$7.84 \cdot 10^5$	180	98.7	88.8	89.8	271	83.6
	R^2	0.80	0.84	0.78	0.77	0.73	0.75	0.81	0.72	0.76	0.84	0.79

Table 8.13: Parameters of the fit for $y/D_t = e_1 \cdot ((x/D_t) - e_2)/((x/D_t)^2 + e_3 \cdot (x/D_t) + e_4)$, with $J = 2.8$ and $J = 3.8$ and $S \in [0:9.87]$ and $M_c = 1.55$. Data for the range $0.5 \leq x/D_t \leq 15$ is used.

Table 8.13 shows that in most cases, the origin of the jet lower shear layer ($x/D_t = c_2$) is found to be in the range $0.5 \leq x/D_t \leq 1.2$. Most coefficients are smaller than 1000, but some combinations of exorbitant values appeared to be optimal. The values of e_1, e_3 and e_4 compensate amplification, such that these coefficients are mostly in the some order of magnitude. However, e_1 appears to be the largest coefficient in all cases and in 16 of the 22 cases, e_1 is smaller than 1000, which is more acceptable.

The coefficients of determination R^2 appear to be acceptable. All values of R^2 are within the range of $0.72 \leq R^2 \leq 0.85$, which indicates that the fits of the jet lower shear layer are good approximations of the data. Therefore, the quantitative description of the location of the jet lower shear layer is acceptable.

In this exploration, it is especially the purpose to investigate the qualitative behaviour of the jet lower shear layer as described by equation 8.25. Figure 8.46 shows the fits for $J = 2.8$ for a number of values of S, for describing the location of the jet lower shear layer. The jet lower shear layer for single jet injection ($S = 0$) appears to have the slowest progression. The progression of the jet lower shear layer is stronger for dual jet injection.
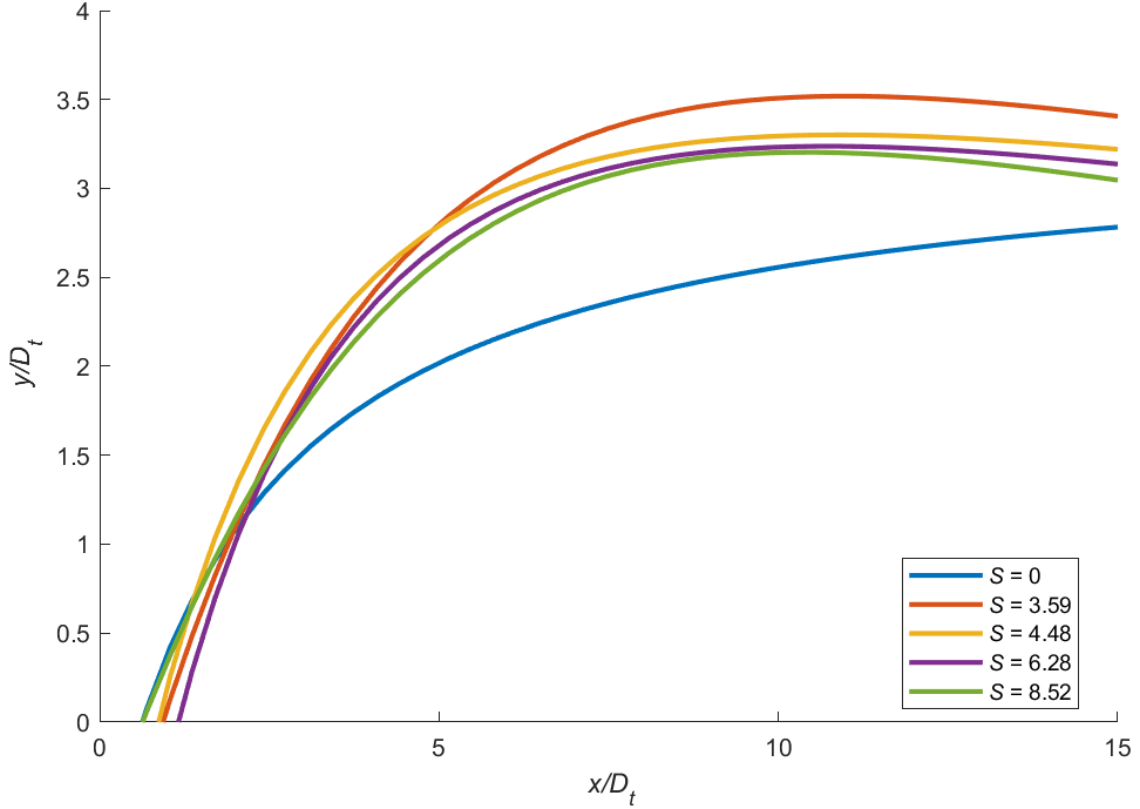
Figure 8.46: Results of the fits for the jet lower shear layer for $J = 2.8$, $\mathrm{M}_c = 1.55$ and a number of values of S that show the location of the jet center line as function of S.

Another observation is even more important. It appears that the jet lower shear layer, for most values of $S > 0$, has a maximum around $x/D_t = 10$. From section 8.2.2 and section 8.2.3, it is known that the jet upper shear layer and jet center line always increase with x/D_t. As a consequence, the jet plume is clearly spreading vertically for dual jet injection, because the location of the jet lower shear layer decreases for $x/D_t > 10$. For single jet injection, a maximum is not observed, implying that the vertical spreading of the jet in downwards direction is smaller than for dual jet injection – even more when taking the lower penetration of the jet upper shear layer for single jet injection into account. This behaviour for the spreading is also observed in for example figure 8.13, figure 8.16 and figure 8.17. Combining these figures results in an example for the quantification of the spreading of the plume δ_{plume}/D_t in figure 8.47. In this figure, the vertical spreading of the plume can be investigated for approximately $x/D_t > 5$, because for $x/D_t < 5$, the jet is settling and turning to downstream direction and as a result, a simple difference in y/D_t direction would distort the data for the spreading. Therefore, the data for the height of the jet plume should be regarded for $x/D_t > 5$. It is observed that for $x/D_t > 6.7$, the jet plume height δ_{plume}/D_t increases continuously with x/D_t. This shows the good mixing behaviour of the dual jet injection for $J = 2.8$, $S = 5.83$ and $\mathrm{M}_c = 1.55$. Especially for single jet injection, this vertical spreading of the plume is smaller. Therefore, the mixing for dual jet injection is better than for single jet injection. Further research might investigate approximate relations for the height of the jet plume as a function of x/D_t, J and S.

Furthermore, it is observed, that the higher the value for S, the lower the location of the jet lower shear layer becomes, while maintaining a similar behaviour for dual jet injection. As a result, the lower side of the jet plume contributes to a larger vertical spreading, provided the penetration of the jet upper shear layer does not compensate this contribution. However, the differences between the jet lower shear layers for dual jet injection are rather small. The jet upper shear layer has a much larger contribution to the vertical spreading i.e. the mixing of the jet with the crossflow. Therefore, for dual jet injection, the jet upper shear layer will dominate the vertical spreading of the plume and therewith the mixing behaviour.
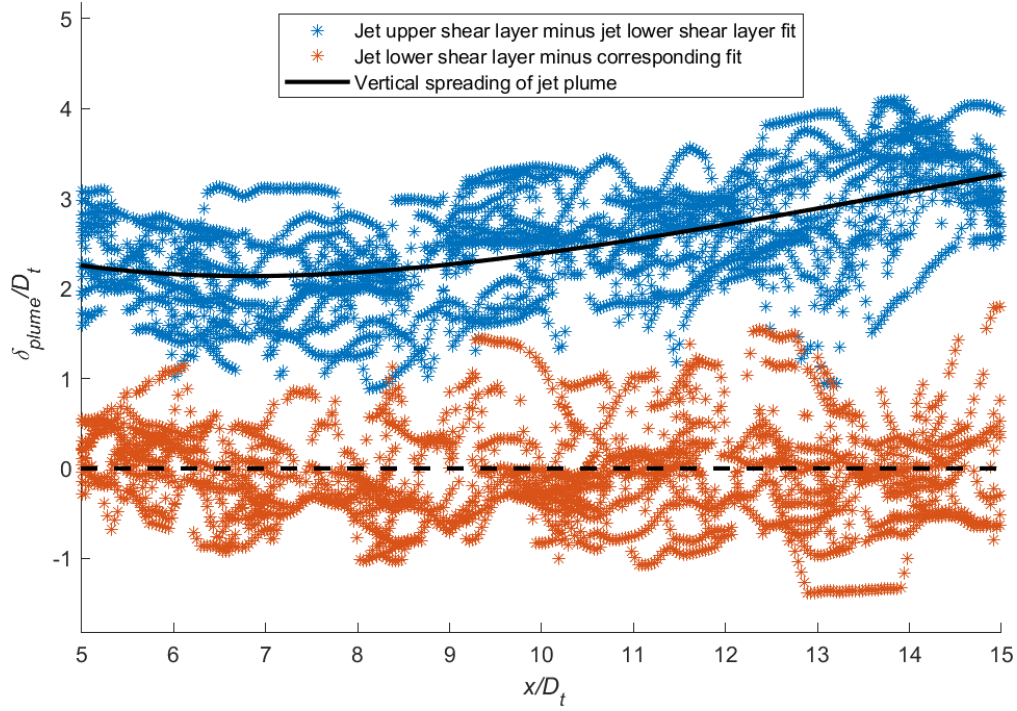
Figure 8.47: Vertical spreading of the jet plume δ_{plume}/D_t, determined by subtracting the fit of the location of the jet lower shear layer from the data of the location of the jet upper shear layer and jet lower shear layer. At $x/D_t = 6.7$, the minimum of the plume is observed, after which the plume spreads out again. Up to $x/D_t = 5$, the jet is in its starting phase and for $x/D_t > 5$, the plume spreading is represented well. Conditions are: $J = 2.8$, $S = 5.83$ and $\mathrm{M}_c = 1.55$, corresponding with figure 8.13 and figure 8.17.

8.2.5   Concluding Remarks on Behaviour Jet

In addition to the remarks presented in section 8.2.2.4, the following concluding remarks are given below.

- There is no clear correlation between the merger point of the bow shocks in front of the two jets and the level of penetration of the main jet. For the range of values of S that the bow shocks merge, penetration increases, but this continues for values of S for which the bow shocks remain spatially separated, such that a correlation does not appear to exist.

- The plume of the jet has a larger vertical spreading i.e. better mixing behaviour for dual jet injection than for single jet injection. In addition, the vertical spreading is especially characterized by the jet upper shear layer for dual jet injection, because the jet center line and the jet lower shear layer do not show much differences for different values of S.

Chapter 9

Conclusions

This chapter provides the conclusions of the present study into the behaviour of the jet shear layer in tandem jet injection based on Schlieren images. Per sub-question, the main conclusions are presented.

Behaviour of the bow shocks in front of the two jets

- The bow shocks that appear in front of the two jets show an oscillatory behaviour. Especially the downstream bow shock shows relatively large fluctuations, induced by the large-scale structures that appear in the downstream jet. The point at which the two bow shocks merge varies accordingly.

- At certain conditions, the bow shocks in front of the two jets merge. The time-averaged position of this merger point is described by:

$$\xi(J, S) = 0.114 J^{-1.864} S^{4.229} \tag{9.1}$$

$$\eta(J, S) = 1.924 J^{-0.572} S^{1.827} \tag{9.2}$$

  with $D_t = \sqrt{D_1^2 + D_2^2}$, $\xi = x/D_t$ and $\eta = y/D_t$. This relation is valid for at least $2.8 \leq J \leq 4.8$, $3.59 \leq S \leq 5.38$ and $\mathrm{M}_c = 1.55$. Due to the limited height of the wind tunnel, the analysis of whether or not the two bow shocks will merge or remain spatially separated is limited to values of $\eta < 19.3$. It has been found that the position of the merger point does not appear to have an effect on the penetration of the jet shear layer.

Behaviour of the jet upper shear layer

- The jet upper shear layer penetrates into the crossflow, however, it features a dip around $x/D_t = 5$; further downstream, the jet penetrates further into the supersonic crossflow. A time-dependent behaviour of the jet upper shear layer is observed that appears to be periodic, which is an indication of the possible presence of the Kelvin-Helmholtz type of instability in the shear layer.

- The penetration of the jet upper shear layer depends on the jet-to-crossflow momentum flux ratio J and on the dimensionless dual distance S. At constant S, penetration increases with increasing J. Penetration is larger for dual jet injection than for single jet injection. At constant J, S has an optimal value at which penetration is maximal. This optimal value of S increases with increasing J.

- For a specific condition, the time-averaged location of the jet upper shear layer can be described by a fit without shift ($y/D_t = c_1(x/D_t - c_3)^{c_2}$) or a fit with shift ($y/D_t = c_1((x/D_t - c_3)^{c_2} + c_4)$). From the comparison between the quality of these fits, it appeared that the fit with shift provides the best performance and is the preferred one.

- In the expression for the fit, the coefficient c_1 is the only coefficient that is clearly a function of both S and J. Similarity analysis shows that the penetration depth at constant J can be scaled by the fit $c_1(S) = k_1 + k_4 \exp\left(-\frac{1}{2}\left(\frac{S - k_2}{k_3}\right)^2\right)$.

- Based on data of the location of the jet upper shear layer for $J \in [2.8, 3.8]$, $S \in [0 : 9.87]$, $\mathrm{M}_c = 1.55$, and validated for $J = 4.8$ with $S \in [0, 5.38]$ and $\mathrm{M}_c = 1.55$, the generalized relation for the time-averaged location of the jet upper shear layer is found to be:

$$\frac{y}{D_t}\left(\frac{x}{D_t}; J, S\right) = 0.432 J^{0.461}\left(2 + \exp\left(-\frac{1}{2}\left(\frac{S - 4.732 J^{0.288}}{6.103 J^{-0.521}}\right)^2\right)\right)\left(\left(\frac{x}{D_t} + 0.68\right)^{0.333} + 0.80\right)$$

(9.3)

  This fit has a coefficient of determination of $R^2 = 0.739$ with respect to the data obtained from 20 Schlieren images per (J, S) combination.

- The bandwidth of the jet upper shear layer is larger for dual jet injection than for single jet injection, which indicates an enhancement of the mixing of the jet with the supersonic crossflow.

Behaviour of the jet plume

- The jet plume shows an increase in vertical spreading of the plume for approximately $x/D_t > 7$. Tandem dual jet injection enlarges the jet plume, which is advantageous for mixing of the jet with the crossflow. The penetration of the jet plume is dominated by the location of the jet upper shear layer. The jet center line and jet lower shear layer do not show much variation for different values of $S > 0$.

Therewith, the main research question has been addressed to sufficient extent. In conclusion, the research carried out in the present thesis has shown that the jet shear layer in tandem dual jet injection has an oscillatory, supposedly periodic behaviour with a certain bandwidth. Its penetration into the supersonic crossflow and mixing with that crossflow is substantially enhanced for tandem dual jet injection compared to single jet injection. At constant J, the penetration depth has an optimum for S. Furthermore, penetration increases with increasing J.

Chapter 10

Recommendations

For further investigation of tandem dual jet injection into a supersonic crossflow, validation of the obtained results and improvement of the techniques utilised, the following recommendations are presented.

- The generalized fit, equation 9.3, which describes the location of the jet upper shear layer as function of x/D_t, J and S, is obtained from data at the conditions $J \in [2.8, 3.8]$, $S \in [0, 3.59 : 9.87]$, $M_c = 1.55$. Although validated for two other conditions ($J = 4.8$ with $S = 0$ and $S = 5.38$, respectively), it should be investigated whether equation 9.3 describes the location of the jet upper shear layer for a larger range of J as well as S. Moreover, the numerical values of the coefficients can be tuned using data from further experiments. It is especially recommended to investigate the location of the jet upper shear layer for $S < 3.59$ and for $S > 10$ in order to validate the behaviour of the scaling by S.

- The experiments performed in the present study for tandem dual jet injection into a supersonic crossflow were performed at a crossflow Mach number of 1.55. Most other studies are also using a fixed Mach number for their numerical or experimental investigations. Therefore, the quantitative effect of M_c on the penetration of the jet has not been investigated for a specific tandem dual jet configuration, whereas in section 4.4, it was found that the penetration is also a function of M_c. Investigation of the quantitative effect of the Mach number of the crossflow would provide a better insight into the penetration of the jet and could possibly give the opportunity to include M_c into the similarity relation (equation 9.3) for the location of the jet upper shear layer in tandem dual jet injection into a supersonic crossflow.

- In the jet upper shear layer, time-dependent behaviour that appeared to be periodic has been observed. With the knowledge of section 4.5.2, this can be an indication of the presence of the Kelvin-Helmholtz type of instability in the jet upper shear layer. Verification of this presence would give the opportunity to integrate the mathematical and physical knowledge of the Kelvin-Helmholtz instability into the description of the vertical spreading i.e. bandwidth of the jet upper shear layer. For this verification and characterization of the Kelvin-Helmholtz instability in the jet upper shear layer, it is needed to measure the roller frequency f_r. This can be determined by measuring the pressure fluctuations as function of time downstream of the rear jet, provided having a pressure sensor with a sample frequency that is in the order of magnitude of 10 MHz.

- In the present research, conventional Schlieren techniques were used, which indirectly qualitatively represent the density gradients of the flow. A relatively novel technique that has been developed since 1998, the so-called Background-Oriented Schlieren (BOS), offers the possibility of quantifying the density in the flow and is increasingly used for flow visualization [58]. Flow structures that are presently difficult to analyze could be understood better using BOS. As a background for the images, a screen with a random dot pattern is used. See the optical path in figure 10.1. A reference image of the dot pattern with the air at rest is combined with an image of the dot pattern when density gradients are present in the flow. As a result of the density gradients, the dot pattern is distorted. Cross-correlation of the two images, similar to the technique used in Particle-Imaging Velocimetry (PIV), provides a displacement field (figure 10.2). This field is used to calculate the density from Poisson's equation (figure 10.3) [59].
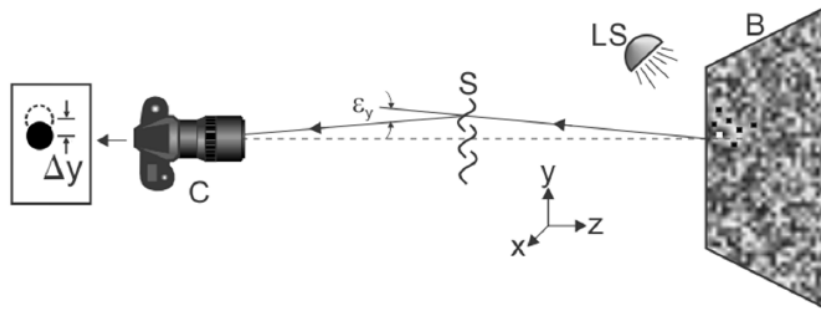
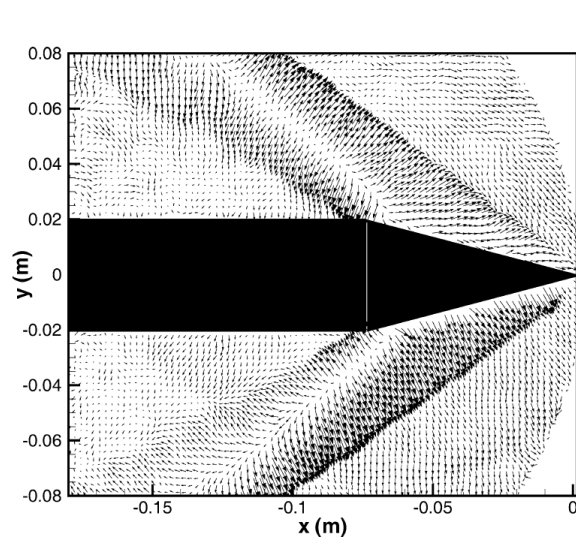Figure 10.1: Configuration of the Background-Oriented Schlieren Technique [58].

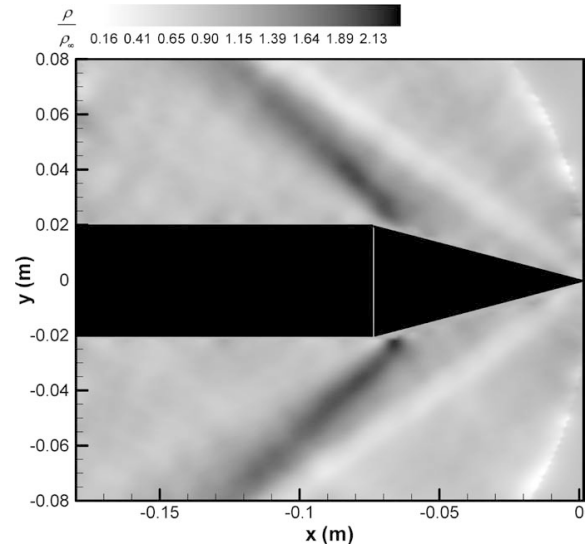Figure 10.2: Average displacement field as determined by the cross-correlation of two images [59].

Figure 10.3: Resulting density field as calculated from Poisson's equation, using the displacement field from figure 10.2 [59].

Bibliography

[1] J. D. Anderson, *A History of Aerodynamics and Its Impact on Flying Machines*. Cambridge University Press, 1st ed., 1998.

[2] J. D. Anderson, *Introduction to Flight*. McGraw-Hill, 6th ed., 2008.

[3] S. de Maag, "Schlieren Flow Visualization for Cascaded Injection in Supersonic Flow employing Power VCSEL Light Sources," Master's Thesis, University of Twente, 2019.

[4] Netherlands Ministry of Defence, "F-35 Lightning II-jachtvliegtuig." `https://www.defensie.nl/organisatie/luchtmacht/materieel/vliegtuigen-en-helikopters/f-35-gevechtsvliegtuig`. Accessed: 29 October 2020.

[5] H. W. M. Hoeijmakers, *Gasdynamics*. University of Twente, 2011.

[6] J. D. Anderson, *Fundamentals of Aerodynamics*. McGraw-Hill, 5th ed., 2011.

[7] E. Giskes, "Design and Optimization of a LED Driven Ultra-Fast Schlieren Imaging Set Up to Investigate a Sonic Jet in Supersonic Crossflow," Master's Thesis, University of Twente, 2015.

[8] R. S. Fry, "A Century of Ramjet Propulsion Technology Evolution," *Journal of Propulsion and Power*, vol. 20, no. 1, pp. 27–58, 2004.

[9] S. H. Lee, "Characteristics of Dual Transverse Injection in Scramjet Combustor, Part 1: Mixing," *Journal of Propulsion and Power*, vol. 22, no. 5, pp. 1012–1019, 2006.

[10] C. H. C. Brouwer, *Aerodynamica voor Vliegtuigen*. Delta Press, 1985.

[11] J. Sinclair and X. Cui, "A Theoretical Approximation of the Shock Stand-off Distance for Supersonic Flows around a Circular Cylinder," *Physics of Fluids*, vol. 29, p. 026102, 02 2017.

[12] B. Eck, *Technische Strömungslehre*. Springer-Verlag Berlin Heidelberg, 7th ed., 1966.

[13] Glenn Research Center, National Aeronautics and Space Administration, "Mass Flow Choking." `https://www.grc.nasa.gov/WWW/k-12/airplane/mflchk.html`, 2018. Accessed: 21 March 2020.

[14] A. Elsenaar, *0.2<Ma<4, 50 years high speed wind tunnel testing in The Netherlands*. Foundation Historical Museum NLR, 1st ed., 2011.

[15] S. G. Chuech, M. C. Lai, and G. M. Faeth, "The Structure of Sonic Underexpanded Turbulent Air Jets in Still Air," Interim Report, Michigan: Department of Aerospace Engineering, The University of Michigan, October 1987.

[16] B. C. R. Ewan and K. Moodie, "Structure and Velocity Measurements in Underexpanded Jets," *Combustion Science and Technology*, vol. 45, no. 5-6, pp. 275–288, 1986.

[17] S. M. Dash and D. E. Wolf, "Interactive Phenomena in Supersonic Jet Mixing Problems, Part I: Phenomenology and Numerical Modeling Techniques," *AIAA Journal*, vol. 22, no. 7, pp. 905–913, 1984.

[18] S. Crist, D. R. Glass, and P. M. Sherman, "Study of the Highly Underexpanded Sonic Jet," *AIAA Journal*, vol. 4, no. 1, pp. 68–71, 1966.

[19] H. Ashkenas and F. S. Sherman, "Structure and Utilization of Supersonic Free Jets in Low Density Wind Tunnels," Technical Report, Jet Propulsion Lab., California Inst. of Tech.; Pasadena, CA, United States, January 1965.

[20] M. M. Orescanin and J. M. Austin, "Exhaust of Underexpanded Jets from Finite Reservoirs," *Journal of Propulsion and Power*, vol. 26, no. 4, pp. 744–753, 2010.

[21] E. Franquet *et al.*, "Free Underexpanded Jets in a Quiescent Medium: A Review," *Progress in Aerospace Sciences*, vol. 77, pp. 25 – 53, 2015.

[22] A. Ben-Yakar, M. G. Mungal, and R. K. Hanson, "Time Evolution and Mixing Characteristics of Hydrogen and Ethylene Transverse Jets in Supersonic Crossflows," *Physics of Fluids*, vol. 18, no. 2, p. 026101, 2006.

[23] Z. A. Rana, B. Thornber, and D. Drikakis, "Transverse Jet Injection into a Supersonic Turbulent Cross-flow," *Physics of Fluids*, vol. 23, no. 4, p. 046103, 2011.

[24] D. E. Everett *et al.*, "Wall Pressure Measurements for a Sonic Jet Injected Transversely into a Supersonic Crossflow," *Journal of Propulsion and Power*, vol. 14, no. 6, pp. 861–868, 1998.

[25] J. G. Santiago and J. C. Dutton, "Velocity Measurements of a Jet Injected into a Supersonic Cross-flow," *Journal of Propulsion and Power*, vol. 13, no. 2, pp. 264–273, 1997.

[26] A. Ben-Yakar and R. K. Hanson, "Ultra-fast-framing Schlieren System for Studies of the Time Evolution of Jets in Supersonic Crossflows," *Experiments in Fluids*, vol. 32, pp. 652–666, 01 2002.

[27] W. VanLerberghe *et al.*, "Penetration and Mixing Studies of a Sonic Transverse Jet Injected into a Mach 1.6 Crossflow," in *Fluid Dynamics Conference*, 1994.

[28] F. S. Billig, R. C. Orth, and M. Lasky, "A Unified Analysis of Gaseous Jet Penetration," *AIAA Journal*, vol. 9, no. 6, pp. 1048–1058, 1971.

[29] M. R. Gruber and L. P. Goss, "Surface Pressure Measurements in Supersonic Transverse Injection Flowfields," *Journal of Propulsion and Power*, vol. 15, no. 5, pp. 633–641, 1999.

[30] D. Papamoschou and D. Hubbard, "Visual Observations of Supersonic Transverse Jets," *Experiments in Fluids*, vol. 14, pp. 468–476, 05 1993.

[31] C. W. Lerink, S. de Maag, and H. W. M. Hoeijmakers, "Shear Layer Analysis for Transverse Sonic Injection in Supersonic Cross-flow using VCSEL Schlieren Imaging." University of Twente, 2020.

[32] M. R. Gruber, A. S. Nejad, T. H. Chen, and J. C. Dutton, "Bow Shock/Jet Interaction in Compressible Transverse Injection Flowfields," *AIAA Journal*, vol. 34, no. 10, pp. 2191–2193, 1996.

[33] M. B. Sun, S. P. Zhang, *et al.*, "Experimental Investigation on Transverse Jet Penetration into a Supersonic Turbulent Crossflow," *Science China Technological Sciences*, vol. 56, no. 8, pp. 1989–1998, 2013.

[34] M. Gamba, V. A. Miller, and G. Mungal, "The Reacting Transverse Jet in Supersonic Crossflow: Physics and Properties," in *19th AIAA International Space Planes and Hypersonic Systems and Technologies Conference*, 2014.

[35] S. de Maag, H. W. M. Hoeijmakers, C. H. Venner, F. B. Segerink, and H. L. Offerhaus, "Investigation of Tandem Injection in Supersonic Flow using Schlieren Visualization," Proceedings AIAA SciTech Forum 2020, Applied Aerodynamics, Orlando, Florida, USA, January 6-10, 2020. AIAA Paper 2020-0040, 22 pages.

[36] J. A. Schetz and F. S. Billig, "Penetration of Gaseous Jets Injected into a Supersonic Stream," *Journal of Spacecraft and Rockets*, vol. 3, no. 11, pp. 1658–1665, 1966.

[37] R. Portz and C. Segal, "Penetration of Gaseous Jets in Supersonic Flows," *AIAA Journal*, vol. 44, no. 10, pp. 2426–2429, 2006.

[38] C. R. McClinton, "Effect of Ratio of Wall Boundary-Layer Thickness to Jet Diameter on Mixing of a Normal Hydrogen Jet in a Supersonic Stream," Technical Report, NASA Langley Research Center, Hampton, June 1974.

[39] M. R. Gruber, A. S. Nejad, T. H. Chen, and J. C. Dutton, "Transverse Injection from Circular and Elliptic Nozzles into a Supersonic Crossflow," *Journal of Propulsion and Power*, vol. 16, no. 3, pp. 449–457, 2000.

[40] M. R. Gruber, A. S. Nejad, T. H. Chen, and J. C. Dutton, "Mixing and Penetration Studies of Sonic Jets in a Mach 2 Freestream," *Journal of Propulsion and Power*, vol. 11, no. 2, pp. 315–323, 1995.

[41] M. R. Gruber, A. S. Nejad, T. H. Chen, and J. C. Dutton, "Compressibility effects in supersonic transverse injection flowfields," *Physics of Fluids*, vol. 9, no. 5, pp. 1448–1461, 1997.

[42] S. Z. Pinckney, "Method for Predicting Compressible Turbulent Boundary Layers in Adverse Pressure Gradients," Technical Report, NASA Langley Research Center, Hampton, August 1971.

[43] R. C. Rogers, "A Study of the Mixing of Hydrogen Injected Normal to a Supersonic Airstream," Technical Report, NASA Langley Research Center, Hampton, March 1971.

[44] A. D. Rothstein and P. J. Wantuck, "A Study of the Normal Injection of Hydrogen Into a Heated Supersonic Flow using Planar Laser-Induced Fluorescence," in *28th Joint Propulsion Conference and Exhibit*, 1992.

[45] T. F. Fric and A. Roshko, "Vortical Structure in the Wake of a Transverse Jet," *Journal of Fluid Mechanics*, vol. 279, p. 1–47, 1994.

[46] L. L. Yuan, R. L. Street, and J. H. Ferziger, "Large-eddy Simulations of a Round Jet in Crossflow," *Journal of Fluid Mechanics*, vol. 379, p. 71–104, 1999.

[47] D. Papamoschou and A. Roshko, "Observations of Supersonic Free Shear Layers," in *24th Aerospace Sciences Meeting*, 1988.

[48] D. Papamoschou and A. Bunyajitradulya, "Evolution of Large Eddies in Compressible Shear Layers," *Physics of Fluids*, vol. 9, no. 3, pp. 756–765, 1997.

[49] A. Ben-Yakar, *Experimental Investigation of Mixing and Ignition of Transverse Jets in Supersonic Crossflows*. PhD thesis, Stanford University, December 2000.

[50] C. C. Mei, "Kelvin-Helmholtz Instability of Flow with Discontinuous Shear and Stratification," 2007. Massachusetts Institute of Technology. `http://web.mit.edu/1.63/www/Lec-notes/chap5_instability/5-2KHdiscont.pdf` Accessed: 30 March 2020.

[51] A. Salih, "Kelvin-Helmholtz Instability," November 2010. Indian Institute of Space Science and Technology, Thiruvananthapuram. `https://www.iist.ac.in/sites/default/files/people/KelvinHelmholtz.pdf` Accessed: 30 March 2020.

[52] A. J. Mestel, "Kelvin-Helmholtz and Rayleigh-Taylor Instabilities," January 2007. Imperial College London. `http://wwwf.imperial.ac.uk/~ajm8/Hydrostab/kelvin.pdf` Accessed: 30 March 2020.

[53] M. Blair, "A Compilation of the Mathematics Leading to the Doublet Lattice Method," Report, Air Force Wright Laboratory, March 1992.

[54] T. Kouchi, T. Hoshino, K. Sasaya, and G. Masuya, "Time-Space Trajectory of Unsteady Jet into Supersonic Crossflow Using High-Speed Framing Schlieren Images," in *16th AIAA/DLR/DGLR International Space Planes and Hypersonic Systems and Technologies Conference*.

[55] W. O. Landsberg, V. Wheatley, and A. Veeraragavan, "Characteristics of Cascaded Fuel Injectors Within an Accelerating Scramjet Combustor," *AIAA Journal*, vol. 54, no. 12, pp. 3692–3700, 2016.

[56] G. S. Settles, *Schlieren and Shadowgraph Techniques*. Springer-Verlag Berlin Heidelberg, 2001.

[57] D. Rouwenhorst, "Experimental Study on Pressure Oscillations Induced by Supersonic Flow past a Rectangular Cavity," Master's Thesis, University of Twente, 2012.

[58] G. S. Settles and M. J. Hargather, "A Review of Recent Developments in Schlieren and Shadowgraph Techniques," *Measurement Science and Technology*, vol. 28, p. 042001, feb 2017.

[59] L. Venkatakrishnan and G. E. A. Meier, "Density Measurements using the Background Oriented Schlieren Technique," *Experiments in Fluids*, vol. 37, no. 2, pp. 237–247, 2004.
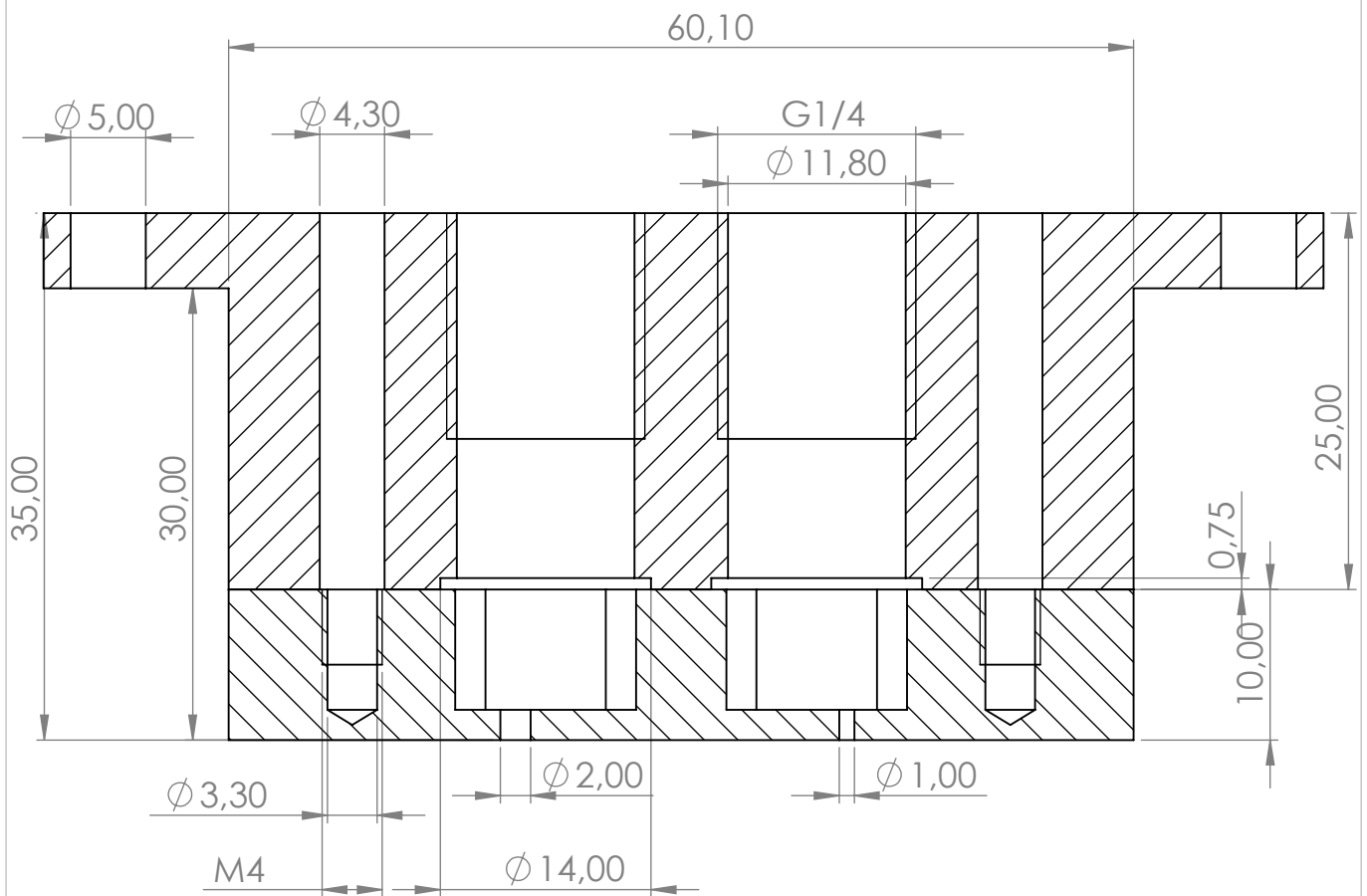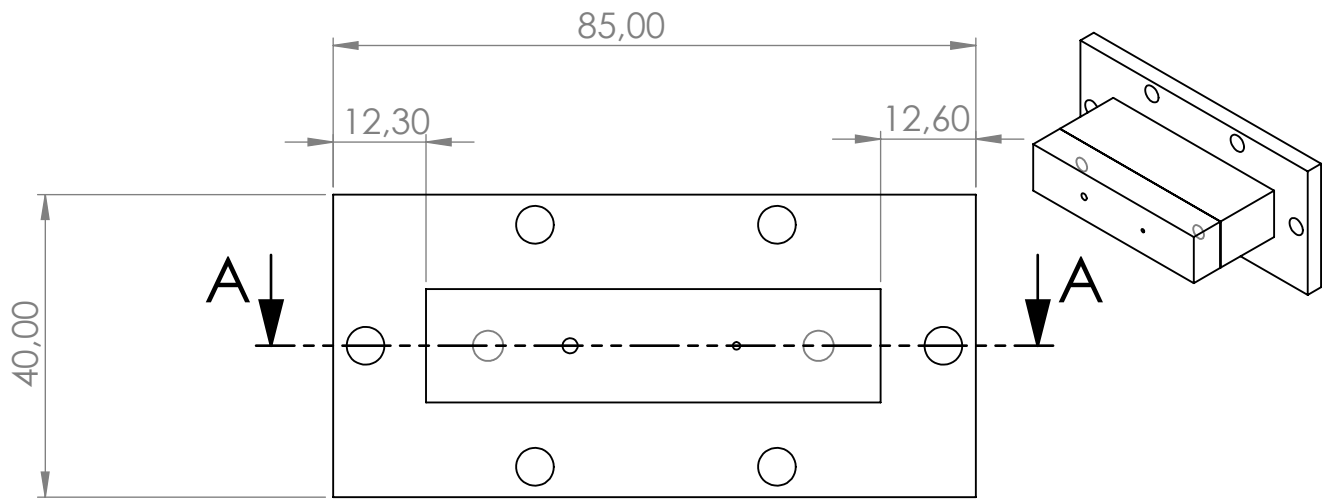
Appendix A

Technical Drawings

This appendix presents the technical drawings for the parts of the injection blocks. The drawing package is built-up as following:
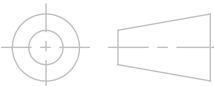
1. Total injection block: an overview drawing of the base block and the top-piece block combined.

2. Injection block base: technical drawing of the injection base block.

3. Injection block top-piece: technical drawing with variable dimensions for ten top-piece blocks for dual jet injection with different distance between two orifices.

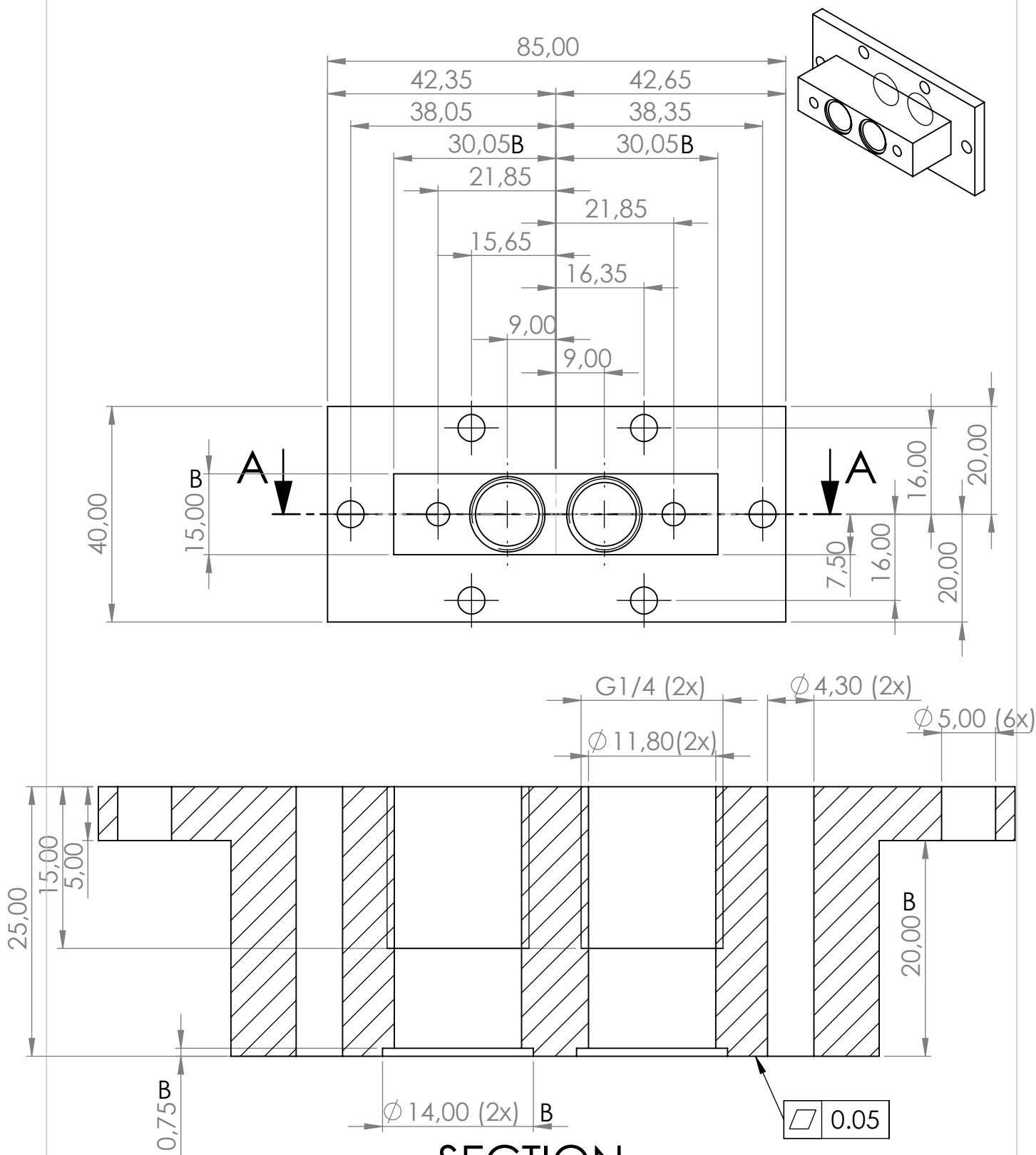4. Injection block top-piece: technical drawing of the top-piece block for single jet injection.

Note that a decimal comma is used for the dimensions in the drawings.
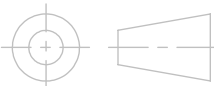
85,00

12,30

12,60

A

A

40,00

60,10

Ø 5,00

Ø 4,30

G1/4

Ø 11,80

35,00

30,00

25,00

0,75

10,00

Ø 3,30

Ø 2,00

Ø 1,00

M4

Ø 14,00

SECTION A-A

SCALE 2 : 1

PROJECTION METHOD		UNLESS STATED OTHERWISE: TOLERANCES ± 0,1 MM	DRAWN	Jan Siemen Smink		DATE	9-6-2020
			CHECKED	--		SCALE	1:1
MATERIAL		SURFACE FINISH	TITLE	Total injection block			REV.
Brass							03
--		--	DRAWING NO.	1			
UNIVERSITY OF TWENTE.			FILE / PART NAME	total_injection_block			A4
FACULTY OF ENGINEERING			DIMENSIONS IN MILLIMETERS			SHEET 1 OF 1	

85,00
42,35
42,65
38,05
38,35
30,05B
30,05B
21,85
21,85
15,65
16,35
9,00
9,00

B
A
A
B
40,00
15,00
16,00
20,00
7,50
16,00
20,00

G1/4 (2x)
Ø 4,30 (2x)
Ø 11,80(2x)
Ø 5,00 (6x)
B
25,00
15,00
5,00
20,00
B
Ø 14,00 (2x)
B
0.05
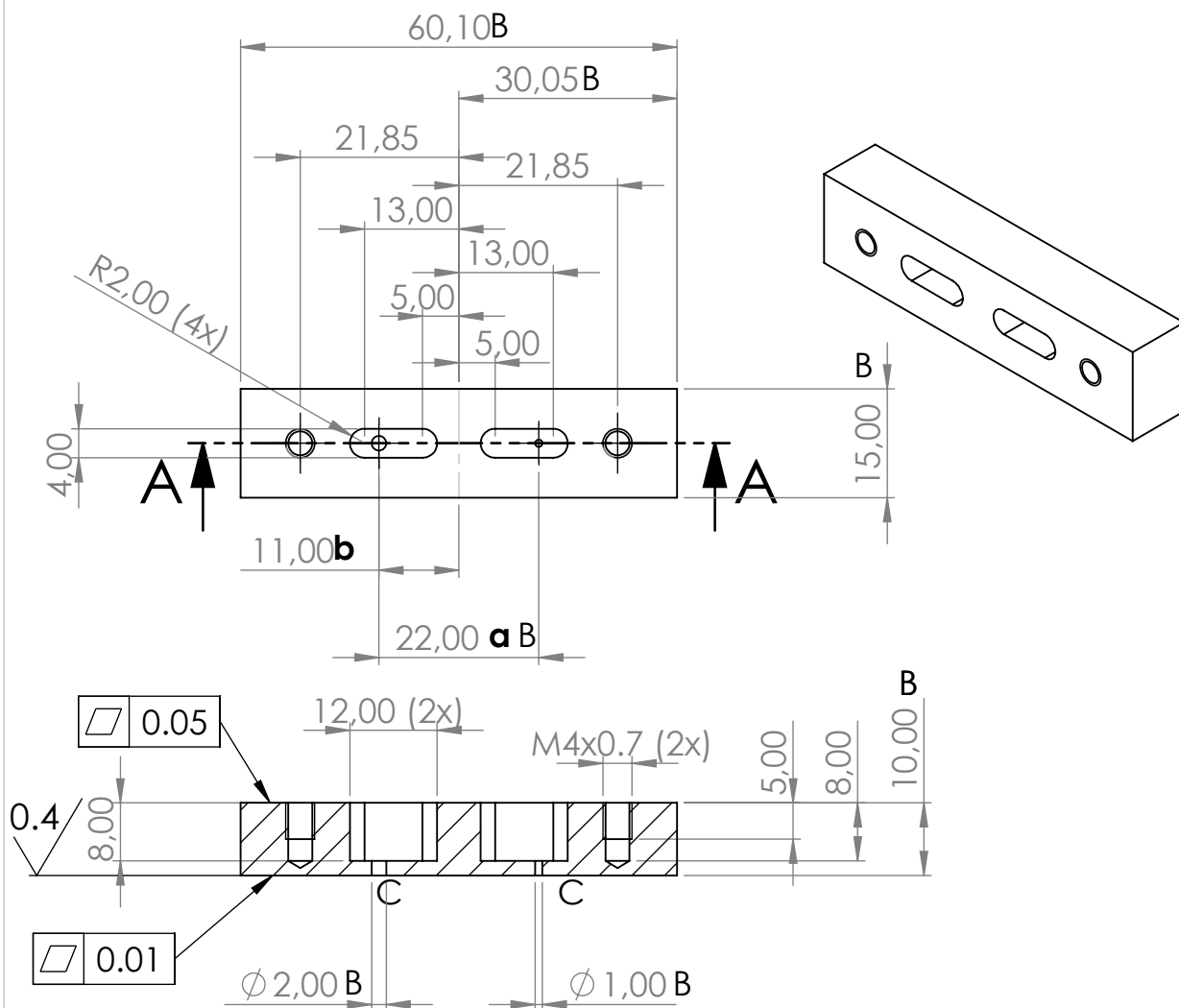0,75
B

SECTION A-A

SCALE 2 : 1
B: These dimensions as precise as possible

PROJECTION METHOD		UNLESS STATED OTHERWISE: TOLERANCES ± 0,1 MM	DRAWN	Jan Siemen Smink		DATE	9-6-2020
			CHECKED	--		SCALE	1:1
MATERIAL		SURFACE FINISH	TITLE		Injection block base		REV.
Brass							03
--		--	DRAWING NO.				
UNIVERSITY OF TWENTE.				2			A4
			FILE / PART NAME		Hoofdblok_injectie		
FACULTY OF ENGINEERING			DIMENSIONS IN MILLIMETERS			SHEET 1 OF 1	

60,10B

30,05B

21,85

21,85

13,00

13,00

5,00

5,00

R2.00 (4x)

4.00

A ↑ ↑ A

B

15,00

11,00**b**

22,00 **a** B

□ 0.05

12,00 (2x)

M4x0.7 (2x)
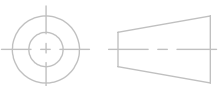
B

5,00 8,00 10,00

0.4

8,00

□ 0.01

C C

⌀ 2,00 B   ⌀ 1,00 B

SECTION A-A

B: These dimensions as precise as possible
C: The edge of the orifice as sharp as possible

Number	a	b
1	8	4.25
2	9	4.5
3	10	5
4	11	5.5
5	12	6
6	13	6.5
7	14	7
8	16	8
9	19	9.5
10	22	11

60,10 B
30,05
21,85
21,85
13,00
5,00
R2,00 (2x)
4,00
15,00
A — A
B
9,00

0.05
12,00
M4x0.7 (2x)
5,00
8,00
10,00
8,00
0.4
Ø 2,23 B
C
0.01

SECTION A-A

B: These dimensions as precise as possible
C: The edge of the orifice as sharp as possible

PROJECTION METHOD		UNLESS STATED OTHERWISE: TOLERANCES ± 0,1 MM	DRAWN	Jan Siemen Smink	DATE	9-6-2020
			CHECKED	--	SCALE	1:1